Alma Mater Studiorum - Università di Bologna

DOTTORATO DI RICERCA IN

FISICA

Ciclo XXVII

Settore Concorsuale di afferenza: 02/A1

Settore Scientifico disciplinare: FIS/01

The XENON1T experiment: Monte Carlo background estimation and sensitivity curves study

Presentata da: **Fabio Valerio Massoli**

Coordinatore Dottorato:
Chiar.^{mo} Prof. Fabio Ortolani

Relatore:
Chiar.^{ma} Prof.^{ssa} Gabriella Sartorelli

Co-relatore:
Dott. Marco Selvi

Esame finale anno 2015

Contents

Introduction **i**

1 The Dark Matter hypothesis **1**

1.1 Dark Matter evidences . . . 1

1.1.1 Galaxy scale Dark Matter evidences . . . 4

1.1.2 Bullet Cluster . . . 6

1.1.3 Dark Matter search with the Microlensing effect . . . 7

1.1.4 Cosmological evidences for Dark Matter . . . 9

1.1.5 Big Bang Nucleosynthesis . . . 12

1.2 Non-baryonic dark matter . . . 13

1.3 WIMPs . . . 16

1.3.1 The neutralino . . . 19

1.4 WIMPs direct detection . . . 23

1.4.1 DAMA/LIBRA . . . 23

1.4.2 CoGeNT . . . 27

1.4.3 EDELWEISS-II . . . 30

1.4.4 superCDMS . . . 32

1.4.5 LUX . . . 33

1.4.6 CRESST-II . . . 35

1.5 WIMPs indirect detection . . . 38

1.5.1 General AntiParticle Spectrometer (GAPS) . . . 46

1.5.2 VERITAS . . . 48

1.5.3 Super-Kamiokande . . . 50

1.5.4 Fermi-Large Area Telescope . . . 54

1.5.5 IceCube . . . 56

1.5.6 AMS-02 . . . 59

2 Dark Matter models **65**
2.1 Resonant Dark Matter Model . . . 65
2.2 Inelastic Dark Matter . . . 69
2.2.1 Magnetic inelastic Dark Matter (MiDM) . . . 71
2.3 The Dark Sector . . . 73
2.4 Exothermic Dark Matter (exoDM) . . . 75
2.5 Xenophobic Dark Matter . . . 77
2.6 MOND: a Universe without dark matter . . . 82

3 Properties of Liquid Xe as target in DM searches **89**
3.1 LXe properties . . . 89
3.2 Particle interactions in LXe . . . 92
3.3 Ionization in LXe . . . 95
3.4 Scintillation in LXe . . . 100
3.4.1 Scintillation decay time . . . 102
3.4.2 Recombination and Electron Extraction . . . 104
3.4.3 Attenuation of the VUV flux . . . 107
3.5 Discriminating particles with LXe . . . 109
3.6 Relative scintillation efficiency ($\mathcal{L}_{eff}$) for nuclear recoils . . . 109

4 The XENON Project **113**
4.1 Dual phase TPC principle detection . . . 113
4.2 XENON10 . . . 115
4.3 XENON100 . . . 121
4.3.1 Spin-independent results . . . 126
4.3.2 Spin-dependent results . . . 128
4.3.3 Solar axion and galactic ALP search results . . . 130
4.4 XENON1T design . . . 136
4.4.1 Muon Veto design . . . 137
4.4.2 LXe purification system . . . 139
4.5 XENON1T upgrade: XENONnT . . . 141

5 XENON1T Monte Carlo geometry simulation **145**
5.1 Cryostats . . . 145
5.2 Field cage . . . 149
5.3 Electrode rings . . . 156
5.4 PMTs and their support structures . . . 160
5.5 Diving bell and bottom filler . . . 165

5.6 XENON1T meshes transparency study . . . 171

6 XENON1T background estimation **175**

6.1 Introduction . . . 175
6.2 Material screening campaigns . . . 178
6.3 ER background from materials . . . 181
6.3.1 Trigger rate . . . 187
6.4 Intrinsic ER background . . . 187
6.4.1 ^{85}Kr . . . 188
6.4.2 ^{222}Rn . . . 188
6.4.3 Solar neutrinos . . . 189
6.4.4 $2\nu2\beta$ decay . . . 190
6.5 Summary of the ER backgrounds . . . 191
6.6 Nuclear recoil background . . . 195
6.6.1 Radiogenic neutrons from the materials . . . 195
6.6.2 Muon-induced neutrons . . . 199
6.7 Conversion from energy to S1 and S2 signals . . . 199
6.7.1 Generation of photons and electrons . . . 200
6.7.2 Light Collection Efficiency (LCE) . . . 203
6.7.3 Generation of S1 and S2 signals . . . 205

7 XENON1T sensitivity **211**

7.1 WIMPs expected rates . . . 212
7.1.1 The nuclear form factor . . . 215
7.1.2 Spin corrections . . . 216
7.1.3 Modulation of the WIMP signal . . . 218
7.1.4 Expected WIMP recoil spectra for spin-independent interactions . 219
7.2 The Maximum Gap method . . . 221
7.3 Sensitivity with LY = 4.6 pe/keV$_{ee}$ . . . 223
7.4 Sensitivity with LY = 5.6 pe/keV$_{ee}$ . . . 228
7.5 Sensitivity for different ^{222}Rn contaminations . . . 230
7.6 Sensitivity as function of the exposure time . . . 232
7.7 An alternative statistical test: the Likelihood Ratio method . . . 235
7.7.1 XENON1T sensitivity based on the Likelihood Ratio . . . 237

Summary and Conclusions **243**

Bibliography **249**

Introduction

A lot of astrophysical and cosmological observations support the hypothesis that a considerable amount of the energy content of the Universe is made of cold dark matter [1, 2, 3, 4], notably the discrepancy between the expected and observed rotational curves (RC) for spiral galaxies and the results from measurements of lensing effect. Recently, more detailed studies of the Cosmic Microwave Background anisotropies have deduced, with remarkable precision [5, 6], the abundance of dark matter to be about 24% of the total energy in the Universe. Candidate particles for dark matter naturally arise in a lot of theories beyond the Standard Model of particle physics, such as Supersymmetry, Universal Extra Dimensions, or little Higgs models. Although they come from different models, the candidate particles share some basic properties, mainly:

- they must be stable or very long lived, otherwise they would have decayed and disappeared long time ago or their abundance would be lower than the expected one;
- they have to be weakly interacting and colorless;
- they have not be relativistic, condition that can be achieved for adequately massive particles.

Due to such characteristics, dark matter candidates are identified under the generic name of Weakly Interacting Massive Particles (WIMPs) [7].
Among the various experimental strategies to directly detect dark matter, detectors using liquid xenon (LXe) have demonstrated the highest sensitivities over the past years. The XENON100 experiment published the world's best upper limits, down to $2.0 \cdot 10^{-45}\mathrm{cm}^2$ for $m_\chi = 55$ GeV/c^2, on spin-independent [8] and, down to $3.5 \cdot 10^{-40}\mathrm{cm}^2$ for $m_\chi = 45$ GeV/c^2, on spin-dependent [9] coupling of WIMPs to nucleons in 2012 and 2013, respectively. In October 2013, the LUX experiment, which also employs LXe as detection medium, confirmed and improved these results [10]. To significantly lower current experimental sensitivities, the XENON collaboration is focusing on the new XENON1T experiment [11]. The detector construction in the Hall B of the Gran Sasso Underground

Laboratory (LNGS) started in the fall of 2013 and will continue until mid 2015. Detector commissioning and a first science run are expected for 2015, while the full dark matter sensitivity will be reached after two years of operation. With a 30 times larger target mass, and a background goal which is 100 times lower than the one of XENON100, the maximal sensitivity to spin-independent WIMP-nucleon cross sections is expected to improve by two orders of magnitude with respect to the XENON100 limits. A robust estimation of the background rate of the XENON1T experiment is therefore mandatory in order to guarantee the success in the search for WIMPs. There are two sources which contribute to the background: the electronic recoils (ER) and nuclear recoils (NR). The ER background is from the radioactivity of the detector materials, from sources intrinsic to the medium itself (^{85}Kr and ^{222}Rn) and from physical backgrounds (solar neutrinos and ^{136}Xe double-beta decays). The nuclear recoil background is from spontaneous fission neutrons, (α, n) reactions and muon-induced interactions (spallations, photo-nuclear and hadronic interactions). Until the current generation of Dark Matter experiments, the main background source was due to ER. This source was very well characterized through Monte Carlo (MC) simulations, with results in good agreement with the expectations in XENON100 [12], EDELWEISS [13] and LUX [14]. The nuclear recoil background was estimated in LUX [14] and in XENON100 [15], but no direct measurements have been possible up to now. The ambitious goal of the XENON1T experiment implies an ultra-low background in the central detector region. Hence, a severe screening and selection program for all detector construction materials (in particular those in the close proximity to the xenon target) and powerful purification techniques to remove the intrinsic contaminants from the xenon are required. The external gammas and neutrons from muons are reduced by operating the detector at deep underground laboratory and by placing active or passive shield materials around the detector.

The purpose of the present work is to evaluate the sensitivity, as function of the WIMP mass, that the XENON1T detector will be able to reach. To this aim a detailed MC simulation code of the detector geometry has been realized. The developed code has been used to characterize the various background sources and to quantify their contribution to the background rate. Using such information and knowing the expected WIMP recoil spectra, the XENON1T sensitivity has been evaluated.

The thesis is organized as follows: in Chapter 1 the dark matter paradigm, also known as the *"missing mass problem"*, is introduced together with some experimental hints (Section 1.1). Different DM candidates are presented (Sections 1.2 - 1.3) as well as different detection techniques based on both direct and indirect observation (Sections 1.4 - 1.5). In Chapter 2, few theoretical models for WIMP interactions are introduced (Sections

2.1 - 2.5) as well as the MOdified Newtonian Dynamics (MOND) theory (Section 2.6) in which the "mass problem" is solved through a modification of the dynamic laws, instead of introducing of a new exotic kind of matter.
In Chapter 3 the Xe properties, as detection medium for WIMP searches, are described (Section 3.1). The details of the particle energy loss mechanisms are presented (Sections 3.2 - 3.4). It is also described the LXe ability to discriminate between ER and NR (Section 3.5) which is of fundamental importance for the background reduction, together with the different scintillation response of NR with respect to the ER (Section 3.6).
In Chapter 4, the XENON project is presented. The main part of the detector, the double-phase Time Projection Chamber (TPC), is introduced in Section 4.1. XENON10 and XENON100 detectors are described together with their main scientific results in Sections 4.2 - 4.3. The XENON1T experiment is introduced in Section 4.4 (it will be described in detail in Chapter 5). Section 4.5 is dedicated to the upgrade of XENON1T: XENONnT.
In Chapter 5, the entire XENON1T detector simulation is presented. The simulation work has been done using the GEANT4 toolkit, version 9.5.p01. To show the high accuracy of the implemented code, numerous images from the simulation have been compared to the CAD drawings. In particular, the volumes described are:

- the two Cryostats (Section 5.1);
- the entire field cage structure (Section 5.2);
- electrode rings (Section 5.3);
- PMTs and their support structures (Section 5.4);
- diving bell and the bottom filler (Section 5.5);
- meshes (Section 5.6).

Chapter 6 is entirely dedicated to the characterization and quantification of the background due to ER and NR. After a general introduction (Section 6.1), a punctual description of all the material contaminations, obtained through a screening campaign, is given in Section 6.2. A detailed analysis of the background from materials and from intrinsic sources is then carried out (Sections 6.3 - 6.6). Section 6.7 is devoted to the description of the procedure used to convert the background and WIMP recoil spectra, that are NR, from energy to photoelectrons (pe) to allow the evaluation of the total number of expected events in a certain energy region.
By using the results from the background analysis and having the WIMP recoil spectra

(Section 7.1), it is possible to evaluate the experimental sensitivity. This work has been done applying the *Maximum Gap* method (Section 7.2). It is a recursive method in which different values of the cross section for the WIMP-nucleon interactions are tested until it is found the one that satisfies the proper requirement about the confidence level (CL). Sensitivity has been evaluated assuming different values for several operational parameters. Specifically, first it has been assumed a value for the Light Yield (LY) equal to 4.6 pe/keV$_{ee}$ (Section 7.3), corresponding to the real transparency of the XENON1T mesh (Section 5.6); then it has been considered the case with LY = 5.6 pe/keV$_{ee}$ (Section 7.4), for a higher mesh transparency. We also analyzed different ^{222}Rn contaminations (Section 7.5): 1 μBq/kg, which is the XENON1T goal for the Rn purification system, 3 and 10 μBq/kg. Finally, different values for the exposure time have been considered (Section 7.6).

The results obtained with the Maximum Gap method have been verified using a different statistical approach based on the *Likelihood Ratio* method (Section 7.7). It is used to test hypotheses in which the test statistic is computed by using the ratio of the likelihood functions evaluated on the data samples. Using the same reference values for the operation parameters, as done with the Maximum Gap method, the XENON1T sensitivity has been evaluated.

A summary of the main results obtained in this PhD thesis and the final conclusions are drawn in the last Chapter.

Chapter 1

The Dark Matter hypothesis

First evidences for the dark matter (DM) existence came from Zwicky observations of the Coma and Virgo clusters in the early 1930s. He found that the velocity of the galaxies were about one order of magnitude higher than the expected one, as if there were non luminous mass acting on the gravitational field. Since Zwicky studies also other evidences that sustained the DM hypothesis were found: anomalies in the rotational curves of spiral galaxies, lensing effects, CMB anisotropies, etc. Triggered by such experimental results, a new campaign of search began with the final goal to "enlighten" this, apparently, new kind of non luminous matter called **dark matter**. At theoretical level, many hypothesis have been formulated about DM properties. Currently it seems that the most viable candidates for this kind of matter rise from extensions of the particle Standard Model (SM). Such candidates are grouped under the common name of Weakly Interacting Massive Particles (WIMPs) that already introduces some of their characteristics. Indeed, such matter has to have only gravitational and weak interactions, thus being "Weakly Interacting", and it has to be massive, thus being made of "Massive Particles". The most quoted candidate as WIMP comes from the *Supersymmetry*: the neutralino. With the aim to discover the existence of the dark matter, several experiments have been built. They are based on different detection techniques, direct and indirect, that allow to search and test different values for the theoretical parameters that characterized the DM properties.

1.1 Dark Matter evidences

As said, during his studies on the Coma Cluster [16], figure 1.1, Zwicky faced gravitational problems while he was trying to measure its mass.

A cluster is a set of galaxies that move together inside their own gravitational field.

Figure 1.1: The Coma Cluster, which provided the first evidence for dark matter. This image combines data from the Spitzer Space Telescope with the Sloan Digital Sky Survey to show many of the thousands of galaxies in the Coma cluster.

The dynamics of such objects is very complex and usually there is not a real centre around which the galaxies move. In order to measure the mass of the Coma cluster, Zwicky first determined the galaxy velocities inside of it, by measuring the Doppler effect of their spectra. After that, using the *Virial Theorem*, he was able to extract the gravitational force acting on each one of them and, finally, to obtain the mass of the system. Then he measured the total light output of the cluster to determine the light to mass ratio. Comparing this value to the one from the nearby Kapteyn stellar system, he found a value for the Coma cluster that was 100 times lower compared to a single Kapteyn star. Since Zwicky's results, others experimental observations showed a discrepancy to what was expected from a universe without the dark matter, thus supporting the hypothesis about its existence:

- anomalies in the rotational curves of spiral galaxies;
- observations of the Bullet Cluster;
- gravitational lensing effects;
- anisotropies in the Cosmological Microwave Background (CMB);
- numerical simulation of the structure formation;

The Virial Theorem

Consider a system of n mass points, where each point has mass m_i and position defined by the vector $\mathbf{r}_i$. Assuming that on each point acts a force $\mathbf{F}_i$ where $\mathbf{F}_i = d\mathbf{p}_i/dt$, with $\mathbf{p}_i = m_i\mathbf{v}_i$ for constant values of m_i. Thus, it is possible to define a scalar quantity given by [17]:

$$G \;=\; \sum_i \mathbf{p}_i\mathbf{r}_i, \tag{1.1}$$

where i runs over all the mass points of the system. By deriving this quantity one has:

$$dG/dt \;=\; \sum_i \mathbf{p}_i(d\mathbf{r}_i/dt) \;+\; \sum_i \mathbf{r}_i(d\mathbf{p}_i/dt). \tag{1.2}$$

The first term of equation (1.2) is twice the kinetic energy of the system:

$$\sum_i \mathbf{p}_i(d\mathbf{r}_i/dt) \;=\; \sum_i m_i\mathbf{v}_i\mathbf{v}_i \;=\; 2E_c. \tag{1.3}$$

The second term can be written as:

$$\sum_i \mathbf{r}_i(d\mathbf{p}_i/dt) \;=\; \sum_i \mathbf{r}_i\mathbf{F}_i. \tag{1.4}$$

Thus, it is possible to rewrite equation (1.2) as:

$$dG/dt \;=\; 2E_c \;+\; \sum_i \mathbf{r}_i\mathbf{F}_i. \tag{1.5}$$

Integrating equation (1.5), with respect to t, over a time interval of $\Delta t = T$ and then dividing the integral by T, one obtains the time average as:

$$\langle dG/dt\rangle \;=\; [G(T) - G(0)]/T \;=\; \langle 2E_c\rangle \;+\; \langle\sum_i \mathbf{r}_i\mathbf{F}_i\rangle. \tag{1.6}$$

Assuming $T \to \infty$ and considering that G does not grow up indefinitely with the time (that means that $\mathbf{r}_i$ and $\mathbf{v}_i$ will remain finite), the first term of the equation (1.6) becomes 0, thus giving:

$$\langle E_c\rangle \;=\; -(1/2)\langle\sum_i \mathbf{r}_i\mathbf{F}_i\rangle, \tag{1.7}$$

where $\langle E_c\rangle$ is the mean, over the time, of the sum of the kinetic energy of all the masses of the system. $\mathbf{F}_i$ is given by the sum of the external forces, $\mathbf{F}_i^{(e)}$, and internal forces, $\mathbf{F}_{ij}$, of the system:

$$\mathbf{F}_i \;=\; \mathbf{F}_i^{(e)} \;+\; \sum_{j\neq i} \mathbf{F}_{ij}. \tag{1.8}$$

Since the internal forces respect the third Newton law, $\mathbf{F}_{ij} = -\mathbf{F}_{ji}$, we have:

$$\mathbf{F}_{ij}\mathbf{r}_i \;+\; \mathbf{F}_{ji}\mathbf{r}_j \;=\; \mathbf{F}_{ij}(\mathbf{r}_i \;-\; \mathbf{r}_j) \;=\; \mathbf{F}_{ij}\mathbf{r}_{ij}, \tag{1.9}$$

where $\mathbf{r}_{ij} = \mathbf{r}_i - \mathbf{r}_j$. Finally we have:

$$\langle T \rangle \;=\; -\frac{1}{2}\langle \sum_i \mathbf{F}_i^{(e)} \cdot \mathbf{r}_i \;+\; \sum_{i<j} \mathbf{F}_{ij} \cdot \mathbf{r}_{ij} \rangle. \tag{1.10}$$

Equation (1.10) represents the **Virial Theorem** for a system of particles. If we consider a system of non-interacting gas particle, then $\sum \mathbf{F}_{ij}$ is equal to zero. If the external force is a central field, then $\mathbf{F}_i^e \cdot \mathbf{r}_i$ becomes $-r_i \frac{dU}{dr_i}$, where $U(r)$ is the potential of the central field. Under these assumptions, we can rewrite the Virial Theorem as:

$$\langle T \rangle \;=\; -\frac{1}{2}\langle U \rangle, \tag{1.11}$$

where T is the total energy of the system and U is the total potential energy ($= \sum_i U_{(r_i)}$).

1.1.1 Galaxy scale Dark Matter evidences

Spiral galaxies, such as the Milky Way, are excellent probes to test the DM hypothesis. Such systems are said "rotationally sustained" since, for them, it is possible to define a clear rotational motion. To measure the velocity distribution until the edge of a galaxy, different techniques can used depending on the used "probe"; for example to measure the velocity of the hydrogen clouds it is used the 21 cm line of the neutral hydrogen (HI) due to its characteristics of low absorption from the interstellar medium. Usually, spiral galaxies are considered as made of a central core (disk+bulge), which is supposed to contain almost all the galaxy mass and whose motion is described as a rigid body, and by an outer region. Following the Newtonian gravitational law, the velocity distribution is given by:

$$v(r) = \sqrt{\frac{GM(r)}{r}} \tag{1.12}$$

where

$$M(r) = 4\pi \int \rho(r) r^2 dr \tag{1.13}$$

is the mass inside a radius r. If we consider $M(r) = \text{const}$, outside the core of the galaxy, we have:

$$v(r) \propto r^{-1/2} \tag{1.14}$$

What is surprising is that outside the disk, and much beyond, the velocity distribution no longer follows this behavior but it remains constant as if there was matter characterized by a density that scales with the root square of the distance: $\rho \propto r^{1/2}$. This behavior is shown in figure 1.2 for the NGC 6503 dwarf spiral galaxy (figure 1.3).

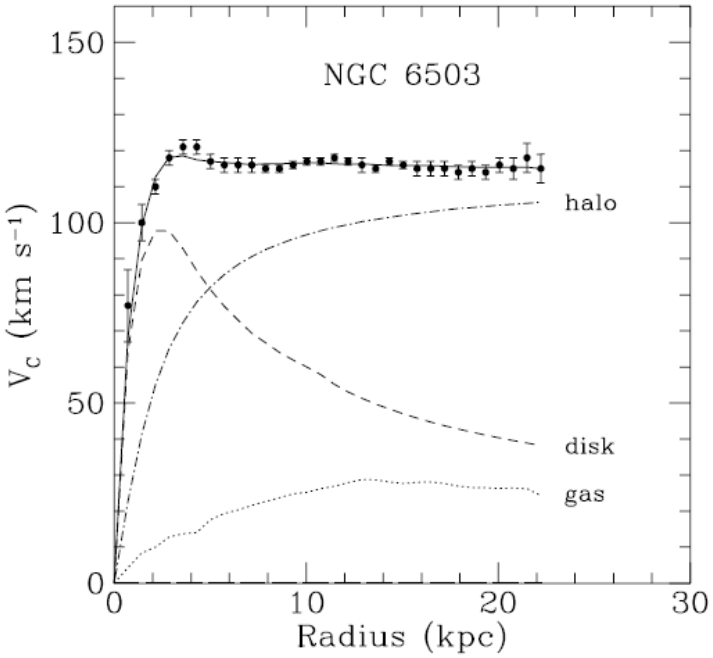

Figure 1.2: Velocity distribution of NGC 6503, a dwarf spiral galaxy located in the region of space called the "Local Void". The black dots are the observation results, while the dashed line is the expected one from the only disk contribution. Also shown are the contribution from the galaxy gas (dotted line) and halo (dash-dotted line) [18].

Figure 1.3: NGC 6503 galaxy from the Hubbles Advanced Camera for Surveys.

Such an unexpected result is explained assuming that the spiral galaxies are enclosed in dark halos with a matter distribution that expands much beyond the distribution of the luminous matter and whose effect dominates in the outer region of the galaxies. One

of the most popular density profile for the dark matter halos is the Navarro-Franck-White (NFW) profile:

$$\rho(r) = \frac{\rho_s}{(r/r_s)(1 + r/r_s)^2} \tag{1.15}$$

where r_s is the halo scale radius and ρ_s is the characteristic density. This formulation reproduces quite well the simulated halos structures in the Cold Dark Matter (CDM) models for a quite large range of masses ($3 \cdot 10^{11} \leq M_{vir}/(h^{-1}M_\odot) \leq 3 \cdot 10^{15}$).

1.1.2 Bullet Cluster

Other strong evidences, for the DM existence, come from the study of the Bullet Cluster (1E0657-558), figure 1.4. It is made by two clusters that are passing through each other. Both of them have a stellar and gaseous component that interact in a different way: the stellar component is slowed by the gravitational field of the other cluster while the two gaseous components behave as a collision particle fluid. The gas interactions result in a X-ray emission that can be measured and used to trace the baryonic matter distribution. What has been found is a discrepancy between the baryonic matter distribution, measured from the X-ray emission (red points in figure 1.4), and the gravitational field distribution obtained from lensing measurements (green lines in figure 1.4). The blue dots in figure 1.4 represent the hypothetical dark matter distribution.

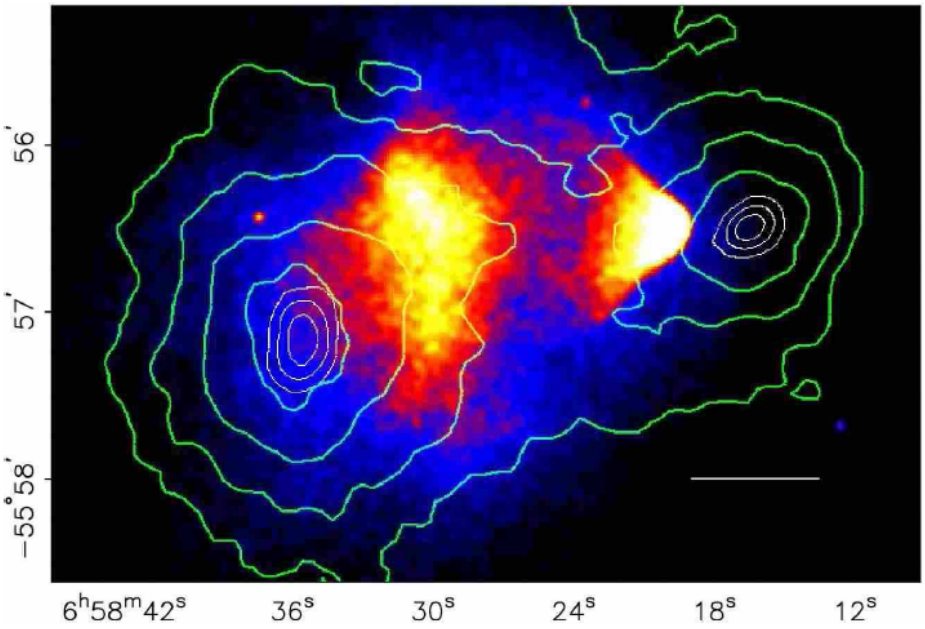

Figure 1.4: X-Ray image of the Bullet Cluster. Superimposed to the baryonic matter distribution (red points) there is the mass distribution from weak lensing measurements (green lines). In blue it is shown the putative dark matter distribution.

The matter distribution in figure 1.4 is justified by the dark matter characteristics: the low interaction characteristics of DM particles, let them to pass through each other without being disturbed along their path while, as said, it is not the case for the hot gas and stellar component. Thus continuing on its trajectory, the dark matter is placed in the outer part of the Bullet Cluster, figure 1.4.

1.1.3 Dark Matter search with the Microlensing effect

Several studies on the dark matter abundance and composition have been based on the *Microlensing* effect. Generally speaking, the lensing effect can take place whenever between a distance source (the observed object) and the observer there is a source of gravitational field (such as stars, galaxy clusters, etc.) that is able of bending the light along its path from the source to the observer. The matter distribution that generate the gravitational field represents "the lens". As a result, the observer can see multiple images or a distorted image of the source, figure 1.5.

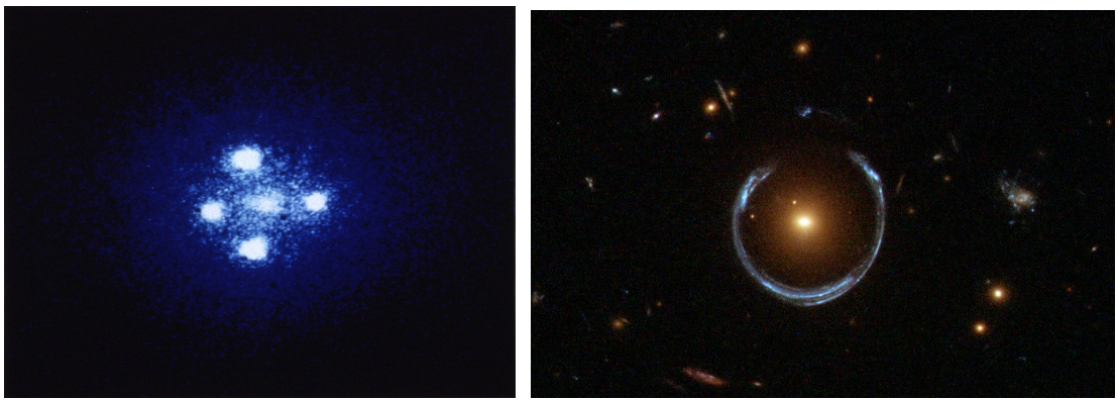

Figure 1.5: Examples of lensing effect. Left, multiple images of a quasar. Right, Einstein arcs of a background galaxy.

The microlensing effect was used to test the hypothesis that the DM was made of the so called MAssive Compact Halo Objects (MACHOs) i.e. astronomical bodies, as brown dwarfs or black holes, which might be the main component of dark matter. Such an effect is observed for lenses with small masses ($10^{-6} \leq M/M_{\odot} \leq 10^{6}$) in systems that extent on the kpc scale. Unlike the *Strong Lensing*, where multiple images of the source are observed, in the Microlensing what is observed is a time modulation of the luminosity curve of the source due to the relative motion between it and the lens:

$$L = \mu(t)\hat{L} \tag{1.16}$$

where $\hat{L}$ is the source intrinsic luminosity and $\mu(t)$ is the magnification due to the lens.

The luminosity variation happens on a time scale defined as the time needed by the source to cross the lens Einstein ring. This time is inversely proportional to the component of the source velocity, relative to the lens, which is perpendicular to the observer's line of sight. In the microlensing study it is usually defined a quantity called *optical depth* (τ), used to quantify the probability of a background source to be lensed. The optical depth is given by:

$$\tau = \frac{1}{\delta\Omega}\int dV n(D_L)\pi\theta_E^2 \tag{1.17}$$

where $\delta\Omega$ is the observation solid angle, $n(D_L)$ is the micro-lens density as function of lens distance (D_L) and $\pi\theta_E^2$ is the micro-lens cross section (with $\theta_E = \sqrt{\frac{4GM}{c^2}\frac{D_{LS}}{D_L D_S}}$, being the Einstein radius). Assuming a flat space-time and constant density along the line of sight, we have:

$$\tau \approx \frac{2\pi}{3}\frac{G\rho}{c^2}D_S^2 \tag{1.18}$$

where D_S is the source distance. For a galaxy like the Milky Way one has:

$$v^2 \approx \frac{GM_g}{r} \rightarrow M_g = \frac{rv^2}{G} \tag{1.19}$$

and

$$\rho \approx \frac{3M_g}{4\pi r^3} \approx \frac{3}{4\pi G}\left(\frac{v}{r}\right)^2. \tag{1.20}$$

Thus, the optical depth is given by:

$$\tau \approx \frac{1}{2}\left(\frac{v}{r}\right)^2 \tag{1.21}$$

For the Milky Way $\tau \approx 10^{-6}$. That means that roughly one out of a million stars in the nearby galaxies will be lensed. In this way, counting the micro-lenses in a particular direction it is possible to characterize the lens population. The possibility of detect such events depends on their duration (the Einstein crossing time). This is determined by the transverse velocity $v_\perp$ and by the lens mass. For micro-lenses in the halo of the galaxy ($D_L \sim 10$ kpc) with velocity ~ 200 km/s, one has:

$$t_E \approx 6\cdot 10^6\ s\left(\frac{M}{M_\odot}\right)^{0.5} \approx 0.2\ \text{yr}\left(\frac{M}{M_\odot}\right)^{0.5} \tag{1.22}$$

If all events had the same time scale, then the number of expected events, N, in the monitoring time Δt is given by:

$$N = \frac{2}{\pi}n\tau\frac{\Delta t}{t_E} \tag{1.23}$$

where n is the total number of considered sources. Several research groups worked on the identification of lenses in the Milky Way's halo looking at sources in the Large and Small

Magellanic Clouds (LMC and SMC). After years of analysis of the data, few microlensing events were observed leading to the conclusion that MACHOs can account only for less than 20% of the halo mass [19, 20], figure 1.6.

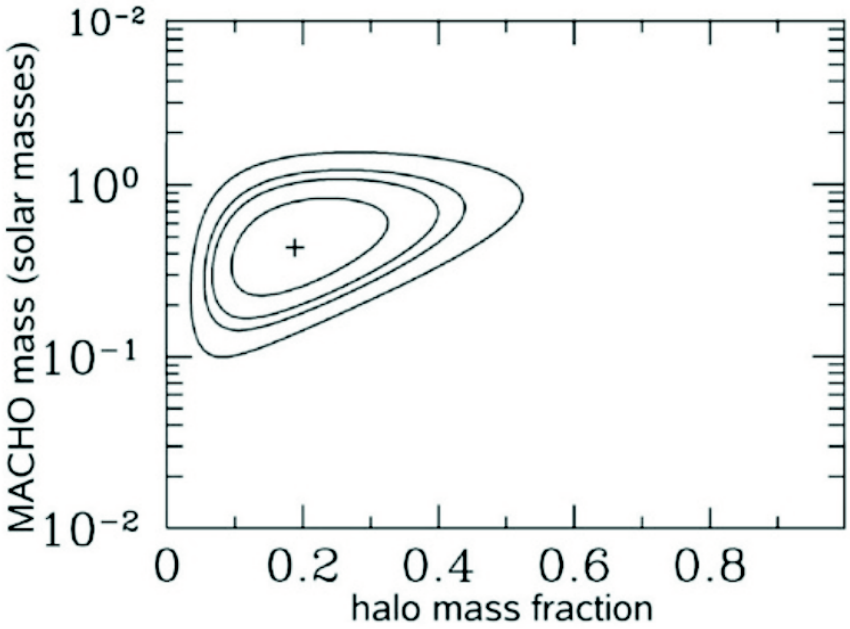

Figure 1.6: Likelihood contours obtained from the MACHO experiment. The abscissa is the fraction of the halo mass contained in MACHOs, the ordinate is the MACHO mass. The contours shown are the 60%, 90%, 95% and 99% confidence levels.

New observation campaigns are currently on going aimed to observe microlensing events in the M31 galaxy (Andromeda galaxy). Due to its larger distance compared to the L/SMC galaxies, it is not possible any more to distinguish single stars and this totally changes the observation strategy. In this case it is the total luminosity of the galaxy that should change and so only high magnification events gives appreciable signal. There are several advantages in looking at M31: due to its inclination along the line of sight, figure 1.7, it is possible to accurately obtain its rotation curve. Also, due to the inclination, the lensing effects show an asymmetry that is not possible to explain only with the stars self-lensing.

1.1.4 Cosmological evidences for Dark Matter

The lensing studies showed that, even if the dark matter exists, it is mainly composed by non-baryonic matter. Other strong experimental evidences that sustain such a scenario come from the CMB power spectrum analysis, the Big Bang Nucleosynthesis (BBN) and the N-body simulations of the structure formation history.

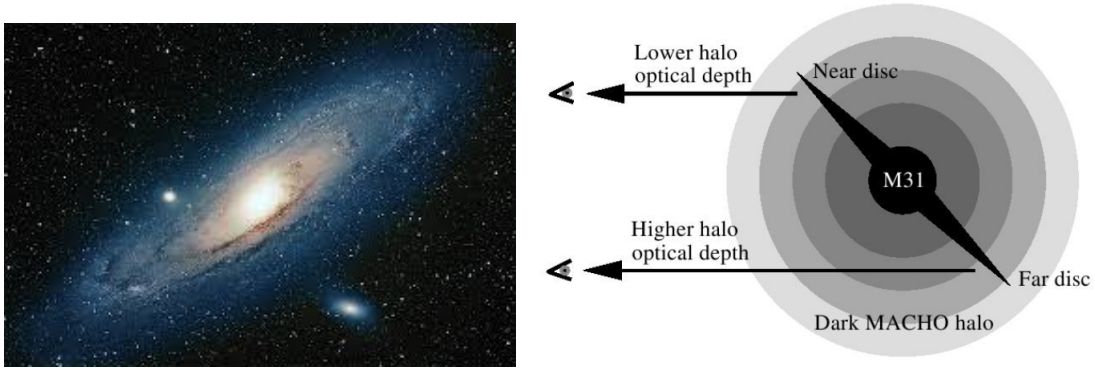

Figure 1.7: Left, picture of the M31 galaxy. Right, representation of the M31 galaxy as seen from the Milky Way.

The Cosmic Microwave Background (CMB), discovered by Arno Penzias and Robert Wilson in 1964 [21], gives important hints on the dark matter existence, composition and in particular on its total abundance in the Universe. The CMB is made of photons from the early Universe as soon as it began transparent to the radiation, i.e. when the temperature dropped at about 3000 K. At such a temperature the electrons recombined with protons and the universe became transparent to the photons as they had not enough energy to ionize the hydrogen. The CMB almost perfectly follows an ideal black body spectrum with a temperature of $T = 2.726$ K. It shows temperature anisotropies (figure 1.8 [22]), at a level lower than 10^{-5}, that give crucial informations on the Universe composition.

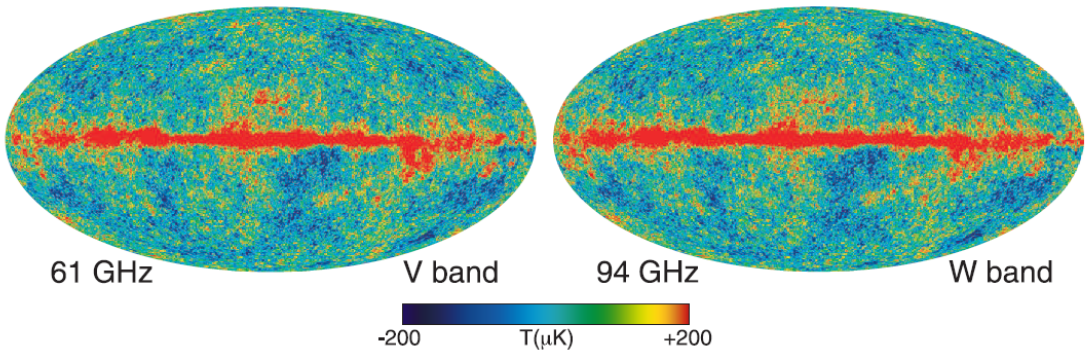

Figure 1.8: Temperature sky maps in Galactic coordinates shown in a Mollweide projection [22].

The anisotropies stem from quantum fluctuations of the inflation fields that were stretched, at cosmological scale, during the inflation and became density fluctuations at its end. At that time, baryons and photons were well coupled and the latter inherited

the density fluctuations as temperature fluctuations. This happened because photons coming from a region with higher density were more redshifted as they lose more energy to overcome the potential well (Sachs-Wolf effect) [23]. The opposite effect of the gravitational force, which attracted the photons into the higher density regions, and the gas pressure, which pushed them apart, gave to the CMB spectrum the characteristic peak structure, figure 1.9. The angular power spectrum is obtained by decomposing the anisotropy map into spherical harmonics, while taking into consideration various distortions such as emissions from galaxies. The anisotropies can be described as:

$$\frac{\delta T}{T}(\theta,\phi) = \frac{T(\theta,\phi) - \langle T(\theta,\phi)\rangle}{\langle T(\theta,\phi)\rangle} = \sum_{l=2}^{+\infty}\sum_{m=-l}^{+l} a_{lm} Y_{lm}(\theta,\phi) \tag{1.24}$$

where $Y_{lm}(\theta,\phi)$ are spherical harmonics.

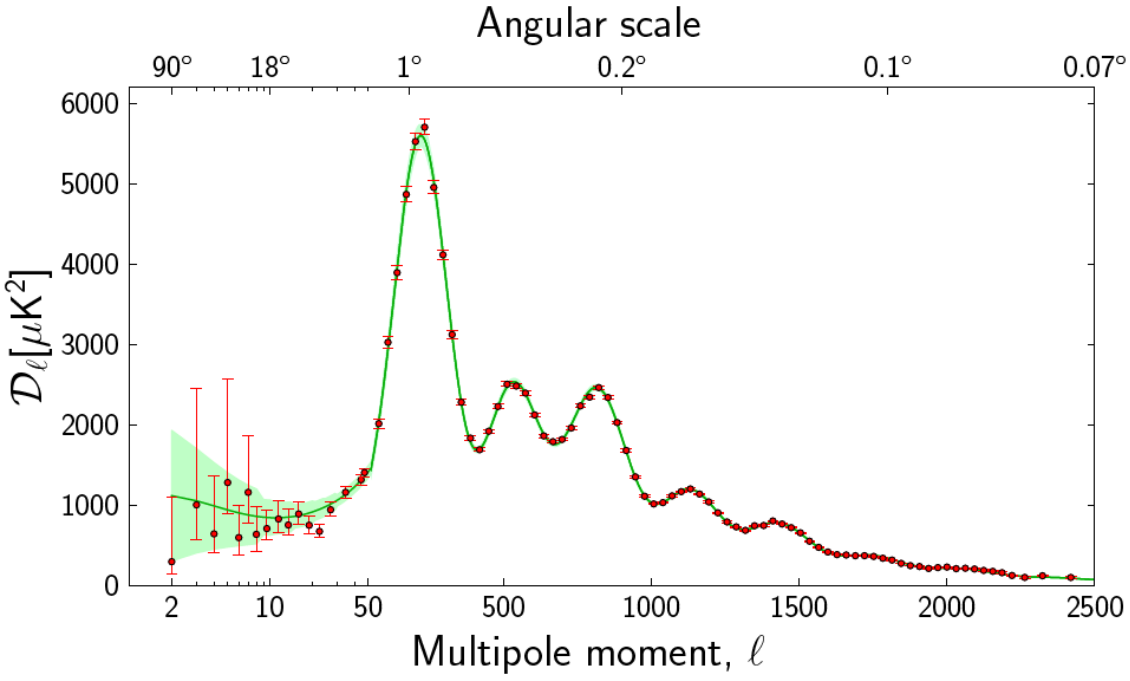

Figure 1.9: The 2013 Planck CMB temperature angular power spectrum. The error bars include cosmic variance, whose magnitude is indicated by the green shaded area around the best fit model [24].

The size and the position of the peaks of the CMB spectrum, figure 1.9, provide valuable information on cosmological parameters, such as the curvature and energy-matter composition of the universe: Ω_{tot}, Ω_b and Ω_{DM}. From the CMB study [22, 25] it is then possible to have a measure for the abundance of non-baryonic dark matter in

the Universe:

$$\Omega_\Lambda = 0.707 \pm 0.010; \tag{1.25}$$

$$\Omega_m = 0.293^{\pm 0.056}_{\pm 0.010}; \tag{1.26}$$

$$\Omega_b h^2 = 0.02211 \pm 0.00034; \tag{1.27}$$

$$\Omega_{DM} h^2 = 0.1162 \pm 0.0020. \tag{1.28}$$

From the values of the cosmological parameters it is clear that the dark energy (Λ) accounts for about 70% of the Universe energy content while the majority of the matter content is in the form of non-baryonic dark matter. The abundance of the baryonic matter is also in agreement with what expected from the BBN, which is another strong point in favor of the DM existence.

1.1.5 Big Bang Nucleosynthesis

The Big Bang Nucleosynthesis (BBN) is the process that describes the formation of light elements during the very hot phase of the universe [26]. The knowledge about this process is crucial because, comparing the observed abundance of light elements with the predicted one, it is possible to constrain the baryonic matter abundance of the universe (Ω_b) and then compare the results with the independently determined values from the CMB anisotropy measurements. The BBN happened about three minutes after the Big Bang, when the Universe was cold enough to allow the formation of atoms, and ended about seventeen minutes after it. At that time, elements beyond beryllium were not created because of the absence of stable nuclei with 5 or 8 nucleons. The predicted primordial mass abundance of light elements is: $\sim$ 75% H, 25% ^{4}He, 0.01% D (^{2}H) and 10^{-10} ^{7}Li [27]. From the study of the H II regions within dwarf galaxies [28], the primordial abundance of ^{4}He is inferred. Its observed amount is far larger than what could have been generated by stellar nucleosynthesis, thus the BBN is required. For what concerns the ^{7}Li, its amount can be deduced by probing the outermost layers of old stars. In such regions much less stellar nucleosynthesis has occurred, thus having a mixture that resembles the primordial fluid [29]. The predicted and measured ^{7}Li abundances have the same order of magnitude. The lack of a better agreement is more likely due to our incomplete understanding of stellar physics rather than of BBN. In figure 1.10 are shown the limits, from the observed abundances, on the baryon fractional density. The results show that: $0.017 \geq \Omega_b h^2 \geq 0.024$ (95% CL) [27]. Also shown is the bound independently determined by the Wilkinson Microwave Anisotropy Probe (WMAP) measurements which remarkably agrees with the bounds set by BBN.

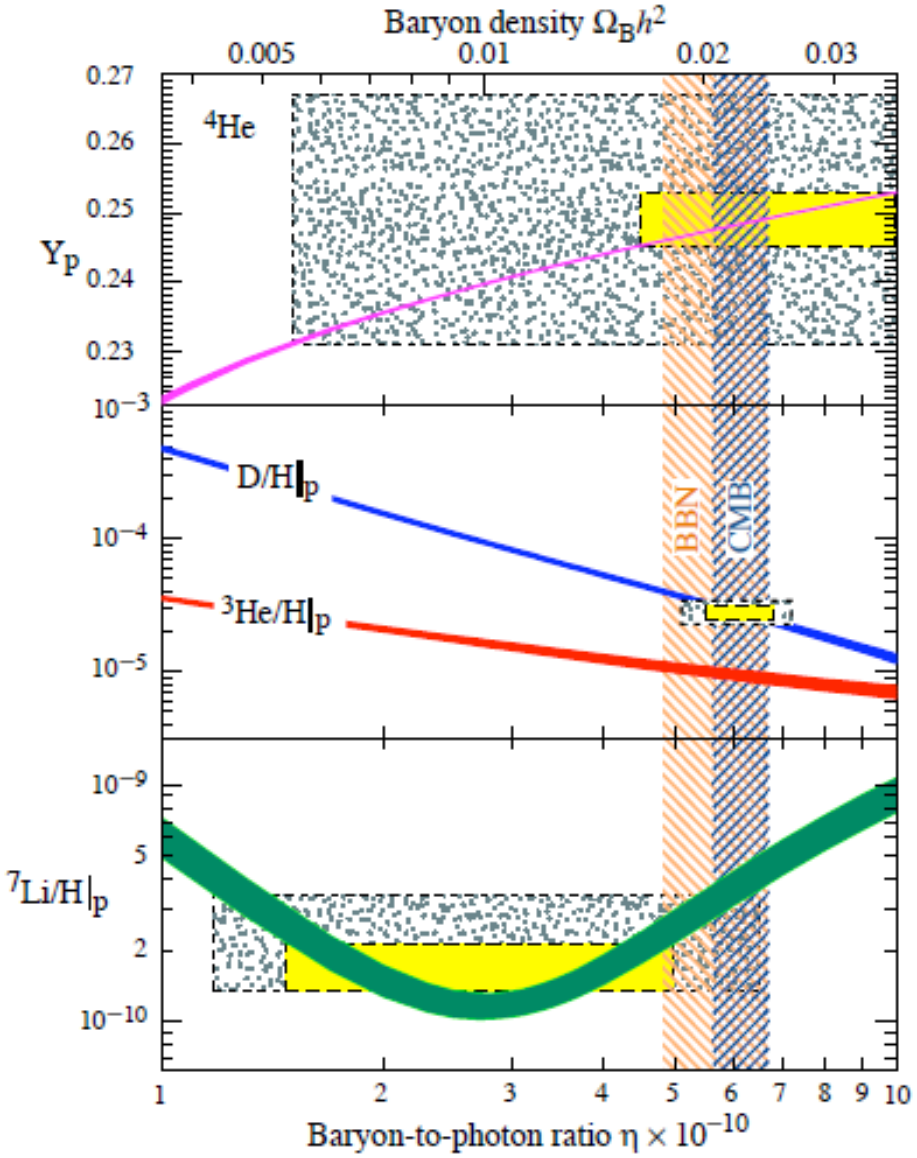

Figure 1.10: The abundance of ^{4}He, D, ^{3}He and ^{7}Li relative to H as a function of the baryon/photon fraction (η) or the reduced baryon density ($\Omega_b h^2$). The blue line indicates the 1σ predicted values. The hatched areas are values determined by measuring various primitive astronomical sources [27].

1.2 Non-baryonic dark matter

From microlensing studies and cosmological observations it is now clear that the majority of the dark matter is non-baryonic. Zeldovich hypothesized a scenario, named *Hot Dark Matter*, where the dark matter particles were relativistic. It implied a top-down

structure formation history where the big structures came first. Anyway, the evolution of such systems were too slow compared with the time scale of the primordial galaxy formation. Moreover, the high energy of the DM particles was in contrast to the formation of such big structures since relativistic particles would be dispersed in the space. Nowadays, the most accepted and supported DM scenario is the *Cold Dark Matter* (CDM), in which dark matter is not relativistic. First evidences for the CDM came from the N-body simulations done by by Jeremiah Ostriker and James Peebles [30], in the 1970s. They simulated the interactions of a distribution of mass points, that represented stars moving in a galaxy, rotating around a central point. To get the correct interactions between the mass points, they used the Newton's law. They found that, in a time less than an orbital period, most of the mass points would have collapsed to a bar-shaped dense concentration, close to the center of the galaxy, with only few mass points at larger radii. This result has nothing to share with the elegant spiral or elliptical shapes of the galaxies that we know. However, when they added a static and uniform distribution of mass, 3 to 10 times the size of the total mass of the mass points, they found more recognizable structures. Thus, Ostriker and Peebles had solid numerical evidence that cold dark matter was necessary to form the types of galaxies we observe in the universe. From the previous discussions it is possible to conclude that the dark matter is made of cold non-baryonic matter. As it is described in the next sections, the Standard Model (SM) of particles does not offer any viable candidate to be the major constituent of this kind of matter. Instead, several candidates arise naturally from SM extensions as the *Supersimmetry* (SUSY) or the *Extra dimensions* models. Concerning SUSY, many interesting features make it attractive, including its role in understanding the fundamental distinction between bosons and fermions and the problems of hierarchy for neutrinos. Also, it provides an excellent dark matter candidate in terms of its lightest stable particle (LSP), the *neutralino*. In the Extra dimensions model [31], the space is considered to have four dimensions needed to include electromagnetism into a "geometric" theory of gravitation. Also in this scenario, the lightest particle (*Kaluza-Klein* particle) is a viable candidate for the dark matter.

Neutrinos

In the Standard Model (SM) context, one of the first hypothesis about the non-baryonic dark matter composition was based on **neutrinos**. They were one of the first suggested candidates due to their properties: they are "stable", interact with the ordinary matter very weakly and are massive. From the cosmology, we have that their relic density is

given by:

$$\Omega_\nu h^2 = \sum_{i=1}^{3} \frac{m_i}{93 \text{ eV}} \tag{1.29}$$

where m_i is the mass of the $i-th$ neutrino. The most stringent constraints on their masses come from [32]:

$$\sum m_\nu < 0.18 \text{ eV (95\% CL)} \tag{1.30}$$

From this upper bound on the neutrino mass, the resulting relic density is not enough to explain the dark matter as mainly composed by them. Besides this, there is also another reason that explains why these particles cannot be valid WIMP candidates. Being relativistic collisionless particles, neutrinos erase (moving from high to low density regions) fluctuations below a scale of $\sim$ 40 Mpc(m_ν/30 eV), called the *free-streaming* length, implying a top-down formation history of the Universe As said, this scenario is excluded by the simulations of the structure formation history and also by the observation that our galaxy appears to be older than the Local Group and the discrepancy between the predicted late formation of galaxies, at redshift $z < 1$, and the observations of galaxies around $z > 4$ [33].

Axion

Remaining in the SM scenario, the **axion** is another dark matter candidate. This particle is a Nambu-Goldstone boson which corresponds to the phase of a complex field, the Peccei-Quinn field, which breaks $U(1)_{PQ}$ by its vacuum expectation value. The $U(1)_{PQ}$ field is a global $U(1)$ symmetry, which carries QCD anomalies, proposed by Peccei and Quinn as solution to the strong CP problem. This symmetry is broken at scale of f_a which is the axion decay constant or PQ scale. The relic abundance of the axions can be expressed, using the QCD scale $\Lambda_{QCD} \sim 200$ MeV [34], as:

$$\Omega_a h^2 = \theta^2 \left(\frac{f_a}{10^{12} \text{GeV}} \right)^{1.175} \tag{1.31}$$

With $\theta \sim 0.1$ and $f_a \sim 10^{12}$ GeV we have that axions can represent an important percentage of the CDM which might consist only of axions. They can be detected through the *Primakoff effect* where an axion is converted into a photon under a proper magnetic field. The CERN Axion Solar Telescope (CAST) [35] and the PVLAS [36] are involved in the search of these particles. While the former looks for solar axions, the latter fires polarized light through a long vacuum region with a 5.5 T magnetic field and searches for anomalous rotations of polarization; according to the theory, the vacuum becomes birefringent, thus photons with polarization aligned with the magnetic field are

delayed as they are preferentially transformed into axions which travel slower than the speed of light. The PVLAS collaboration initially claimed the detection of an irregular rotation corresponding to an axion mass of 1-1.5 meV, but retracted their results upon obtaining a null result after upgrades. The current strongest limits, on the axion mass, have been set by the XENON100 experiment [37] (section 4.3.3) that excludes masses above 0.3 eV/c^2, DFSZ model [38], and above 80 eV/c^2, KSVZ model [39].

1.3 WIMPs

Going beyond the standard model, dark matter particles are identified with the general definition of: Weakly Interacting Massive Particles (WIMPs). They are stable, cold, non-baryonic and interact only through gravitational and weak forces. There are several WIMP candidates raising, for example, from Supersymmetry; the most promising among them is lightest supersymmetric particle (LSP), the *neutralino*. It has a mass that ranges from few up to hundreds of GeV and it is stable if the R-parity is conserved. If WIMPs are stable, there is a cosmological relic abundance produced during the Big Bang. Assuming for such particles a mass m_χ, one has that for $T > m_\chi$ they were in thermal equilibrium while at temperatures below m_χ they decoupled and their abundance started to lower. Finally, when the expansion rate of the Universe became larger than the annihilation rate ($\Gamma < H$, where H is the Hubble constant), the WIMPs abundance "freezes out" resulting in the current relic abundance. The evolution of the WIMP density is described by the Boltzmann equation:

$$\frac{dn_\chi}{dt} + 3Hn_\chi = -\langle\sigma_a v\rangle[(n_\chi)^2 - (n_\chi^{eq})^2], \tag{1.32}$$

where n_χ^{eq} is the number density at the thermal equilibrium and $\langle\sigma_a v\rangle$ is the thermally averaged total annihilation cross section. For massive particles (non-relativistic limit) and in the Maxwell-Boltzmann approximation, n_χ^{eq} is given by:

$$n^{eq} = g\left(\frac{m_\chi T}{2\pi}\right)^{3/2} e^{-m_\chi/T} \tag{1.33}$$

where g is the number of degree of freedom, m_χ is the particle mass and T is the temperature. As said, the "freeze out" is verified for $\Gamma = H$ that results in a temperature $T = m_\chi/20$. Introducing the entropy density $s = 2\pi 2 g_* T^3/45$, where g_* counts the number of relativistic degrees of freedom, and using the conservation of entropy per co-moving volume one has:

$$(n_\chi/s)_0 = (n_c hi/s)_f = \frac{H(T_f)}{\langle\sigma_a v\rangle s(T_f)} \equiv 100\frac{1}{g_*^{1/2} m_\chi m_{Pl}\langle\sigma_a v\rangle}, \tag{1.34}$$

where m_{Pl} is the Planck mass and the subscripts 0 and f denote values for today and at freeze-out, respectively. Thus, the relic density can expressed as function of the annihilation rate:

$$\Omega_\chi h^2 = \frac{m_\chi n_\chi}{\rho_c} \equiv 3 \cdot 10^{-27} \frac{\mathrm{cm^3 s^{-1}}}{\langle \sigma_a v \rangle} \tag{1.35}$$

that is independent from m_χ. The annihilation cross section of a new particle interacting at the weak scale can be estimated as: $\langle \sigma_a v \rangle \sim 10^{-25}$ cm^3 s^{-2}. This value is close to that derived from cosmological arguments which strongly suggests that if a stable particle associated with the electro-weak scale interactions exists, then it is likely to be the dark matter particle. This coincidence has provided strong motivation for finding WIMPs.

Sneutrino and Gravitino

In the SUSY context the **sneutrino** and **gravitino**, the superpartners of the SM neutrino and graviton, have been considered as DM candidate. Concerning the former, it is a viable candidate if its mass is in the range [550, 2300] GeV/c^2. Despite this possibility, it has been rejected since its cross section would be higher than the current found limits. The gravitino has only the gravitational interaction and this makes it very hard to detect [40]. The most important coupling for the gravitino is given by:

$$\begin{aligned} \mathcal{L} = &-\frac{1}{\sqrt{2} m_P} \mathcal{D}_\nu \phi^{i*} \overline{\tilde{\phi}}_\mu \gamma^\nu \gamma_\mu \psi^i - \frac{1}{\sqrt{2} m_P} \mathcal{D}_\nu \phi^i \overline{\psi}^i \gamma^\mu \gamma^\nu \overline{\psi}_\mu - \\ &- \frac{i}{8 m_P} \overline{\tilde{\psi}}_\mu [\gamma^\nu, \gamma^\rho] \gamma^\mu \tilde{\lambda}^a F^a_{\nu\rho} \end{aligned} \tag{1.36}$$

where $\tilde{\psi}_\mu$ is the gravitino field, ϕ^i and ψ^i are the complex scalar fields and the corresponding chiral fermion fields, $\tilde{\lambda}^a$ are the gaugino fields, m_P is the reduced Planck scale ($\simeq 2.44 \cdot 10^{18}$ GeV) and D_ν is the covariant derivate. Gravitinos can be produced in $2 \rightarrow 2$ processes such as scalar-fermion-gravitino or gaugino-gauge boson-gravitino vertices [40]. The relic gravitino abundance is given by [41]:

$$\Omega_{\tilde{G}} h^2 \approx 0.2 \left(\frac{T_r}{10^{10} \text{ GeV}} \right) \left(\frac{100 \text{ GeV}}{m_{\tilde{G}}} \right) \left(\frac{m_{\tilde{g}}(\mu)}{1 \text{ TeV}} \right) \tag{1.37}$$

where $m_{\tilde{g}}$ is the gluino mass.

Axino

The **Axino**, $\tilde{a}$, is the superpartner of the axion and it is a Majorana chiral fermion. Its mass is strongly model-dependent ([1 eV, $\mathrm{M_{SUSY}}$]) and meaning that it can be the

lightest particle, thus stable, in SUSY models. The most important couplings for $\tilde{a}$ can expressed as:

$$\mathcal{L} = i\frac{3\alpha_Y C_{aYY}}{8\pi f_a}\overline{\tilde{a}}\gamma_5[\gamma^\mu,\gamma^\nu]\tilde{B}B_{\mu\nu} + i\frac{3\alpha_S}{8\pi f_a}\overline{\tilde{a}}\gamma_5[\gamma^\mu,\gamma^\nu]\tilde{g}^b F^b_{\mu\nu} \tag{1.38}$$

where B and $\tilde{B}$ are the gauge and gaugino fields corresponding to $U(1)_Y$, F^b and $\tilde{g}^b$ are the gluon and gluino fields, α_Y and α_S are the $U(1)_Y$ and strong fine-structure constant and C_{aYY} is model-dependent coefficient of order of unity. A production channel for $\tilde{a}$ is the decay of non-thermal particles. An example of this process is the decay of the lightest stau mass eigenstate $\tilde{\tau}_2$.

Kaluza-Klein

Kaluza-Klein dark matter was proposed by Kaluza and Klein [31], in the *Extra dimensions* model. If standard model particles propagate in such Extra dimensions and KK parity is conserved, the lightest KK particle is stable, becoming an excellent candidate for DM [31]. The mass of the first stable KK particle ranges from several hundreds of GeV up to few TeV, and can be detected via elastic scattering in the dark matter direct search experiments, or indirectly via annihilation products, such as positrons from the galactic halo, gamma rays from the galactic center, high energy neutrinos from the core of the Sun or the Earth, and antiproton. Due to their characteristics, a tonne-scale detector is required to detect their interactions thus, it is necessary to wait for experiments as XENON1T.

Wimpzillas

The **Super heavy dark matter** (the *wimpzillas*), particles with masses above 10^{10} GeV/c^2, has also been proposed as a valid dark matter candidate. In the early Universe there were different available channels to produce such particles as the gravitational production at the end of inflation, resulting from the expansion of the background space-time. The interaction cross section of such particles with ordinary matter, can vary from very weak to strong (in the latter case super-massive particles are sometimes called simpzillas). The wimpzillas have been proposed as a first explanation for the observed ultra high energy cosmic rays, above the GZK cut-off ($\sim 5 \cdot 10^{19}$ eV). Above this energy the Universe, on cosmological scale ($\geq$ 50 Mpc), is opaque to protons. Since sources for such energetic protons have not been observed yet, a possible explanation for their existence is that they are produced in the decay or annihilation of super heavy dark matter particles (top-down cosmic-ray models [42]).

1.3.1 The neutralino

The Minimal Supersymmetric Standard Model (MSSM) contains the smallest possible field content necessary to give rise to all the Standard Model (SM) fields. All of the SM particles have R-parity equal to 1 and all sparticles, their superpartners, have $R = -1$. Thus, from R-parity conservation (first introduced to suppress the rate of proton decay), sparticles can only decay into an odd number of sparticles (plus Standard Model particles). The Lightest Supersymmetric Particle (LSP) is, therefore, stable and can only be destroyed via pair annihilation, making it an excellent dark matter candidate. Among few alternatives, the most promising LSP is the lightest *neutralino*, which is uncharged under electromagnetic or strong interaction.
In the MSSM, binos ($\tilde{B}$), winos ($\tilde{W}_3$) and higgsinos ($\tilde{H}_1^0$ and $\tilde{H}_2^0$) states mix into four Majorana fermionic mass eigenstates, called neutralinos. The four neutralinos are labeled as: $\tilde{\chi}_1^0$, $\tilde{\chi}_2^0$, $\tilde{\chi}_3^0$ and $\tilde{\chi}_4^0$. The first of them is the lightest one and it is referred as **the neutralino**, $\chi = \tilde{\chi}_1^0$. Its mass matrix is given by:

$$\mathbf{M}_\chi = \begin{pmatrix} M_1 & 0 & -M_Z \cos\beta \sin\theta_W & M_Z \sin\beta \sin\theta_W \\ 0 & M_2 & M_Z \cos\beta \cos\theta_W & -M_Z \sin\beta \cos\theta_W \\ -M_Z \cos\beta \sin\theta_W & M_Z \cos\beta \cos\theta_W & 0 & -\mu \\ M_Z \sin\beta \sin\theta_W & -M_Z \sin\beta \cos\theta_W & -\mu & 0 \end{pmatrix}$$

where M_1 and M_2 are the gauge boson masses, μ is the higgsino mass, θ_W is Weinberg angle and β is the ratio of the vacuum expectation value of the Higgs bosons. Defining the *gaugino fraction*, $a_G = \epsilon_{11}^2 + \epsilon_{12}^2$, and the *higgsino fraction*, $a_H = \epsilon_{13}^2 + \epsilon_{14}^2$, the neutralino mass is given by:

$$m_\chi = \epsilon_{11}\tilde{B} + \epsilon_{12}\tilde{W}_3 + \epsilon_{13}\tilde{H}_1^0 + \epsilon_{14}\tilde{H}_2^0 \tag{1.39}$$

The most relevant neutralino interactions for dark matter searches are self annihilation and elastic scattering with nucleons. At low velocities, the leading channels for neutralino annihilations are into fermion-antifermion, gauge bosons pairs and final states containing Higgs bosons. Neutralinos annihilate into fermion pairs by three level tree diagrams, through s-channel exchange of pseudoscalar Higgs and Z^0-bosons and t-channel exchange of sfermions (figure 1.11). The cross section of this process is given by:

$$\sigma v(\chi\chi \to f_i\bar{f}_i)_{v\to 0} = \frac{c_f \beta_f}{128\pi m_\chi^2} |A_A(f_i\bar{f}_i) + A_{\tilde{f}}(f_i\bar{f}_i) + A_Z(f_i\bar{f}_i)|^2, \tag{1.40}$$

where the sum is over the three annihilation channel amplitudes, $\beta_f = \sqrt{1 - m_f^2/m_\chi}$ and c_f is a color factor which is equal to three for quark final states and one otherwise.

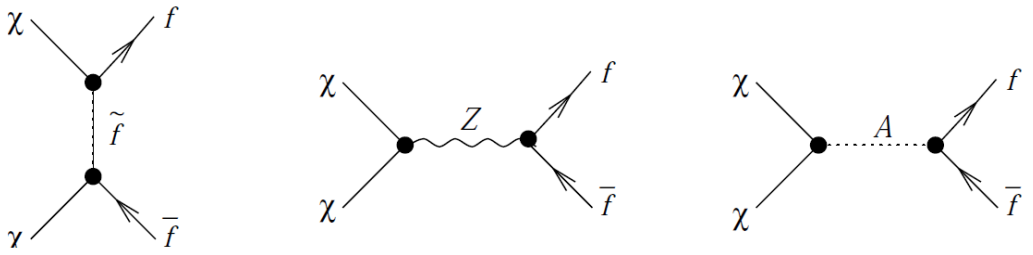

Figure 1.11: Tree level diagrams for neutralino annihilation into fermion pairs [7].

Neutralino annihilation diagrams to fermion pairs have amplitudes which are proportional to the final state fermion mass, thus annihilations are dominated by heavy final states, $b\bar{b}$, $\tau^+\tau^-$ and, if kinematically allowed, $t\bar{t}$. The annihilation into gauge bosons, in the low velocity limit, is allowed through t-channel processes via chargino or neutralino exchange, figure 1.12.

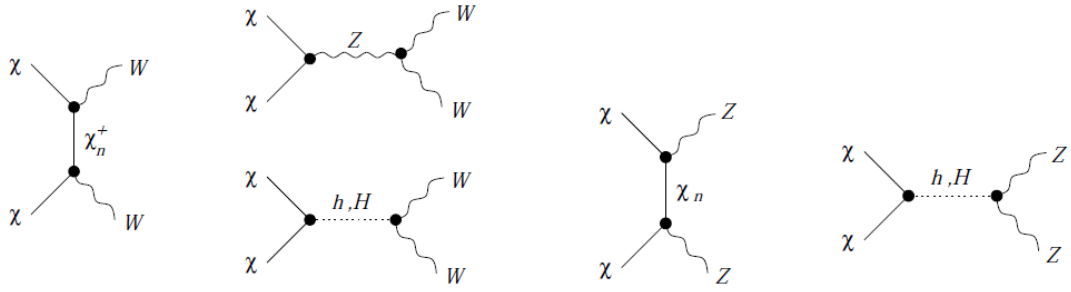

Figure 1.12: Tree level diagrams for neutralino annihilation into gauge boson pairs [7].

The cross section for this annihilation channel is given by:

$$\sigma v(\chi\chi \to GG)_{v\to 0} = \frac{1}{S_G}|A(\chi\chi \to GG)|^2, \tag{1.41}$$

where G is the gauge boson considered and S_G is a statistical factor equal to one for annihilations into W^+W^- and two for Z^0Z^0. For the annihilation into Higgs and gauge bosons there are several available channels: chargino exchange, Z^0 exchange, etc. The Feynman diagrams for annihilations into a Z and Higgs boson are shown in figure 1.13.

The annihilation cross section for neutralino annihilations into Higgs boson is given by:

$$\sigma v_{(\chi\chi\to XY)_{v\to 0}} \propto |A(\chi\chi \to XY)|^2, \tag{1.42}$$

where X and Y refer to the final state particles. For what concerns the annihilations into gammas, loop level processes to $\gamma\gamma$ and γZ^0 are required in the Feynman diagrams

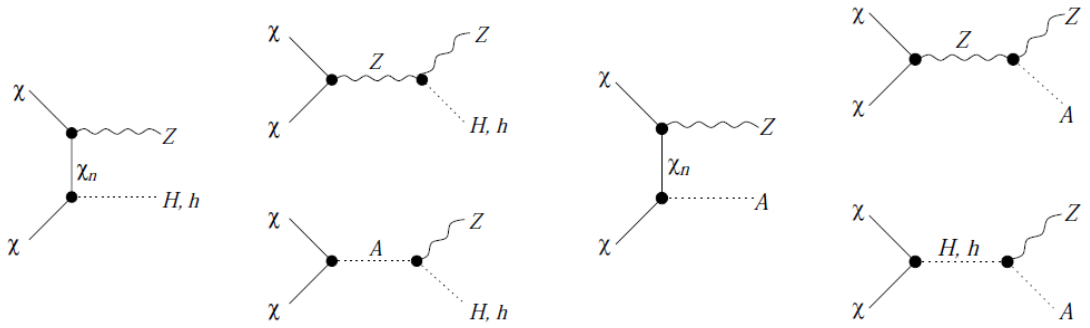

Figure 1.13: Tree level diagrams for the case of neutralino annihilation into a Z and a Higgs boson [7].

since neutralinos do not couple directly to photons, figure 1.37.
All the annihilation processes are of interest for the indirect dark matter searches (Section 1.4). In the case of direct detection techniques (Section 1.3) they are investigated the elastic scattering processes. In what follows, a brief introduction to the WIMP elastic processes is presented. A detailed discussion about expected event rates from DM direct interactions into detectors is given in Section 7.1.
Generally speaking, they are considered two types of interactions of WIMPs with the matter: spin-independent (SI) and spin-dependent (SD). A scalar interaction, i.e. SI, with quarks can be expressed as:

$$\mathcal{L}_{scalar} = a_q \overline{\chi}\chi\overline{q}q \tag{1.43}$$

where a_q is the WIMP-quark coupling. The scattering cross section is given by:

$$\sigma_{scalar} = \frac{4m_r^2}{\pi} f_{p,n}^2 \tag{1.44}$$

where m_r is the reduced mass of the nucleon and $f_{p,n}$ is the coupling to protons and neutrons. The total scalar cross section for interactions with a nucleus is given by the sum over all the nucleons:

$$\sigma = \frac{4m_r^2}{\pi}\Big(Zf_p + (A-Z)f_n\Big)^2 \tag{1.45}$$

The equation (1.45) shows the scalar cross section in the case of zero transfer momentum, figure 1.14.

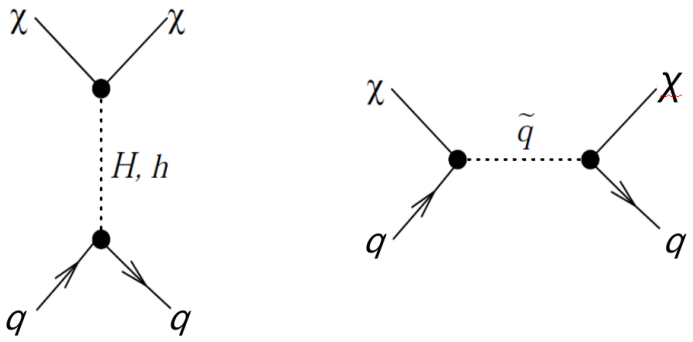

Figure 1.14: Tree level Feynman diagrams for neutralino-quark scalar (spin-independent) elastic scattering [7].

If this condition is no longer satisfied, it is necessary to introduce a term, called nuclear form factor, in the equation (1.45). A spin-dependent interaction, i.e. axial-vector interaction, between WIMPs and quark can be expressed as:

$$\mathcal{L}_{AV} = d_q \overline{\chi}\gamma^\mu\gamma_5\chi\overline{q}\gamma^\mu\gamma_5 q \tag{1.46}$$

where d_q is the generic coupling. Feynman diagrams for this kind of interactions are shown in figure 1.15.

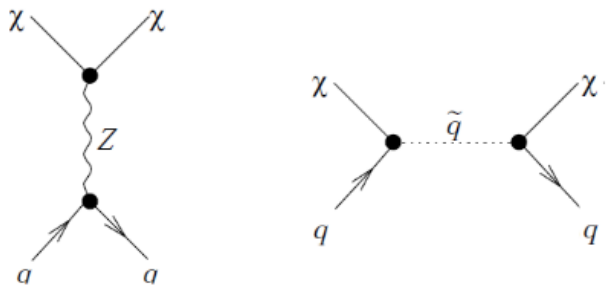

Figure 1.15: Feynman diagrams for WIMP (spin-dependent) axial-vector interactions [7].

The cross section for SD interactions is given by [43]:

$$\frac{d\sigma}{d|\vec{v}|^2} = \frac{1}{2\pi v^2}\overline{|T(v^2)|^2} \tag{1.47}$$

where v is the WIMP velocity relative to the target and $T(v^2)$ is the scattering matrix element. At zero transfer momentum, one has:

$$\begin{aligned}\overline{|T(0)|^2} = \frac{4(J+1)}{J}|(d_u\Delta_u^p + d_d\Delta_d^p + d_s\Delta_s^p)\langle S_p\rangle + \\ + (d_u\Delta_u^n + d_d\Delta_d^n + d_s\Delta_s^n+)\langle S_n\rangle|^2\end{aligned} \tag{1.48}$$

where J is the total nuclear spin of the target nucleus, $\Delta^{n,p}_{u,d,s}$ are the fractions of the nucleon spin carried by a given quark and $\langle S_{p,n} \rangle$ are the expectation values of the total spin of protons and neutrons, respectively. For target nuclei with even numbers of protons and neutrons, the total spin is equal to 0. Thus, for such nuclei, the spin-dependent cross section vanishes. Also, we can consider WIMP-quark vector interactions:

$$\mathcal{L}_V = b_q \overline{\chi} \gamma_\mu \chi \overline{q} \gamma_\mu q \tag{1.49}$$

where b_q is the WIMP-quark vector coupling. The zero transfer momentum cross section, [44], is then given by:

$$\sigma = \frac{m_\chi^2 m_N^2 [2Zb_p + (A-Z)b_n]^2}{64\pi (m_\chi + m_N)^2}, \tag{1.50}$$

with $b_q = G_F(T_q^3 - 2e_q \sin^2\theta_W)/\sqrt{2}$, where G_F is the Fermi constant, T_q^3 and e_q are the weak isospin and electric change of the quark q, respectively, and θ_W is the Weinberg angle [45].

1.4 WIMPs direct detection

Currently there are several experiments which aim to detect dark matter particle interactions with an ordinary matter target. The choice of the detection technique and of the target material allows to search in a particular range of the parameter space of the DM models. The best results, at least for WIMP masses above 8 GeV/c^2, have been obtained by XENON100 [8], for 2012, and LUX [10], for 2013. For lower masses there are other experiments as CoGeNT and CDMS, that have a better sensitivity. In the next sections some of these experiments are introduced with the exception of XENON100 since to this detector and its results it will be dedicated the section 4.3.

1.4.1 DAMA/LIBRA

The DAMA/LIBRA detector is the upgrade of the previous DAMA/NaI [46]. Its sensitive part is made of 25 highly radio-pure NaI(Tl) crystals, each one of 9.70 kg, arranged in a 5×5 matrix. Each crystal is read by two photomultipliers (PMTs), one at each edge, coupled by means of a quartz light guide, 10 cm long. The crystals and their PMTs are placed in a Cu shield enclosed in a sealed low radioactive OFHC Cu box, continuously flushed with HP N_2. To reduce the external background, a passive shield has been designed, figure 1.16.

Outside the Cu box, this shield is made of more than 10 cm of low radioactive copper, 15 cm of low radioactive lead, 1.5 mm of cadmium and a layer of polyethylene/paraffin.

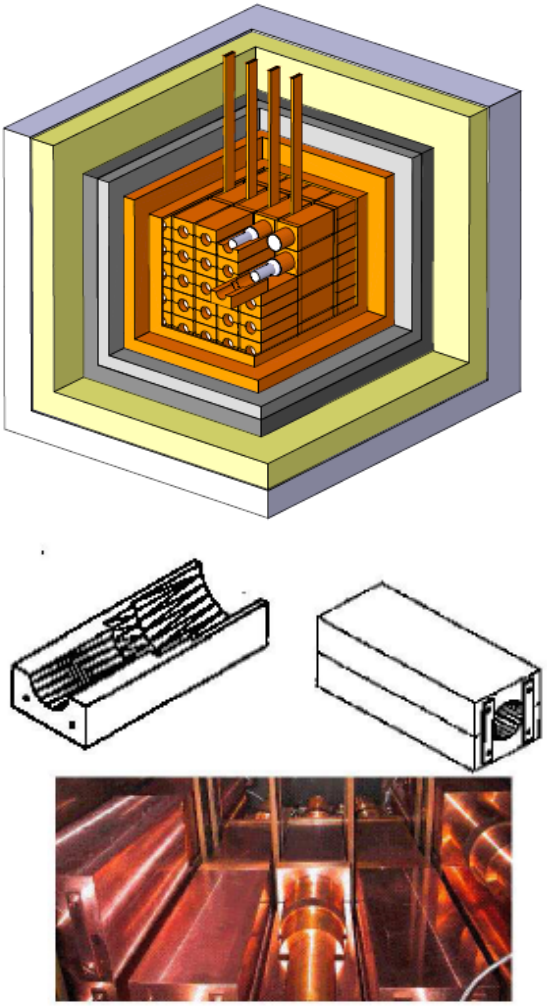

Figure 1.16: Top: DAMA/LIBRA schematic view of the 25 highly ra-diopure NaI(Tl) scintillator crystals within the passive shield. Bottom: example PMT and its low-radioactivity copper shield [46].

For the dark matter search, the modularity of DAMA/LIBRA is very useful since WIMPs are expected to give only one interaction in the entire stuck of detectors. Moreover, the characteristics of the scintillators allow to reject noise events. Typical signals from scintillation into the crystals are characterized by a decay time of ~ 240 ns while noise events are single photoelectrons pulses with a decay time of tens of ns, figure 1.17. With the exception of the noise rejection, in DAMA/LIBRA it is not possible to distinguish between nuclear and electromagnetic recoils. Thus, the detector can be only sensitive to the modulation of the WIMP signal, due to the Earth motion around the Sun, that is searched in the $[2,\ 20]$ keV energy region.

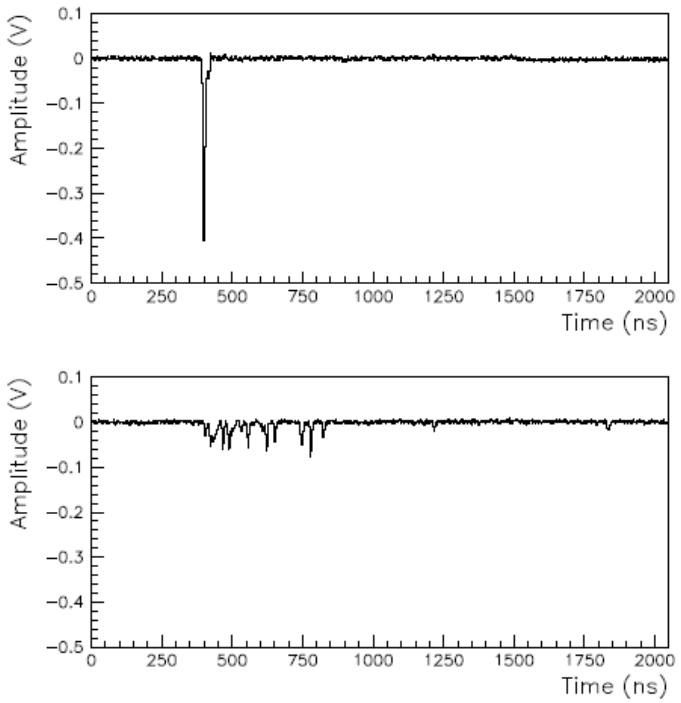

Figure 1.17: Typical pulse profiles of PMT noise (top) and of scintillation event (bottom) with the same area, just above the energy threshold of 2 keV [46].

With a total exposure of 1.04 t·y, DAMA/LIBRA has observed a signal modulation that could be explained as due to the modulation of the dark matter flux [47], figure 1.18.

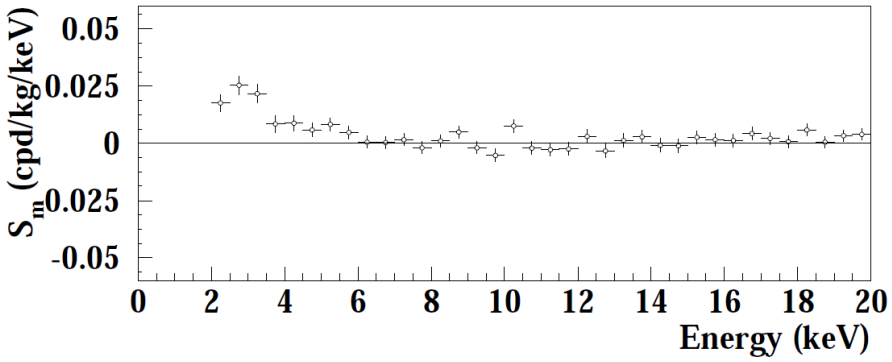

Figure 1.18: Energy distribution of the modulation amplitude S_m for the total cumulative (DAMA/LIBRA plus DAMA/NaI) exposure of 1.33 t-y obtained with maximum likelihood analysis. The energy bin is 0.5 keV. A clear modulation is present in the lowest energy region, while S_m values compatible with zero are present just above [47].

The modulation of the signal, observed for 14 annual cycles (7 from DAMA/NaI and 7 from DAMA/LIBRA) has now a significance of 9.3 σ. It shows a period of about 1 year and a phase of 144 ± 7 days. From figure 1.18 it appears that the modulate signal shows up only in the low energy region, where it is expected from spin-independent scatters from light WIMP in a thermal halo model. Several explanations for the modulation signal have been proposed to investigate a possible background as source of this signal. For example, since DAMA/LIBRA does not have a muon veto, it was hypothesized that it was the modulation of the muon flux to generate the signal [48]. However, recently it was shown that the muon flux is too low to explain the observed signal [49]. The signal amplitude modulation can be expressed as [50]:

$$\begin{aligned} S_{ik} &= S_{0,k} + S_{m,k}\cos\omega(t_i - t_0) + Z_{m,k}\sin\omega(t_i - t_0) = \\ &= S_{0,k} + Y_{m,k}\cos\omega(ti) - t^* \end{aligned} \tag{1.51}$$

where $S_{0/m,k}$ is the non-modulate/modulate amplitude in the k-th energy bin, respectively, and t_i is the i-th time interval. From the total exposure of DAMA/LIBRA, the value of $Z_{m,k}$ has been found compatible with zero in the [2, 6] keV and [6, 14] keV energy region, while $S_{m,k}$ is compatible with zero only in the [6, 14] keV energy region, figure 1.19.

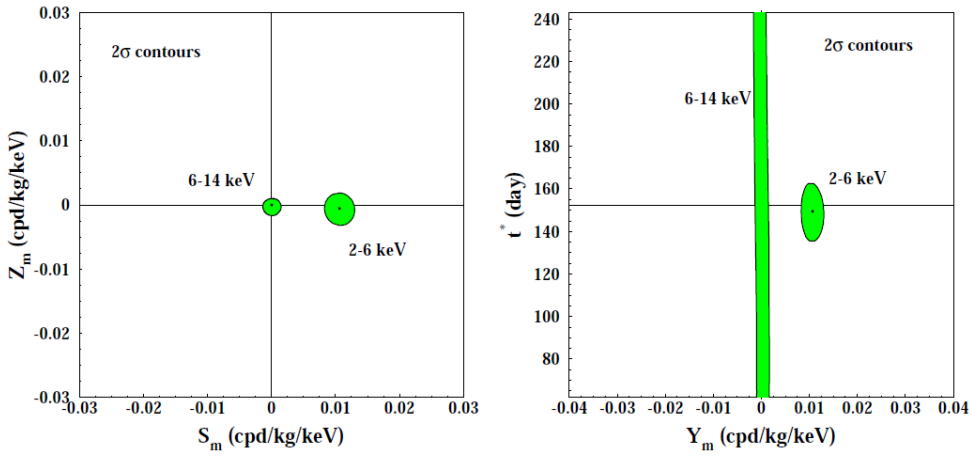

Figure 1.19: Left, 2 σ contours in the $S_{m,k}$ and $Z_{m,k}$ plane. Right, 2 σ contours in the $Y_{m,k}$ and t^* plane in [2,6] keV and [6,14] keV. A modulation amplitude is present in the lower energy intervals and the phase agrees with that expected for DM induced signals [50].

From the data it has also been found $t^* \simeq 152.5$. These results are in agreement with what is expected from WIMP scatters in several dark matter halo models.

1.4.2 CoGeNT

The CoGeNT detector [51], made of one p-type point contact (PPC) Ge crystal of 440 g, is focused on the search for WIMP interactions in the [0.4, 3] keV energy region. Due to its very low energy threshold, this detector is particularly suitable for the low mass WIMP search (m_χ below $\sim$ 10 GeV/c^2). It is placed in the Soudan Underground Laboratory (SUL), at a depth of 2090 meters water equivalent (m.w.e.), to guarantee a shield against cosmic rays and their associated backgrounds. To reduce even more the background, a passive shield has been realized, figure 1.20. In order to be operative it requires a cryogenic system and for this reason, the crystal is housed in a copper cryostat. On one side of the Cu cryostat is placed a stainless steel cryostat which provides the electrical feed-through.

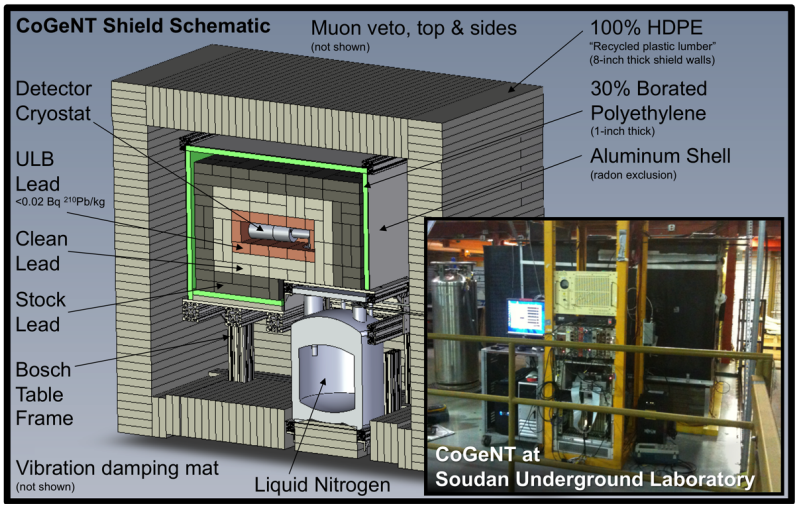

Figure 1.20: Schematic view of the CoGeNT structure with its passive shield.

The two cryostats are enclosed in a three level lead shield: a innermost lead layer 5 cm thick, a middle layer and an external layer 10 cm thick. The three layers are made of different types of lead with different contaminations. The lead shield is enclosed in a 2.5 cm thick layer of 30% borated polyethylene that acts as a thermal neutrons absorber. The entire structure is placed inside of an aluminum sheet-metal box which inner volume is continuously flushed with boil-off N_2 gas from a dedicated pressurized dewar. The outermost part of the CoGeNT's shield is made of a 18.3 cm thick layer of high-density polyethylene (HDPE) deck, acting as a neutron moderator. Outside this passive shield there is also an active muon veto, made of flat panels read by PMTs which offers $\sim$ 90% coverage of the whole structure.
In 2010 [52] CoGeNT observed an excess of events, at low energies, in the bulk of the

Ge crystal. Several analyzes have been performed to explain this excess as due to dark matter interactions, assuming a Maxwellian velocity distribution with $v_0 = 230$ km/sec, and $v_{esc} = 500$ km/sec. For a spin-independent model, with equal coupling to protons and neutrons and without any unknown background, the WIMP hypothesis gives a nice agreement, especially in the very low energy region, with the observed data (figure 1.21).

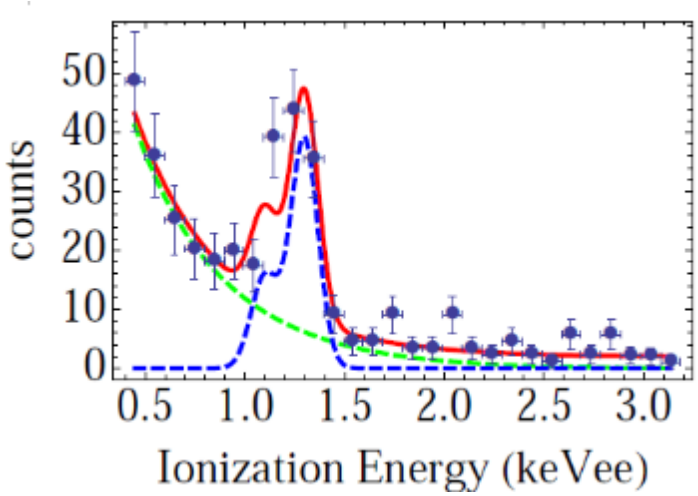

Figure 1.21: Best fit (red-solid) to the CoGeNT low energy data (blue dots) with a WIMP signal component (green light-dashed) and a background model (blue dashed). The fit has been obtained for $m_\chi = 9.4$ GeV/c^2 and $\sigma = 0.84 \cdot 10^{-40}$ cm^2, with a background model describing the L-shell energy levels associated with electron capture in ^{68}Ge and ^{65}Zn and without any other unknown background [52].

The best results were obtained for $m_\chi = 9.4$ GeV and $\sigma = 0.84 \cdot 10^{-40}$ cm^2. Unfortunately, such results are excluded by other experiments such as CDMS-Si. Instead, considering also an unknown exponential background with proper characteristics [52] and $m_\chi = 7$ GeV with $\sigma = 0.64 \cdot 10^{-40}$ cm^2, the dark matter gives an appreciable contribute only in the first two energy bins, figure 1.22. In this case, it is the background that gives the highest contribution to the observed events above the second energy bin. In their results from a 1129 live days run [53], a modulated signal has been observed. The period of this modulation is compatible, within the errors, with a period of one year and the t_{max} is compatible with the DAMA/LIBRA one. However, a discrepancy of a factor $\sim 4 - 7$ is found for the amplitude if the signal would be given by a low mass WIMP in a standard halo model. If instead, it is used a non-Maxwellian halo, considering effects such as tidal streams, extra-galactic components, etc., an agreement between the CoGeNT and DAMA/LIBRA allowed region in the parameter space can be reached, figure 1.23. However this interpretation is ruled out by LUX results [10].

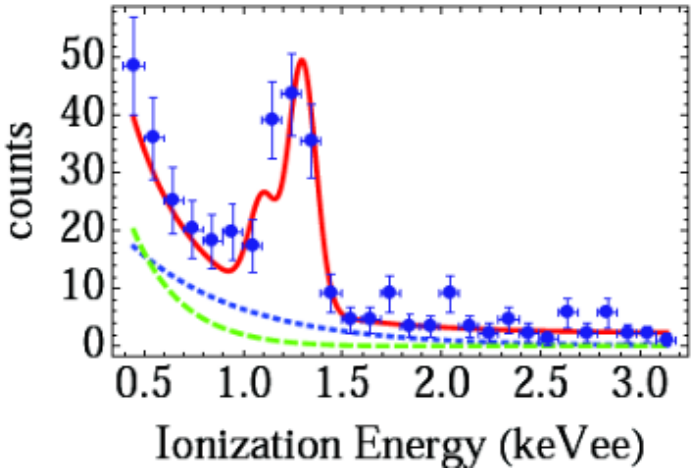

Figure 1.22: Same as figure 1.21 but with the best fit obtained for $m_\chi = 7$ GeV/c^2 and $\sigma = 0.64 \cdot 10^{-40}$ cm^2 with an exponential background [52].

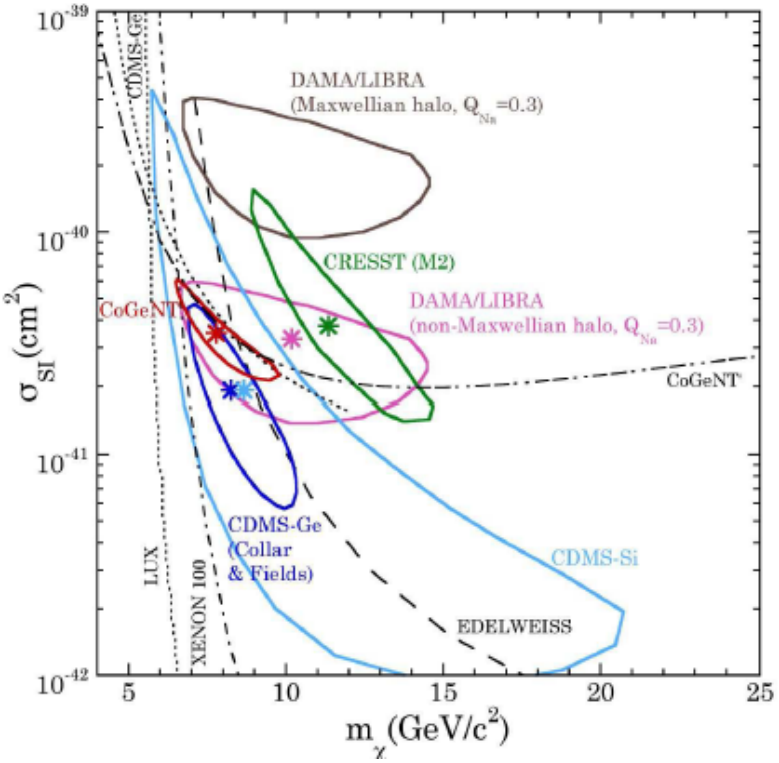

Figure 1.23: Displacement towards lower spin-independent scattering cross-section σ_{SI} of the DAMA/LIBRA region of interest (ROI), if a fractional modulation amplitude corresponding to that found for CoGeNT data is assumed. ROIs for recent dark matter detector anomalies are indicated by colored solid lines, their best-fits highlighted by asterisks. These are 99% CL regions, except for CRESST (95% C.L.) [53].

1.4.3 EDELWEISS-II

The EDELWEISS-II detector [54], at the Laboratoire Souterrain de Modane (LSM) under 4800 m.w.e., is enclosed in a passive shield made, from the outer to the inner part, by: 50 cm of thick polyethylene, covered by a muon veto system for thoroughgoing muons, and 20 cm of lead that protects the cryostat from external γ-rays. Inside the cryostat there is the core of the detector, based on ten bolometers of hyper-pure Ge crystals of cylindrical shapes with a diameter of 70 mm and a height of 20 mm. Five bolometers have a mass of 360 g while the mass of the other five is 410 g. They are placed in individual copper casings, stacked in towers of two to three detectors. For each event, two signals are recorded: one from the temperature increase, measured using neutron transmutation doped (NTD)-Ge thermometric sensors glued on each detector, and one from the charges produced in the interaction that are recorded by proper electrode wires on both side of the Ge bolometers, [55]. On each face of the cylinder there are six wires and only the innermost two, the **fiducial electrodes**, are used in order to record interesting events. In 2012, the collaboration carried out an analysis on low-energy (E $<$ 20 keV) WIMP-induced nuclear recoils [54]. For a WIMP mass of 30 GeV/c^2, three events have been found as possible candidates figure 1.24.

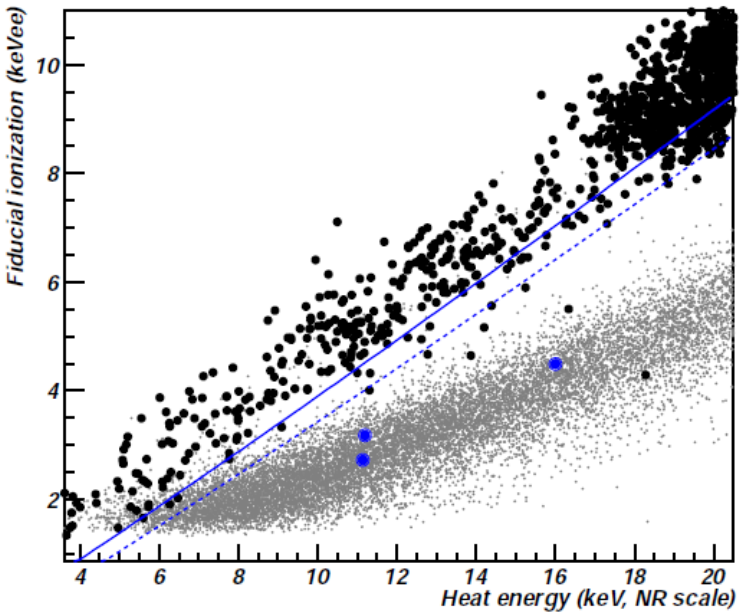

Figure 1.24: Heat vs ionization for the events in the 113 kg·d of exposure run. The mean of the ER band (blue line) and the 95% ER rejection line (blue dashed) are shown. The nuclear recoil calibration events are also shown (gray dots). The blue circled points are the events contained in the WIMP search region [54].

The data indicated no evidence for an exponential distribution of low-energy nuclear recoils that could be attributed to WIMP elastic scattering after an exposure of 113 kg·d. For WIMPs of mass 10 GeV/c^2, the observation of one event in the WIMP search region results in a 90% CL limit of $1.0 \cdot 10^{41}$ cm^2 [54] on the spin-independent WIMP-nucleon scattering cross-section, which constrains the space parameters associated with the findings reported by the CoGeNT, DAMA and CRESST experiments. Thus, for m_χ in the range [7, 30] GeV/c^2 only limits have been set [54], figure 1.25 [54].

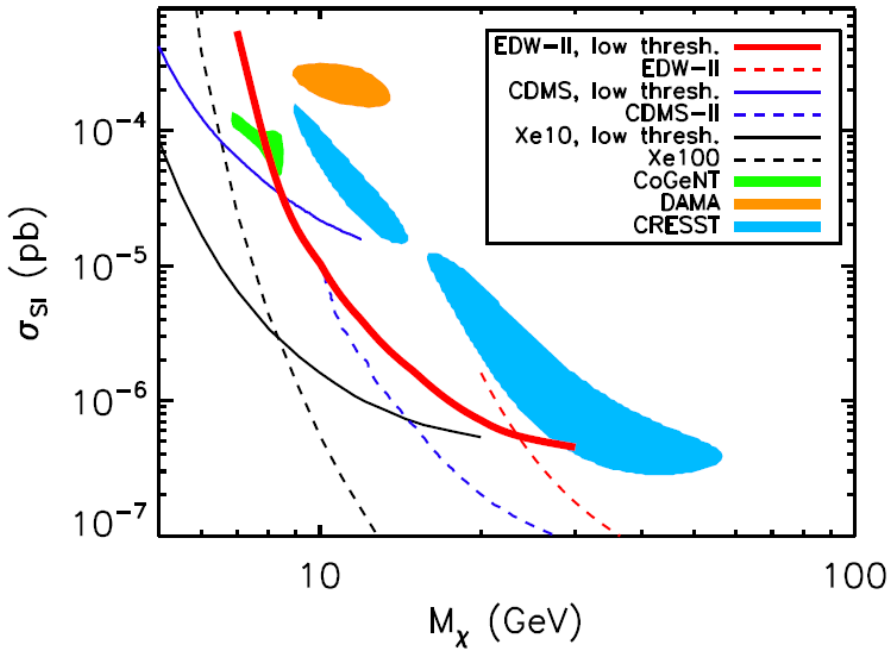

Figure 1.25: 90% CL Poisson limit on SI cross section as a function of WIMP mass (bold red line). Also shown are the locations of potential WIMP signals from the CoGeNT, CRESST and DAMA experiments, as well as constraints from EDELWEISS-II [56], CDMS-II and XENON100, and the dedicated low mass searches from CDMS-II and XENON10.

From figure 1.25 it is clear that they are excluded the entire zones corresponding to the interpretation of DAMA [57] and CRESST [58] results in terms of elastic, spin-independent WIMP scattering. These zones extend down to a WIMP mass of 9 GeV/c^2, which is the region where the EDELWEISS-II experimental sensitivity is around 1% of the total WIMP signal recoil spectrum. While the CoGeNT parameter space is significantly constrained, EDELWEISS-II cannot exclude the region corresponding to $m_\chi < 8$ GeV/c^2 due to lack of sensitivity to nuclear recoil energies below 5 keV.

1.4.4 superCDMS

The superCDMS detector is a bolometer, at Soudan Underground Laboratory [59]. To operate, a cryogenic system based on He-3/He-4 dilution refrigerator has been realized. The core of the detector is made of fifteen 600 g Ge crystals from which it is possible to extract the phonon and the charge signals. The crystals have cylindrical shape with a diameter of 76 mm and height of 25 mm. A total of 8 phonon sensors, four on each side of the crystals flat surfaces, and 4 charge sensors, 2 on each side, provide the signals. This kind of detectors is also called iZIP (interleaved Z-sensitive Ionization Phonon), figure 1.26.

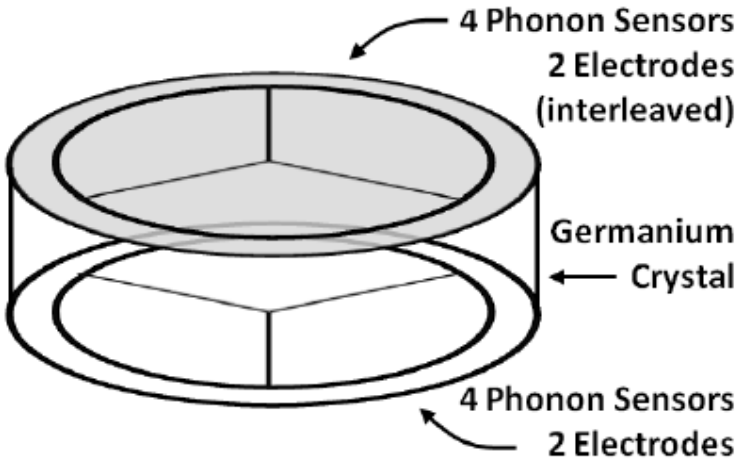

Figure 1.26: Schematic view of a superCDMS detector crystal.

The phonon sensor is a superconducting ^{174}W film held in the transition state from the superconducting to the normal state (therefore called Transition Edge Sensor or TES). A small change in the temperature leads to a large variation in the measured resistance. The charge sensors are made of electrodes biased at a certain voltage. For events near the surface, the charge carriers distribute between the electrode and the phonon sensors (acting as ground reference) on the same side of the detector. From the different ratio of the charges on both sides it is possible to reject events closed to the surface (usually due to background) [60]. In 2014, the collaboration carried out the analysis of a run characterized by an exposure of 577 kg·d [61]. They focused on WIMP masses below 30 GeV/c^2 considering an energy search region [1.6, 10] keV. With these results, superCDMS set an upper limit on the spin-independent WIMP-nucleon cross section of $1.2 \cdot 10^{-42}$ cm^2 for $m_\chi = 8$ GeV/c^2 [61], figure 1.27.

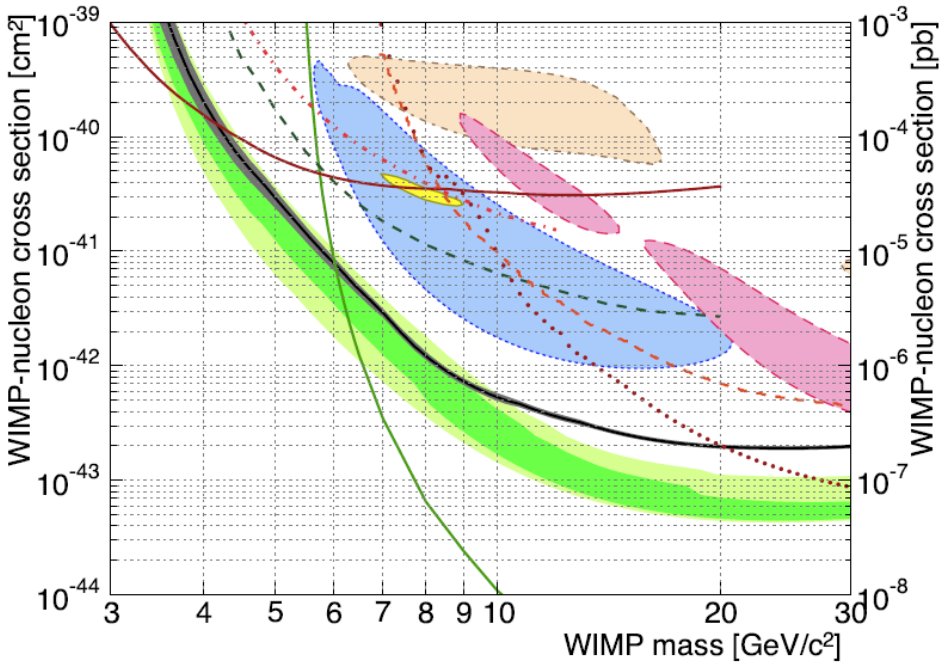

Figure 1.27: The SuperCDMS 90% confidence upper limit (solid black). The pre-unblinding expected sensitivity in the absence of a signal is shown as 68% (dark green) and 95% (light green) CL bands. Closed contours shown are CDMS-II Si [62] (dotted blue, 90% CL), CoGeNT [51] (yellow, 90% CL), CRESST-II [58] (dashed pink, 95% CL), and DAMA/LIBRA [63] (dash-dotted tan, 90% CL). 90% CL exclusion limits shown are CDMS-II Ge [64] (dotted dark red), CDMS-II Ge low-threshold [65] (dashed-dotted red), CDMSlite [66] (solid dark red), LUX [10] (solid green), XENON10 S2-only [67] (dashed dark green), and EDELWEISS low-threshold [54] (dashed orange).

1.4.5 LUX

The Large Underground Experiment (LUX) [68] is based on the same work principles of XENON100. It is a double phase Time Projection Chamber (TPC) which contains Xe in liquid and gaseous phases. The TPC, which contains an active volume of LXe of about 300 kg, is hosted in a double vessel structure that guarantees thermal isolation, figure 1.28. The detector is placed at the Stanford Underground Research Facility (SURF) at a depth of 4850 feet and it is surrounded by a water tank that acts as muon veto. The TPC has a diameter of 47 cm and a height of 48 cm. The prompt scintillation signal, S1, and the electroluminescence one, S2, are read by two PMTs arrays. In order to drift the electrons towards the LXe/GXe interface, an electric field of about 181 V/cm is applied while an extraction field of 6.0 kV/cm is used to extract the electrons in the GXe region.

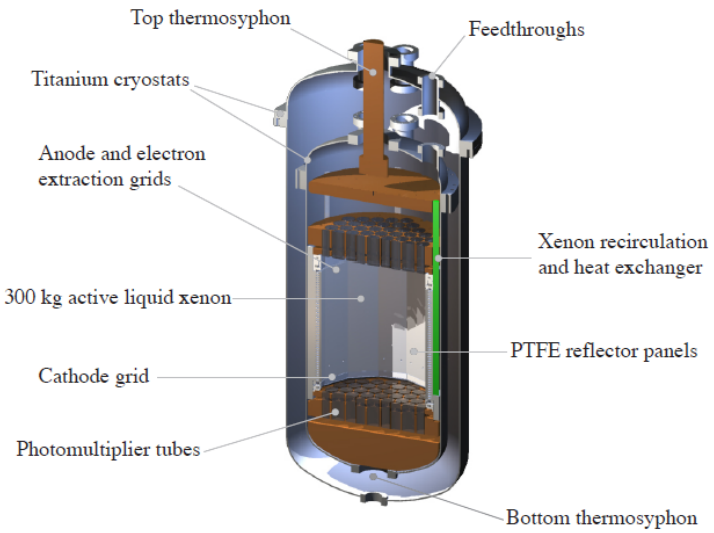

Figure 1.28: LUX cryostats and TPC structures.

To reduce the background, a volume cut has been used in the analysis of LUX latest measurements [10] from a run of 85.3 live-days. The chosen volume, called the fiducial volume, has been selected to lie between drift times of 38 μs and 305 μs, from which is possible to infer a cut on the $z-$coordinate, ending with a fiducial volume of about 118.3 kg. After all the cuts used in the analysis, 160 events have been observed in the WIMP search region ([2, 30] pe), figure 1.29.

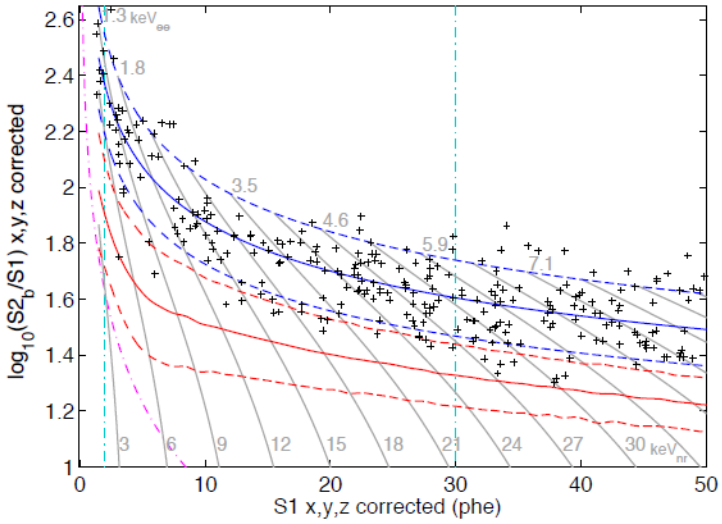

Figure 1.29: LUX events in the WIMP search region (between vertical cyan dashed lines). The red (blue) line is the median of the nuclear (electromagnetic) band in the ($\log_{10}$(S2/S1), S1) space [10].

From a profile likelihood analysis [10], all the events have been found compatible with the background-only hypothesis resulting in new upper limits for the DM spin-independent cross section, figure 1.30. The minimum has been found at $7.6 \cdot 10^{-46}$ cm^2 for a WIMP mass of 33 GeV/c^2.

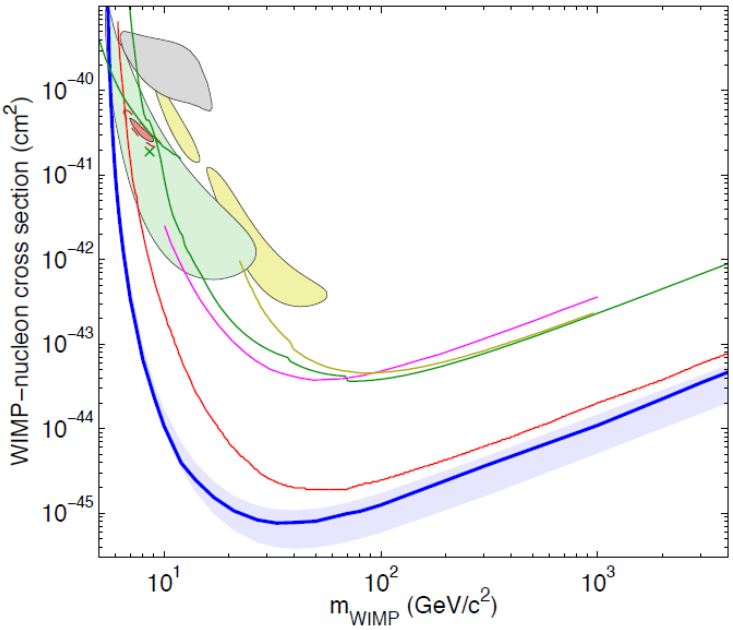

Figure 1.30: LUX 90% confidence limits on the SI elastic WIMP-nucleon cross section (blue) [10], together with the $\pm$ 1σ variation (light blue area) and XENON100 results from 225 live days run (red curve) [8]. Also shown are limits from: Edelweiss II [56] (dark yellow line), CDMS II [64] (green line), ZEPLIN-III [69] (magenta line), CDMSlite [66] (dark green line), XENON10 S2-only [67] (brown line), SIMPLE [70] (light blue line) and XENON100 100 live-day [65] (orange line). The colored regions come from measurements from annual modulation in CoGeNT [71] (light red, shaded), along with exclusion limits from low threshold re-analysis of CDMS II data [65] (upper green line), 95% allowed region from CDMS II silicon detectors [61] (green shaded) and centroid (green x), 90% allowed region from CRESST II [58] (yellow shaded) and DAMA/LIBRA allowed region [57] interpreted by [63] (gray shaded). Results sourced from DMTools [72].

1.4.6 CRESST-II

CRESST-II is the upgrade of the CRESST detector [73] that includes a new neutron shield and a muon veto. It uses simultaneously two independent detectors for revealing heat/phonon and light. The core of the detector is made of modules that consist of a $CaWO_4$ 300 g crystal, the target, and a silicon-on-sapphire (SOS) wafer used for

measuring the scintillation light. In their interaction inside the crystals, WIMPs lose energy producing phonons and a small amount of scintillation light. The reading of signals from crystals and SOS is obtained by a Transition Edge Sensor (TES) attached to them. All these elements are enclosed in a reflective and scintillating case, figure 1.31.

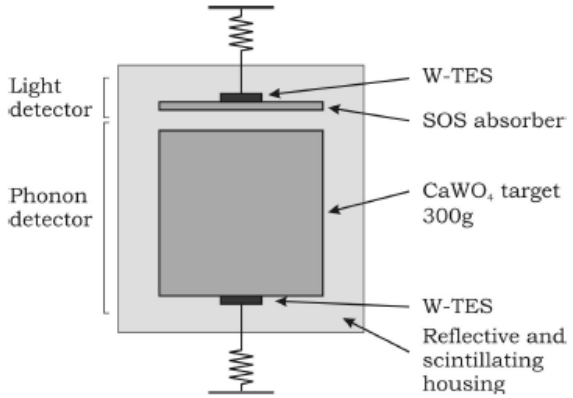

Figure 1.31: Scheme of CRESST-II module.

The detector modules are placed inside a passive shield consisting of 14 cm thick low background copper and 20 cm of lead layers. This shielding is entirely enclosed within a gas-tight radon box which is continuously flushed with N_2 gas. The use of two detectors allows for precise measurements of the deposited energy and background discrimination. For example, the electromagnetic background rejection can be achieved using the scintillation to phonon signals ratio. The nuclei of Ca, W and O_2 nuclei, make the $CaWO_4$ crystals a target for WIMPs with different masses, figure 1.32.

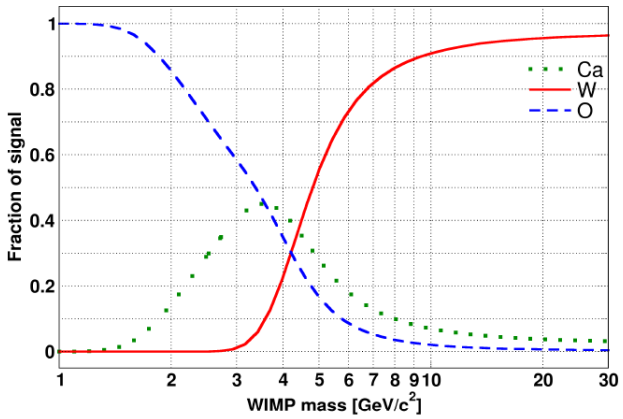

Figure 1.32: Fraction of the expected recoil signals, from the target elements in the crystal, as function of the WIMP mass.

For very low masses, the major contributions to the expected signal come from the Ca and O_2 nuclei while for masses above 5 GeV/c^2 the W contribution becomes dominant thanks to its large coherent factor ($\sim A^2$) in the spin-independent interactions. In 2014, the CRESST-II collaboration has published its results, figure 1.33 [74], from the analysis of a 29.35 kg·d focused on the [0.6, 40] keV energy region.

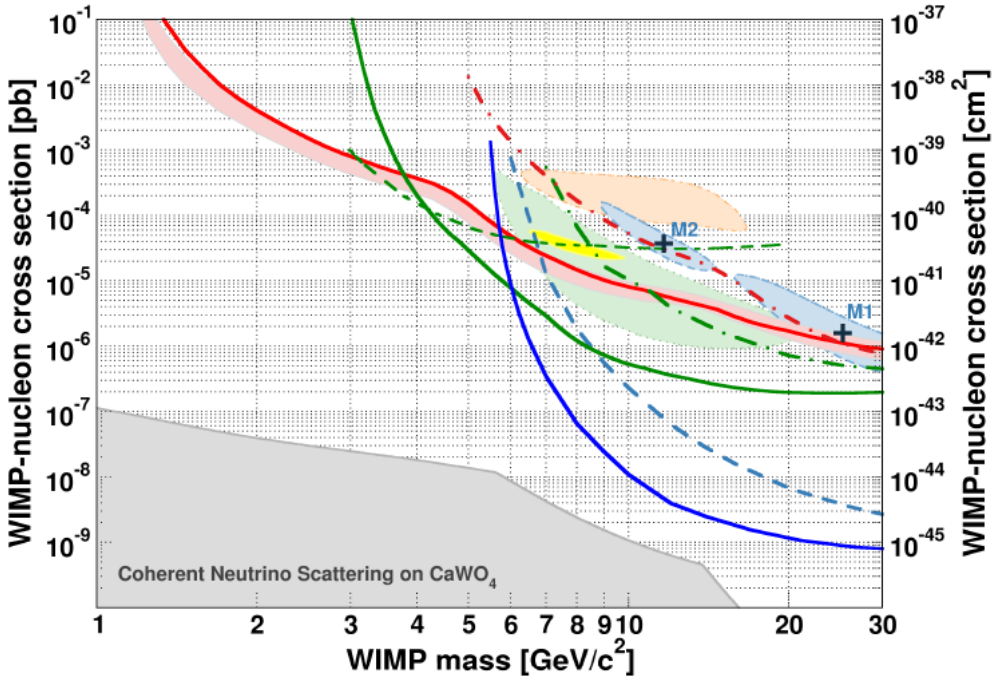

Figure 1.33: WIMP parameter space for spin-independent WIMP-nucleon scattering. The 90% C.L. upper limit (solid red) is depicted together with the expected sensitivity (1 σ C.L.) from the background-only model (light red band). The CRESST 2 σ contour reported in [58] is shown in light blue. The dash-dotted red line refers to the reanalyzed data from the CRESST commissioning run [75]. Shown in green are the limits (90% C.L.) from Ge-based experiments: SuperCDMS (solid) [61], CDMSlite (dashed) [66] and EDELWEISS (dash dotted) [54]. The parameter space favored by CDMS-Si [62] is shown in light green (90% CL), the one favored by CoGeNT (99% CL [71]) and DAMA/Libra (3 σ CL [63]) in yellow and orange. The exclusion curves from liquid xenon experiments (90% CL) are drawn in blue, solid for LUX [10], dashed for XENON100 [8]. Marked in gray is the limit for a background-free $CaWO_4$ experiment arising from coherent neutrino scattering (dominantly from solar neutrinos) [76].

1.5 WIMPs indirect detection

Unlike the direct dark matter searches, where the focus is on the observation of WIMP interactions in the detectors, indirect techniques aim to detect DM decay or annihilation products. Indeed, it is usually assumed that WIMPs can annihilate in SM particles. Dark matter can annihilate/decay producing particle which, in turn, can decay. What it is possible to observe are thus the final, stable, products. Viable signatures for such kind of processes are the productions of: neutrinos, γ-ray, positrons, anti-protons and anti-deuterons.
Since the annihilation scales as N^2, the searches for this kind of process is usually addressed towards regions with high density of dark matter, such as the galactic center (GC) or the Sun.

WIMPs in the Sun

Concerning the Sun, it can happen that a WIMP, after hitting an atom, can lose enough energy so that its velocity will be below the solar escape velocity. In this way the dark matter particle can be trapped into the Sun. This process was first proposed and calculated in [77, 78]. The abundance of DM inside the Sun results from the balancing among DM capture, annihilation and evaporation processes. Thus, the DM density number, N, is given by:

$$\frac{dN}{dt} = C_\odot + (C_s - E_\odot)N - (A_\odot + C_{se})N^2 \tag{1.52}$$

where $A_\odot$ is connected to the annihilation rate, $C_\odot$ and $E_\odot$ are the capture and evaporation rate, respectively, C_s is the rate at which DM is captured due to their scattering with other WIMPs already trapped in the Sun and C_{se} is the evaporation rate induced by the interaction between dark matter particles in the Sun.
The general form for the total capture rate is given by [79]:

$$C_\odot = 4\pi \sum_i \int_0^{R_\odot} dr\ r^2\ \frac{dC_{\odot,i}}{dV}, \tag{1.53}$$

where $R_\odot$ is the solar radius and $dC_{\odot,i}/dV$ is the differential contribution of nuclei i at the radius r. The sum in equation (1.53) runs over all types of atoms in the Sun (from ^{1}H to ^{28}Ni). The term $dC_{\odot,i}/dV$ depends from the WIMP-nuclei scattering cross section and from the form factor of the nuclei. The form factor introduces a suppression in the interaction rate for heavy nuclei while it can be set to 1 in the case of the hydrogen.

Considering SI and SD interactions, figure 1.34, the capture is [7]:

$$C_{\odot}^{SI} \simeq 1.24 \cdot 10^{-24}\mathrm{s}^{-1}\left(\frac{\rho_0}{0.3\ \mathrm{GeV/cm}^3}\right)\left(\frac{270\mathrm{km/s}}{\bar{v}}\right)^3\left(\frac{\mathrm{GeV}}{m_\chi}\right)^2 \left(\frac{2.6\sigma_H^{SI} + 0.175\sigma_{He}^{SI}}{10^{-6}\mathrm{pb}}\right) \tag{1.54}$$

for the SI case while for the SD case it is given by:

$$C_{\odot}^{SD} \simeq 3.35 \cdot 10^{-24}\mathrm{s}^{-1}\left(\frac{\rho_0}{0.3\ \mathrm{GeV/cm}^3}\right)\left(\frac{270\mathrm{km/s}}{\bar{v}}\right)^3\left(\frac{\mathrm{GeV}}{m_\chi}\right)^2 \left(\frac{\sigma_H^{SD}}{10^{-6}\mathrm{pb}}\right) \tag{1.55}$$

where ρ_0 is is the local DM density, $\bar{v}$ is the velocity dispersion, $\sigma_H^{SD(SI)}$ is the SD (SI) DM-hydrogen scattering cross section, σ_{He}^{SI} is the SI DM-helium cross section and m_χ is the DM mass.

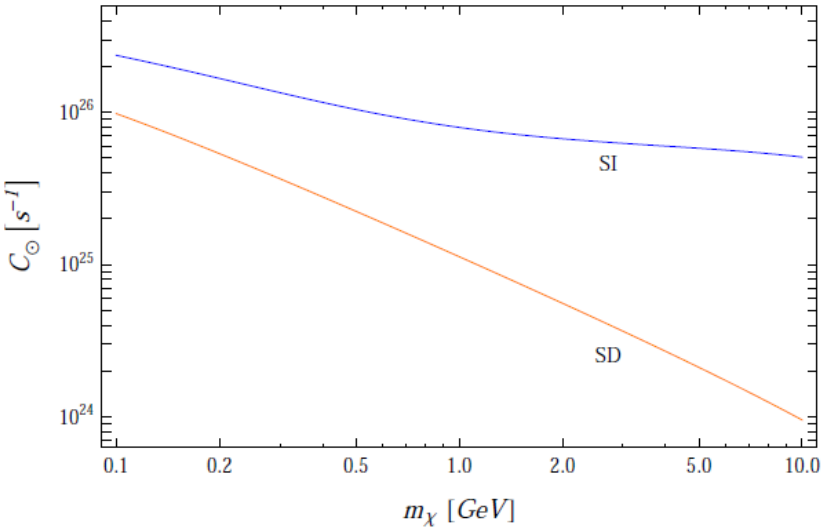

Figure 1.34: Capture rate, as function of the WIMP mass, for spin-dependent and spin-independent WIMP interactions assuming $\sigma_p = 10^{-40}$ cm^2 [80].

After being trapped into the Sun, WIMPs continue to interact with the matter until they thermalize. Indeed, also for small cross section ($\sim 10^{-43}$ cm^2) the number of collisions they undergo over the solar lifetime is $\sim t_\odot \langle\sigma v\rangle N = 3 \cdot 10^7$, which is sufficient to thermalize [81].
The annihilation rate is given by:

$$\Gamma_\odot = A_\odot N^2/2, \tag{1.56}$$

where, for $m_\chi \geq 1$ GeV, $A_\odot$ is given by:

$$A_\odot = 4.5 \cdot 10^{-30} \text{cm}^{-3} \left(\frac{m_\chi - 0.6 \text{ GeV}}{10 \text{ GeV}} \right)^{3/2} \langle \sigma_a v \rangle_\odot, \tag{1.57}$$

where the last term is the mean annihilation cross section weighted on the velocity.
Besides the annihilation, a dark matter particle can also have a chance to escape. This process is called "evaporation" and it can take place if a WIMP, after a scatter with a nucleus, gains enough energy to escape from the Sun. The evaporation is usually ignored in the DM evolution equation since it is negligible for $m_\chi \gtrsim 4$ GeV [80]. Its rate, for SI and SD interactions, is given by as [79]:

$$E_\odot \simeq \frac{8}{\pi^3} \frac{\sigma_{evap}}{\bar{r}^3} \bar{v} \frac{E_{esc}}{T_\odot(\bar{r})} e^{\left[-\frac{E_{esc}}{2T_\odot(\bar{r})} \right]}, \tag{1.58}$$

where σ_{evap} is the evaporation cross section given by the total cross section of all the nuclei within $r_{0.95}$, defined as $T_\odot(r_{0.95}) = 0.95 \cdot T_\odot(\bar{r})$ (i.e. $r_{0.95}$ represents the radius at which the Sun temperature $T_\odot$ is equal to the 95% of its value at the mean WIMP orbit radius $\bar{r}$), E_{esc} is the escape energy at the center of the Sun and $\bar{v}$ is the mean WIMP speed for the thermal velocity distribution, inside the Sun, given by [79]:

$$\bar{v} = \sqrt{\frac{8T_\odot(\bar{r})}{\pi m_\chi}}. \tag{1.59}$$

The DM self-capture rate, C_s, is given by [82]:

$$C_s = \sqrt{\frac{3}{2}} n_\chi \sigma_{\chi\chi} \frac{v_{esc}(R_\odot)^2}{\bar{v}} \langle \phi_\chi \rangle \frac{erf(\eta)}{\eta} \tag{1.60}$$

where $\langle \phi_\chi \rangle$ is a dimensionless average solar potential experienced by the captured DM within the Sun, n_χ is the local number density of halo DM, $\sigma_{\chi\chi}$ is the elastic scattering cross section of DM with themselves, $v_{esc}(R_\odot)$ is the Sun escape velocity at the surface, $\eta^2 = 3(v_\odot/\bar{v})^2/2$ is the square of a dimensionless velocity of the Sun through the Galactic halo with $v_\odot = 220$ km/s and $\bar{v} = 270$ km/s. Also the self-interaction induced evaporation is due to DM particles that interact among themselves. In such a process, WIMPs trapped in the Sun can scatter with other trapped DM ending with a velocity greater than the solar escape velocity, thus evaporating. The rate for such a process is given by [83]:

$$C_{se} = \frac{\int_\odot d^3r \; dC_{se}/dV}{\left(\int_\odot n_\chi(r) d^3(r) \right)^2} \tag{1.61}$$

where dC_{se}/dV is the sum upon all the possible states of the incident DM and n_χ is the DM number density inside the Sun.

The general solution to equation (1.52), assuming as negligible the contribution from the evaporation process and $N(0) = 0$, is given by:

$$N(t) = \frac{C_\odot \tanh(t_\odot/\tau_{eq})}{\tau_{eq}^{-1} - (C_s - C_e)\tanh(t_\odot/\tau_{eq})/2} \tag{1.62}$$

where $t_\odot \simeq 1.5 \cdot 10^{17}$ s is the age of the Sun and τ_{eq}:

$$\tau_{eq} = 1/\sqrt{C_\odot(A_\odot + C_{se}) + (C_s - C_e)^2/4}$$

is the time scale required to reach equilibrium between capture and annihilation. Assuming $C_s = C_{se} = 0$, i.e. absence of DM self-interactions, $N(t)$ becomes:

$$N(t) = \sqrt{\frac{C_\odot}{A_\odot}}\tanh(t_\odot/\tau_{eq}). \tag{1.63}$$

Thus, the annihilation rate, equation (1.56), is given by [84]:

$$\Gamma_\odot = \frac{1}{2}A_\odot N^2 = \frac{1}{2}C_\odot \tanh^2(t_\odot/\tau_{eq}) \tag{1.64}$$

If $\tau_{eq} << t_\odot$ there is equilibrium between capture and annihilation: $\Gamma_\odot = 0.5 \cdot C_\odot$. The thermal cross section, equation (1.57), can be expanded as: $\sigma_a v = a + bv^2 + \mathcal{O}(v^4)$ where the first (second) term is dominant in the case of s-wave (p-wave) annihilations. In order to have equilibrium between capture and annihilation, the cross section has to be velocity-independent ($\sigma_a v = a$, with $a = \mathcal{O}(10^{-26})$ cm^3/s). For pure p-wave annihilations ($a = 0$), the thermally averaged annihilation cross section in the Sun is reduced by a factor $T_\odot/T_F$ compared to freezeout. In this case capture-annihilation equilibrium is typically not reached and $\Gamma_\odot < C_\odot/2$. Anyway, also for $b \neq 0$ and $a << b$ it is still possible to reach equilibrium between capture and annihilation. In addition to the previous discussion, also the ratio between the solar age and the equilibrium time [84]:

$$\frac{t_\odot}{\tau_{eq}} = 10^3 \left(\frac{C_\odot}{10^{25}\mathrm{s}^{-1}}\right)^{1/2} \left(\frac{\langle\sigma_a v\rangle}{3 \cdot 10^{-26}\mathrm{cm}^3\mathrm{s}^{-1}}\right)^{1/2} \left(\frac{0.01 \cdot R_\odot}{r_{th}}\right)^{3/2}, \tag{1.65}$$

implies that equilibrium has been reached long time ago. In equation (1.65), r_{th} is the thermal radius and $R_\odot$ is the radius of the Sun.

Instead, if $\tau_{eq} >> t_\odot$ the annihilation becomes negligible and the equilibrium is attained by capture and evaporation and the number of DM particles becomes [80]: $N \simeq C_\odot/E_\odot$ (figure 1.35). N reaches its maximum around $m_\chi \sim 3$ GeV, figure 1.35, because below this value the evaporation becomes dominant, yielding fewer N, and above that the number of DM particles passing through the Sun decreases as $\rho_0/m_\chi \sim 0.3$ GeV cm$^3/m_\chi$.

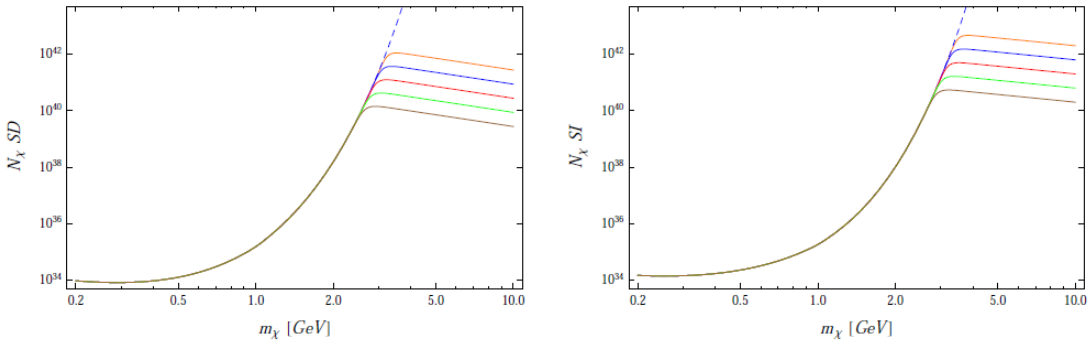

Figure 1.35: The number of DM particles in the Sun, N, as a function of the WIMP mass, for SD (left panel) and SI (right panel), for different values of the DM-proton cross section $\sigma_p = 10^{-40}, 10^{-39}, 10^{-38}, 10^{-37}, 10^{-36}$ cm^2 (from bottom to top) and assuming $\langle \sigma_a v \rangle = 3 \cdot 10^{-26}$ cm^3/s. The blue dashed line corresponds the values that N tends to when the evaporation-capture equilibrium is reached [80].

Concerning the evaporation, it is possible to define two quantities that can be used to describe its impact on N: the evaporation mass, m_{evap}, defined as the mass for which the inverse of the evaporation rate is equal to the age of the Sun and the minimum mass, m_{min}, corresponding to the DM mass for which N approaches the equilibrium value $C_\odot = E_\odot$ and becomes independent from σ_p. What turns out is that actually m_{min} (and not m_{evap}) qualifies the inability of extracting constraints on σ_p, since the number of DM particles N is not sensitive to σ_p anymore, for $m_\chi \leq m_{min}$. For example, for $m_\chi \lesssim 4$ GeV, data on neutrinos from the Sun are not able to provide information on the DM-proton scattering cross section below $\sigma_p \lesssim 10^{-31}$ cm^2 figure 1.36. On the other hand, for a given value of the scattering cross section there is a minimum DM mass which can be probed by neutrino fluxes from the Sun.

Indirect search signatures

As introduced in section 1.3, there are different annihilations channels available for the WIMPs. Since the DM does not couple directly to photons, the annihilation in channels as $\chi\chi \to \gamma\gamma$ or γZ requires a loop in the Feynman diagrams, figure 1.37, and thus are suppressed. Trying to detect gammas, their absorption probability has to be considered. The GC has a high density of WIMPs but has also high gamma background, while for the galactic halo the situation is the opposite (low background but also low WIMP density).

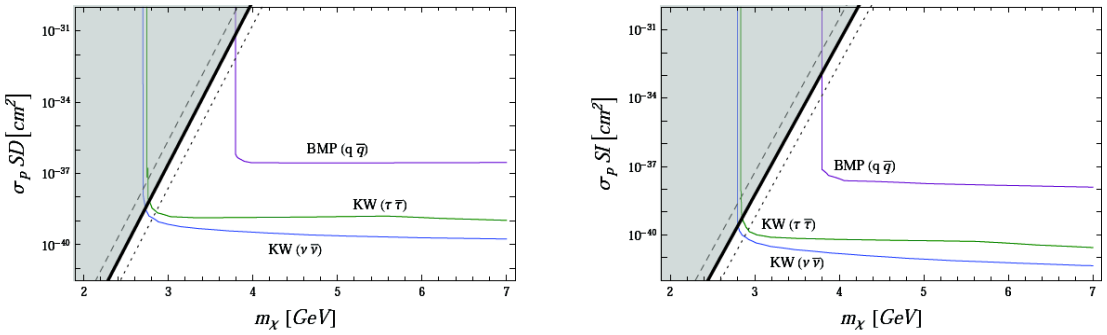

Figure 1.36: The region in the $(m\chi,\ \sigma_p)$ plane (shaded area) which is not testable by detectors of neutrinos from the Sun for SD (left panel) and SI (right panel) interactions. The thick black line corresponds to m_{min} for the reference annihilation cross section $\langle\sigma_a v = 3 \cdot 10^{-26}$ cm^3/s, the dotted (dashed) black lines correspond to $\langle\sigma_a v = 0.1(10)$ times the reference value. For comparison, are also show the exclusion curves obtained by BMP for $\chi\chi \to q\bar{q}$ and KW for $\chi\chi \to \tau\bar{\tau},\ \nu\bar{\nu}$.

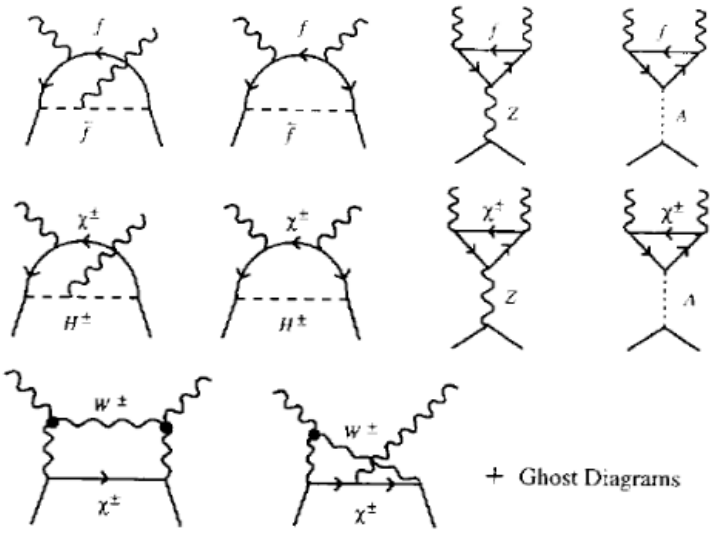

Figure 1.37: Feynman diagrams of neutralino annihilations into photons. Top, fermion-sfermion loops. Middle, charged Higgs-chargino loops. Bottom, chargino-W-boson loops [7].

The measurable γ-ray flux (for neutrinos the formula is the same) from dark matter self-annihilation can be expressed as:

$$\frac{d\Phi_\gamma}{dE_\gamma} = \frac{1}{4\pi}\frac{\langle\sigma_{ann}v\rangle}{2m_\chi^2}\sum_f \frac{dN_\gamma^f}{dE_\gamma}B_f \times \int_{\Delta\Omega} d\Omega' \int_{los} \rho^2 dl(r,\theta') \tag{1.66}$$

where the sum runs over the γ-ray yields for a certain annihilation channel f multiplied by the branching ratio into that channel (B_f). The integrals (called the J-factor) represent the line-of-sight integral of the square of the dark matter density ρ. The production of γ-rays can happen directly or through the production of other particles which then decay. Since the WIMPs are slow moving, in the first case they are expected a mono-energetic gammas while in the second case gammas have a smooth energy distribution, which weakly depends on m_χ, and with an exponential cutoff at the mass of the dark matter particle $E_\gamma = m_\chi$. The fact that the energy is limited by the rest mass of the annihilating particles, provides a unique spectral signature. Since γ-rays, during the propagation, are mostly unaffected by the interstellar medium (IM) and Galactic magnetic fields (GMFs), they retain informations on the position of the emission site, thus identifying the source. Unlike the annihilation, the decay is proportional to the first power of the density and this leads to a weaker dependence from the adopted halo model. There are mainly two types of telescopes that look to such gammas: space and ground-base telescopes. Space telescopes usually detect gammas through their pair conversion when they pass through a series of high-Z material foils. Then, tracking systems, calorimeters and other sensor are used to characterize the observed event, figure 1.38 (left). Concerning the ground-based experiments, such as VERITAS (section 1.4.2), they look to the Cherenkov light emission in the gamma ray interactions with the atmosphere. The typical range for the emitted light is [300, 400] nm and it is spread over a radius $\sim$ 100 m. The telescopes reflect, through mirrors, the Cherenkov radiation onto a camera made by many PMTs, figure 1.38 (right).

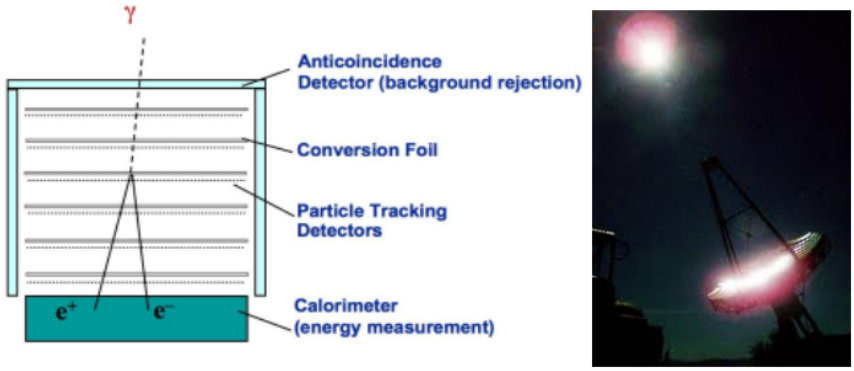

Figure 1.38: Left, gamma ray detection principles in space telescopes. Right, example (VERITAS) of detection of gamma rays from ground-based experiments.

Concerning neutrinos, along their path inside the Earth, they interact with matter

producing leptons. Electrons and taus are not observed since the former are quickly absorbed while the latter suffer a suppression in the generation due to the high mass. Thus, muon neutrinos are detected by experiments. As an example, the Super-Kamiokande (Section 1.5.3) detector look for the muons produced by ν. For such muons, a continuum spectrum is expected since neutrinos are not only produced directly in the annihilations but also in processes as $\chi\chi \to f\bar{f}$, in which f can decay into neutrinos or can hadronize and then produce neutrinos. Among the various annihilation/decay products, the antimatter is a more suitable choice than the matter since it is characterized by a lower background. The idea of searching for an excess of antiprotons in cosmic rays were proposed in the 1980s [85, 86]. The antiproton abundance at a distance r from the galactic center can be expressed as:

$$q_{\bar{p}}(r,T) = \frac{\rho_\chi^2(r)}{m_\chi^2} \frac{\langle \sigma v_{rel} \rangle}{2} \frac{dN_{f\bar{f}}^{\bar{p}}}{dT}, \tag{1.67}$$

where $dN_{f\bar{f}}^{\bar{p}}/dT$ is the antiproton energy spectrum per annihilation in a given $f\bar{f}$ channel. The background of secondary antiprotons from cosmic rays has an energy spectrum peaked at $\sim$2 GeV, figure 1.39, while WIMP antiprotons should show a continuum below $\sim$1 GeV.

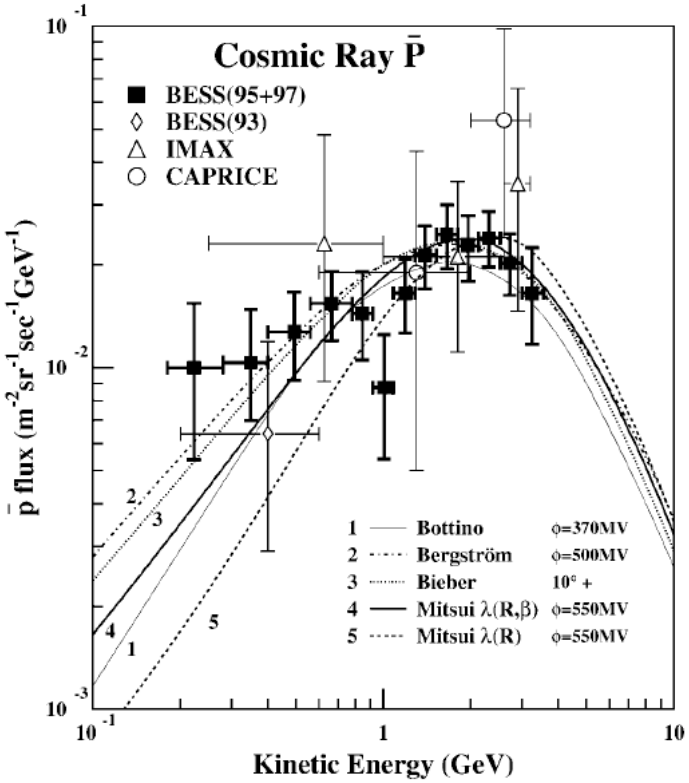

Figure 1.39: Secondary antiprotons flux from various experiments [87].

If the WIMPs are more massive than the $W^{\pm}$ or Z^0 bosons ($W^+ \rightarrow e^+ + \nu_e$ and $Z^0 \rightarrow e^+ + e^-$), then a positron excess would provide a very distinct signature in the cosmic-ray positron flux. Looking at charged particles, it is necessary to take into account processes of energy loss such as Bremsstrahlung, synchrotron emission and inverse Compton losses. In the case of positrons, for example, their spectrum is given by:

$$\frac{dN_{e^+}}{dE_{e^+}} = \int dt \int d^3x \int dE^{'} G(x, t, E, E^{'}) Q(E^{'}, x) \tag{1.68}$$

where $G(x, t, E, E^{'})$ is the Green's function which gives the intensity of positrons seen at $x = 0$, time t and energy E, given an impulse at position x and energy $E^{'}$. $Q(E^{'}, x)$ is the annihilation rate given by:

$$Q(E, x) = 4\pi \frac{dN_{e^+}}{dE d^3x dt} = \sum_i \frac{\langle \sigma v \rangle_i}{M_\chi^2} \frac{dN_{e^+,i}}{dE} \rho(r)^2 \tag{1.69}$$

The Alpha Magnetic Spectrometer (AMS-02) observed an excess in the positron flux, with respect to the expected one [88] (Section 1.5.6), that could be explained as due to dark matter, under proper assumption. For example, if the spectrum shows a real fast decrease at a certain energy, then the DM annihilation hypothesis could be realistic.

1.5.1 General AntiParticle Spectrometer (GAPS)

The GAPS experiment [89], figure 1.40, will search for antideuterons as signature for the dark matter annihilations.

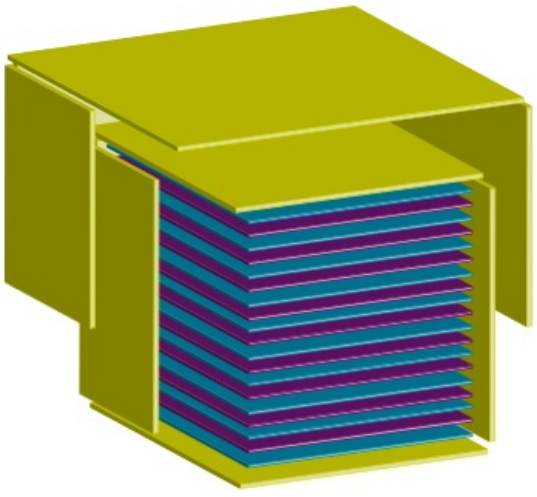

Figure 1.40: A rendering of the GAPS detector design.

Secondary antideuterons can be produced in collisions of cosmic rays (CR) with the IM. Due to the mass of such nuclei, low energy productions are quite disadvantaged

leading to a reduced background in the search for low energy nuclei. The theoretically expected antideuteron flux from different dark matter models compared to the secondary background is shown in figure 1.41, together with flux limits from BESS [90] and the sensitivity reached by AMS [89].

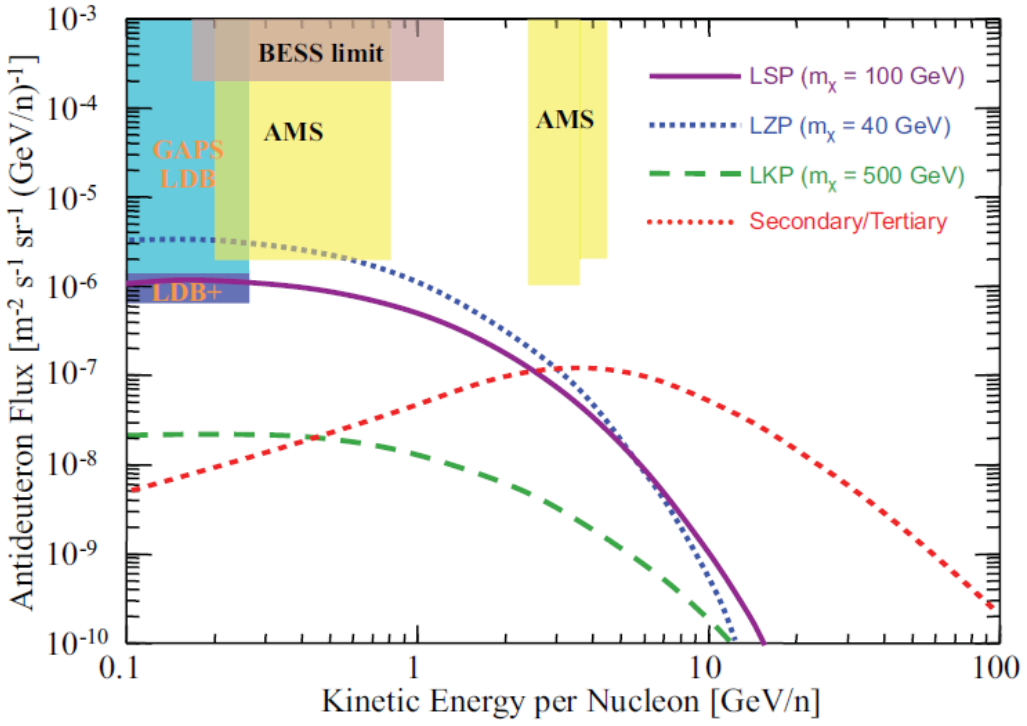

Figure 1.41: Predicted antideuteron fluxes from different dark matter models (purple, red, green lines) [91, 92] and secondary/tertiary background flux from CR interactions with the IM (blue line) [93]. The solid black line corresponds to a WIMP with mass 100 GeV/c^2 annihilating with BR=1 into a $b\bar{b}$ pair; the red dotted line to a 1000 GeV/c^2 WIMP annihilating with BR=1 into W^+W^- pairs; the green dot-dashed line to a 500 GeV/c^2 B(1) (the Kaluza-Klein first excitation of the hypercharge gauge boson), LKP in the UED scenario; while the blue dashed line to a LZP particle pair annihilating dominantly through the Z s-channel resonance, with a mass of 40 GeV/c^2. Antideuteron limits from BESS [90] and sensitivities for the running AMS and the planned GAPS experiments are also shown [89].

Due to the background characteristics, the GAPS detector will be optimized for low energy antideuterons in particular in the range [100, 500] MeV. The first data acquisition is planned for the 2017. The detector will consist of a inner part made of 10 layers of Lithium-drifted Silicon (Si(Li)) modules for an overall cubic shape of 2 m edge. The inner

tracker will be enclosed in a time-of-flight system (TOF) made of plastic scintillators with photomultipliers tubes (PMTs) for the readout. Also the TOF system will have a cubic shape with 4 m edge. GAPS will detect the X-ray emission after de-excitation of an exotic atom made of a target atom where an external electron is replaced by an antideuteron. After the de-excitation, the antideuteron annihilates with the nucleus, thus producing pions and protons. The detector will be able to measure the velocity and the charge of the incoming particle in the TOF as well as the stopping depth of the particle in the tracker and the development of the energy loss per layer throughout the slowing process. The main source of background for the antideuteron signal comes from antiprotons. Therefore, a good X-ray energy resolution along with a reliable tracking and counting systems for pions/protons are essential for the background reduction.

1.5.2 VERITAS

The VERITAS telescope [94], figure 1.42, consists of four Davies-Cotton optical reflectors, 12 m of diameter.

Figure 1.42: VERITAS telescope array.

They focus the light from γ-ray air showers, in the energy range from 100 GeV up to 50 TeV, onto four 499 pixel PMT camera. Its observations are mainly directed to dSph galaxies, galaxy clusters and GC. The dSph galaxies are gravitational-bound objects and are believed to contain up to $\mathcal{O}(10^3)$ times more mass in dark matter than in visible matter, making them widely discussed as potential targets for indirect dark

matter detection. One of the most important results from VERITAS comes from the observation of the gamma-ray flux, from Segue 1 [94], perhaps originated by annihilation or decay of dark matter. Since no signal above the background has been observed, only upper limits on the gamma-ray flux have been set considering different annihilation channels, figure 1.43.

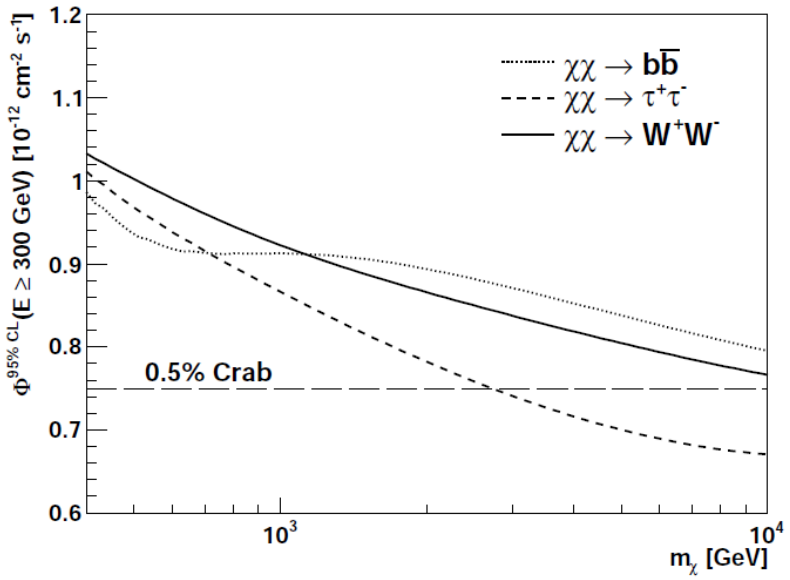

Figure 1.43: Upper limits, at 95% CL, on the integrated γ-ray flux above $E_{min} = 300$ GeV, from the VERITAS observations of Segue1. They are considered three different channels for the dark matter annihilation/decay: W^+W^-, $b\bar{b}$ and $\tau^+\tau^-$. For comparison, 0.5% of the integrated Crab Nebula flux above $E_{min} = 300$ GeV, equal to $7.5 \cdot 10^{-13}$ cm^{-2} s^{-1}, is also reported [94].

Upper limits on the flux can be then translated into upper limits on the dark matter annihilation cross section or on the mean lifetime for the decay channels. For what concerns the annihilation, the most stringent limit at 95% CL on the velocity-weighted annihilation cross-section is for the W^+W^- channel: $\langle\sigma v\rangle \leq 8 \cdot 10^{-24}$ cm^3 s^{-1} at a dark matter mass of 1 TeV, figure 1.44 (left panel). The $b\bar{b}$ and $\tau^+\tau^-$ exclusion curves illustrate the range of uncertainties on the $\langle\sigma v\rangle$ upper limits from the dark matter particle physics model. Considering the leptonic channels, the limits are of the order of 10^{-23} cm^3 s^{-1}, figure 1.44 (right panel). For what concerns the decay lifetime, there are models where the DM is treated as fermionic, and others where it is treated as bosonic. For both cases, lower limits at 95% CL are found in the range $\tau \sim 10^{24} - 10^{25}$ [94], figure 1.45.

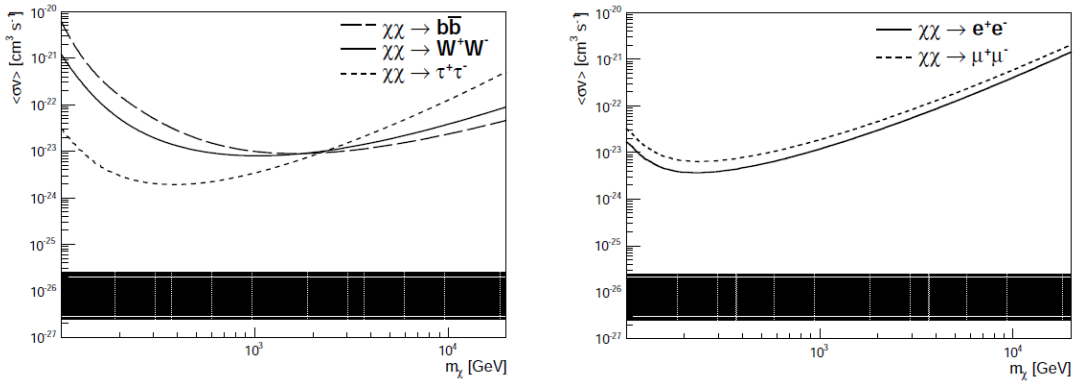

Figure 1.44: 95% CL upper limits on the WIMP velocity-weighted annihilation cross-section $\langle \sigma v \rangle$, as a function of the WIMP mass, from the VERITAS observations of Segue 1 considering different annihilation channels: left for hadronic channels, right for leptonic channels. The black area represents a range of generic values for the annihilation cross-section in the case of thermally produced dark matter [94].

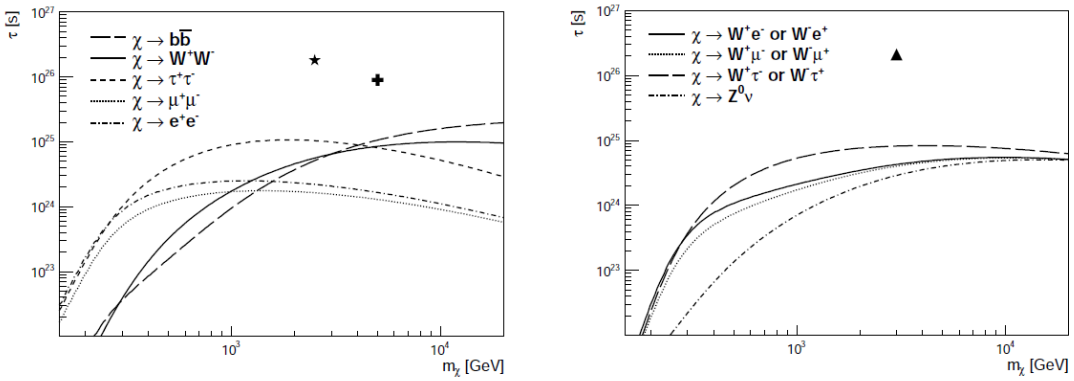

Figure 1.45: 95% CL lower limits from the VERITAS observations of Segue 1 of the decay lifetime as a function of the dark matter particle mass. Left, bosonic dark matter decay: $W^+W^-, b\bar{b}, \tau^+\tau^-, e^+e^-$ and $\mu^+\mu^-$. The black star and the black cross denote the best fits to the Fermi and PAMELA data considering the $\mu^+\mu^-$ and the $\tau^+\tau^-$ channels, respectively [95]. Right, fermionic dark matter decay: $W^{\pm}l^{\mp}$ and $Z^0\nu$. The black triangle indicates the best fit to the Fermi and PAMELA data considering the channel $W^{\pm}\mu^{\mp}$ [95].

1.5.3 Super-Kamiokande

The Super-Kamiokande (SK) detector [96], figure 1.46, is a kton water Cherenkov detector of cylindrical shape with height of 36.2 m and radius of 16.9 m.

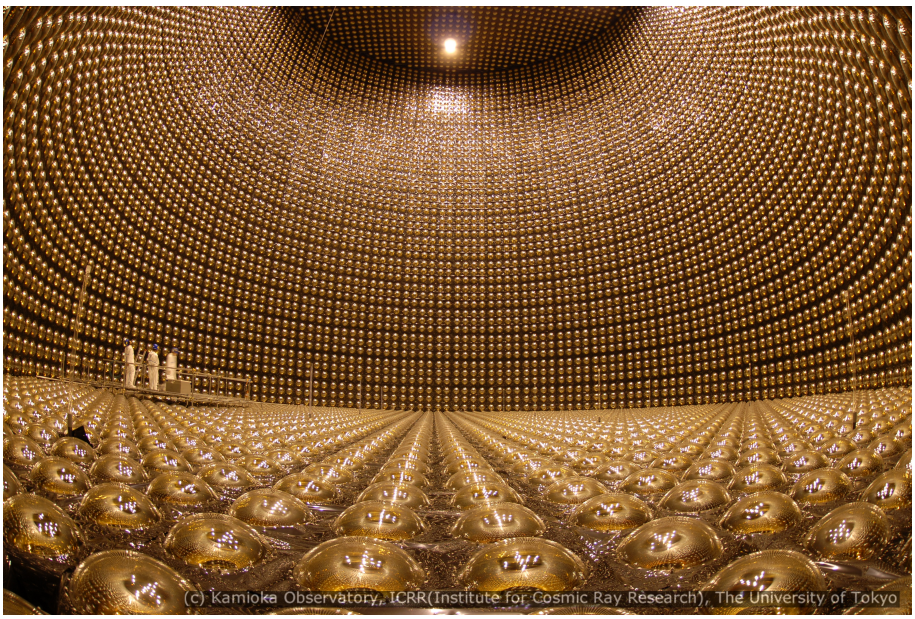

Figure 1.46: Super-Kamiokande detector.

It is located in the Kamioka-Mozumi mine in Japan under about 1000 m rock. It consists of a inner detector with 11.146 inward-facing 50 cm PMTs and an outer detector equipped with 1885 outward-facing 20 cm PMTs, serving as a cosmic ray veto counter. The goal of this detector is the indirect search of dark matter through the detection of an excess of upward-going muons (upmu). These muons are generated by the muon neutrinos (generated in DM annihilations in the Sun) interactions with rocks that surround the detector. For their last results, the collaboration used data acquired from April 1996 to August 2008 [97] (3109.6 days). Muon events in the detector have been divided into three categories: "stopping", muons with the lowest energy that stop in the detector ($E_\nu << 10$ GeV); "showering", muons that produce showers in the detector and "non-showering", which don't produce any shower. Using DARKSUSY calculations [98], the 90% CL limit on SD cross section has been evaluated as function of the WIMP mass [97], figure 1.47. The limits have been calculated in the case of soft, $\bar{b}b$, and hard, W^+W^-, annihilation processes. The minimum for the cross section is reached at a WIMP mass of 100 GeV/c^2 and it is equal to $4.5 \cdot 10^{-39}$ cm^{-2} and $2.7 \cdot 10^{-40}$ cm^{-2} in the soft and hard annihilation channels, respectively. Considering only fully contained events (where the muon is created and stopped inside the detector) and upward stopping muons, one can set limits especially for low mass dark matter for the spin-independent case [79], figure 1.48, and for the spin-dependent case [79], figure 1.49.

For the spin-independent case, figure 1.48, it results that the CoGeNT and DAMA confidence regions are excluded for WIMPs which annihilate into neutrinos or taus,

s-wave, while only DAMA remains excluded in the case of p-wave annihilations.

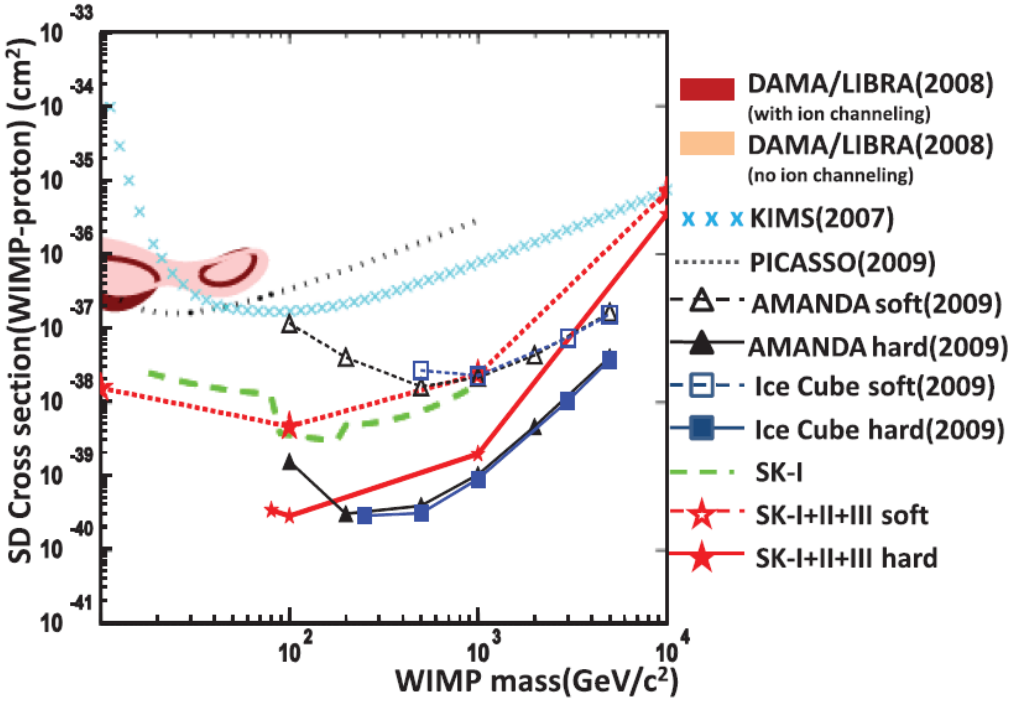

Figure 1.47: Limits on the WIMP-proton SD cross section as function of WIMP mass. Also shown are limits from: DAMA/LIBRA [63] (dark red and light red filled), KIMS [99] (light blue crosses), PICASSO [100] (gray dotted line), AMANDA [101] (black line with triangles), IceCube [98] (blue line with squares), and SK results from the 3109.6 days run (red line with stars). The previous limit from Super-K (green dashed line) is also shown.

Requiring a contemporary explanation for CoGeNT and DAMA limits, all the channels apart from the neutrino and tau ones remain acceptable also in the case of p-wave annihilation. It is also possible to consider a model where the WIMPs annihilate into light Higgs pairs which in turn decay into taus or charms [102]. Having a suppression for the decay into 4-τ, the model can explain CoGeNT and DAMA results for p-wave annihilations. Concerning the spin-dependent limits, results from CoGeNT and DAMA are excluded for all decay channels for both s-wave and p-wave annihilations. In order to reconcile the direct search results between several experiments, an isospin violating dark matter model has been proposed, (see the next chapter). Also in this case, the results from Super-Kamiokande excludes the limits from the other experiment, especially for the neutrinos channel, for s-wave and p-wave annihilation, figure 1.50.

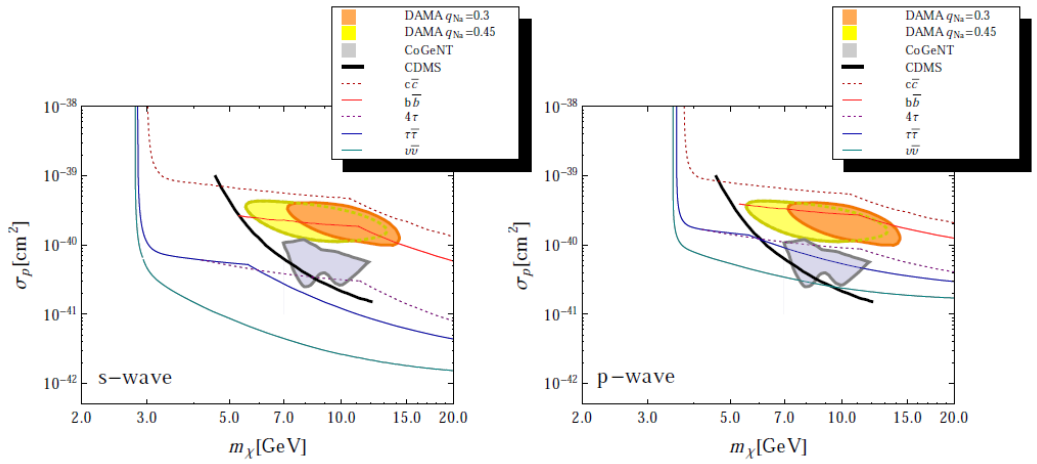

Figure 1.48: Super-Kamiokande 90% upper limits on the spin-independent WIMP nucleon cross section for various annihilation channels (equal couplings to proton and neutron are assumed) [79]. The annihilation cross section is chosen such that the thermal WIMP abundance matches the observed dark matter abundance for s-wave annihilation (left panel) and p-wave annihilation (right panel). At low WIMP mass the limits arise from fully contained events, at higher WIMP mass from upward stopping muons. Below the evaporation mass all constraints disappear rapidly. Also shown are confidence regions and limits from direct detection experiments.

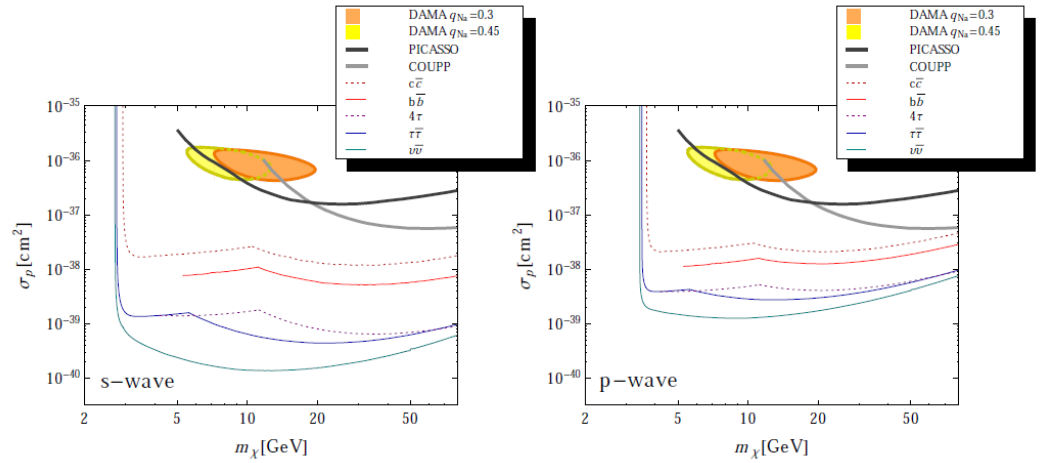

Figure 1.49: Same as figure 1.48, but for the spin-dependent case [79].

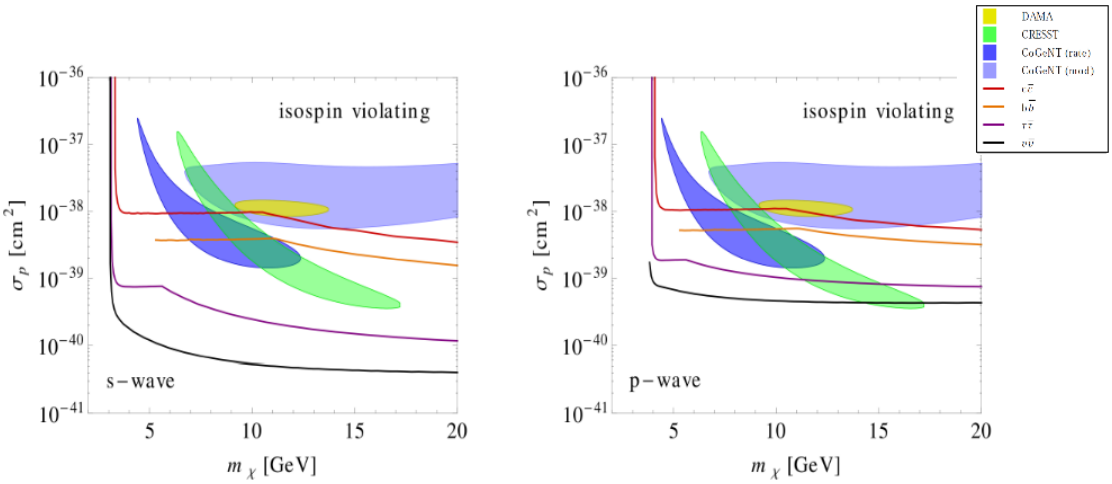

Figure 1.50: The Super-Kamiokande 90% upper limits on the WIMP proton cross section for spin-independent interactions with $f_n = -0.7 f_p$ (black line). Different WIMP annihilation channels have been considered. S-wave (p-wave) annihilation with a thermal cross section is assumed in the left (right) panels. Also superimposed are the 90% confidence regions from DAMA, CoGeNT and CRESST.

1.5.4 Fermi-Large Area Telescope

The Fermi-Large Area Telescope (Fermi-LAT) is a gamma-ray telescope placed on board the Fermi Observatory [103], figure 1.51, sensitive to energies from 20 MeV up to over 300 GeV.

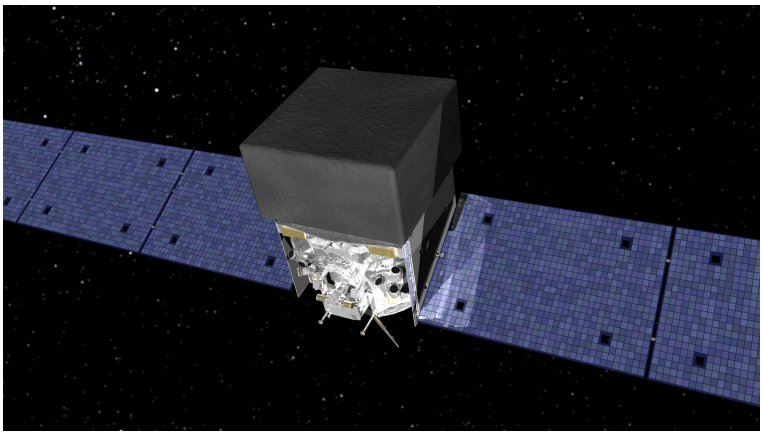

Figure 1.51: Picture of the Fermi-LAT telescope.

One of the goals of this telescope is to find a DM signature in the diffuse gamma-ray emission. At galactic level, it is expected that the signal comes from annihilation of

WIMPs in a smooth halo around the galaxy while the extra-galactic signal arises from DM annihilation processes throughout the universe. For the galactic halo study, the Fermi-LAT collaboration explored the energy range [1, 400] GeV [104]. The limits were set both for annihilation and decay of the DM particles, figure 1.52 and 1.53.

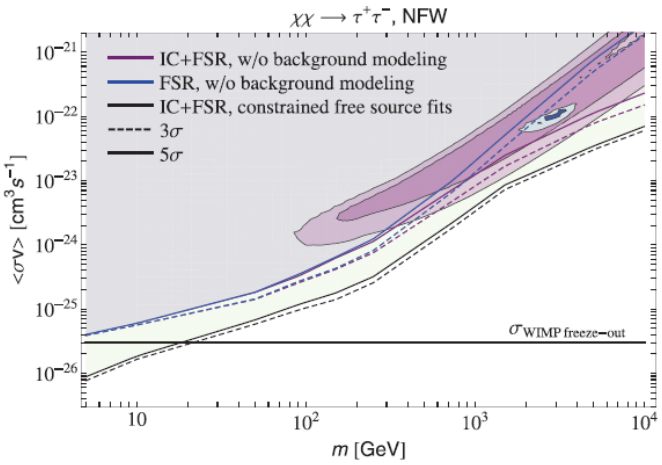

Figure 1.52: Upper limits, considering the Navarro-Franck-White halo model, of the averaged velocity cross section for DM annihilation to $\tau^+\tau^-$ including a model of the astrophysical background. The region excluded by the analysis with no model of the astrophysical background is indicated in light blue, while the additional region excluded by the analysis with a modeling of the background is indicated in light green. The regions of the parameter space which provide a good fit to PAMELA ([105], purple) and Fermi-LAT ([106], blue) CR electron and positron data are shown and scaled by a factor of 0.5, to account for different assumptions on the local DM density [104].

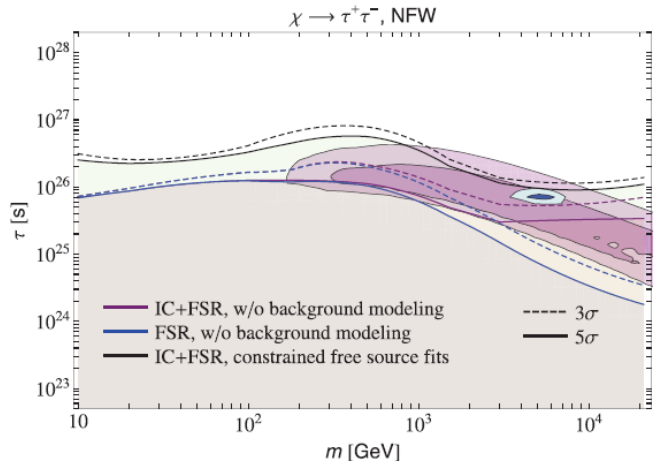

Figure 1.53: Lower limits, considering the Navarro-Franck-White halo model, on the lifetime of decaying DM [104]. Curves and colors as in figure 1.52.

A possible gamma-ray emission line hypothesis has also been considered [104]. After positive results there were not found, after new analyzes and background calculations, any evidences for a clear signal from DM γ-ray line [104, 107]. Thus, new upper limits were set for the dark matter annihilation channel, figure 1.54.

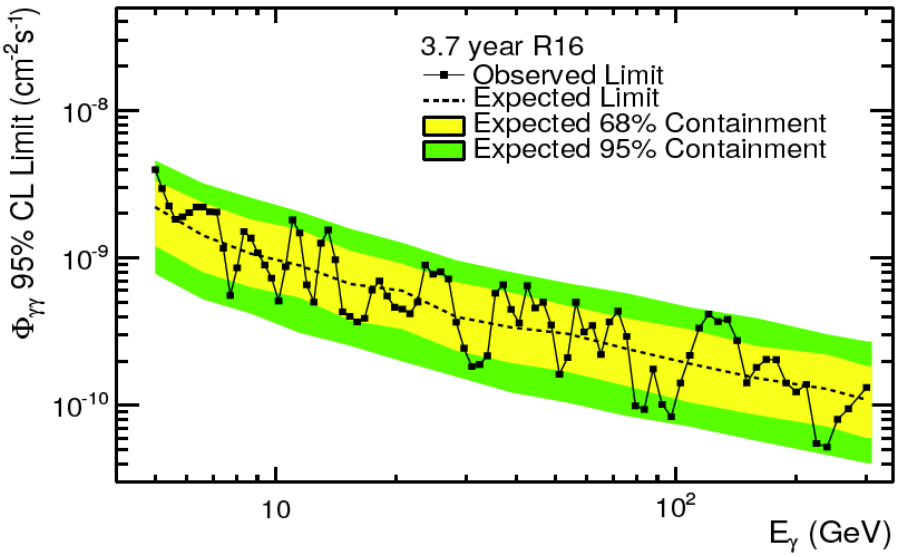

Figure 1.54: 95% CL $\Phi_{\gamma\gamma}$ in the R16 ROI (black). Yellow (green) bands show the 68% (95%) expected containment derived from 1000 single-power law, no DM, MC simulations. The dashed lines show the median expected limits from those simulations [107].

1.5.5 IceCube

IceCube is a neutrino telescope placed at the south pole that aims to detect the Cherenkov light emitted by muons, created by neutrinos, interactions with the Antarctica ice. The neutrinos of interest are generated by dark matter annihilations in the Earth and in the Sun. The telescope consists of 86 vertical strings equipped with Digital Optical Modules (DOMs), figure 1.55, that contain a digitizer board and a PMT. 78 of these strings carry 60 DOMs, placed at intervals of 17 m from a depth of 1450 m up to 2450 m below the ice surface. The other 8 are infill-specialized for a sub-array dubbed DeepCore, placed in the central region of the telescope. IceCube is sensitive to neutrinos in the energy range from 100 GeV up to 1 TeV, while DeepCore can reach sensitivity down to 10 GeV neutrinos. This means that the entire telescope is sensitive to neutralinos down to masses of about 50 GeV [108]. The last results of the IceCube collaboration come from the analysis of 317 live-days of data taken between June 2010 and May 2011 [65]. The main background of the telescope is due to muons and neutrinos produced by cosmic

rays that interact in the atmosphere.

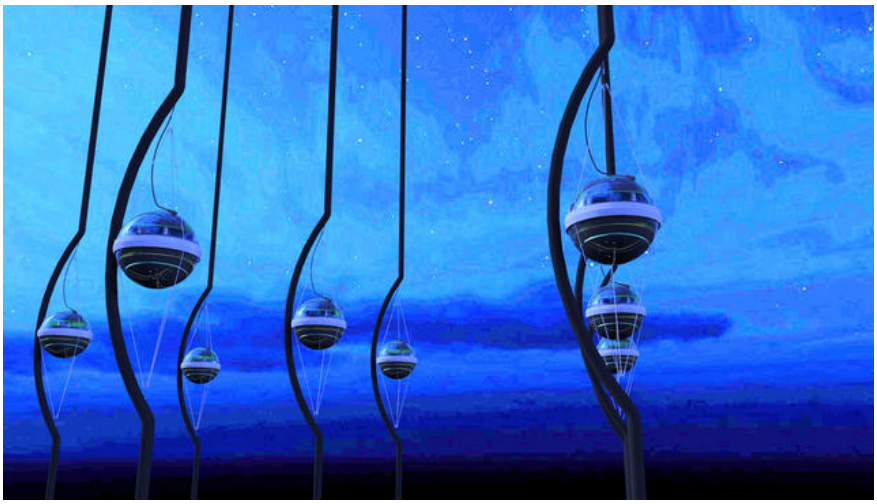

Figure 1.55: Representations of IceCube's DOMs.

Also the background from solar atmospheric neutrinos, originating from cosmic rays interactions in the Sun's atmosphere, has been calculated and it has been found to be of the order of 1 event [65, 109]. To take into account all the possible background variations, the dataset was divided into three parts: summer season, focused on low energy neutrinos, and winter season which is, in turn, divided into a low and high energy sample. After all the cuts and track selection criteria, the observed distributions of the event directions have been compared with the expected background distributions from atmospheric muons and neutrinos [65] finding compatibility with the only-background hypothesis. The obtained upper limits on the expected number of signal events, μ_s^{90}, can be translated into upper limits for the annihilation rate, Γ_a, of WIMPs in the Sun that, in turn, can be converted into limits on the spin-dependent, $\sigma_{SD,p}$, and spin-independent, $\sigma_{SI,p}$, WIMP-proton scattering cross-sections. Considering a local dark matter density of 0.3 GeV/c^3 and a Maxwellian WIMP velocity distribution with an RMS velocity of 270 km/s, limits on the spin-dependent WIMP-proton cross section for WIMPs annihilating into W^+W^- or $\tau^+\tau^-$, with masses above 35 GeV/c^2, were set [65], figure 1.56 and figure 1.57. The IceCube data have been also used to infer information and set limits on the super heavy dark matter, i.e. for $m_\chi > 100$ TeV [110]. These values of masses imply a much lower density of dark matter which results in a reduced sensitivity for direct detection experiments. Due to the low density, this kind of search is based on the detection of the decay products such as high energy neutrinos. Considering dark matter with $m_\chi \sim 100$ TeV that decays into two neutrinos, IceCube already set limits on the lifetime giving the strongest limit: $\tau > 10^{27}$ y [111].

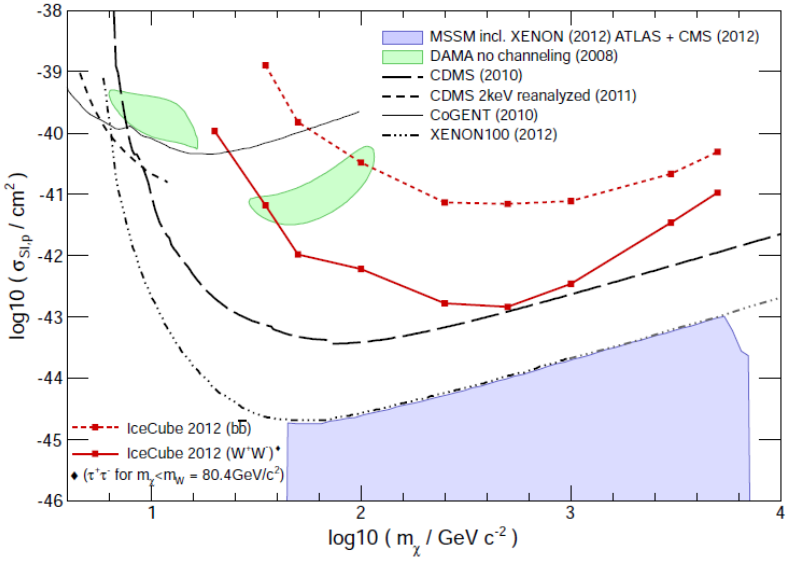

Figure 1.56: 90% CL upper limits on $\sigma_{SI,p}$ for hard and soft annihilation channels over a range of WIMP masses. The shaded region represents an allowed MSSM parameter space. Systematic uncertainties are included. Results from other experiments are also shown as comparison [65].

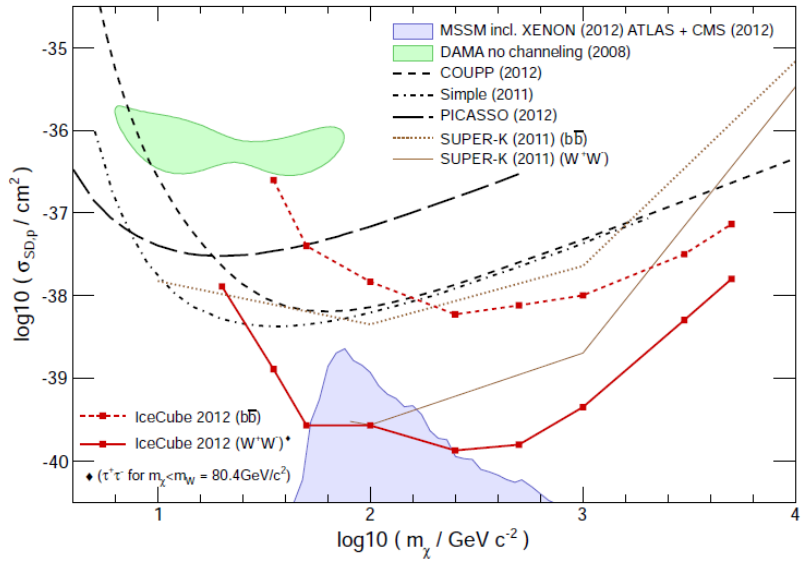

Figure 1.57: 90% CL upper limits on $\sigma_{SD,p}$ for hard and soft annihilation channels over a range of WIMP masses. The shaded region represents an allowed MSSM parameter space. Systematic uncertainties are included. Results from other experiments are also shown as comparison [65].

Concerning the Galactic signal, two components are expected from $\chi \rightarrow \nu h$: one from a continuum (from the decay cascade of h) and a nearly mono-energetic line at $E_\nu \equiv m_\chi/2$. Using the observation of high energy extraterrestrial neutrinos [110], limits on the lifetime of heavy dark matter have been set, figure 1.58.

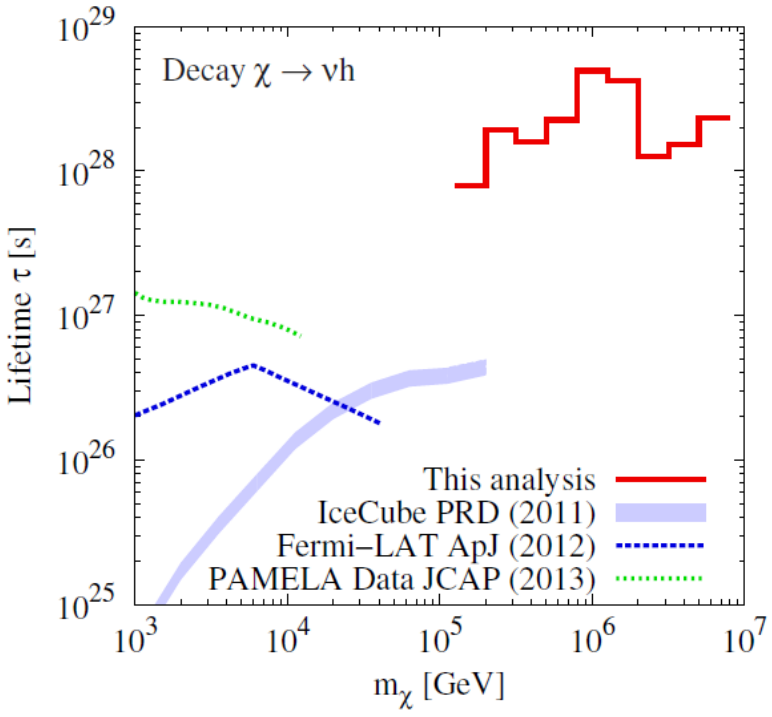

Figure 1.58: Derived limit, on the lifetime of heavy dark matter, of IceCube using the observed high-energy neutrino flux. Superimposed are also results from IceCube (previous results), Fermi LAT and PAMELA [110].

1.5.6 AMS-02

The Alpha Magnetic Spectrometer (AMS), currently in its second phase AMS-02, is an antimatter search experiment placed on the International Space Station (ISS), figure 1.59. In its latest results [112] the AMS collaboration has found an excess in the positron fraction at energies > 8 GeV, figure 1.60, above the expected background due to secondary positrons originate in the spallation of cosmic rays on the interstellar medium. The positron fraction stops to increase at ~ 275 GeV and this excess seems to be isotropic within 3% suggesting that the energetic positrons may not be coming from a preferred direction in space. Considering also the antiproton results from PAMELA [105], where the antiproton flux is compatible with the expected background, a scenario that consider a leptophilic dark matter, as possible source of positrons, is viable [113].

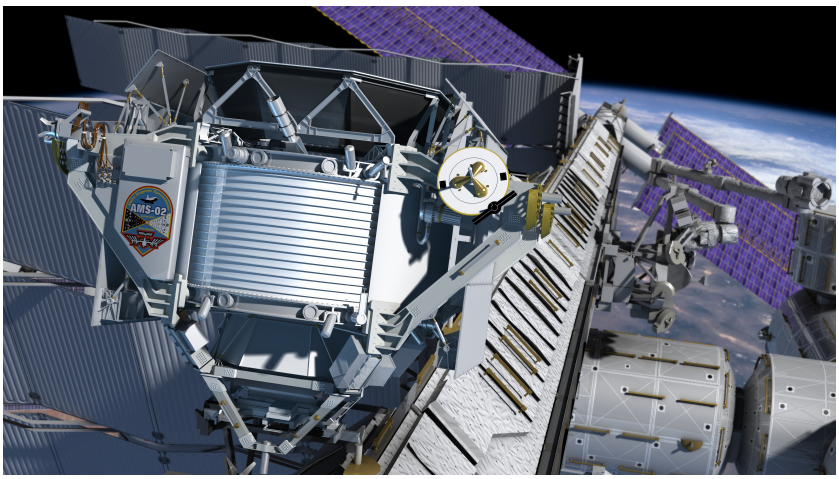

Figure 1.59: AMS-02 experiment on the ISS.

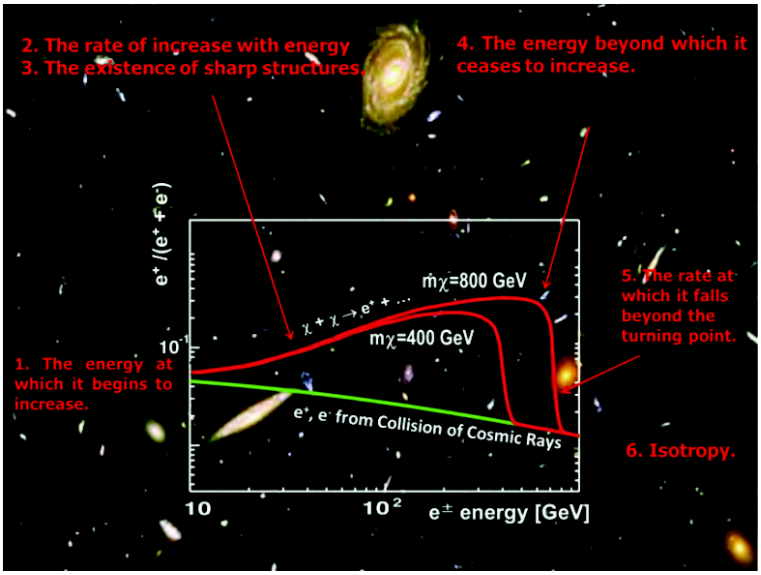

Figure 1.60: Excess in the positron fraction [114].

These kind of candidates annihilate predominately into leptons producing a large amount of energetic positrons while the antiproton flux remains suppressed. Using this kind of WIMP and considering masses above 500 GeV, the AMS-02 collaboration has evaluated the annihilation cross section for leptophilic channels that can explain the observed positron fraction [113]; the value for the annihilation cross section is of the order $10^{-23} - 10^{-22} \mathrm{cm}^3\mathrm{s}^{-1}$ that is about 10^3 times larger than the thermal cross section. Besides the previous case, it is also possible to let the dark matter to decay into gauge bosons. Using two values for the WIMP mass [113], 600 and 800 GeV, and considering its decays through leptonic and bosonic channels, it is still possible to explain the observed

excess, figures 1.61 and 1.62.

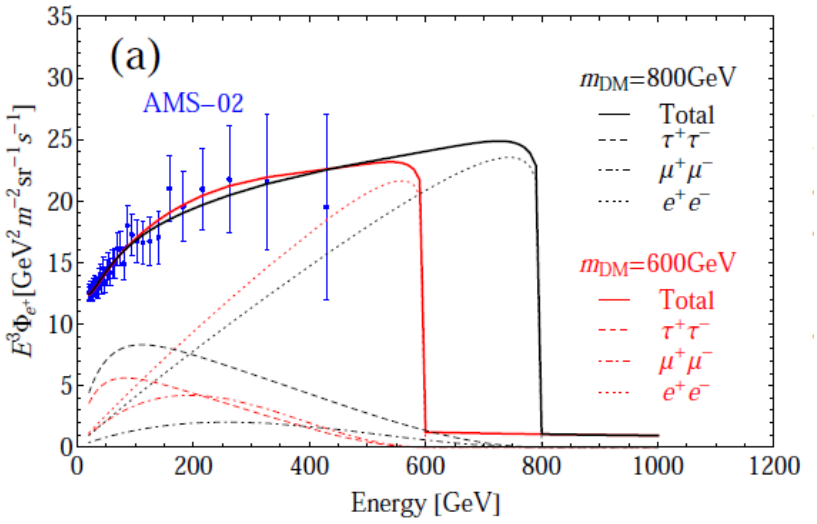

Figure 1.61: Comparison between AMS-02 positron fraction data [112] and prediction from dark matter considering only leptonic annihilation

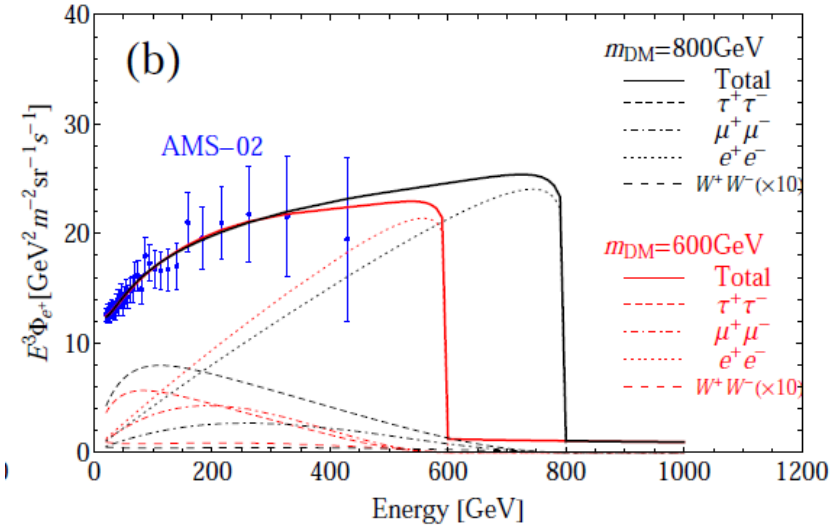

Figure 1.62: Same as figure 1.61 but including gauge boson modes.

From figures 1.61 and 1.62 we can see that the fraction falls to its background value at an energy that corresponds to the dark matter mass. This behavior of the spectrum can give important informations about the WIMP mass. Including also the bosonic channel for the annihilation, one has a production of antiprotons whose spectrum has been found compatible with the background. Limits have been set also for lower dark

matter masses. In their analysis, the AMS-02 collaboration considered several energy windows [115]. Looking at the best limits for each energy window, 2σ exclusion lines can be evaluated for each mass, figure 1.63.

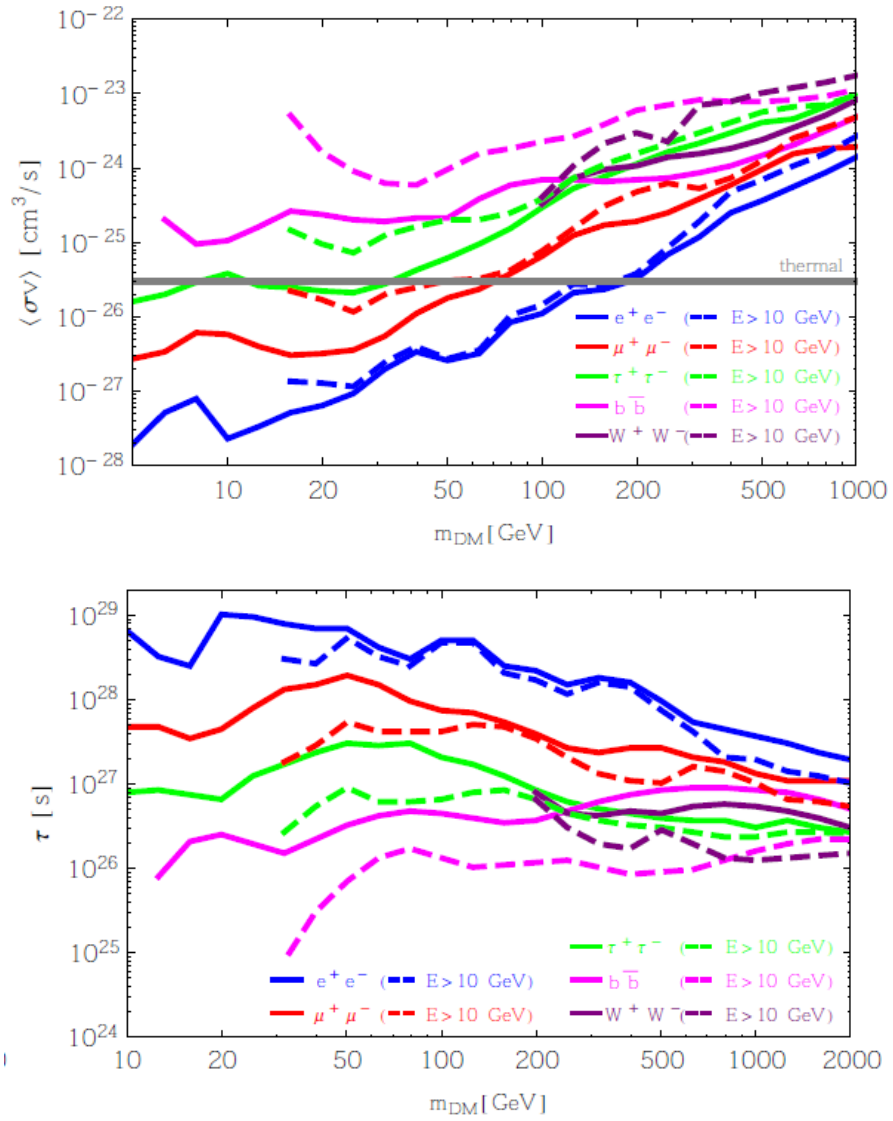

Figure 1.63: Limits on the annihilation cross section (top) and the lifetime (bottom) derived from the AMS-02 data on the positron flux [115], assuming the final states e^+e^-, $\mu^+\mu^-$, $\tau^+\tau^-$, $b\bar{b}$ and W^+W^- and the MED propagation model. The limits shown as solid lines were derived from sampling over various energy windows, while the dashed lines are from windows that include only data with energies above 10 GeV.

In figure 1.63 the dashed lines are obtained considering energy windows above 10 GeV. This allows to be less sensitive to the solar modulation giving more robust results.

The limits for masses below ~ 100 (60) GeV are stronger than the thermal cross section $\langle \sigma v \rangle = 3 \cdot 10^{-26}$ cm^{3}s^{-1} for the e^+e^- ($\mu^+\mu^-$) annihilation channel. Figures 1.64 and 1.65 shows a comparison between AMS-02 results [116] and the ones from HEAT [117], PAMELA [118] and FERMI-LAT [119], for two annihilation/decay channels: $b\bar{b}$ and $\mu^+\mu^-$. For the $\mu^+\mu^-$ annihilation channel, the AMS-02 limits are stronger than the ones from FERMI-LAT for all the masses from 1 GeV up to 1 TeV.

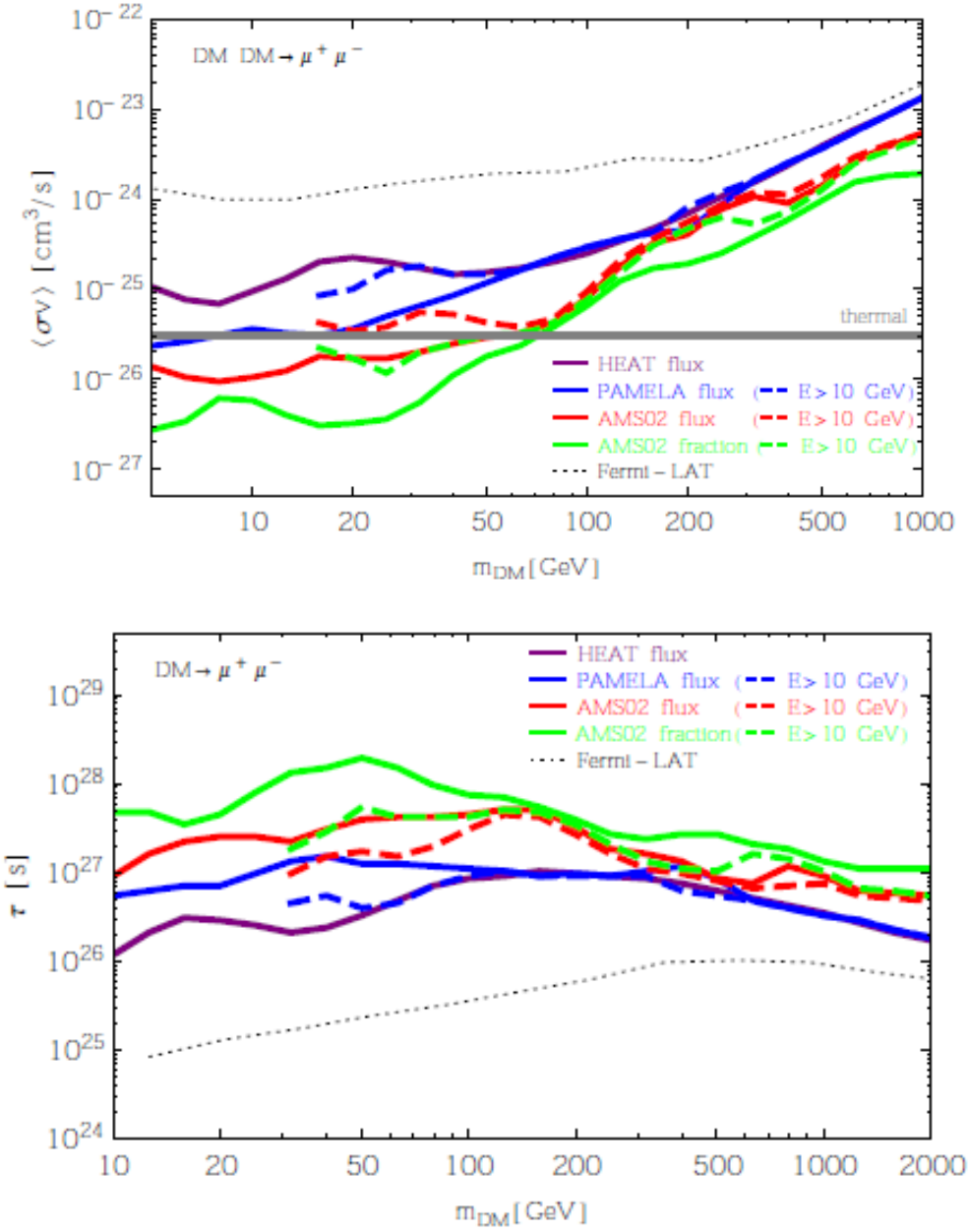

Figure 1.64: Comparison between limits, for the $\mu^+\mu^-$ channel, from AMS-02, HEAT, PAMELA and FERMI-LAT [115].

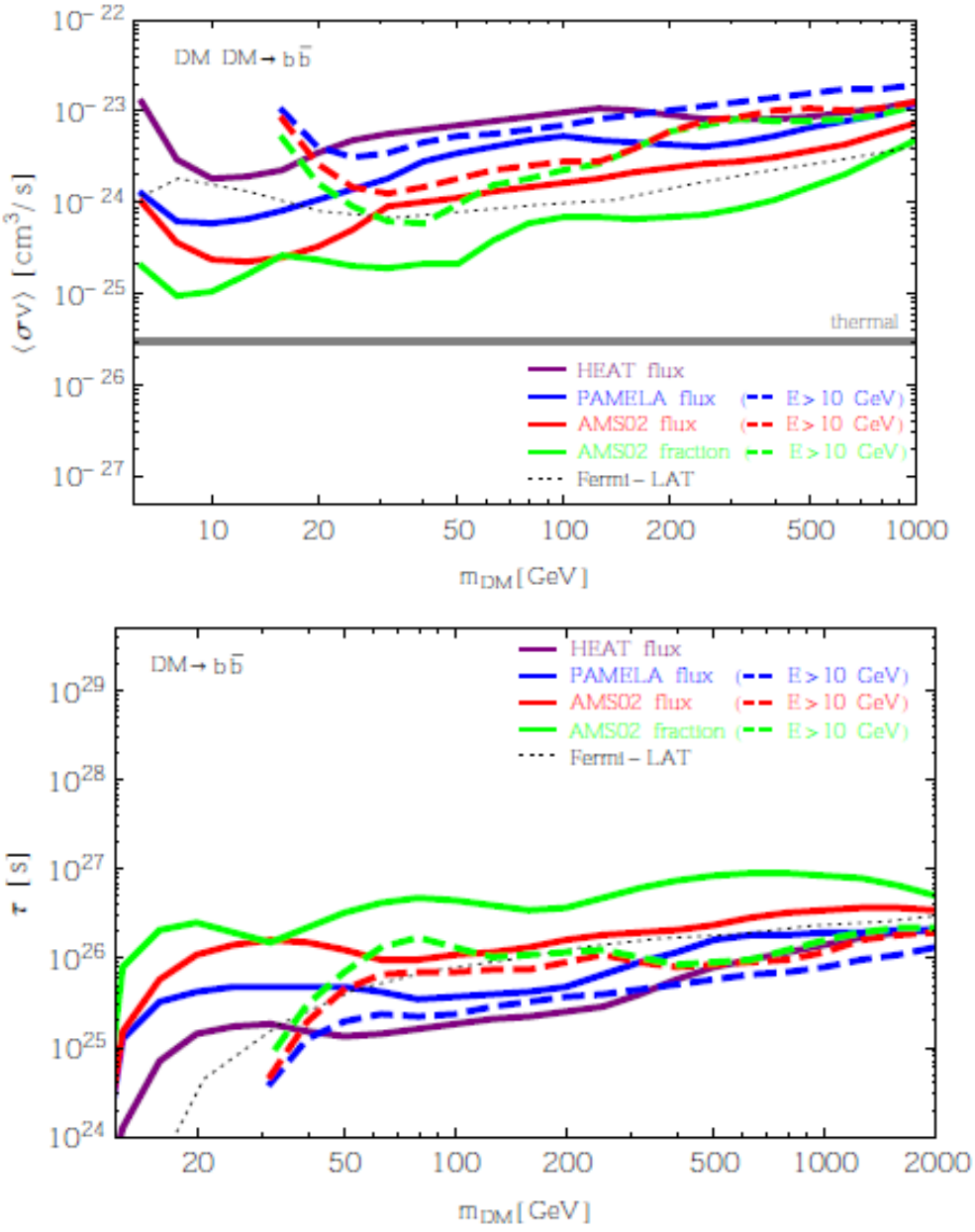

Figure 1.65: Comparison between limits, for the $b\bar{b}$ channel, from AMS-02, HEAT, PAMELA and FERMI-LAT [115].

Chapter 2

Dark Matter models

In the last few years, several experimental results have been published regarding cross section limits for dark matter interactions. The WIMP low mass region, below $\sim$ 10 GeV, is particularly interesting for experiments such as DAMA [120], CoGeNT [121] and CDMS-Si(Ge) [122]. For higher masses, other experiments, as XENON100 [8] and LUX [10], have better sensitivities. The DAMA/LIBRA results combined with the DAMA/NaI ones have shown a clear modulation signal with a significance $\geq 8\sigma$ [57] that can be interpreted as due to DM. For the usual WIMP-nucleus elastic scatters, it is almost impossible to explain these results without going in contrast with the null ones obtained in XENON100, LUX, CRESST, etc.
To reconcile such different experimental results, several DM interaction models have been proposed. In this Chapter few of them are presented. Moreover, in section 2.6 it is presented a model that gives a different solution to the "missing mass problem", without assuming any kind of new matter.

2.1 Resonant Dark Matter Model

One of the "alternative" DM models is the **Resonant Dark Matter** (rDM) [123]. In such a model the WIMP-nucleus interactions consist of a scattering process that can come together with a photon or neutron emission (the proton emission could be also possible but, practically, it is suppressed because of the Coulomb barrier of the nucleus). Other than this new signal characteristic, rDM introduces two more novel features:

- there is a resonance effect that shows up as a narrow window, around a specific velocity, in the WIMP Maxwell-Boltzmann velocity distribution; such an effect depends from several parameters of the model, such as the Z of the target nucleus;

- the DM is the neutral component of a fermionic weak triplet with almost degenerate masses, $\mathcal{O}(10)$ MeV.

In the rDM model, dark matter particles form a short-lived bound state of mass m_r with the target nuclei. This results in a narrow allowed energy range, equation (2.9), and in a subsequent enhancement of the modulation level, for high mass targets such as the DAMA one, and in a decrease of the signal in other direct detection experiments.
Usually, the nuclear cross section for DM-nuclei interactions is express in terms of the nucleon one (σ_p):

$$\sigma_N = \frac{(Z f_p + (A-Z) f_n)^2}{f_p^2} \frac{\mu_{N_\chi}^2}{\mu_{n_\chi}^2} \sigma_p \tag{2.1}$$

where $\mu_{N_\chi(n_\chi)}$ is the DM to nucleus (nucleon) reduced mass. In the non-relativistic limit and for an energy close to m_r, in the center of the mass reference frame, σ_N becomes:

$$\sigma_N = \frac{2J_r + 1}{(2s_\chi + 1)(2s_N + 1)} \frac{\pi}{k^2} \frac{\Gamma_{r\to\chi N}^2}{(E - m_r)^2 + \Gamma_{tot}^2/4} \tag{2.2}$$

where $s_{\chi(N)}$ is the dark matter (nucleus) spin, J_r is the resonant bound state total angular momentum, $\Gamma_{r\to\chi N}$ is the partial width of the bound state decay into χ (the DM particle) plus N (the target nucleus) and $k = \mu_{N\chi} v$ is the DM momentum. Defining the resonance velocity, figure 2.1 (top), as:

$$v_r^2 = \frac{2(m_r - m_\chi - m_N)}{\mu_{\chi N}}, \tag{2.3}$$

and its width as:

$$\delta^4 = \frac{\Gamma_{tot}^2}{\mu_{\chi N}^2}, \tag{2.4}$$

it is possible to express σ_N as:

$$\sigma_N = \sigma_0 \frac{v_r^2}{v^2} \frac{\delta^2/\pi}{(v^2 - v_r^2)^2 + \delta^4} \tag{2.5}$$

where σ_0 is a normalization factor. In the narrow resonance case with $\delta << v_r$, it is:

$$\sigma_N = \sigma_0 \ \delta(v^2 - v_r^2) \tag{2.6}$$

In the resonant model, the modulation is enhanced because there is a narrow range available for the process and there is not an average over the seasons. Considering a WIMP mass of 500 GeV/c^2 and a recoil energy range of 3 keV$_{ee}$ $< \overline{E_R} <$ 3.5 keV$_{ee}$ (for the keV$_{ee}$ definition see Section 3.6), it is possible to have relative modulation (summer with respect to the winter) as high as 100%, figure 2.1 (bottom).

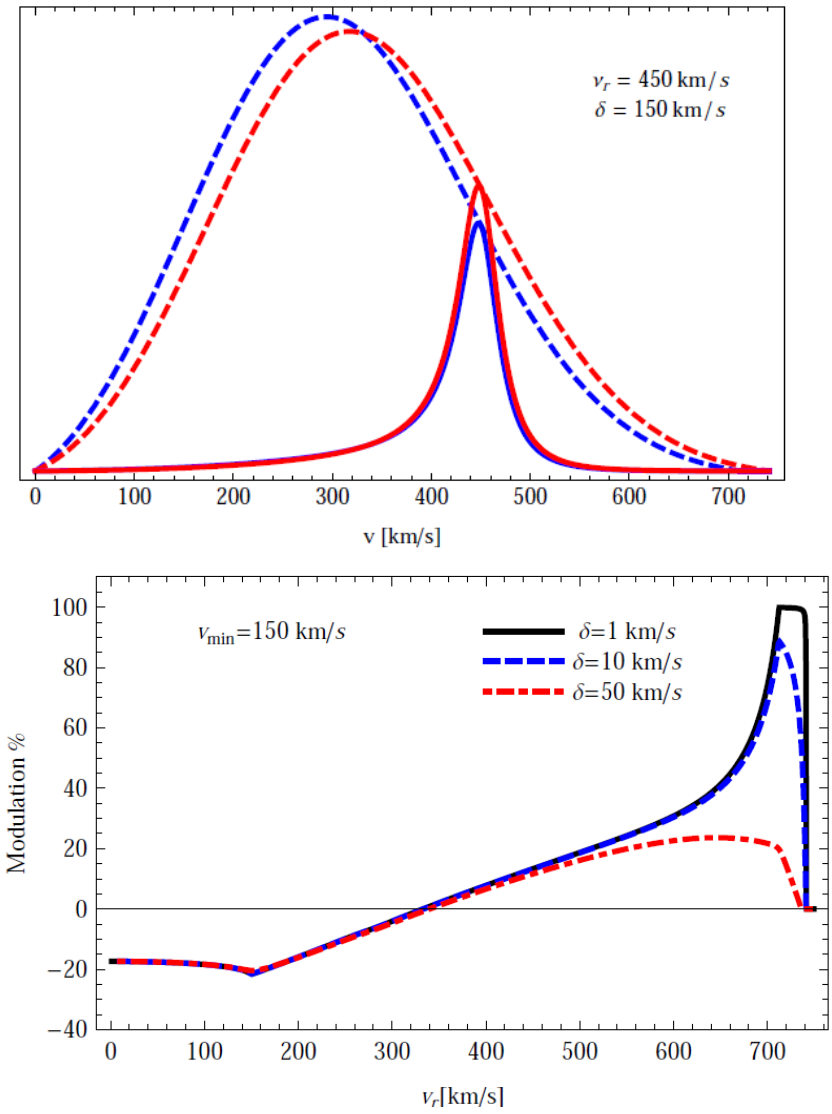

Figure 2.1: Top: DM velocity distribution in summer (red dashed) and in winter (blue dashed) for the usual Maxwell-Boltzmann distribution together with a resonance (solid) at 450 km/s with width of 150 km/s. The escape velocity is 500 km/s. Bottom: Modulation signal (summer with respect to winter) as function of v_r for several values of the velocity width: $\delta = 1$ km/s (black solid), $\delta = 10$ km/s (blue dashed) and $\delta = 50$ km/s (red dot-dashed). If the resonance velocity is below the peak of the Maxwell-Boltzmann distribution, it is possible to have a modulation ratio that is negative because below the peak the distribution is higher in the winter than in the summer [123].

The rDM model can explain the DAMA modulation signal because it is possible to choose a resonant velocity that is element dependent. This opens up the possibility to have the iodine as the only element with an available resonance while in other exper-

iments the signal rate would suppressed by $\sim (\delta/v_r)^4 \leq 10^{-4}$ [123]. As mentioned at the beginning of the section, in the rDM model the dark matter is the neutral component of a weak triplet. The splitting can come after the electroweak symmetry breaking through electromagnetic radiative corrections. The mass splitting is independent from the WIMP for $m_\chi >> M_W$ and, it is typically given by:

$$m_{\chi^\pm} - m_\chi = \Delta \sim \mathcal{O}(10) MeV \tag{2.7}$$

The lifetime of the charged partners is of the order of $\sim 3 \cdot 10^{-3}$s for $\Delta = 15$ MeV. The most stringent limit on the mass of such a DM comes from CDF [124]: $m_\chi \geq 121$ GeV/c^2 with 95% CL.
The concept that is behind the rDM model is that, as anticipated before, a WIMP can form a bound state with a nucleus, figure 2.2.

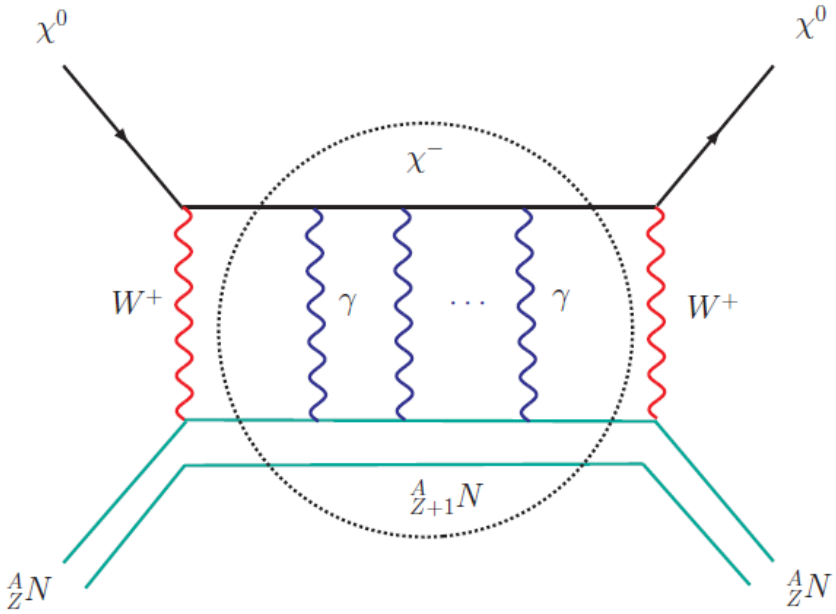

Figure 2.2: Feynman diagram of the elastic scatter of a WIMP on a target nucleus with an intermediate bound state.

The bound state is composed by a χ^- and $^A{}_{Z+1}$N. For nuclei with large Z, the orbital radius is smaller than the Bohr radius thus, WIMPs are bound inside the nucleus. If the incoming WIMP has enough kinetic energy, the bound state can be also in an excited state. Defining the total excitation energy of the resonance state above its ground state as ω, the resonance mass is given by:

$$m_r = m_{\chi^-} + m^A_{Z+1} + \omega - E_b. \tag{2.8}$$

from which it is possible to derive the resonant speed for a WIMP:

$$v_r = \sqrt{\frac{2(\Delta + m^A_{Z+1} - m^A_Z + \omega - E_b)}{\mu_{\chi N}}} \tag{2.9}$$

If the splitting, Δ, is comparable to the other terms in the numerator of equation (2.9), then for some element there will be a bound state which is accessible to the DM. Since the binding energy depends on Z, it is possible that some targets have a resonantly enhanced elastic scattering rate while for others the signal is suppressed by a factor of δ^4/v_r^4. If the bound state is formed in its ground state, it can only decay into $\chi^0 + N^A_Z$ and the process is similar to an elastic scatter. If it is in an excited state, then there is the possibility for de-excitation through photon and/or neutron emission. Between the photon and neutron emission there is a fundamental difference: while in the first case it is possible for the photon to be emitted with a lower energy than the kinetic energy of the incoming WIMP, that would give the possibility to come back to the initial state $\chi^0 + N^A_Z$, in the second case the neutron carries away enough energy to forbid the re-emission of the WIMP.
In conclusion, the resonance effects can dramatically change the "traditional" dark matter elastic direct detection calculation. Resonant DM can enhance the modulation effect and relies strongly on the detailed nuclear properties of different elements. The modulated data at DAMA can be explained and the constraints from unmodulated data can be satisfied. Furthermore, the rDM can reconcile the apparent contradiction between DAMA and other experiments like CDMS, XENON, KIMS, ZEPLIN and CRESST.

2.2 Inelastic Dark Matter

Inelastic Dark Matter (iDM) [125] is a model where the signal comes from electromagnetic recoils (ER) instead of nuclear recoils (NR). This model has been proposed to reconcile DAMA results with the ones from experiments that use lighter target nuclei, as Ge, and with results from no modulation searches. In iDM scenario, dark matter particles are expected to interact inelastically with the target nuclei and to go in an excited level, χ^*, with a mass $m_{\chi^*} - m_\chi = \delta \equiv \beta^2 m_\chi \sim 100$ keV heavier than the ground state. Only the particles that satisfy the condition:

$$\beta_{min} = \sqrt{\frac{1}{2m_N E_R}}\left(\frac{m_N E_R}{\mu} + \delta\right) \tag{2.10}$$

have sufficiently kinetic energy to up-scatter and, hence, to interact with target nuclei. This condition on the velocity means that one is actually probing the right tail of the

WIMP velocity distribution. After the excitation, the DM particle decays with a lifetime given by:

$$\tau = \frac{\mu_\chi^2 \delta^3}{\pi} \tag{2.11}$$

For a typical level splitting $\delta = 120$ keV and a dipole momentum $\mu_\chi = 3 \cdot 10^{-3} \mu_N$ we have $\tau = 5.1$ μs. This will result in the emission of a photon with an energy of the order of 100 keV (in the case of only one possible excited state). The emission of such a photon inside the detector volume gives to the signal the typical energy of an electromagnetic recoil. From equation (2.10) it is also clear that for particular values of E_R and δ, heavier nuclei have access to a wider range of velocities than lighter nuclei. Thus, experiments as CDMS-Ge have a suppression in the signal rate resulting in a lower sensitivity compared to higher mass target based experiments. This situation is also in favor of a modulated signal because one is probing the higher velocity tail of the WIMP distribution, where the rate spectrum is quite low. Thus, a small change in the particles flow (such as summer/winter flow variation) can give a considerable change in the number of the observed interactions. The possibility of the existence of such a kind of dark matter is not ruled out by experimental results such as the ones from XENON100 [8]. There are two points on which the iDM model and DAMA modulation signal are supported against the XENON100 results: the 225 live-days data have been taken from October 6 to February 14, which happens to be roughly during the time when the Earth travels with the galactic WIMP wind. Thus, there is not the possibility to observe any kind of modulation. Moreover, iDM interactions can be seen in a higher energy region (they are ER) than the one where the XENON100 signal has been studied (NR energy region); indeed, in the model it is used a γ emission as signature for dark matter interactions. Thus, the sensitivity of experiments as XENON100 are suppressed and it is possible to reconcile their results with the DAMA ones. In fact, for example, a WIMP of mass in the range $\sim 70 - 300$ GeV/c^2 with an inelasticity of $\delta \sim 100 - 150$ keV and a magnetic momentum of $\mu_\chi \sim 1 - 3 \cdot 10^{-3} \mu_N$ can explain the DAMA results, while being consistent with the other experiment null results.

The hypothesis of decaying dark matter can suggest the development of new kind of detectors focused on the detection of the emitted photon (figure 2.3), thus looking for ER instead of NR. Such detectors can be realized with a high density shield, where the dark matter is supposed to interact and be excited, and a sensitive volume where the emitted photon is detected. Due to the low value of the splitting δ, compared to the WIMP mass ($\sim 10 - 10^3$ GeV/c^2), the decay is expected to have a monochromatic signature that would make this process easy to detect. Considering usual assumptions for the galactic escape velocity, $v_{esc} = 544$ km/s, and for the Sun's velocity with respect

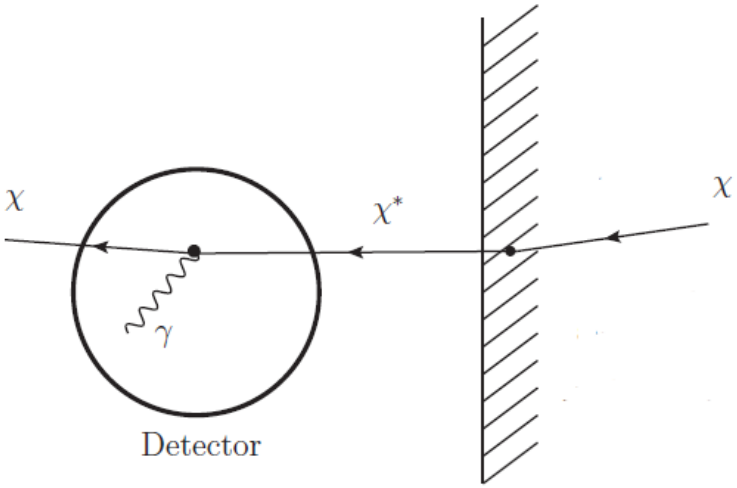

Figure 2.3: A schematic view of a hypothetical detector which aims to detect the WIMP decay in the iDM scenario.

to the halo, $v_{\odot} = 220$ km/s, the maximum speed for an incoming dark matter particle is of the order of $\sim 10^{-3}$c. This results in laboratory accessible excited WIMP states of less than ~ 700 keV, for heavy WIMPs and of about 3 keV$\cdot(m_{\chi}/\text{GeV})$ for lighter ones.

2.2.1 Magnetic inelastic Dark Matter (MiDM)

The Iodine (I), that is contained in the DAMA scintillator crystals, differs from other heavy nuclei, as Xe, for its large nuclear magnetic momentum. Introducing the magnetic properties of nuclei in the iDM model, a new scenario for DM interactions, has been proposed: the **Magnetic inelastic Dark Matter** (MiDM) [126]. Thus, having a dependence of the WIMP-nuclei cross section from the magnetic momentum, the signal rate can be suppressed in Xe based experiment with respect to the DAMA expected one. The most important parameter in the MiDM model, is the target element weighted dipole momentum (figure 2.4):

$$\overline{\mu} = \left(\sum_{isotope} f_i \mu_i^2 \frac{S_i + 1}{S_i} \right)^{\frac{1}{2}} \tag{2.12}$$

where f_i is the element abundance, μ_i is its nuclear magnetic momentum and S_i its spin. The dipole of iodine is mainly due to the angular momentum of unpaired protons [127] with the additional contributions from neutron and proton spins. In the MiDM environment the DM is considered inelastically magnetically-coupled particle. The possibility for the DM to have a magnetic dipole has been studied in [128]. In magnetic

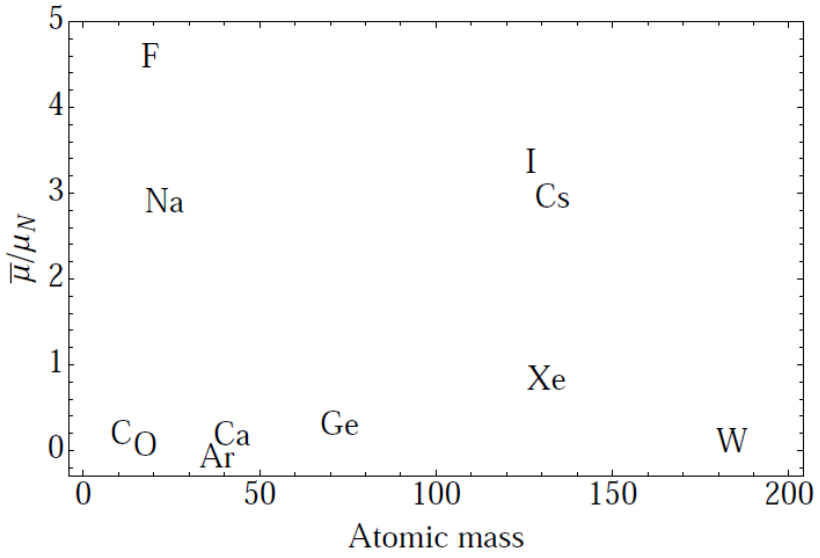

Figure 2.4: The atomic mass and weighted-magnetic dipole moment, in units of the nuclear magneton μ_N, for various dark matter search targets (C,O,Ca and Ar have been shifted slightly to avoid overlaps between each other) [126].

interactions there are two contributions to the differential cross section: a dipole-dipole (DD) and a dipole-charge (DZ) contribution. While the first one is dominant, in the case of the WIMP-iodine scatters, the second one gives the most important contribution in WIMP-other nuclei interactions. The total differential cross section is given by:

$$\frac{d\sigma}{dE_R} = \frac{d\sigma_{DD}}{dE_R} + \frac{d\sigma_{DZ}}{dE_R}, \tag{2.13}$$

where

$$\frac{d\sigma_{DD}}{dE_R} = \frac{16\pi\alpha^2 m_N}{v^2}\left(\frac{\mu_{nuc}}{e}\right)^2\left(\frac{\mu_\chi}{e}\right)^2\left(\frac{S_\chi+1}{3S_\chi}\right)\cdot \cdot\left(\frac{S_N+1}{3S_N}\right)F_D^2(E_R), \tag{2.14}$$

and

$$\frac{d\sigma_{DZ}}{dE_R} = \frac{4\pi Z^2\alpha^2}{E_R}\left(\frac{\mu_\chi}{e}\right)^2\left[1-\frac{E_R}{v^2}\left(\frac{1}{2m_N}+\frac{1}{m_\chi}\right)-\right. - \left.\frac{\delta}{v^2}\left(\frac{1}{m_\chi}+\frac{\delta}{2m_N E_R}\right]\left(\frac{S_\chi+1}{3S_\chi}\right)F^2(E_R),\right. \tag{2.15}$$

where $F_D(E_R)$ is the magnetic dipole form factor. Results from the analysis of DAMA data, are shown in figure 2.5.

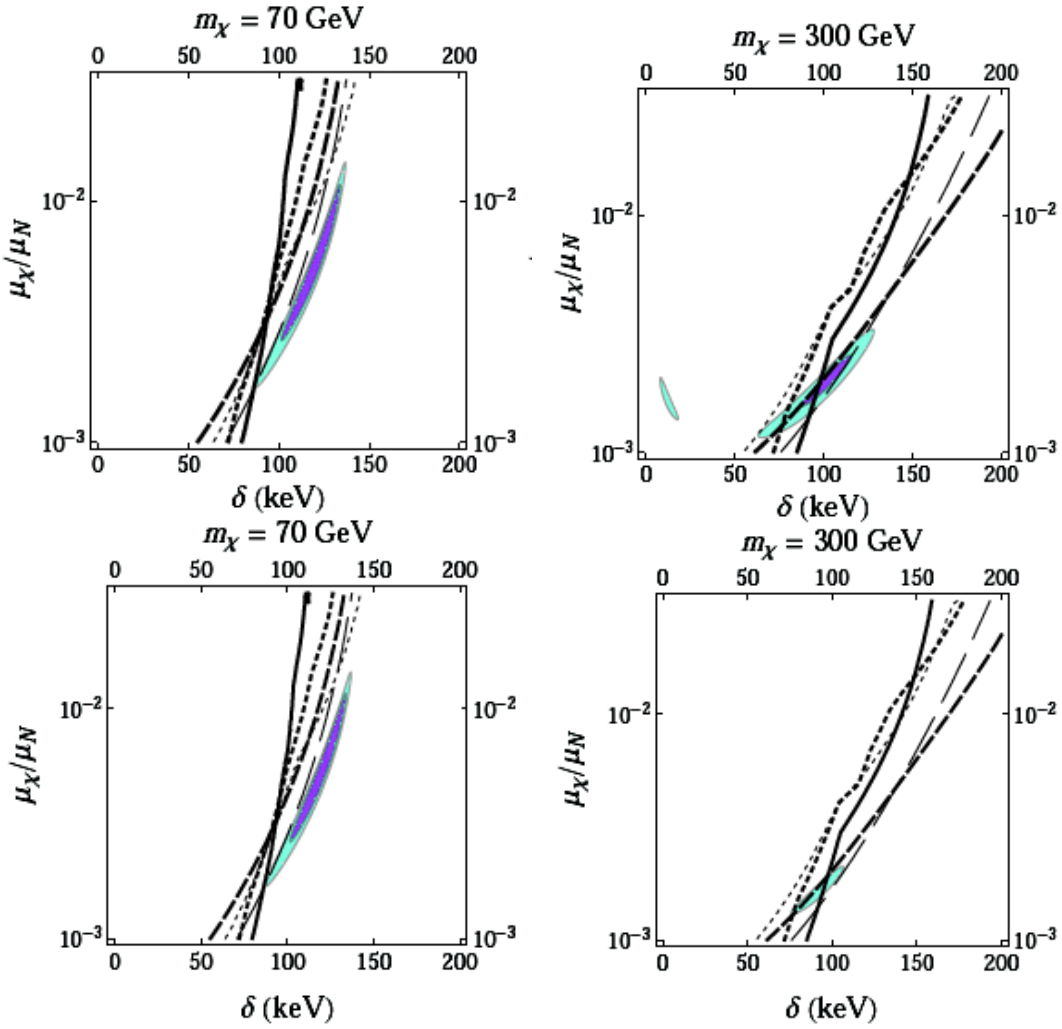

Figure 2.5: Allowed ranges of the parameter space for inelastic scattering of a magnetic dipole (dominated by dipole-dipole scattering for iodine). Purple (dark) and blue (light) regions are 90% and 99% allowed confidence intervals, respectively, for a χ^2 fit to the DAMA modulation. Constraints are: CDMS (solid), CRESST-II (short light dashed), XENON10 (short dark dashed), KIMS (long dark dashed), and ZEPLIN-III (long light dashed). In the upper row, it has been utilized only the $2-8$ keV bins in DAMA; in the lower row the entire range of [2, 14] keV has been used.

2.3 The Dark Sector

In addition to the previous discussions on the iDM and MiDM, it is also possible to think about the WIMPs as part of a larger **Dark Sector** with new forces and interactions. In this new theory, the dark matter particles interact through new dark forces that can be mediated, for example, by a massive vector-boson. After such an interaction, the

WIMP can be left in an excited state characterized by the splitting $\delta = m_{\chi^*} - m_\chi$. If $\delta < 2m_e$, the excited state is very long-lived [129] and this makes WIMP decays almost impossible to be detected. In this scenario, the MiDM plays a fundamental role since it is hypothesized that the magnetic transition takes care of the de-excitation, while the responsible for the excitation process is the dark force , figure 2.6.

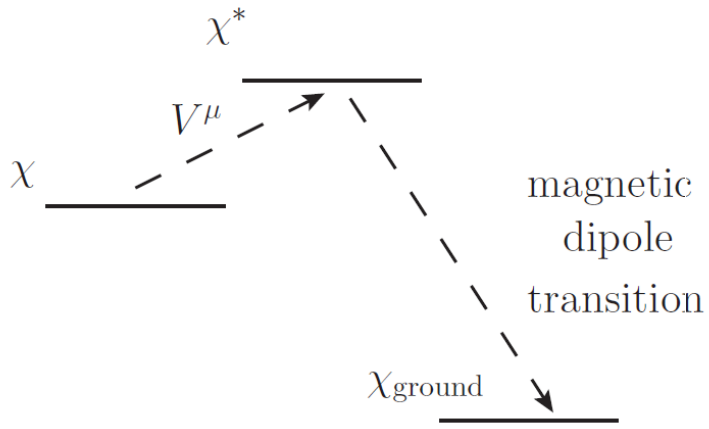

Figure 2.6: Scheme of the possible excitation and de-excitation processes in the new dark sector.

For the new dark sector the Lagrangian of the model is the sum of two contributions:

$$\mathcal{L}_{dark\ sector} = \mathcal{L}_{dark\ force} + \mathcal{L}_{DD} \tag{2.16}$$

The first term is given by:

$$\begin{aligned}\mathcal{L}_{dark\ force} = {} & i\overline{\chi}\overline{\sigma}^\mu\partial_\mu - m_\chi\bar{\chi}\chi + i\overline{\chi}^*\overline{\sigma}^\mu\partial_\mu\chi^* + m_{\chi^*}\overline{\chi}^*\chi^* + \\ & + g_V\overline{\chi}^*\overline{\sigma}_\mu V^\mu\chi + g_V\overline{\chi\sigma}_\mu V^\mu\chi^* - \\ & - \frac{1}{4}V_{\mu\nu}V^{\mu\nu} + \frac{1}{2}m_V^2V_\mu V^\mu + \\ & + \frac{\epsilon}{2cos\theta_W}V_{\mu\nu}B^{\mu\nu},\end{aligned} \tag{2.17}$$

where V_μ is the new massive vector-boson, $V_{\mu\nu} = \partial_\mu V_\nu - \partial_\nu V_\mu$ is its field strength, m_V is the mass and g_V is gauge coupling, $B_{\mu\nu}$ is the field-strength of the Standard Model hypercharge gauge field and θ_W is the weak mixing angle. The DD Lagrangian is instead given by:

$$\mathcal{L}_{\mathcal{DD}} = \left(\frac{\mu_\chi}{2}\right)\overline{\chi}^*\sigma_{\mu\nu}F^{\mu\nu}\chi + h.c. \tag{2.18}$$

where μ_χ is the dipole momentum, $F^{\mu\nu}$ is the electromagnetic field-strength tensor and $\sigma_{\mu\nu} = i[\gamma_\mu, \gamma_\nu]/2$ is the commutator of two Dirac matrices.
It is possible to have transitions at the MeV scale instead of keV scale and, under proper

assumptions, it is possible to obtain an analytical form for the expected decay rate inside a detector. One can consider a detector and its shield of spherical symmetric geometry. The total expected rate counts on two contributions: the differential rate for the excited states and the probability for a WIMP to decay into the detector. In particular, the latter is given by:

$$P_{\text{deacy}} = e^{(-\frac{t_{\text{enter}}}{\tau})} - e^{(-\frac{t_{\text{exit}}}{\tau})}, \tag{2.19}$$

where $t_{\text{enter(exit)}}$, the time at which the excited state enter (exit) the detector after the excitation collision, is given by:

$$t_{\text{enter/exit}} = \frac{r\cos\theta \pm \sqrt{\rho^2 - r^2\sin^2\theta}}{v_\chi}, \tag{2.20}$$

where ρ is the radius of the detector, r is the distance of the first collision from the center of the detector, θ is the angle between the final direction of the particle and the position axis determined by the detector center and the collision spot, and v_χ is the WIMP velocity ($\sqrt{2E_\chi m_{\chi^*}}$). Considering a volume shield V, a WIMP energy E_χ and the total solid angle Ω, the total expected decay rate inside the detector is then given by:

$$R = \int dE_\chi \int \Omega \int_{\text{shield}} dV\mathcal{R} \cdot P_{\text{decay}}(E_\chi, V, \Omega) \tag{2.21}$$

An example of the total rate is shown in figure 2.7.

2.4 Exothermic Dark Matter (exoDM)

The **exothermic Dark Matter** (exoDM) model [130] is analogous to iDM. Indeed, also in this case the DM is made of nearly degenerate mass states. The difference is that the excitated states already exist and the scatters with nuclei are down-scatters. Since also this model has been developed to reconcile DAMA results with the ones from other experiments, some of the model parameters are constrained by the fit to the DAMA data. In particular, it is usually considered a dark matter with mass in the range $2-5$ GeV/c^2 and mass splitting $\delta \sim 5-10$ keV. For such a light DM with kinetic energy below the mass splitting, the peak of the recoil energy is given by: $E_R = \delta(m_\chi/m_N)$. In the exoDM model, the inelastic single-proton cross section for down-scatters, in low transfer momentum regime, is given by:

$$\sigma = \frac{C\mu_n^2}{16\pi\Lambda}\sqrt{1+\frac{2\delta}{\mu_n v^2}} \tag{2.22}$$

where μ_n is the reduced mass of DM-nucleon system and $C = 4$ (with fermionic DM). The DAMA fit also requires $\Lambda \sim 340$ GeV. It is also assumed that the elastic scattering is

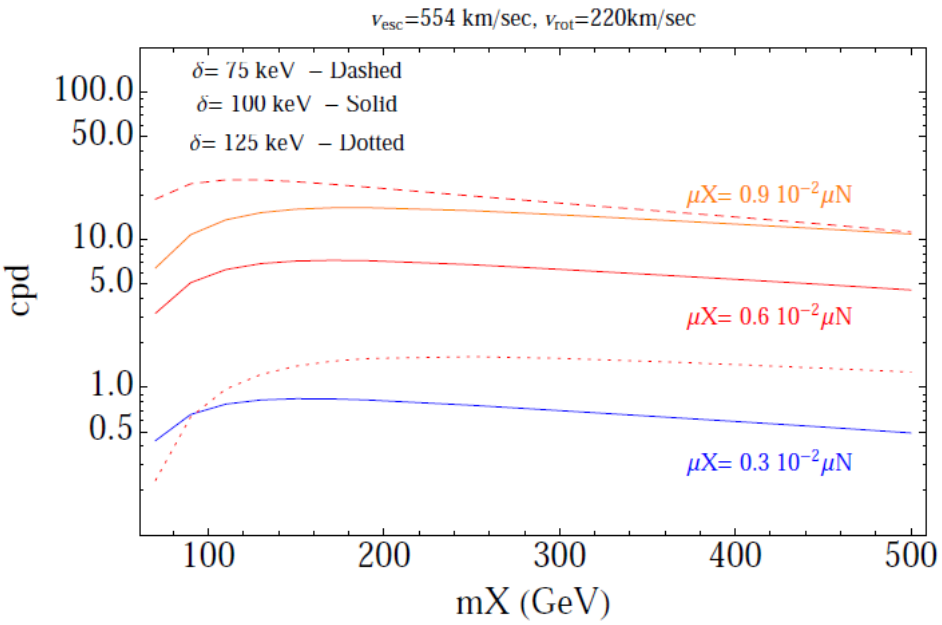

Figure 2.7: Expected decay rate (counts per day), as function of the WIMP mass, for several values of the magnetic dipole momentum. The outer detector shield is modeled as a spherical shell with an outer radius of 118 cm and a inner radius of 93 cm; the inner shield has an outer radius of 35 cm and a inner radius of 31 cm; the spherical detector has a radius of 31 cm [131].

highly suppressed [132]. When the mass splitting is much lower than the kinetic energy of the collision, the so called elastic limit is reached:

$$\sigma_{el\ limit} = C\frac{\mu_n^2}{16\pi\Lambda^4} \tag{2.23}$$

As seen in sections 2.2 and 2.3, the possibility for the existence of DM excited states can be inferred through a dark sector which involves a new gauge boson, the *dark photon*. This boson has a mass $m_{A'}$ that enters in the definition of the mass splitting together with the dark fine structure constant α_D. For a mass splitting of the order of $\sim$ 10 keV and $\alpha_D \sim 10^{-4}$, the resulting mass of the dark photon is $\sim$ 100 MeV. Under these hypothesis the correct rates in DAMA and also in CoGeNT are reproduced. Since this dark photon will couple with the SM fields, there are ongoing searches for it, for example through the $\Upsilon(3S)$ decays. Assuming $m_{A'} < m_\chi$, dark matter annihilates into two dark photons which decay into SM particles. Due to the low value of the mass splitting, the excited state life time will result greater than the Universe age. The recoil spectrum is peaked around a certain energy value and the spread around this value is proportional to the DM kinetic energy and so it will be modulated, figure 2.8.

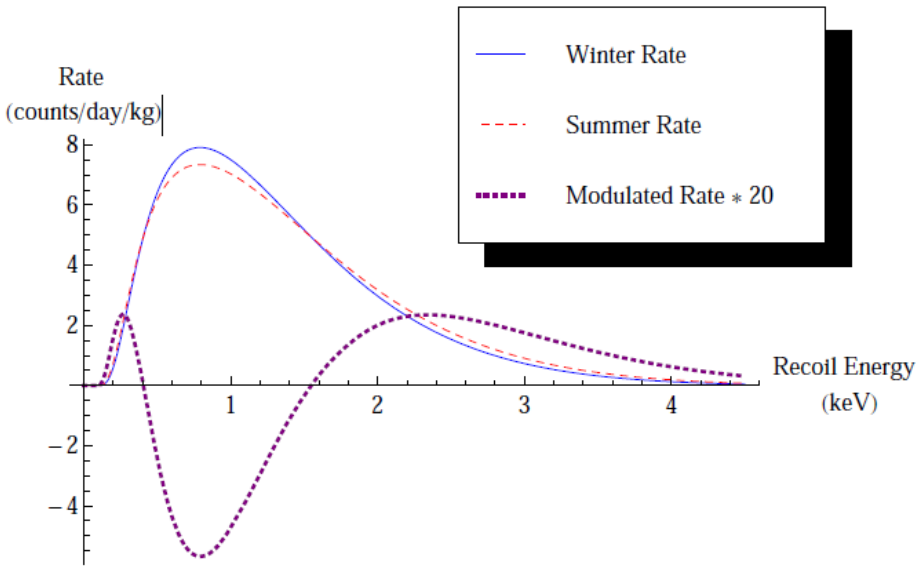

Figure 2.8: Recoil energy spectra for down-scattering off of sodium during winter when the Earth is moving with the DM halo (blue line) and during summer when it is moving against the halo (red dashed). The modulation spectrum is half of the difference between these two curves, shown here enlarged by a factor of 20 (purple dotted). In the plot a WIMP of mass $m_\chi = 3.5$ GeV and a splitting of $\delta = 6$ keV have been considered. The cross-section has been chosen to fit the DAMA modulation signal.

The peak is proportional to the DM mass splitting and inversely proportional to the target mass. Thus, for heavy nuclei the recoil spectrum will be peaked at very low energies. For experiments that use heavier targets, the nuclear recoil signal will be in sub-keV region that is below their typical energy threshold. For example, with the model parameters defined previously, there is a large number of expected events below 4 keV in CDMS-Si while the rate drops above 5 keV, figure 2.9.

2.5 Xenophobic Dark Matter

In the **isospin-violating Dark Matter** (IVDM) [133, 135], the DM has a different coupling with protons and neutrons. In this theory, the sensitivity of xenon-based experiments is highly suppressed by destructive interference between proton and neutron interactions. For such a reason, the model is also known as "*Xenophobic Dark Matter*" model. A suppression of the expected DM interactions rate, for a certain experiment, can be obtained varying the WIMP coupling to protons, f_p, and to neutrons, f_n. In any case, it is not possible to have a completely destructive interference for an element

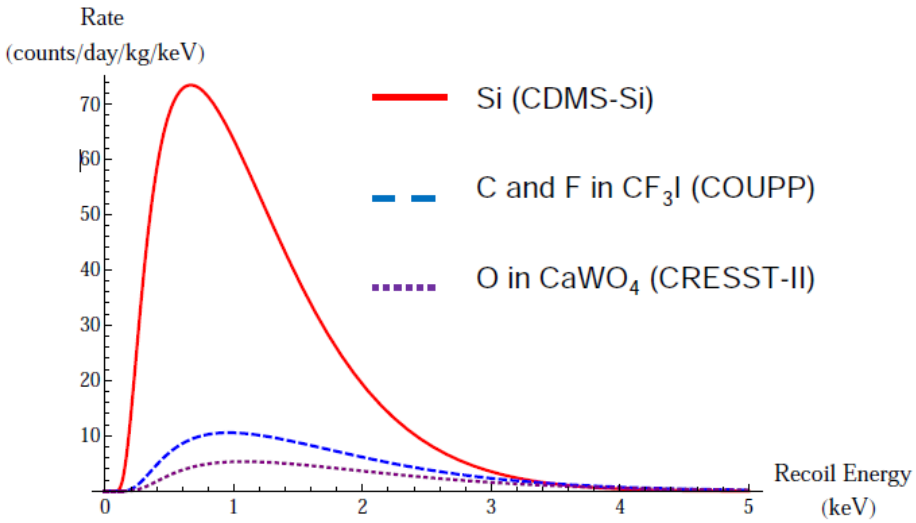

Figure 2.9: The spectra for recoils off of light nuclei in CDMS-Si, COUPP, and CRESST-II. Detector response effects (such as the efficiency in CDMS-Si, which is 5% at 5 keV) have not been included.

as the Xe due to its numerous isotopes. The isospin violation can have its justification in the fact that WIMP interactions are typically related to the hypercharge symmetry. Since right-handed up and down quarks have different hypercharge, it could be natural to expect these interactions to depend on the isospin. By considering a generic model of dark matter, and in particular a model that explains the low-mass data, one should treat the relative coupling to protons and neutrons as a free parameter that can only be determined from the data. This assumption is sufficient for comparing direct detection experiments, since the relative coupling to protons and neutrons completely define the parameter space. The general form for the differential cross section for WIMP-matter spin-independent elastic interactions is given by:

$$\frac{d\sigma}{dE_R} = \frac{\mu_A^2}{M_*^4}[f_p Z + f_n(A-Z)]^2 \left[\frac{m_A}{2\mu_A^2 v^2} F^2(E_R)\right] \tag{2.24}$$

where E_R is the recoil energy of the hit target nucleus and m_A its mass, μ_A is the WIMP-nucleus reduced mass and $F(E_R)$ is the nuclear form factor. f_n and f_p parameterize the strength of DM couplings to neutrons and protons. Clearly, it results $f_n = f_p$ in the non isospin-violating case. The expected total rate of events is proportional to the zero-momentum transfer cross section, σ_0, given by:

$$\sigma_0 = \frac{\mu_A^2}{M_*^4}[f_p Z + f_n(A-Z)]^2 \tag{2.25}$$

It is useful to define the *normalized-to-nucleon cross section*, σ_N^Z, that is the quantity that experiments usually quotes; it represents the nucleon-dark matter scattering cross section that would be inferred, assuming $f_n = f_p = 1$, from the data of a detector using a target with Z protons. For a given isotope with Z protons and A nucleons, the normalized-to-nucleon cross section is related to the dark matter-nucleus zero-momentum transfer cross section by:

$$\sigma_N^Z = (\sigma_0/A^2) \cdot (\mu_p^2/\mu_A^2), \tag{2.26}$$

where μ_p is the dark matter-proton reduced mass. In the case of isospin-violating DM, the cross sections for protons (σ_p) and neutrons (σ_n) are not equal and are connected to σ_N^Z through the **degradation factors** given by:

$$D_p^Z \equiv \frac{\sigma_N^Z}{\sigma_p} = \frac{\Sigma_i \eta_i \mu_{A_i}^2 \Big[Z + (f_n/f_p)(A_i - Z) \Big]^2}{\Sigma_i \eta_i \mu_{A_i}^2 A_i^2} \tag{2.27}$$

$$D_n^Z \equiv \frac{\sigma_N^Z}{\sigma_n} = D_p^Z \left(\frac{f_p}{f_n} \right)^2 \tag{2.28}$$

where the sum runs over the isotopes with abundance η_i. If an element has only one isotope, then it is possible to choose f_n and f_p such that $D_{p,n}^Z \to 0$. Considering a WIMP of mass $m_\chi = 8$ GeV/c^2 the behavior of σ_p as function of f_n/f_p is shown in figure 2.10 [135]. From figure 2.10, bottom plot, it is clear that, for the Xe, the maximum of the xenophobia is reached for $f_n/f_p = -0.7$. In such a case, the *degradation parameter* reaches its minimum, that is: $D_p^{Xe} \sim 10^{-4}$. For this value of f_n/f_p the Ge and Si-based experiment ROIs don't overlap. It may occur overlap for $f_n/f_p = -0.64$. In such a case the overlapping is also permitted by the XENON100 exclusion limit and this can finally reconcile the results from the various experiments, at least for low WIMP masses. The cross section limits for different values of f_n/f_p, as function of the WIMP mass, are shown in figure 2.11 [135]. The maximum xenophobia scenario ($f_n/f_p = -0.70$) is shown in figure 2.11 (middle panel). Nevertheless, the best overlapping between the Ge and Si-based detectors, according to the exclusion limits from LUX, is reached for $f_n/f_p = -0.64$ (figure 2.11, bottom panel).

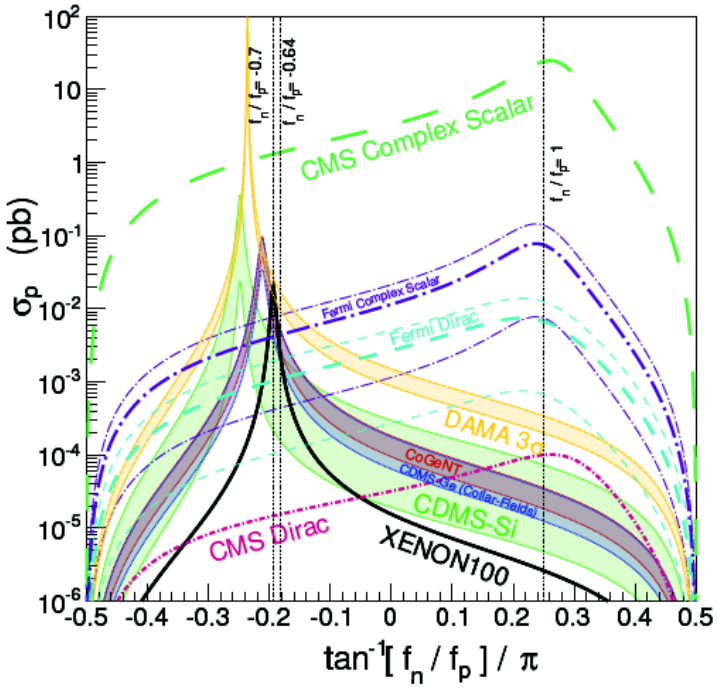

(a) Entire f_n/f_p range

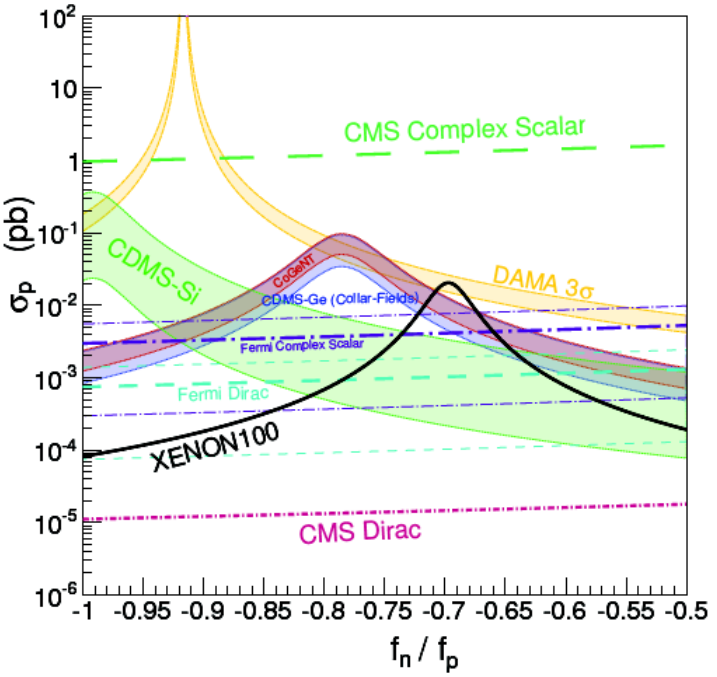

(b) Xenophobic region

Figure 2.10: Proton cross section for various experiments as function of f_n/f_p, for $m_\chi = 8$ GeV/c^2. Plotted are also the slices of the 90% CL ROIs from CDMS-Si, CoGeNT, and CDMS-Ge (Col- lar/Fields), the 3σ ROI for DAMA, and exclusion contours from XENON100. Also plotted are 90% CL exclusion contours for CMS [134] and for Fermi-LAT [103].

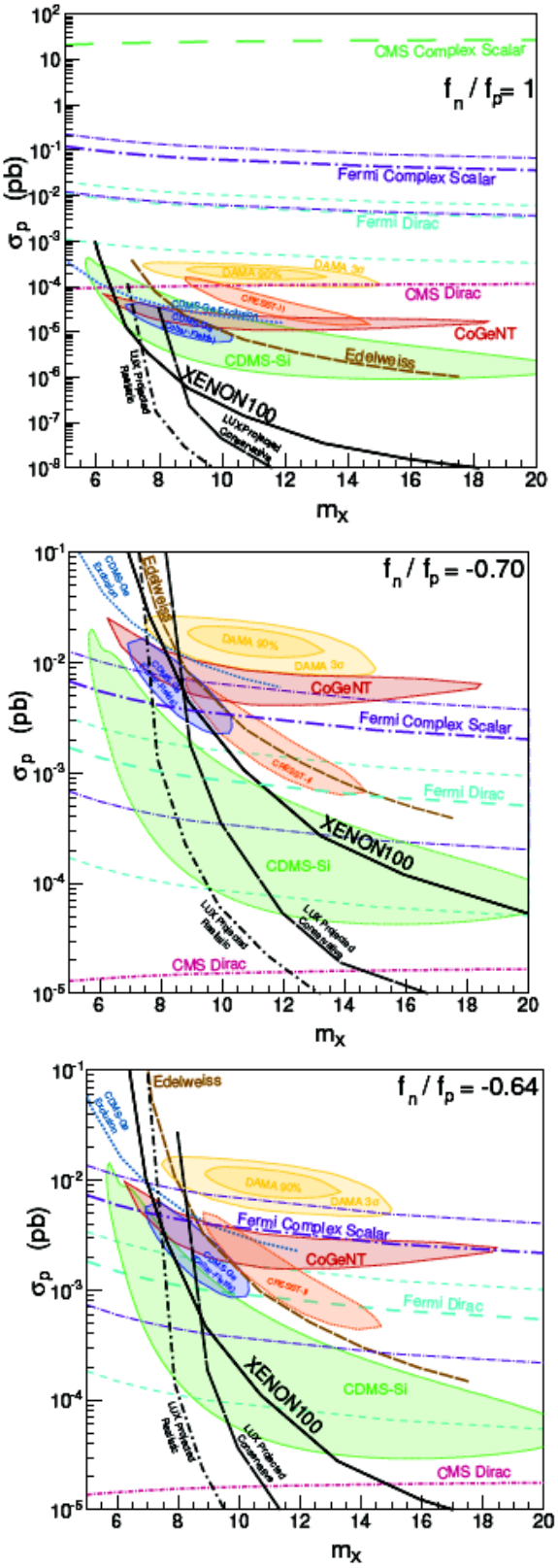

Figure 2.11: Regions of interest and exclusion contours in the $(m_\chi/\text{GeV}, \sigma)$ for neutron-to-proton coupling ratios $f_n/f_p = 1$ (top), $f_n/f_p = -0.70$ (center) and $f_n/f_p = -0.64$ (bottom). Plotted are also the 90% CL ROIs for CDMS-Si [122], CoGeNT [121], and CDMS-Ge (Collar/Fields) [136]; 90% and 3σ ROIs for DAMA [120]; exclusion contours from XENON100 [8], Edelweiss [54], and CDMS [122]; projected exclusion bounds from LUX [137].

2.6 MOND: a Universe without dark matter

Despite of the efforts that the scientific community is investing in the direct and indirect detection of DM particles, several scientists believe that the "missing mass problem" should be tackled from a different point of view. They raised up the idea that the dynamics should be changed under some specific conditions instead of introducing a new kind of exotic matter. Such a concept is explained in the **MOdified Newtonian Dynamics** (MOND) [138, 139] theory. It states that, since the General Relativity (GR) is tested only at local scale, no one can ensure its validity outside the solar system i.e. in space regions where the gravitational fields are weak, namely systems of mass M and size R such that the Newtonian gravitational potentials satisfy the condition:

$$\Phi \sim \frac{MG}{r} << c^2 \tag{2.29}$$

In such regions it is then necessary to slightly change the dynamic laws for celestial bodies. What is interesting and fascinating is that not any complex modification of the Newtonian laws is required. Indeed, it needs only a scale factor, that is found to be a universal constant, named *Milgrom constant*. Despite of this, apparently, very easy solution to the missing mass problem, there are conflicting opinions about MOND validity. On one hand, this modification of the usual dynamic can reproduce some scale relations like the Tully-Fisher, for late type galaxies, that naturally does not come from the Newtonian laws; on the other hand, MOND is not supported by any physical mechanism, it is merely phenomenological. Consider now a system of mass M_0. In the standard gravity scenario, a probe particle feels an acceleration $g = g_N = GM_0/r^2$. The circular velocity of the probe, around the central body, is then: $v_c^2 = GM_0/r$. From the spiral galaxy rotational curves, we know that in the outer regions $v_c \sim$ *constant*. To obtain this result, it is necessary to introduce a modification in the definition of the field strength g:

$$g \rightarrow g_N = \mu(x) \cdot g, \tag{2.30}$$

where $x = g/a_M$. The parameter a_M is the *Milgrom constant* and it has the dimensions of an acceleration. The $\mu-$function is given by:

$$\mu(x) \;=\; \tfrac{x}{1+x} \;=\; \begin{cases} 1; & x >> 1 \\ x; & x << 1 \end{cases} \tag{2.31}$$

The first case is the formal limit, $a_M \rightarrow 0$, where no modifications to the dynamics are required. This is analogous to the correspondence principle in quantum theory for the limit ($\hbar \rightarrow 0$), or to the non-relativistic limit ($c \rightarrow \infty$). The second case corresponds to

the MOND limit where it is necessary to modify the dynamics. It is trivial to see that:

$$v_c^2 = g \cdot r \rightarrow g' \cdot r = \frac{g_N \cdot r}{\mu(x)} = \frac{1}{\mu(x)} \frac{GM_0}{r} = \\ = \frac{GM_0 a_M}{g \cdot r} \Rightarrow v_c^4 = GM_0 a_M = const \tag{2.32}$$

Equation (2.32) shows that in the MOND framework, the flat rotational curves and the Tully-Fisher relation naturally arise. For a dynamically hot system ($g << a_M$), one also finds the relation:

$$\sigma^4 \propto M_0 = const \tag{2.33}$$

It has been found that "casually", a_M is connected to some cosmological quantities:

$$a_M \approx \frac{cH_0}{2\pi} \approx \frac{c^2}{2\pi}(\Lambda/3)^{1/2} \tag{2.34}$$

where H_0 is the Hubble constant and Λ is the observed equivalent of the cosmological constant. It is also possible to define a characteristic length (l_M) and mass (M_M) for the MOND theory:

$$l_M \approx 2\pi \frac{c}{H_0}, \quad M_M \approx \frac{2\pi c^3}{GH_0} \tag{2.35}$$

A first conclusion from previous equations is that a_M is a function of time, being dependent on the Hubble parameter. It is also clear that it is not possible to find a system that is relativistic and satisfies the MOND regime. In fact, for the relativistic case $MG/r \sim c^2$ while the MOND regime requires $MG/r^2 \leq a_M$. These relations imply $r \geq l_M > l_H$, i.e. such a system should be bigger than today cosmological horizon. Fitting data from several kind of galaxies, a good agreement between the new dynamic laws and data is achieved with $a_M \approx 1.15 \cdot 10^{-10}$ m·s^{-2}, figure 2.12 [139]. The agreement between the MOND description and the observed scale relations is found over eight orders of magnitudes in size and fourteen in mass. Under certain assumptions, it is also possible to get the Tully-Fisher relation from the not modified Newtonian dynamics. In this case the question concerns just the assumptions. If we consider the not modified relation between the velocity and the centripetal acceleration we have: $v_c^4 = (GM_0/r)^2$. If we now define a surface mass density as: $\Sigma_0 = M_0/(\pi r^2)$; we obtain: $v_c^4 = M_0 \Sigma_0$. To have the Tully-Fisher scale relation, the quantity Σ_0 should be constant for all the baryonic systems, but this is not true. Indeed, it is easy to demonstrate that in the case of the not modified dynamics it results: $g \propto \Sigma_0$, while in the MOND case: $g \propto \sqrt{\Sigma_0}$. From data, a good agreement is found in the last case, figure 2.13.

The analysis of the dwarf galaxies is crucial for a theory like the MOND. In fact, those kinds of galaxies are characterized by the largest discrepancy between the luminous and dynamic mass and, due to their small acceleration, they are perfectly in the MOND

regime. In 1989 Lake [140] asserted that MOND could not reproduce the observed RCs of a certain sample of dwarf galaxies.

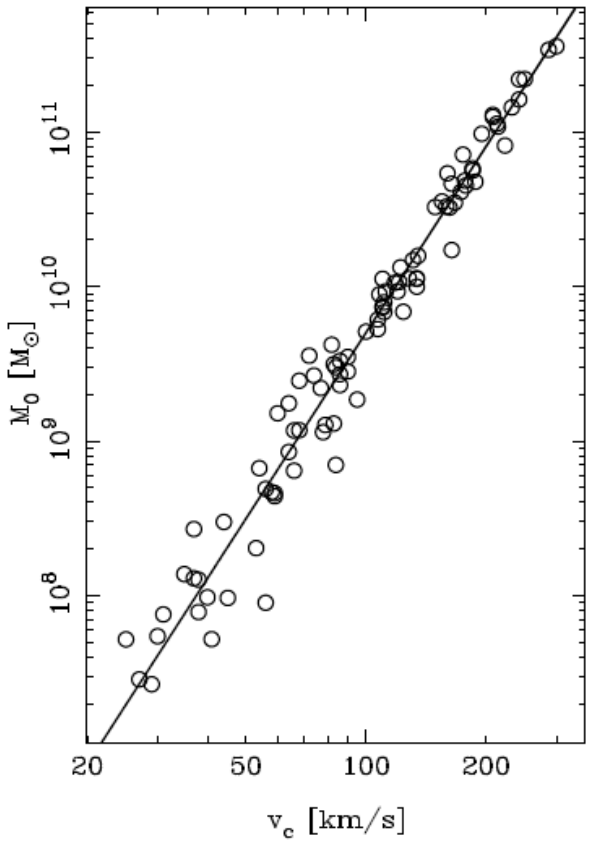

Figure 2.12: Tully-Fisher scale relation. Observed data (open circle) and MOND fit (black line).

The main objection from Milgrom to the assertions of Lake was related to the large errors in distance and inclination measurements of the sample.
Looking at the DM distribution, it is usually accepted the isothermal halo profile (ISO) with a characteristic constant central density core. For the ISO model, the density distribution is given by:

$$\rho_{ISO}(R) = \frac{\rho_0}{1 + (\frac{R}{R_c})^2}, \tag{2.36}$$

while the rotational curve (RC) is given by [141]:

$$V_{rot}^2 = V_{gas}^2 + V_{halo}^2 + V_{star}^2. \tag{2.37}$$

The three contributions are due to the gas, halo and stellar component of the galaxy, respectively. In the case of the MOND, the RC is given by:

$$V_{rot}^2 = \sqrt{V_d^2 + V_b^2 + V_g^2} \cdot \sqrt{a_M \cdot r + V_d^2 + V_b^2 + V_g^2} \tag{2.38}$$

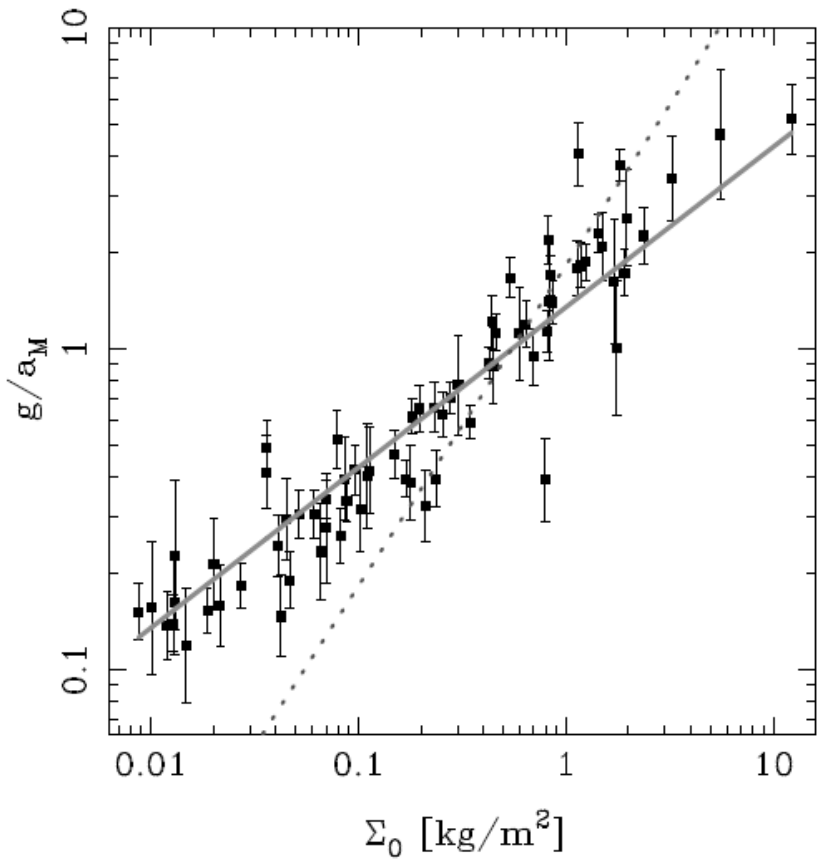

Figure 2.13: Surface Density-Acceleration relation (SDA). The solid line is the fit with the MOND assumption while the dashed line is the fit with the Newtonian assumption [139].

where $V_{d,b,g}$ are the contributions from the stellar disk, the bulge and from the gas, respectively. The stellar mass content can be inferred starting from the surface brightness profile through the relation [142]:

$$\Sigma[M_{\odot}pc^{-2}] = (M/L)_{\star} \cdot 10^{-0.4\cdot(\mu - C)} \tag{2.39}$$

where $(M/L)_{\star}$ is the stellar mass-to-light ratio, μ is the surface brightness profile and C is a constant used for the conversion from mag/arcsec^2 to $L_{\odot}/pc^2$. Using the previous formulas and a sample composed of several type of galaxies, Randriamampandry and Carignan [141] tested the agreement between the DM and MOND descriptions with the observed RCs, figure 2.14. By using the same M/L value, they obtained a mean value for the reduced chi-square equal to 1.18 and 2.37 for ISO and MOND model, respectively. In the MOND model, Randriamampandry and Carignan considered two cases: in the first one they considered a fix value for the a_M parameter, while in the second one it

was free to vary.

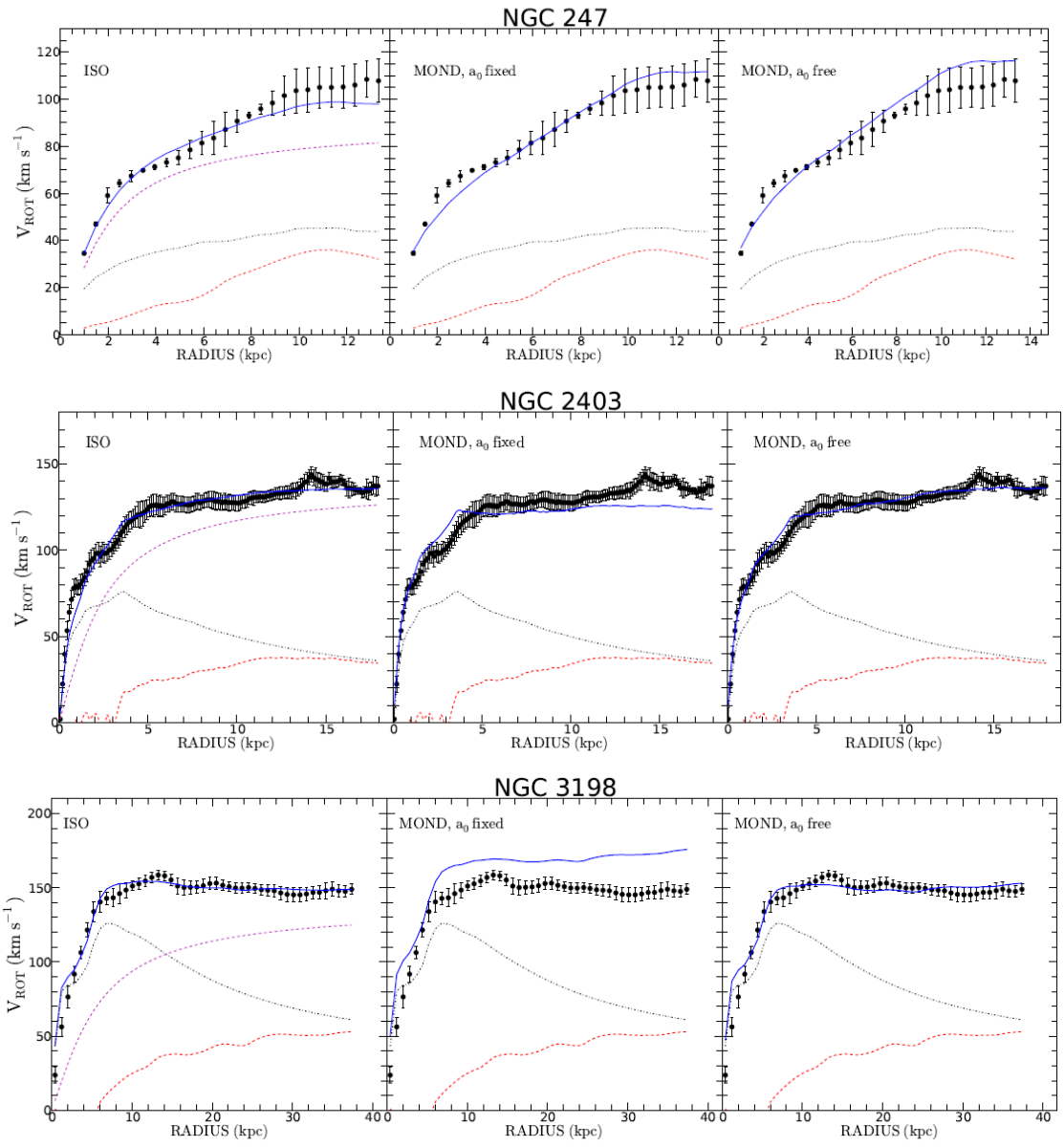

Figure 2.14: Fit results for ISO model (left panels), MOND with a_M fixed (middle panels) and with a_M free (right panels). The colored curves represent contributions from: the HI disk (red dashed), the stellar disk (dash-dotted black), the stellar bulge (dashed green) and from the dark matter component (dashed magenta). The bold blue lines are the model best-fit and the black points are the measurements of the rotational velocities [141].

From the best fit to the data they obtained $a_M = (1.13 \pm 0.50) \cdot 10^{-8}$ cm·s^{-2}. For the MOND case, it has also been observed that considering M/L as a free parameter and

only constrains the distances of the galaxies, it resulted in a lower value of the chi-square. On the basis of these results, it is then clear that exist different possible ways that can be followed to address to the "missing mass problem".

From a historical point of view, this situation can be compared to what happened before the Neptune discovery. After the discovery of the anomalous motion of Uranus, the French astronomer U. Le Verrier and the English astronomer John Couch Adams conjectured the existence of another planet, not yet seen, responsible for such anomalies. In 1846 J.G. Galle discovered Neptune, the "not yet seen planet". Different was the case for the anomalies in the motion of Mercury. In fact, in this case the explanation of the anomalies came from Einstein theory of general relativity, i.e. the introduction of a more refined description of the laws of gravitation. From this discussion we can conclude that the dark matter scenario could not represent the only answer to the modern missing mass problem. As for the case of the Uranus and Mercury there could be different solutions and explanations for the observed anomalies.

The MOND theory represents an alternative to the usual DM scenario. One of the strongest points that sustains this model is the fact that by considering the existence of the dark matter, there are not physical reasons able to explain the Tully-Fisher or other scale relations, in the Newtonian case. Instead, such relations are naturally found in the MOND scenario. Hence, no any new exotic particle that have not been seen yet is required. It only needs a universal constant a_M that is the only parameter of the theory. In addition, using the DM paradigm another problem arises: *the missing satellite problem*. In fact, in the dark matter scenario it is assumed that most of the mass of a galaxy is stored in a spherical dark halo. In this case a certain number of dwarf satellites should be present around each galaxy. What is currently observed is that the number of these satellites is roughly one order of magnitude lower than the expected one. Despite the positive results, the MOND model has many opponents. The main criticism against it is that there is not a physical process that could justify the modification of the Newton laws. In the history of the MOND, tests on several samples of galaxies found a weak correlation between the *Milgrom's constant* and the central surface brightness of the galaxies [141, 143]. From figure 2.15, it seems that for higher values of the central surface brightness, higher values of a_M are required while lower central surface brightness requires lower values of a_M. This is a very big challenge for the MOND theory since in such a scenario a_M is supposed to be a universal constant. The main objection to such observation, as already done for the Lake assertions, was that the measurements of distances and inclinations were affected by large errors.

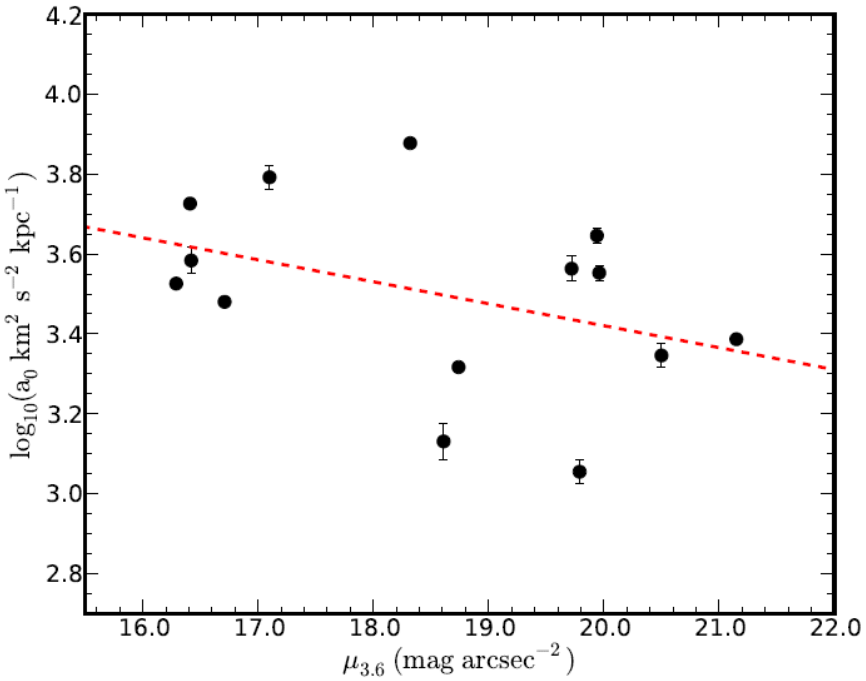

Figure 2.15: *Milgrom constant* as function of the the central surface brightness of the stellar disk in the 3.6 micron band [141].

Chapter 3

Properties of Liquid Xe as target in DM searches

In dark matter searches, the target material has to satisfy several requirements in order to be chosen as detection medium:

- transparency to its own radiation;
- high density, in order to have greater cross section;
- fast response;
- discrimination ability for different kind of incoming particles;
- auto-shield ability, in order to reduce the background from external sources.

The liquid Xe (LXe) has all those characteristics and this makes it an optimal choice as detection medium in dark matter search experiments. It was discovered in 1898 by Sir Williams Ramsay and Morri Travers who named it with the Greek word "$\xi\epsilon\nu o\nu$" meaning "strange". Besides the dark matter field the Xe is utilized in many applications. It is used, for example, in solar neutrino searches and also in medical fields for imaging procedure [144] as the Liquid Xenon Position Emission Tomography (LXePET), figure 3.1.

3.1 LXe properties

The Xe abundance in the atmosphere is ~ 0.1 ppm and it is obtained as a byproduct of the liquefaction and separation of air. In table 3.1 are shown some Xe properties compared with other noble gases. Two of the Xe isotopes are characterized by non-zero

nuclear spin (^{129}Xe and ^{131}Xe) and this gives to it sensitivity to both spin-independent (SI), equation (1.47) and spin-dependent (SD) dark matter interactions, equation (1.49).

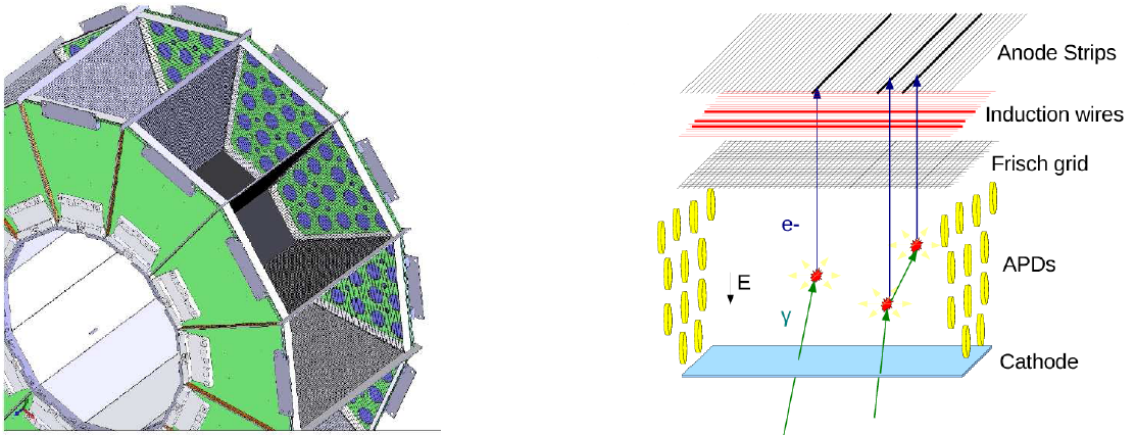

Figure 3.1: Left, LXe micro-PET ring. Right, sketch of the LXe PET detector.

Property	He	Ne	Ar	Kr	Xe
Symbol	He	Ne	Ar	Kr	Xe
Atomic Number	2	10	18	36	54
Atomic Radius (pm)	31	38	71	88	108
Gas Density at 1 atm, 298 K (g/l)	0.16	0.82	1.63	3.43	5.40
Liquid Density at 1 atm, $T_{boiling}$(g/cm^3)	0.12	1.21	1.40	2.41	2.94
Boiling Temperature at 1 atm (K)	4.22	27.07	87.30	119.93	165.03
Melting Temperature at 1 atm (K)	-	24.56	83.80	115.79	161.4
Critical Temperature (K)	5.19	44.4	150.8	209.4	289.7
Critical Pressure (atm)	2.24	27.2	48.1	54.3	57.6
Critical Density (g/cm^3)	0.0696	0.482	0.544	0.91	1.10
Triple Point Temperature (K)	N/A	24.56	83.81	115.78	161.41
Triple Point Pressure (atm)	N/A	0.424	0.68	0.722	0.805
Dielectric Constant of Liquid	1.049	1.188	1.51	1.66	1.95

Table 3.1: Physical properties of Xe and other noble elements [145].

In table 3.2 are listed the xenon isotopes and some of their properties. Thanks to the size of its nucleus ($A \sim 130$), Xe has a high cross section for WIMP-nucleus interactions [146] (Section 7.1):

$$\sigma(q) = F(q)\frac{4m_r^2}{\pi}\Big(Zf_p + Nf_n\Big)^2,$$

where Z and N are the number of protons and neutrons in the nucleus, respectively, $f_{p(n)}$ is the WIMP coupling to protons (neutrons), $F(q)$ is the nuclear form factor [147] and m_r is the reduced mass of the nucleon ($m_r \simeq m_{p,n}$ for WIMPs heavier than ~ 10 GeV/c^2). LXe has also a high density (~ 3 g/cm^3) that, together to its high atomic mass, makes it very efficient to stop the penetrating radiation, section 3.2.

Isotope	Atomic Mass	Natural Abundance [atom %]	Nuclear Spin (I)	Magnetic Moment
^{124}Xe	123.9	0.09	0	
^{126}Xe	125.9	0.09	0	
^{128}Xe	127.9	1.92	0	
^{129}Xe	128.9	26.4	1/2	-0.778
^{130}Xe	129.9	4.08	0	
^{131}Xe	130.9	21.2	3/2	0.692
^{132}Xe	131.9	26.9	0	
^{134}Xe	133.9	10.4	0	
^{136}Xe	135.9	8.87	0	

Table 3.2: Xe isotope properties [145].

At atmospheric pressure, the liquid phase of Xe extends from 162 K to 165 K, figure 3.2, and due to its boiling point it is required a cryogenic system for gas liquefaction.

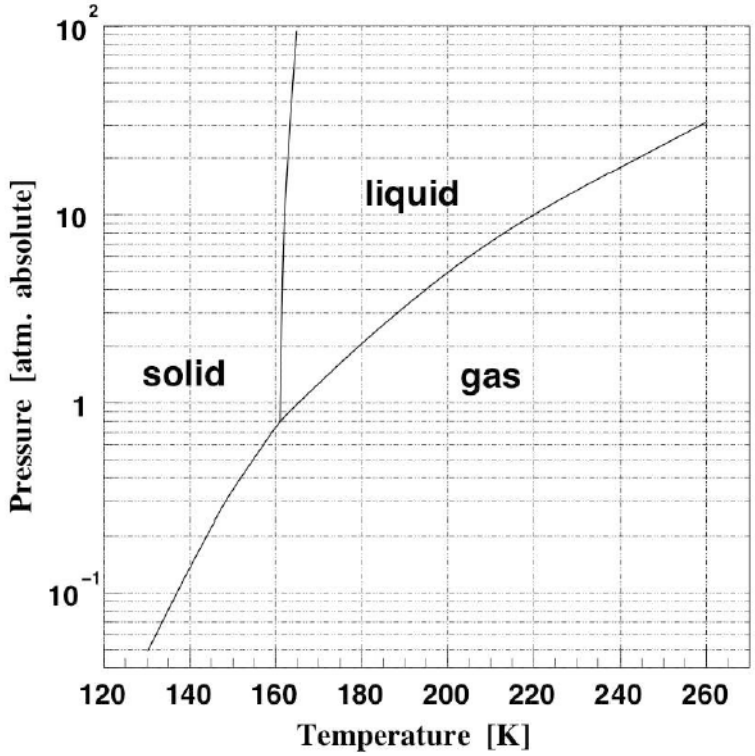

Figure 3.2: Xe phase diagram.

3.2 Particle interactions in LXe

The characteristics of particle interactions in LXe depend on the kind of particle and on its charge, mass and momentum. Charged particles such as α or e^- lose energy interacting, through electrostatic forces, with the external electrons and nuclei of the target. For such particles, inelastic collisions with atomic e^- produce excitations and ionizations both identified as electronic excitations. To quantify the energy lost through inelastic collisions it is defined the *electronic stopping power* that represents the amount of energy lost in interactions with atomic electrons, by an incoming particle, per unit path path length. Figure 3.3 shows the electronic stopping power for e^-, α and nuclear recoils in LXe.

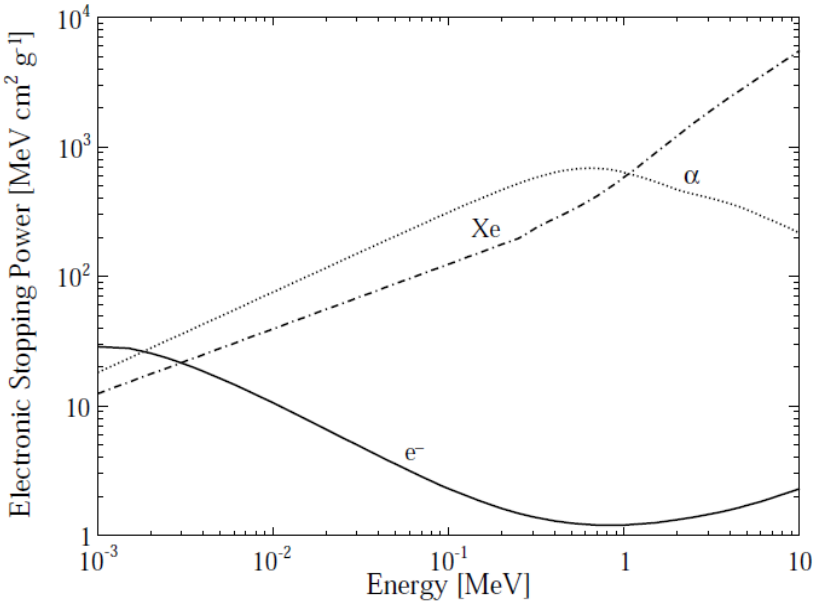

Figure 3.3: The electronic stopping power for electrons, α-s and nuclear recoils in LXe [148, 149, 150].

Electrons show a higher stopping power at lower energies, meaning that they have a higher density of electronic excitations at the end of their tracks. The behavior for nuclear recoils is the opposite. In the WIMP search energy region, below hundred of keV, electronic recoils show tracks $\lesssim 10$ μm. Such a characteristic is fundamental for the background reduction. For nuclear recoils it is also introduced the *nuclear stopping power*, used to defined the probability for an elastic collision with target nuclei. This mechanism leads to lose energy through atomic motion, i.e. heat, which does not give any measurable signal (nuclear quenching).
During de-excitation processes of the excited atoms, scintillation photons are emitted.

Also the ionization, through the recombination of the electrons-ions pairs, contributes to the scintillation emission. Indeed, after the recombination, the Xe atoms are in an excited state that will de-excitate through photon emission. This mechanism has been confirmed by the experimental observation of a dependence of the scintillation quenching from applied electric fields [151]. In dual phase detectors, as XENON10, XENON100 and XENON1T (Chapter 4), where the Xe is used in both liquid (LXe) and gaseous (GXe) phases, also the ionization electrons that do not recombine can be used to produce a second scintillation signal obtained by extracting the electrons from the LXe into the GXe. The measure of the two signals is fundamental since it allows for particle discrimination (Section 3.5).
For what concerns γ rays, there are several interaction channels available: the *Rayleigh scattering*; the *photoelectric absorption*, with $\sigma \propto Z^4/E_\gamma^{7/2}$; the *Compton scattering*, with $\sigma \propto Z/E_\gamma$, and the *pair production* (if $E_\gamma \geq 2m_{e^-}$), with $\sigma \propto Z^2 \ln(2E_\gamma)$. In figures 3.4 and 3.5 are shown the attenuation coefficient and the mean free path in LXe, as function of the particle energy, for γ interactions.

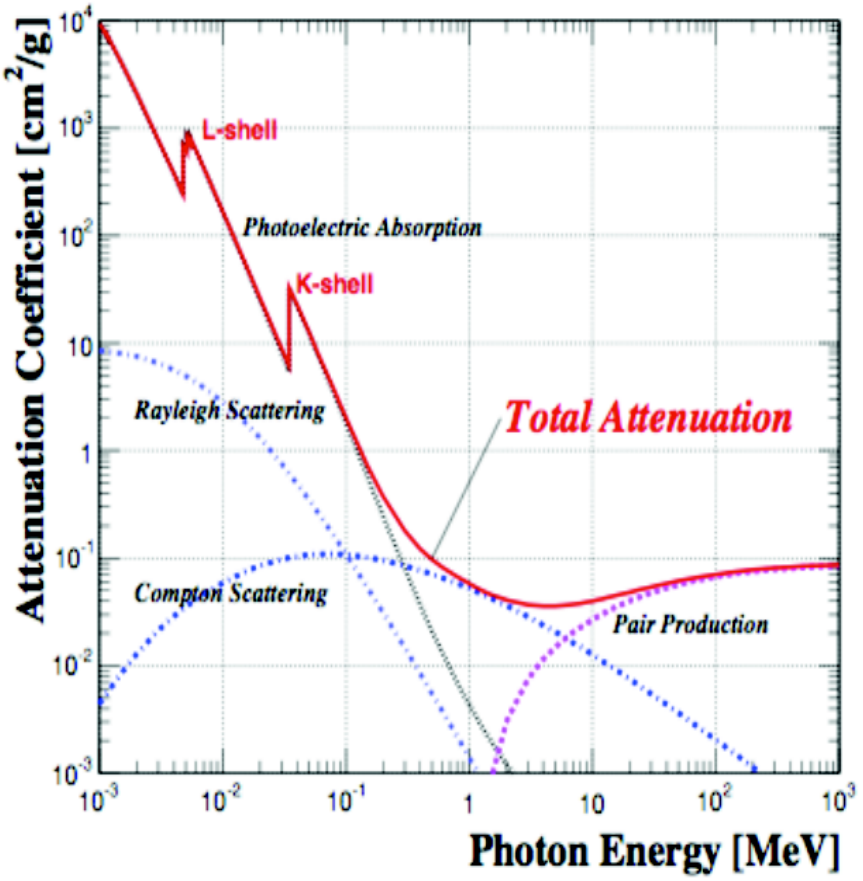

Figure 3.4: Attenuation coefficient, as function of the energy, for γ interactions in LXe.

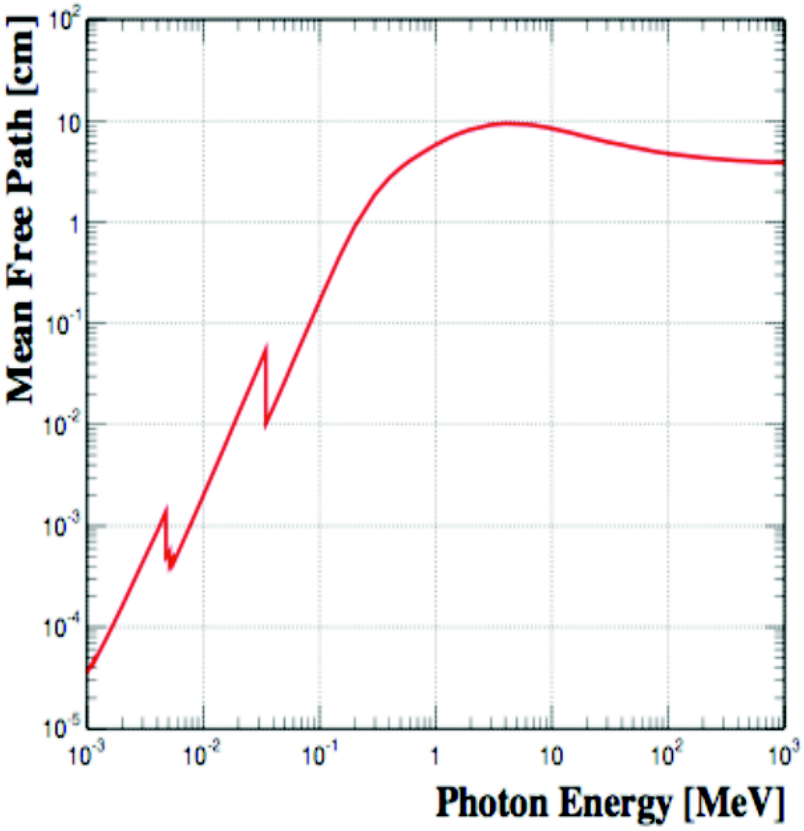

Figure 3.5: Mean free path, as function of the energy, for γ in LXe.

The structures at ∼5 keV and ∼30 keV represent the L-shell and K-shell absorption edges. At energies of 1 MeV the mean free path for a γ, in LXe, is of about 6 cm. Thus, the main external gamma ER background comes from low-energy single Compton scatters.

For what concerns nuclear recoils (NR), neutrons can experience elastic or inelastic interactions. In an elastic collision (for $E_n < 100$ keV), the recoiling nucleus receives an average energy of $2E_nA/(A+1)^2$ from the neutron. In the case of an inelastic collisions (at MeV energies), a certain amount of the energy is used to excitate the nuclei of the target which decay by photon emission in a very short time ($\leq$ 1 ns). Figure 3.6, shows the neutron cross section for the described processes. The inelastic scatters of neutrons do not constitute a critical background since the γ emission during the nuclear de-excitation pushes the energy above the WIMP search energy region. Different is the case for the elastic scatters since such processes mimic the expected dark matter signal. In the case of inelastic processes, there are meta-stable states characterized by long decay times. For example, ^{125m}Xe has a half-life of 57 s while ^{131m}Xe half-life is 11.8 days. Such a property can be used to uniformly calibrate the inner part of a detector since the

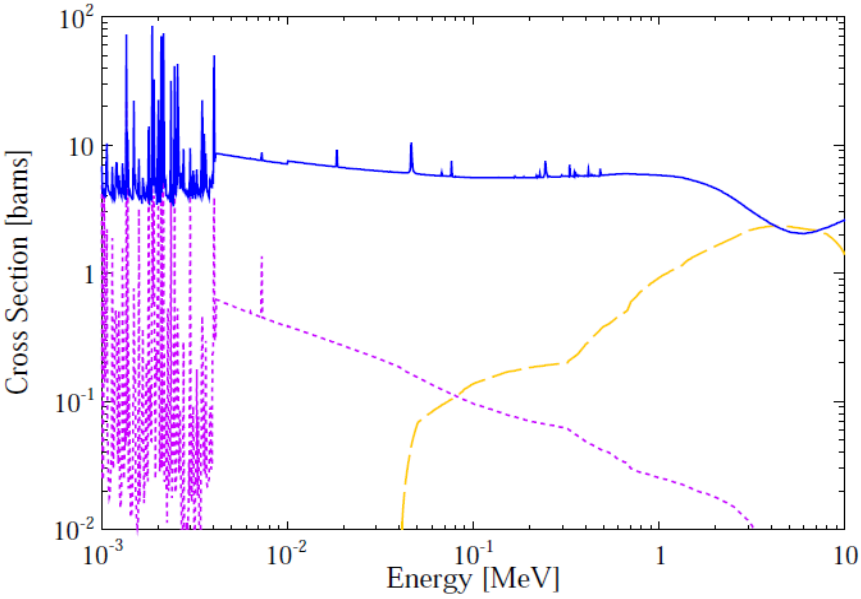

Figure 3.6: Neutron total elastic scattering (solid blue), total inelastic scattering (long dashed orange), and radiative capture (dashed violet) cross sections in LXe.

isotopes have enough time to reach such regions.
Indeed, using an external γ source it is not possible to reach the inner LXe volume, being the mean free path for a 1 MeV γ in LXe of about 6 cm due to the xenon self-shielding ability. This ability is very useful for the background reduction since it allows to have an inner volume of LXe, called *fiducial volume* (FV, see section 4.1), characterized by a very low level of background. By the way, neutrons can penetrate deeper in the target volume; their elastic scattering mean free path ranges from ∼13 cm, at 100 keV, up to ∼20 cm, at 10 MeV. Fortunately, fast neutrons are very likely to scatter multiple times in larger scale detectors and hence easy to be rejected as background.

3.3 Ionization in LXe

A particle that passes through LXe loses energy and leaves behind it a track of ionized and excitated atoms (Section 3.2). In relation to the ionization process, it is defined the quantity W-value (W_i), that defines the amount of energy required to produce an e^--ion pair. For LXe it is equal to 15.6 eV and it is slightly larger than the ionization energy of Xe since, as discussed in Section 3.2, there are processes under which the particles lose energy without producing ionization or excitation. Among the noble elements, LXe has the smallest W-value, hence the largest ionization yield. Table 3.3 shows some ionization properties of the noble elements.

Property	He	Ne	Ar	Kr	Xe
1st ionization energy [eV]	24.6	21.6	15.8	14.0	12.1
2nd ionization energy [eV]	54.5	41.0	27.7	24.4	21.2
3rd ionization energy [eV]	–	63.6	40.8	37.0	32.2
$W-value$ in liquid for relativistic e^-	–	–	23.6	20.5	15.6
$W-value$ in gas for relativistic e^-	41.3	–	26.4	–	21.9
$W-value$ in gas for α particles	42.7	–	26.3	–	–
Fano factor in liquid	–	–	0.06	0.07	0.12
Electron binding energy (K) [keV]	0.025	0.87	3.21	14.33	34.56

Table 3.3: Ionization properties of noble elements [145].

The total number of the e^--ion pair produced, per unit of absorbed energy, defines the so called *ionization yield*. In order to correctly measure this quantity, it is necessary to:

- minimize the loss of charge carriers due to impurity attachment, that requires an ultra-pure liquid;
- minimize the recombination of electron-ion pairs, that requires the application of an electric field;
- estimate correctly the deposited energy.

Assuming that an ionizing particle loses all its energy in a detection medium, Fano [152] showed that the standard deviation (δ), of the number of the produced e^--ion pairs (N_i), does not follow a Poisson statistics but it is given by:

$$\delta^2 = \langle (N - N_i)^2 \rangle = F \times N_i; \tag{3.1}$$

where F is a constant smaller than one, called *Fano factor*, that depends on the material. The standard deviation becomes Poissonian when $F = 1$. Using only the ionization channel, the energy resolution of LXe is then given by:

$$\Delta E(\text{keV}) = 2.35\sqrt{F \cdot W(\text{eV}) \cdot E(\text{MeV})}; \tag{3.2}$$

where ΔE is the energy resolution, expressed as FWHM, E is the energy lost in MeV, F is the Fano factor and W is the $W-$value. Once e^- and ions are created, they

start to move. Their motion can be analyzed as function of the applied electric field (figure 3.7), concentration of impurities and liquid temperature.

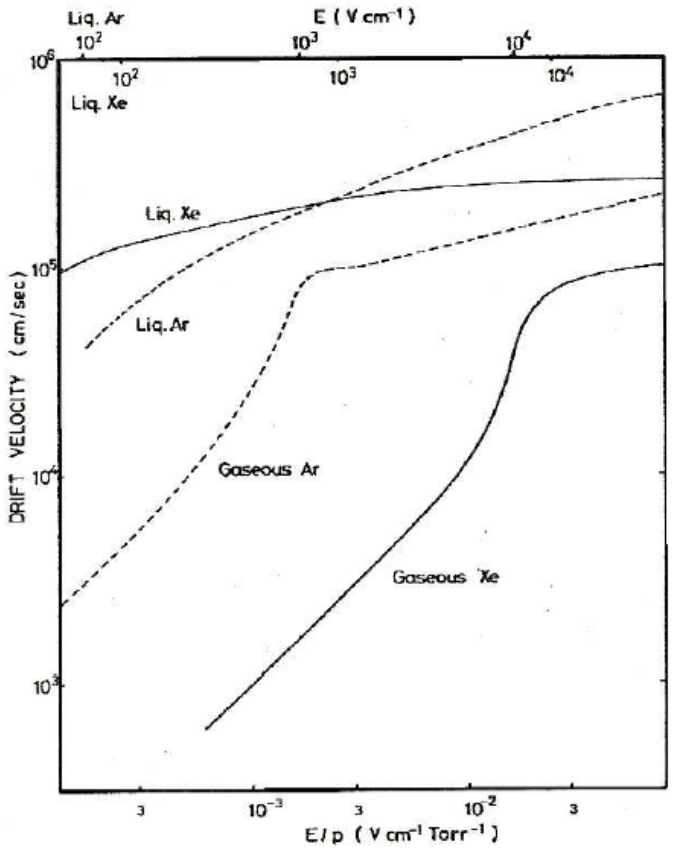

Figure 3.7: Electron drift velocity for Xe and Ar as function of the applied electric field.

At low fields, the electron velocity (v_d), is proportional to the strength of the electric field through the electron mobility (μ): $v_d = \mu \cdot \mathrm{E}$, where E is the electric field. In LXe, $\mu \sim$ 2000 cm^{2}V^{-1}s^{-1}. At high fields, v_d saturates. Also, the drift velocity changes slightly with temperature: almost inversely proportional to it with a rate of about $0.5\%/^oC$ [153]. During the drift, the electron cloud shows a certain diffusion (a process that affect the position resolution in the LXe detector as the XENON ones, Chapter 4). The cloud has a longitudinal, D_L, and transverse, D_T, component of the diffusion coefficient with respect to the electric field direction, and typically $D_L \sim 1/10\ D_T$. The final transverse spread of an electron cloud, after a drift path d, is given by:

$$\sigma_{D_T} = \sqrt{D_T t_d}, \tag{3.3}$$

where $t_d = d/v_d$. Figure 3.8 shows the diffusion coefficient as function of the density-normalized electric field.

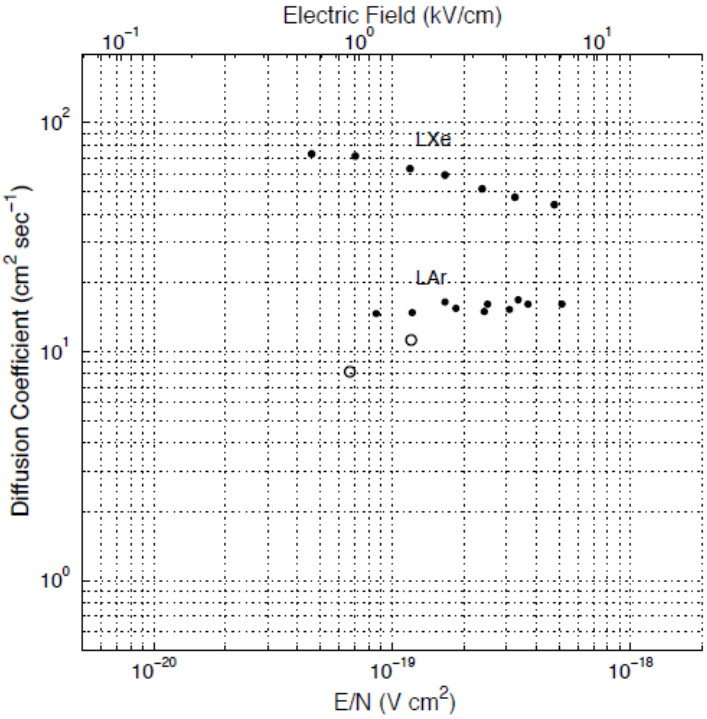

Figure 3.8: Diffusion coefficient as function of the density-normalized electric field for LXe and LAr [154].

Along the drift path, electrons can be catched by electro-negative impurities. This process lowers the ionization yield and can introduce a position dependence of the signal. The latter is crucial for double phase detectors where the depth of the event determines the length of the path that electrons have to cross. To reduce this effect, the concentration of such impurities has to be below 1 part per billion (ppb). The electron capture process can happen through three mechanism:

1. radiative attachment

$$e + AB \rightarrow AB^- + h\nu \tag{3.4}$$

2. dissociative attachment

$$e + AB \rightarrow A + B^- \tag{3.5}$$

3. three-body attachment

$$e + AB \rightarrow (AB^-)^* \tag{3.6}$$

$$(AB^-)^* + Xe \rightarrow AB^- + Xe \tag{3.7}$$

The evolution, as function of the time, of the electron concentration $[e]$ is given by:

$$[e(t)] = e(0) \cdot e^{(-k_S[S]t)} \tag{3.8}$$

where t is the time needed by the electrons to cross a drift distance d at drift velocity v_d, $[S]$ is the impurity concentration in mol/l and k_S is the attachment rate constant (l/mol·s). The quantity

$$\tau = (k_S[S])^{-1} \tag{3.9}$$

is called the *electron lifetime*. It represents the mean time after which an electron is catched by an impurity. Instead of τ, it is often measured the *attenuation length*, λ_{att}, given by:

$$\lambda_{att} = \mu \cdot E \cdot \tau, \tag{3.10}$$

where μ is the electron mobility and E is the electric field. There are typically two kinds of impurities: those characterized by a k_S that decreases with increasing the electric field, such as O_2, and those with an opposite behavior, such as N_2O, figure 3.9.

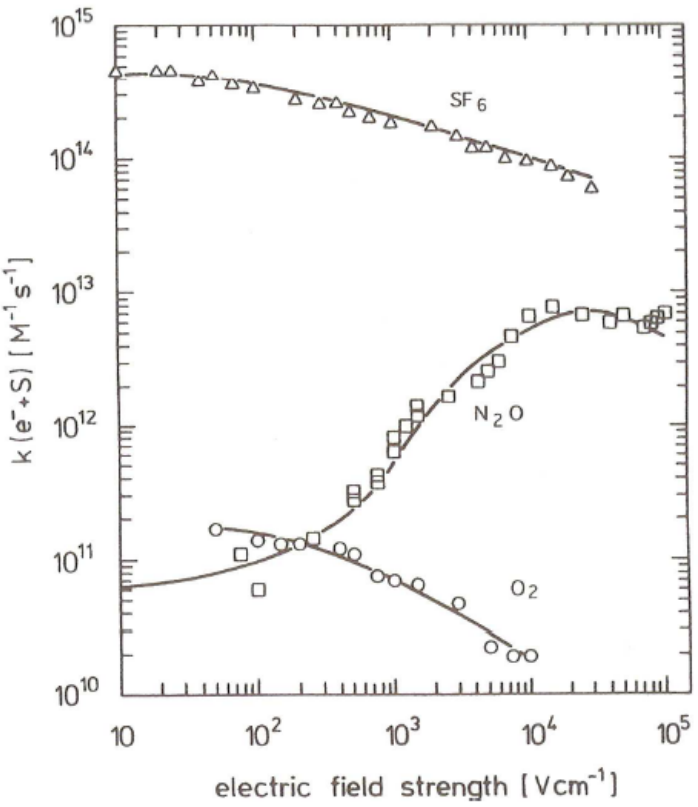

Figure 3.9: k_S in LXe ($T = 167\ K$) for: ($\triangle$) SF_6, ($\square$) N−2O and ($\circ$) O_2 [155].

To reduce the impurity concentration, several purification methods have been developed such as, for example, absorption and chemical reaction methods, filtration, separation, electrical discharges and irradiation with gamma-rays.

3.4 Scintillation in LXe

The energy lost by a particle in LXe under excitation and ionization processes is converted in scintillation light through de-excitation and recombination mechanisms, figure 3.10, respectively given by:

$$Xe^* + Xe + Xe \rightarrow Xe_2^* + Xe, \tag{3.11}$$

$$Xe_2^* \rightarrow 2Xe + h\nu; \tag{3.12}$$

and

$$Xe^+ + Xe \rightarrow Xe_2^+, \tag{3.13}$$

$$Xe_2^+ + e \rightarrow Xe^{**} + Xe, \tag{3.14}$$

$$Xe^{**} \rightarrow Xe^* + heat, \tag{3.15}$$

$$Xe^* + Xe + Xe \rightarrow Xe_2^* + Xe, \tag{3.16}$$

$$Xe_2^* \rightarrow 2Xe + h\nu; \tag{3.17}$$

where Xe^+ is a singly-ionized atom, Xe^* and Xe^{**} are the first and the second excited level of xenon, Xe_2^* is the excited dimer (excimer) and $h\nu$ is the VUV scintillation photon energy. Equations (3.12) and (3.17) evidence that the scintillation light is not produced by the de-excitation of Xe atoms, but rather by the one of Xe molecules. Due to the different configuration of the energy levels of dimers and atoms, the photons emitted by dimers will not be re-absorbed by the atoms making LXe transparent to its own scintillation light. The emission spectrum is quite broad, $\Delta\lambda = 14$ nm, with a peak at 178 nm which corresponds to a photon of 7 eV. As for the ionization, also for the scintillation it is introduced a W-value, W_{ph}, that is defined as the average energy required to produce a scintillation photon. If we assume a complete recombination and, then, that each recombination and excitation will produce a photon, the W-value is given by:

$$W_{ph} = E/(N_{ex} + N_i) = W_i/(1 + N_{ex}/N_i), \tag{3.18}$$

where N_i and N_{ex} are the numbers of the e^--ion pairs and excitations produced by a recoil of energy E, respectively. An upper bound of 0.20 on N_{ex}/N_i was obtained [154] which lead to estimate the maximum scintillation yield in LXe as $W_{ph}(max) = 13.8 \pm 0.9$ eV.

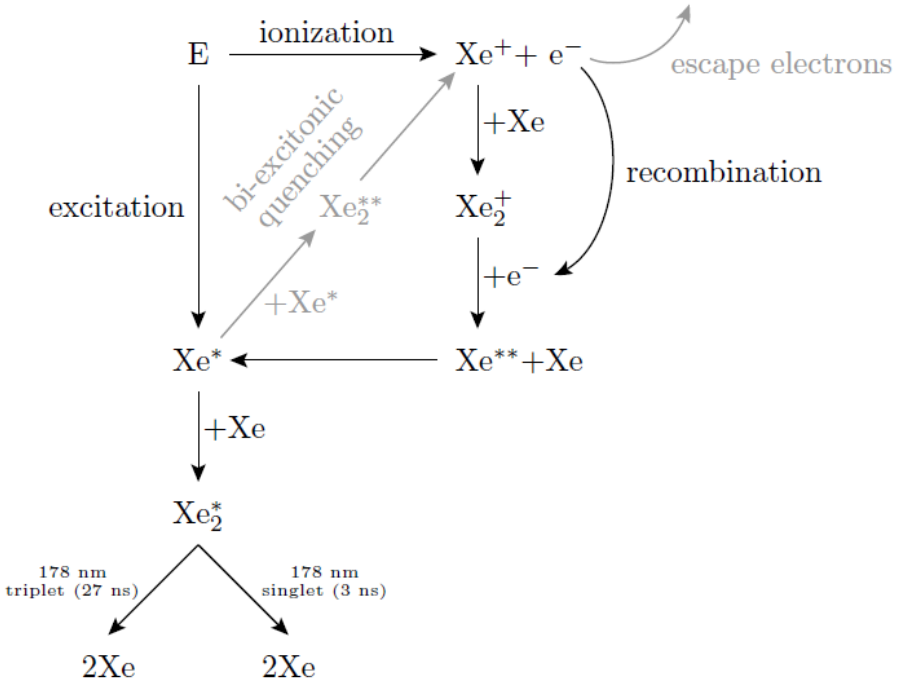

Figure 3.10: Scintillation mechanism in LXe (black) and different processes that can lead to the quenching of scintillation light (gray).

The scintillation yield per unit of deposited energy defines the *scintillation efficiency*, also called *quenching factor*, q. It counts on two contributions: the electronic, q_{el}, and the nuclear, q_{nr}, quenching. For $q = 1$ all the deposited energy is converted in scintillation. Birk [156], through its equation, tried to connect the quenching to the particle Linear Energy Transfer (LET, $-dE/dx$):

$$\frac{dL}{dx} = \frac{C_1(-dE/dx)}{1 + C_2(-dE/dx)} \tag{3.19}$$

where $C_{1,2}$ are fitted parameters. This description works for organic scintillators but it fails in case of liquefied rare gases for which q is not a simply function of the LET.
As introduced in Section 3.2, a recoil atom loses its energy, E, under electronic excitation, T, and atom motion, $E - T$. Thus, the nuclear quenching can be defined as: $q_{nr} = T/E$. For what concerns q_{el}, a possible source of this quenching mechanism are the *biexcitonic collisions* [150, 157]:

$$Xe^* + Xe^* \rightarrow Xe + Xe^+ + e^-. \tag{3.20}$$

In those reactions, two excitons collide giving one electron that can recombine producing only one VUV photon instead of two. This effect depends on the LET of the particles since for high LET the density of ionization e^- along the tracks is high, thus giving a high probability for biexcitonic collisions. At high LET a flat scintillation yield is observed for relativistic heavy ions, assumed to be the maximum value in LXe, figure 3.11.

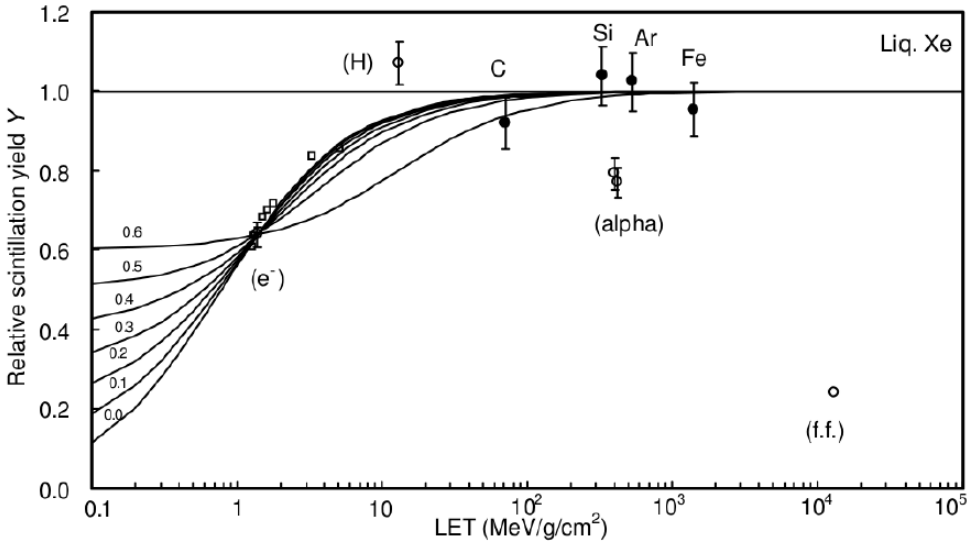

Figure 3.11: LET dependence of the scintillation yield for various types of particles in LXe: relativistic heavy ions (solid circles), relativistic electrons (solid square) and electronic recoils from γ-rays (open squares), α particles and fission fragments (f.f.) [154].

At lower LET values, relativistic electrons and electronic recoils from γ-rays are interpreted to have a reduced scintillation yield due to incomplete recombination (escape electrons) while the reduced scintillation yield of α particles, at higher LET, is attributed to biexcitonic quenching [158], equation (3.20). For what concerns particles such as α or Xe ions, the track structure can be described as a central core surrounded by a penumbra zone. Looking at the initial radial distribution in the track core, figure 3.12 [158], it can be concluded that the distributions for Xe ions and α are quite similar, thus it is possible to use the same values for their quenching.

3.4.1 Scintillation decay time

The scintillation light in LXe has two decay components (characterized by two different decay times): the singlet (**S**, faster) and triplet (**T**, slower) states of the excited dimers Xe_2^*. The corresponding electronic states, $^1\Sigma_u^+$ (lifetime of 2.2 ns for relativistic e^- and

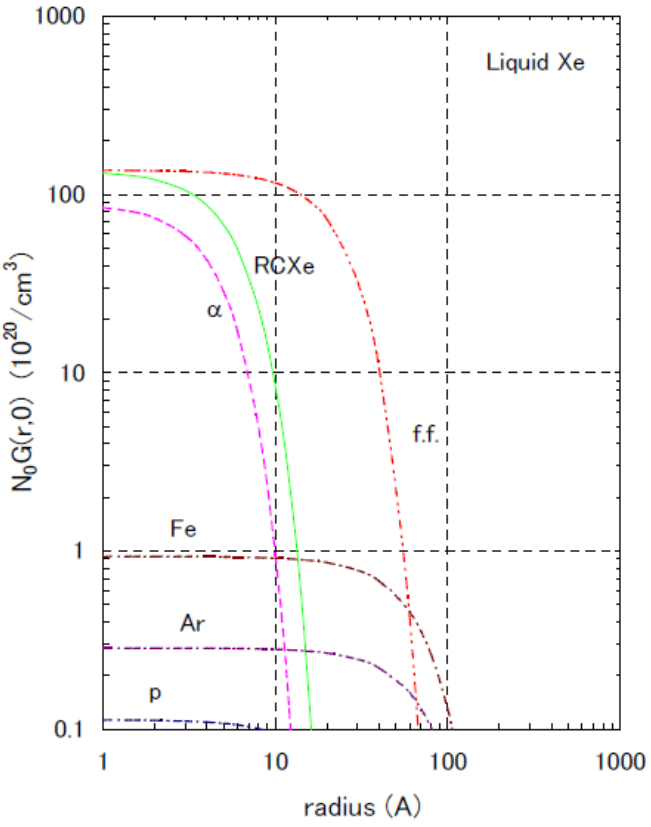

Figure 3.12: The initial radial distribution of excited species in the cylindrical track core in liquid Xe due to various ions and fission fragments (f.f.). Solid curve shows 60 keV recoil Xe ions. Proton have an energy of 38 MeV and, Ar and Fe ions are relativistic.

4.2 ns for α particles) and $^3\Sigma_u^+$ (27 ns for relativistic e^- and 22 ns for α particles), are essentially the same. The singlet and triplet lifetimes depend only weakly on the density of excited states, while the ratio of their density strongly depends from the LET: it is greater at higher LET. The different ratio is due to the thermalization and recombination velocity that, in liquid rare gases [150], is higher (lower) for high (low) LET particles. Since different particles have different LET, they will show different singlets to triplets ratios, thus allowing their discrimination, figure 3.13 (top). What happens is that a thermal electron can collide with an excited state, a $^1\Sigma_u^+$, and move it to a $^3\Sigma_u^+$:

$$S + e^- \rightarrow T + e^-,$$

producing more triplets states. Since the recombination is faster for high LET particles, the previous mechanism is less probable so, the **S/T** ratio remains higher. Low LET particles, like electrons, show a decay signal dominated by a slow and non-exponential recombination component with a decay time of 45 ns [158] (with no electric field applied).

Applying an electric field this component disappear thus allowing to obtain the fast and slow decay components, figure 3.13 (bottom).

3.4.2 Recombination and Electron Extraction

The distribution of the energy lost in ionization and scintillation depends not only on the number of excited and ionized atoms produced initially, but also on the recombination rate. Recombination occurs whenever an electron and an ion are sufficiently close to each other. Its rate is proportional to the ionization density, which is roughly proportional to the electronic stopping power. Consequently, higher recombination rate is expected at higher LET. The number of the excited atoms after the recombination is given by:

$$N_{ex}^{'} = N_{ex} + r \cdot N_i = N_i(r + \frac{N_{ex}}{N_i}), \tag{3.21}$$

where r is the recombination rate and $N_{ex/i}$ is the number of excitations/ionizations. Due to quenching effects, the number of emitted photons (N_{ph}) might be different from $N_{ex}^{'}$. In equation (3.21), the ratio N_{ex}/N_i is energy independent [159]. A model by Thomas and Imel [160] has been successfully used to describe recombination in liquid xenon. This model gives:

$$\frac{N_q}{N_i} = 1 - r = \frac{4}{\gamma N_i} ln(1 + \frac{\gamma N_i}{4}), \tag{3.22}$$

where γ is a free parameter of the theory. N_q, the number of electrons after the recombination, is given by:

$$N_q = (1 - r) \cdot N_i. \tag{3.23}$$

The values proposed by the XENON10 collaboration [67] give:

$$\frac{N_{ex}}{N_i} \approx 1.09, \tag{3.24}$$

and

$$\gamma \approx 0.032. \tag{3.25}$$

The application of an electric field can reduce the recombination, thus quenching the emitted light. The effect of such an electric field is different for particle with different LET. Indeed, for high ionization tracks (α and NR) there is a larger probability for the electrons to recombine with ions than in the case of electron recoils. This difference is crucial for the particle discrimination (Section 3.5). The relative scintillation and ionization yields, as function of the applied electric field, are shown in figure 3.14.
As anticipated, in dual phase detectors the drifted electrons are extracted from LXe to GXe. By means of the application of a sufficiently high electric field, it is possible to

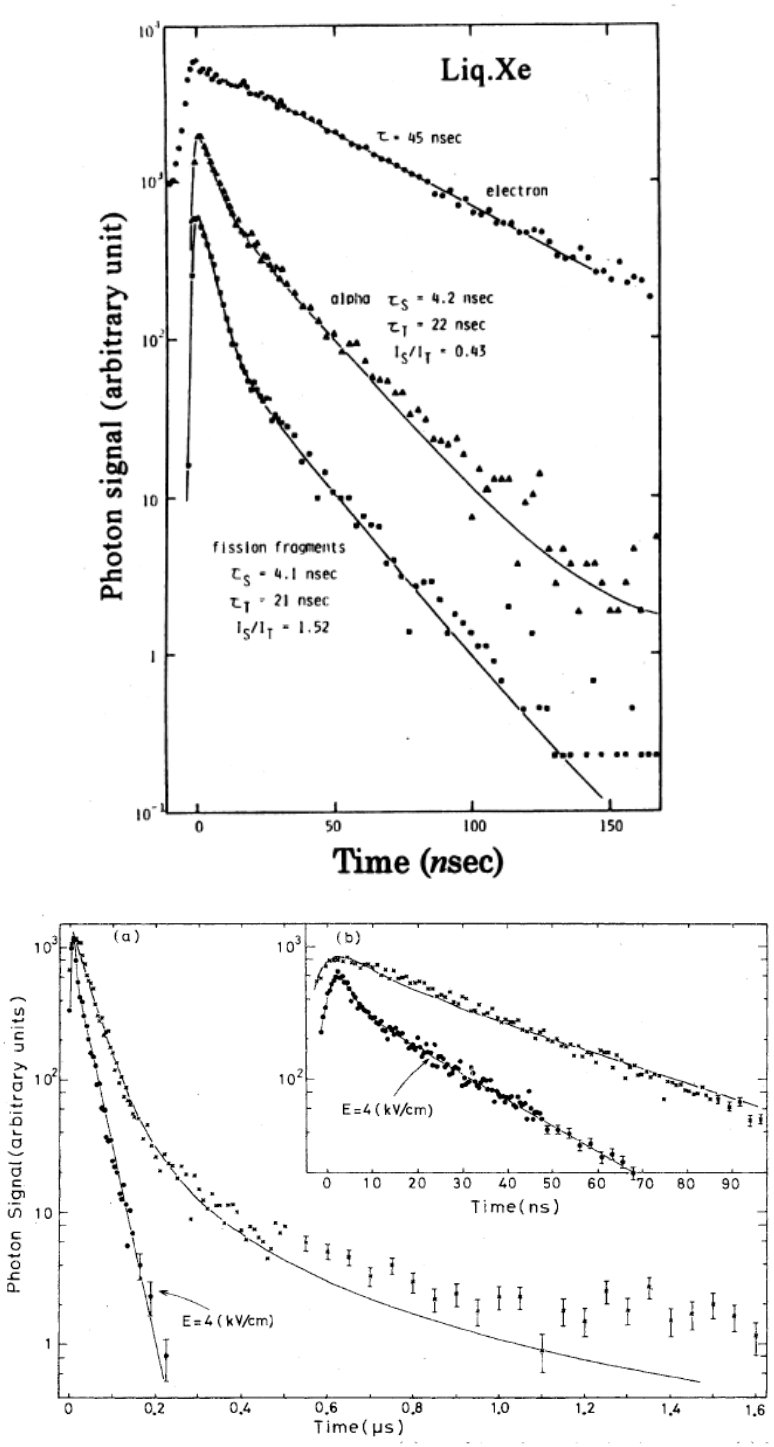

Figure 3.13: Top: decay curves of scintillation from electrons, α-particles and fission fragments (f.f.), without an applied electric field, in LXe [158]. Bottom: electron recoil scintillation pulse at electric fields of zero and 4.0 kV/cm [161].

"heat" the electrons so that their average kinetic energy results high enough to allow for their extraction. Electrons with the component of the momentum orthogonal to the LXe/GXe interface ($p_\perp$) greater than the potential barrier are then readily extracted into the gas phase.

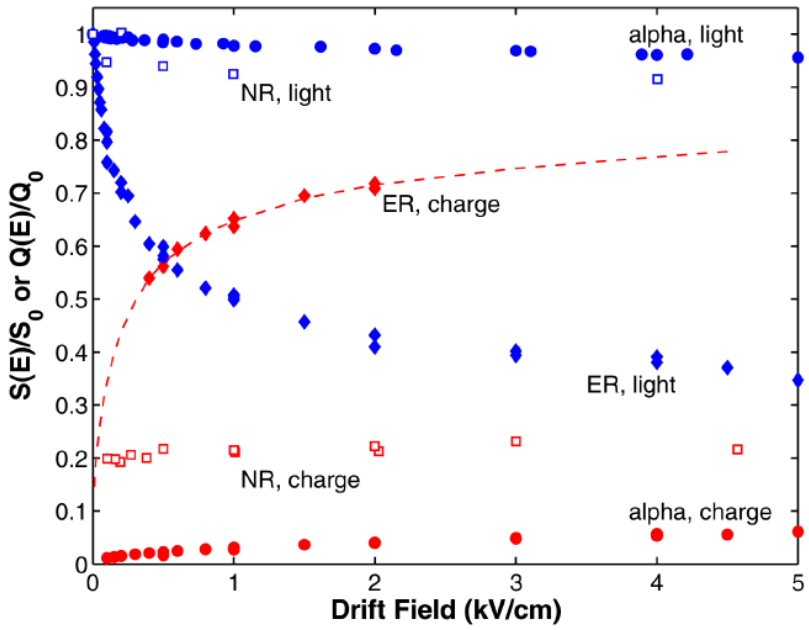

Figure 3.14: Field dependence of scintillation and ionization yield in LXe for 122 keV$_{ee}$ electron recoils (ER), 56.5 keV$_r$ nuclear recoils (NR) and 5.5 MeV alphas, relative to the yield with no drift field [162]. The definition of keV$_{ee}$ and keV$_r$ is given section 3.6.

This mechanism allows to the ionization electrons to be used to generate a second scintillation signal. The potential energy, at the interface, is given by:

$$V_1(Z) = V_0 - eE_1Z + A_1, \quad Z < 0; \tag{3.26}$$

$$V_2(Z) = -eE_2Z + A_2, \quad Z > 0; \tag{3.27}$$

with

$$A_{1,2} = \frac{-e^2(\epsilon_1 - \epsilon_2)}{4\epsilon_{1,2}(Z + \beta Z/|Z|)(\epsilon_1 + \epsilon_2)} \tag{3.28}$$

where V_0 is the ground state energy of the electron in the liquid, $\epsilon_{1,2}$ are the dielectric constant of the liquid and gas, respectively, β is the thickness of the liquid-gas interface, $Z < 0$ is the liquid phase. Electrons with the momentum component, orthogonal to the LXe/GXe, greater than $\sqrt{2m_e|V_0|}$ can be extracted from the liquid into the gas. In GXe, under the effect of a high electric field, drifting electrons can acquire enough energy between two successive collisions, with Xe atoms, to excite the atoms and produce

scintillation light. This effect is called *electroluminescence*, or proportional scintillation, being the scintillation produced proportional to the number of extracted electrons. The photon yield per unit of path length per electron, dN_{ph}/dx, is empirically determined as [163]:

$$\frac{dN_{ph}}{dx} = \alpha(\frac{E_g}{p} - \beta)p \tag{3.29}$$

with $\alpha = 70$ photons/kV and $\beta = 1$ kV/(cm·atm), where E_g is the electric field in the gas and p the pressure. This process, coupled with the extraction of electrons from the liquid phase, provides an extremely efficient way of amplifying the ionization signal of LXe TPCs and even leads to the detection of single electron signals [164].

3.4.3 Attenuation of the VUV flux

Besides the electron capture, impurities in LXe can also reduce the scintillation yield absorbing the produced light. The attenuation of the emitted photon number is given by:

$$I_{(x)} = I_0 e^{(-x/\lambda_{att})}, \tag{3.30}$$

where λ_{att} is the attenuation length that has two components: the absorption length, that describes the loss of photons, and the scattering length. The attenuation length is given by:

$$1/\lambda_{att} = 1/\lambda_{abs} + 1/\lambda_{sca}. \tag{3.31}$$

The most dangerous impurities for the VUV light are the O_2 the water vapor, that are largely contributed by the outgassing of the materials used to build detectors. Figure 3.15 shows the absorption coefficient of water vapor and oxygen with a concentration of 1 ppm. Elastic scattering is dominated by Rayleigh scattering. The Rayleigh scattering length is given by:

$$\lambda_{sca}^{-1} = \frac{\omega^4}{6\pi c^4}\left[kT\kappa_T\rho^2\left(\frac{\partial\epsilon}{\partial\rho}\right)_T^2 + \frac{kT^2}{\rho c_v}\left(\frac{\partial\epsilon}{\partial T}\right)_\rho^2\right] \tag{3.32}$$

where ω is the angular frequency of the scintillation light, c is the speed of the light, k is the Boltzmann's constant, T is the temperature, ρ is the liquid density, κ_T is the isothermal compressibility, c_v is the heat capacity at constant volume and ϵ is the dielectric constant [165]. Equation (3.32) shows how the spatial density fluctuations due to temperature gradients can increase the amount of Rayleigh scattering. Since $\lambda_{sca} \propto \lambda_{Xe}^4$, where λ_{Xe} is the scintillation wavelength, increasing the wavelength can extend the Rayleigh scattering length.

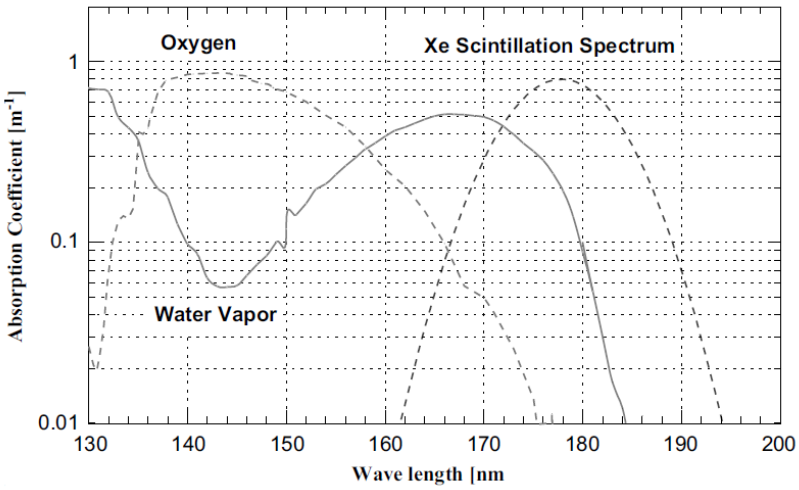

Figure 3.15: Absorption coefficient for VUV photons assuming 1 ppm concentration of water vapor and O_2. Also shown is the LXe scintillation spectrum [166].

Most of the photons are confined into the liquid medium due to the large mismatch in refractive indices of the liquid and gas (the critical angle for total internal reflection at 170 K is about 36°). The refractive index of the GXe is ~ 1 while the refractive index of LXe depends on the radiation wavelength (figure 3.16) and liquid temperature (figure 3.17).

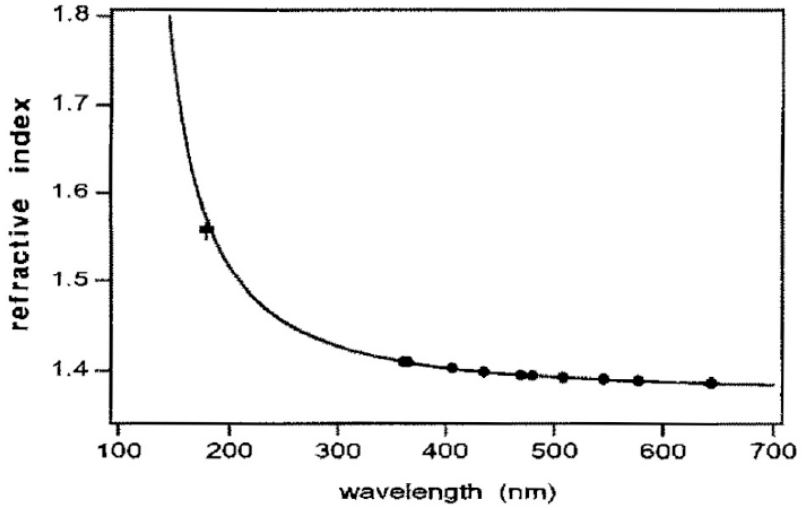

Figure 3.16: Refractive index of liquid xenon at the triple point, as function of the wavelength [167].

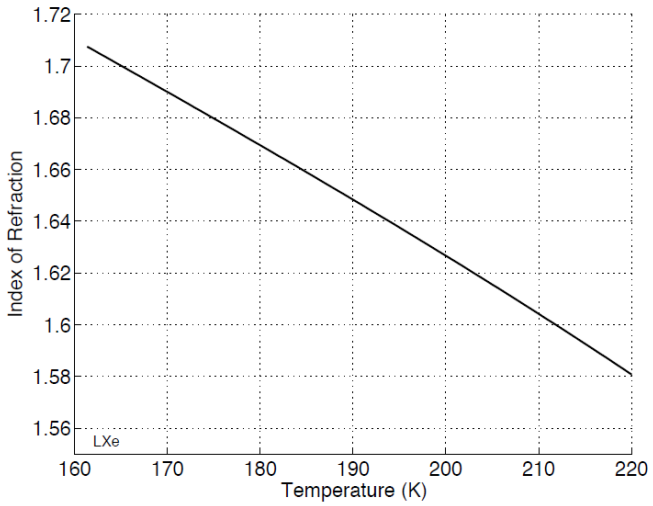

Figure 3.17: Refractive index of liquid xenon as a function of the temperature [167].

3.5 Discriminating particles with LXe

The ability to discriminate among different particles is essential for a dark matter experiment. This because WIMPs produce NR while most of the background radiation produces ER [146]. In dual phase detectors two scintillation signals are measured: one from the excitation and recombination (S1), and another one (S2) from the ionization electrons extracted from the LXe into the GXe. Different LET particles have different S2/S1 ratio and this allows to discriminate among them. Indeed, a NR has a higher recombination rate, due to its higher LET, than an ER. A higher recombination gives a lower S2 and a higher S1 thus, a lower the S2/S1 ratio. This characteristic of the signals implies the anti-correlation between ionization and scintillation signals, which is experimentally observed, figure 3.18.

Thus, using the ratio of the signal as discrimination parameter, it is possible to distinguish between the two type of recoils (see figure 4.4 in Chapter 4). Having such a separation between the ER and NR bands, in the S2/S1 parameter, it is possible to set a discrimination level for the ER which allows to reach, or at least to lower, the desired background level, Section 7.3.

3.6 Relative scintillation efficiency ($\mathcal{L}_{eff}$) for nuclear recoils

As described in Sections 3.2-3.4, in nuclear recoils part of the energy is lost to nuclear stopping power. Such an energy is spent for atomic motion which gives a not measurable

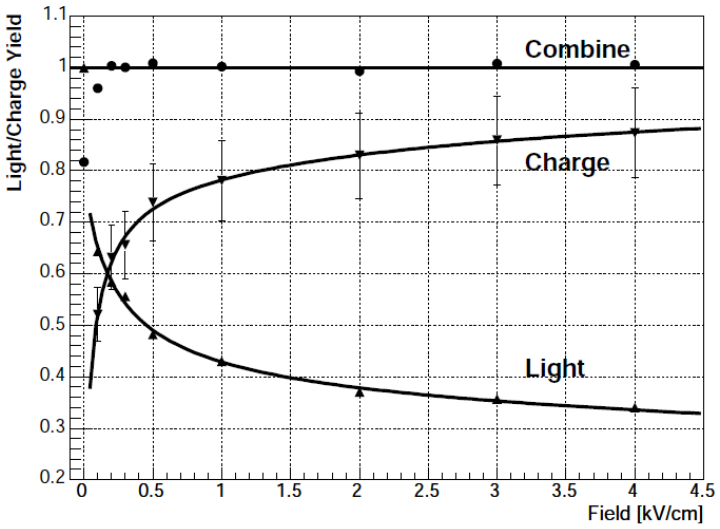

Figure 3.18: Light and charge yield as a function of drift field for 662 keV$_{ee}$ γ-rays from ^{137}Cs [168].

signal. Thus, to reconstruct the energy lost in ER and NR it is necessary to take into account their different scintillation properties. A well known quantity used to define the fraction of the energy lost to electronic excitation in a NR event is the Lindhard factor [169] $\mathcal{L}$, given by:

$$\mathcal{L} = \frac{k \cdot g(\epsilon)}{1 + k \cdot g(\epsilon)}, \tag{3.33}$$

where

$$\epsilon = 11.5 E_r(\text{keV}) Z^{-7/3};\ k = 0.133 Z^{2/3} A^{1/2};\ g(\epsilon) = 3\epsilon^{0.15} + 0.7\epsilon^{0.6} + \epsilon. \tag{3.34}$$

A better agreement between data and Lindhard theory is reached, in LXe, considering together with the nuclear quenching also the electronic quenching (Section 3.4).
Experimentally, it is usually quoted the relative scintillation efficiency of nuclear recoils $\mathcal{L}_{eff}$ instead of the Lindhard factor. It is an energy dependent quantity and it is given by:

$$\mathcal{L}_{eff}(E_{nr}) = \frac{L_{y,nr}(E_{nr})}{L_{y,er}(E_{er} = 122 \text{ keV})}, \tag{3.35}$$

where E_{nr} is the released energy in a nuclear recoil, $L_{y,nr}(E_{nr})$ is the scintillation yield of the nuclear recoil and $L_{y,er}(E_{er})$ is the scintillation yield of electronic recoils from photoabsorbed 122 keV γ rays from a ^{57}Co source at zero field. Using a collimate beam of neutrons, of known energy, it is possible to directly measure the $\mathcal{L}_{eff}$ through Coulomb scattering on Xe atoms:

$$E_{nr} \approx 2E_n \frac{m_n M_{Xe}}{(m_n + M_{Xe})}(1 - cos\theta), \tag{3.36}$$

where E_n is the energy of the incoming neutron, m_n and M_{Xe} are the masses of the neutron and Xe nucleus, respectively, and θ is the scattering angle. Knowing E_n and θ, E_{nr} is inferred from equation (3.36). Then, measuring the scintillation yield $L_{y,nr}(E_{nr})$, the $\mathcal{L}_{eff}$ can be evaluated from equation (3.35), as function of E_{nr}, figure 3.19.

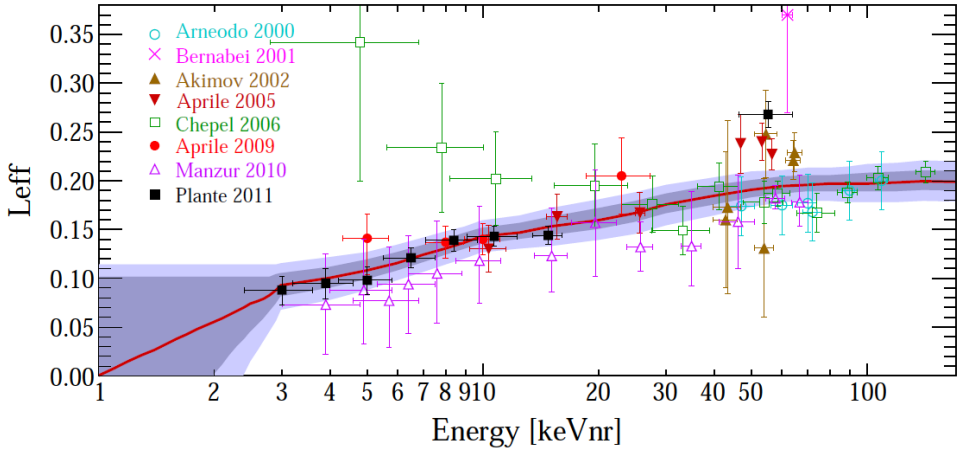

Figure 3.19: Direct measurements of $\mathcal{L}_{eff}$ [170, 171] described by a Gaussian distribution to obtain the mean (solid line) and the uncertainty band 1σ and 2σ (light and dark gray, respectively). Below 3 keV$_r$ the trend is logarithmically extrapolated to $\mathcal{L}_{eff} = 0$ at 1 keV$_r$.

Knowing the $\mathcal{L}_{eff}$ it is then possible to correctly reconstruct the released energy in NR. For ER and NR, two different energy scales are used. They are indicated as "keV$_{ee}$" for the electronic recoils and "keV$_r$" for nuclear recoils. The first one is the energy scale where a γ ray calibration source is used to obtain the conversion between energy and the detector response for ER. The second one is obtained from the scintillation signal, S1, and using the $\mathcal{L}_{eff}$:

$$E_{nr}(\text{keV}_r) = \frac{S1}{L_y}\frac{1}{\mathcal{L}_{eff}}\frac{S_{er}}{S_{nr}}, \tag{3.37}$$

where $S1$ is the scintillation signal measured in photoelectrons, L_y is the light yield of photoabsorbed 122 keV γ rays, $\mathcal{L}_{eff}$ is the relative scintillation efficiency in LXe and $S_{er(nr)}$ is the the field quenching factor of the scintillation light for electronic (nuclear) recoils.

Chapter 4

The XENON Project

The first detector of the **XENON** project was **XENON10** [172]. The main goal of this experiment was to test the possibility to realize a dual phase, LXe/GXe, detector on the kg scale to detect dark matter interactions. The good results, obtained in 2007, pushed towards the realization of a new and larger detector, **XENON100** [173], based on the same detection and work principles. Both detectors, have been placed in the interferometer tunnel at the Laboratori Nazionali del Gran Sasso (LNGS), Italy, at an average depth of 3600 m water equivalent. XENON100, in 2012, [8] set the most stringent limit on the spin-independent WIMP-nucleon elastic scattering cross section for WIMP masses above 8 GeV/c^2, with a minimum of 2×10^{-45} cm^2 at 55 GeV/c^2, at a 90% confidence level. This result has been the best limit up to the LUX results [10] in October, 2013. In parallel, since 2010, the **XENON1T** design started. It will be the largest dual phase Xe-based detector ever realized and, after its approval by INFN in 2011, it is now under construction in the Hall B at LNGS.

4.1 Dual phase TPC principle detection

The "heart" of the various XENON detectors is a dual phase (LXe/GXe) Time Projection Chamber (TPC) which contains xenon in liquid phase (LXe) and, above it, in gaseous phase (GXe). A particle interacting in LXe (Section 3.2) produces a prompt scintillation signal (S1) through excitation, and ionization electrons. The electrons can recombine, participating to the S1 signal, or can be drifted by an appropriate electric field towards the liquid-gas interface where they are extracted into the GXe (Sections 3.3 - 3.4) to produce the secondary scintillation signal, S2. On the bottom, the TPC is closed by the Cathode (at negative voltage) while on its top it is closed by the Gate mesh (grounded). This structure encloses the LXe active region, called the *sensitive volume*,

that represents the volume used to detect the interactions and available for the electrons drift. Along the vertical axis, equally spaced, are distributed thin copper rings that, together with the Cathode and the Gate mesh, generate a uniform electric field used to drift the electrons. Above the Gate mesh there is the Anode and in between them is set the LXe/GXe interface. Gate mesh and Anode produce the extraction field which has a strength of $\mathcal{O}(10)$ kV/cm, that guarantees an extraction level close to 100%. Two PMT arrays, one on top of the TPC inside the GXe and one at its bottom below the cathode, in LXe, are used to detect the scintillation light. From the pattern of the hit PMTs it is determined the x-y position of the events while from the time difference between S1 and S2 signals it is inferred the z coordinate. Combining all these informations, a 3D vertex reconstruction is possible. The knowledge of the interaction point allows the selection of the events that happen in the inner part of the LXe, usually called *fiducial volume* since the majority of background events are expected to be found outside of it (Section 3.2), using the outermost volume as shield, thus reducing the background from external sources.

Also the S1 and S2 signals are used to lower the background, through their different ratio for ER and NR (Section 3.5). A schematic view of the TPC structure and an example of the two signals are shown in figure 4.1.

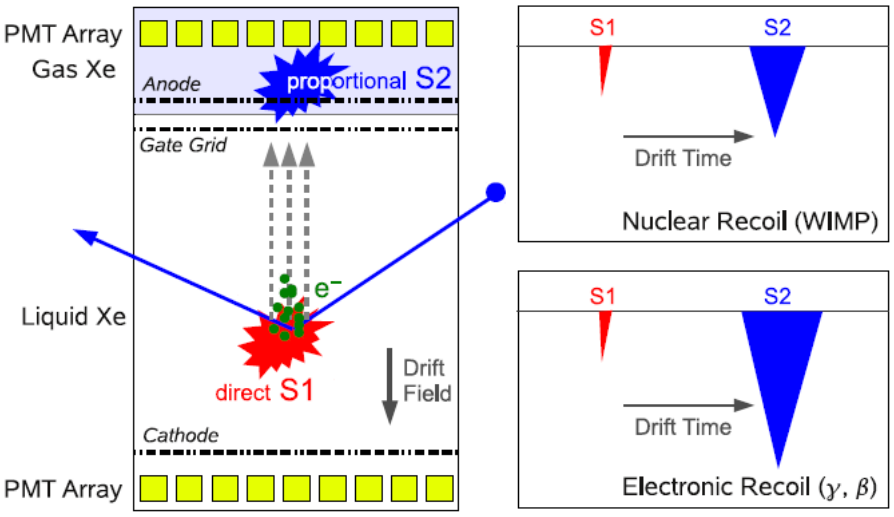

Figure 4.1: Left, XENON detector TPC schematic view and its work principle. Right, drawings of wave forms due to different kind of events. The different ratio of S2/S1 allows for the discrimination between ER and NR [173].

4.2 XENON10

The TPC of XENON10 was made of a PTFE cylinder with a inner diameter of 20 cm and a height of 15 cm. The detector contained a total amount of 25 kg of Xe, 15 of which were used as active volume [172]. The TPC was placed in a double-walled SS vessel which contained vacuum between the jackets. The vacuum insulated the LXe keeping it thermally decoupled from the external environment, figure 4.2. In order to assure the continuous operation of the detector, several devices were added into the design: a diving bell, a cryogenic system, a purification and a recirculation systems. The diving bell was required to keep constant the level of the LXe/GXe interface, since from it depends the extraction and so the multiplication properties of the system. The cryogenic system was based on a Pulse Tube Refrigerator (PTR) specifically designed for XENON10, mounted on the cryostat top flange and put in direct contact with the liquid, figure 4.2.

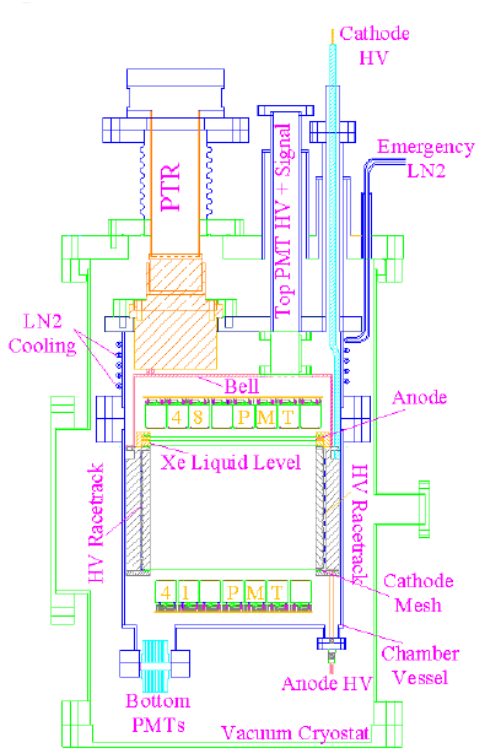

Figure 4.2: Schematic view of the XENON10 detector.

Besides the anode, cathode and gate mesh (Section 4.1), this detector used another mesh, at ground voltage and placed above the anode, that was used to close the field lines in order to protect the PMTs. Above and below the PTFE structure the two PMT arrays produced the signals. The PMTs used for XENON10 were developed by the Hamamatsu Photonics Co. [174]. They were 1" square with a bialkali photocathode

(Rb-Cs-Sb), equipped with a quartz window, whose quantum efficiency was $> 20\%$ for the light emitted by the LXe ($\sim$178 nm). One of the most important requirements for a rare events search experiment is to have a very low background. In order to reduce the external background, the whole structure was placed in a cubic steel-framed structure, consisting of 20 cm high density polyethylene inside 20 cm Pb, figure 4.3.

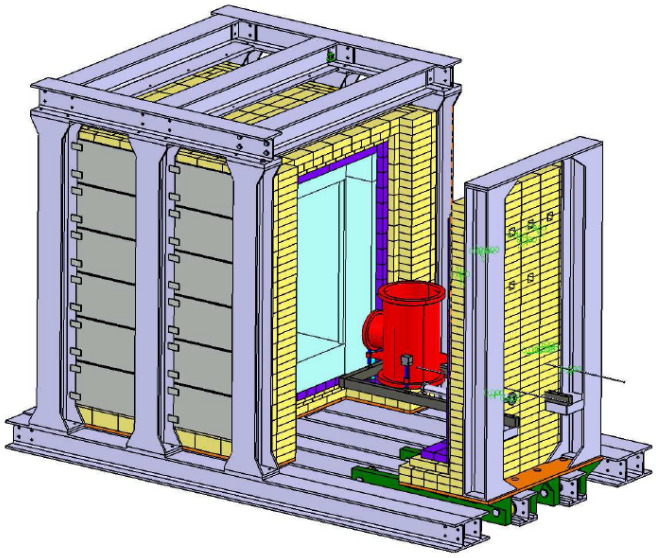

Figure 4.3: Schematic view of the XENON10 detector shield structure.

Simulations showed that, with this external shield, it was possible to have a background reduction of a factor $\sim 10^7$ in the energy region below 25 keV. This shield was also designed to allow the introduction of external calibration sources without exposing the detector cavity to the outside air. The gamma calibration sources were ^{60}Co (1.2 and 1.3 MeV) and ^{137}Cs (662 keV). For the NR calibration an ^{241}AmBe(α, n) source was used. The ER and NR calibration bands are shown in figure 4.4 [172]. In the figure, the keV$_{ee}$ scale is used. As described in section 3.6, to take into account the different scintillation properties of ER and NR, two energy scales are used: keV$_{ee}$ for the former and keV$_r$ for the latter. A further background reduction was achieved through volume fiducialization (Section 4.1) and thanks to an intensive screening material campaign where materials with the lowest activity were found. Due to the 15 cm drift path, the LXe had to be of high purity to allow to the electrons to reach the extraction interface with the highest probability. This required a level for the electronegativity impurities below 1 part per billion (ppb).

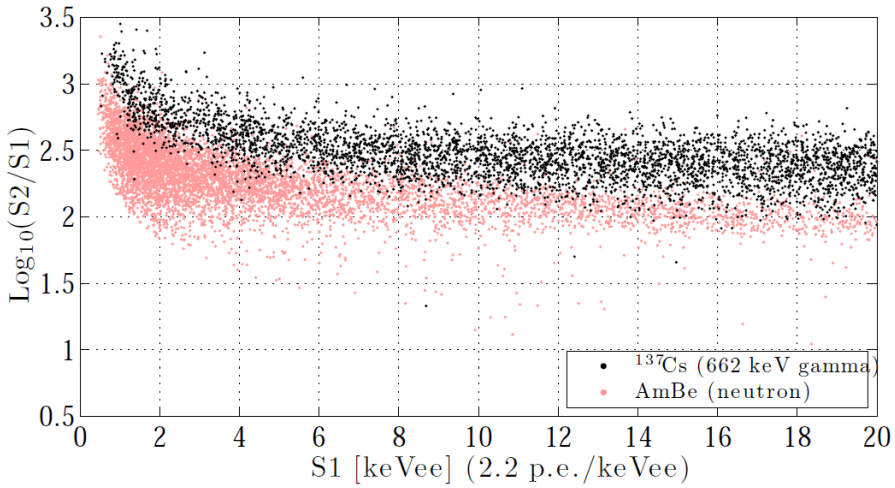

Figure 4.4: Calibration bands for ER from a ^{137}Cs (662 keV) source (black points) and for NR from an AmBe source (red points).

Due to the Van der Waals interactions of the LXe with the TPC material, the LXe is able to extract those impurities; hence it was crucial to remove them. To this aim, in addition to a purification device, also a recirculation system was required to continuously purify the liquid. This goal was achieved through a high temperature getter, figure 4.5.

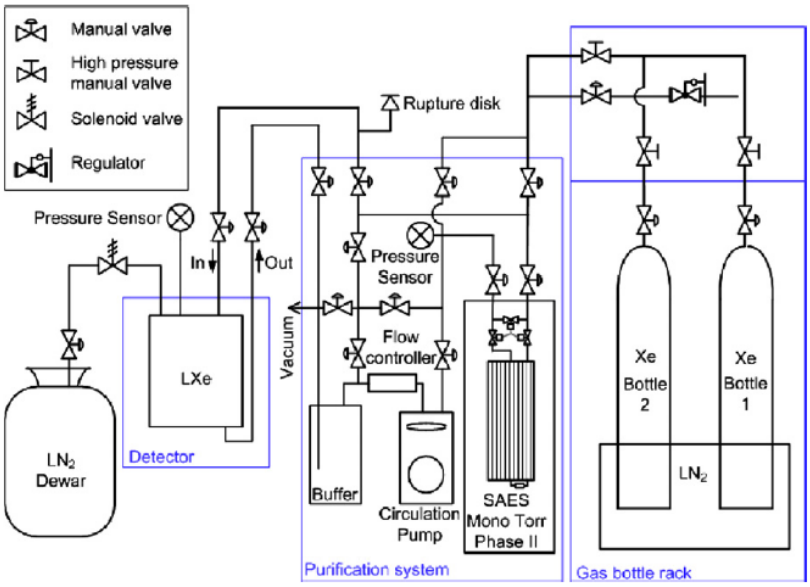

Figure 4.5: Scheme of the Xe purification system with closed-loop re-circulation. LXe from the bottom of the detector is evaporated and pressed by a gas circulation pump through the getter, for continuous purification.

A possible WIMP signal was searched in a certain S1 window with a lower bound

connected to the energy threshold of the experiment and with the upper bound chosen in order to maximize the integrated WIMP rate. To simplify the analysis, a flattening of the ER and NR bands was performed subtracting to both of them the mean of the ER band, figure 4.6.

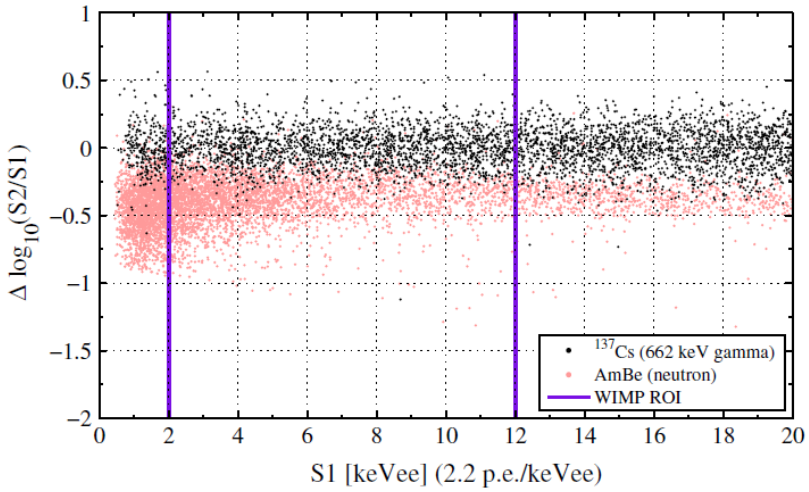

Figure 4.6: Flattened bands for ER (black points) and NR (red points) in XENON10. The violet vertical lines enclose the S1 WIMP search region [172].

The WIMP acceptance window was defined to lie in the range:

$$(\mu - 3\sigma) < \Delta\log_{10}(S2/S1) < \mu,$$

where μ and σ were the mean and the sigma of the NR band, figure 4.7. The NR acceptance was defined as the fraction of AmBe events that fall within this window, for each bin. The best result for XENON10 detector was achieved after the analysis of a 58.6 live-days WIMP search run (October 6, 2006 - February 14, 2007). The same dataset was used in a spin-independent (SI, [175]) and a spin-dependent analysis (SD, [176]). The energy region chosen was [4.5, 26.9] keV$_r$ (Section 3.6). In the analysis the mean light yield (L_y) was $3.0 \pm 0.1(\text{stat}) \pm 0.1(\text{stat})$ photoelectrons/keV$_{ee}$ (pe/keV$_{ee}$) at a drift field of 0.73 kV/cm. Rejection of the ER background was obtained using the different values of the $\log_{10}(S2/S1)$, figures 4.4 and 4.6. For the SI analysis, ten events were found in the 5.6 kg chosen fiducial volume, figure 4.8. They were found compatible with the background thus, only upper limits on the sensitivity were set. The minimum of the sensitivity, $4.5 \cdot 10^{-44}$ cm^2 with a 90% CL, was achieved for a WIMP mass of 30 GeV/c^2, figure 4.9. For what concerns the SD interactions, Xe is mostly sensitive to WIMP-neutron couplings. For a such kind of interactions, the minimum WIMP-nucleon cross section of $\sim 6 \cdot 10^{-39}$cm^2 was achieved at a WIMP mass of ~ 30 GeV/c^2 [176].

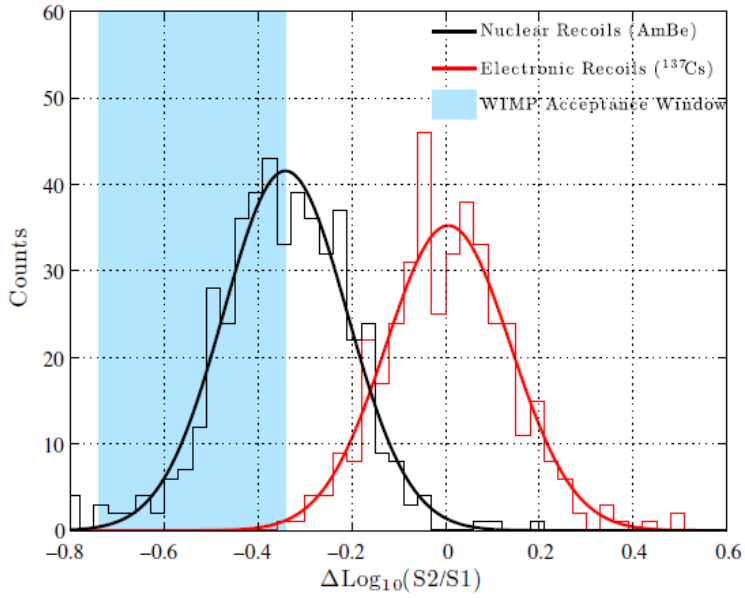

Figure 4.7: WIMP acceptance region (light blue shaded area) for the [13.4, 17.2] keV$_r$ energy window of the NR distribution.

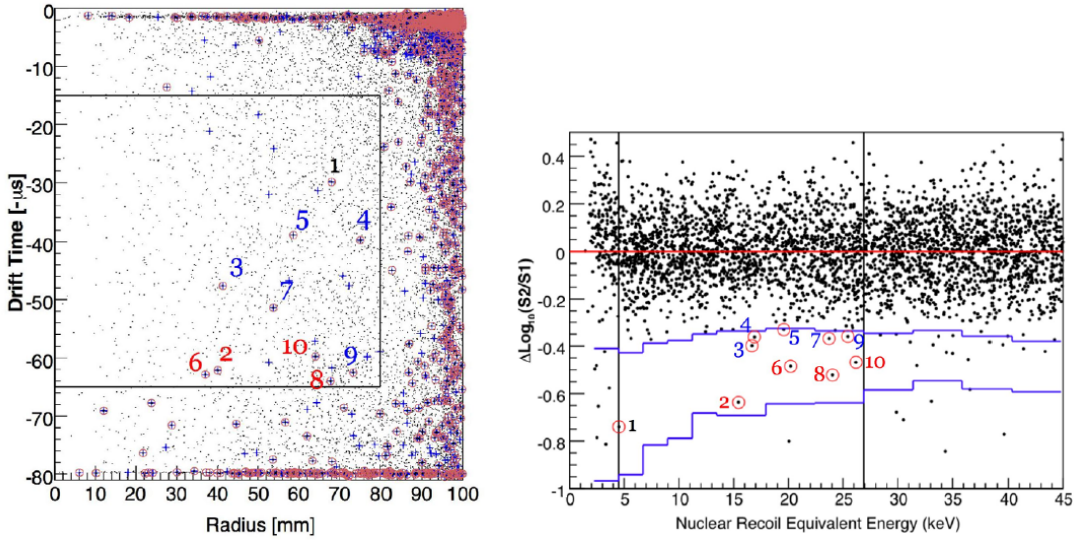

Figure 4.8: Analysis results for the XENON10 58.6 live-days run [175]. Left, XENON10 LXe active region. The solid line encloses the chosen fiducial volume. The numbered points are the events found inside the WIMP search region, after the analysis. Right, $\log_{10}S2/S1$ as function of the nuclear recoil energy. The vertical and horizontal lines enclose the WIMP search region ([4.5, 26.9] keV$_r$) with a nuclear recoil acceptance of about 50%.

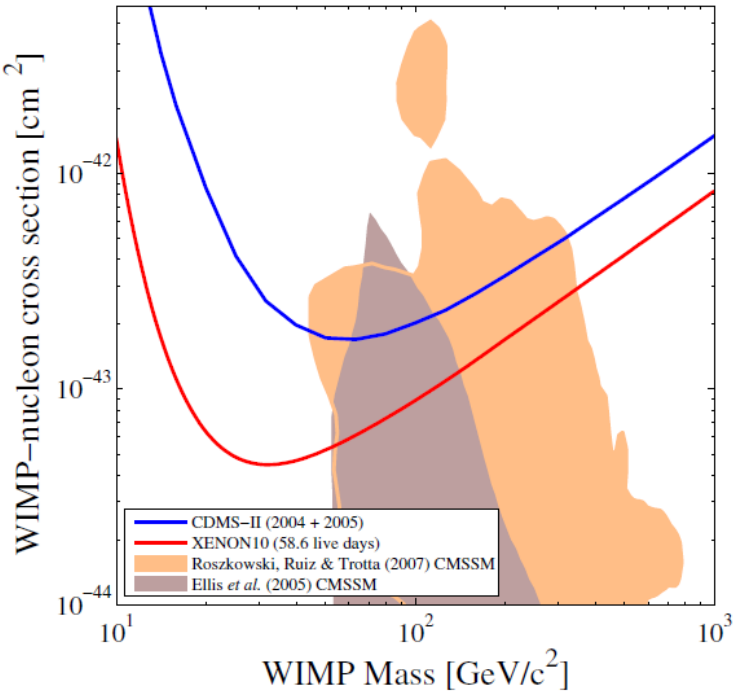

Figure 4.9: Cross section limit, 90% CL, on spin-independent WIMP interactions (red line), from the 58.6 live-days dataset [175]. The blue line is the best limit from CDMS experiment [177]. The shaded areas represent the allowed parameter region in the constrained minimal supersymmetric models.

XENON10 detector was also used for light dark matter searches [67]. One of the major difficulties in the detection of this kind of particles is the very small recoil energy and so only detectors with a very low threshold can face this search. The light dark matter is usually considered for masses below $\sim$ 10 GeV and this gives a maximum recoil energy, in xenon, of 6 keV$_r$. For this amount of energy only the S2 signal can be used used. Indeed, for very low energy releases, the S1 signal is not observed. Thus, the discrimination imposed on the $\log_{10}(S2/S1)$ is not possible anymore. For this kind of search, the S2 scintillation gain was raised of a about 12%, with respect to previous runs, and the S2 threshold was lowered to one electron. In this configuration of the detector, a single electron ended up with 27 photoelectrons which allowed for a nice $x-y$ event reconstruction. For the z coordinate, since in this case the S1 signal was not available, a relation between the spread of the S2 signal, σ_e, and its z position was used. The fiducial volume was considered inside a radius of 3 cm. Using S2-only signals, it was mandatory a good knowledge of the charge yield, $\mathcal{Q}_y$, i.e. the number of electrons produced per keV$_r$ of recoil energy, figure 4.10:

$$\mathcal{Q}_y = \frac{n_e}{E_{nr}} \tag{4.1}$$

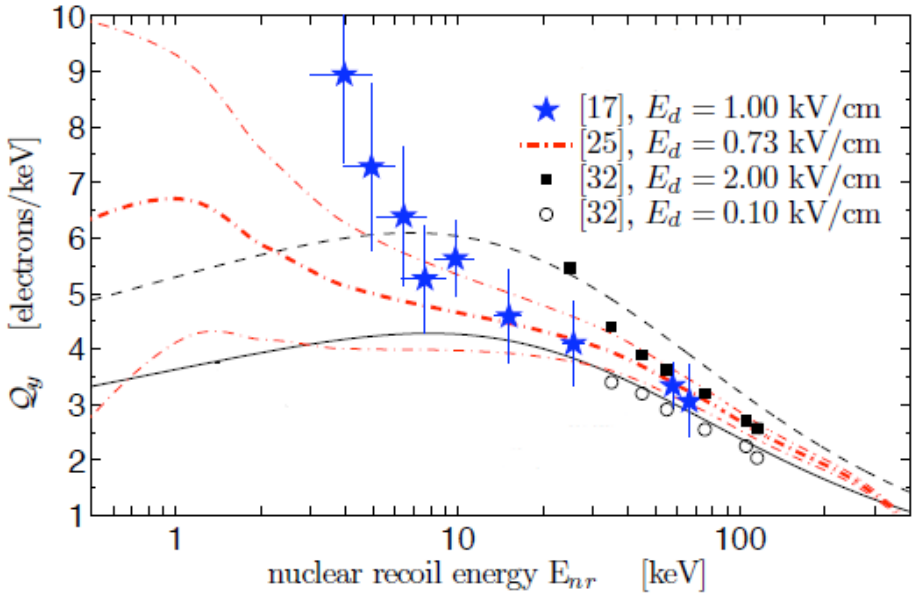

Figure 4.10: Charge yield as function of the recoil energy [67]. The solid black line is the parameterisation used in XENON10. Also shown are measurements from [178] ($\star$), [179] (dash-dot curve, with $\pm 1\sigma$ contours) and [180] ($\circ$ and black square).

For such an analysis, a 12.5 live-days run and an energy threshold of 1.4 keV$_r$ were used. The energy resolution was defined as:

$$\mathcal{R}(E_{nr}) = (\mathcal{Q}_y E_{nr})^{-\frac{1}{2}} \tag{4.2}$$

Using the p_{max} method [181], the 90% CL cross section limit for elastic spin-independent light dark matter was set, figure 4.11 [67].

4.3 XENON100

The XENON100 detector [173] (figure 4.12), currently working at the LNGS, has been based on the same detection principles as its predecessor. The goal of this experiment has been to lower the sensitivity by two orders of magnitude with respect to XENON10. The XENON100 TPC has a radius of 15.3 cm and a height of about 30.5 cm and it contains 62 kg of LXe. In this case the TPC has been realized using 24 interlocking panels in an almost cylindrical shape. The interlocking structure is mandatory to avoid light leaks through the panels after their shrinkage ($\sim 1.5\%$) at LXe operative temperature (-91 ^{o}C). As in XENON10 the active region is defined by the TPC and two, out of five, meshes: the cathode, at the bottom of the TPC, and the gate mesh, on its top. The cathode is biased at ~ -16 kV while the gate mesh is grounded. With this configuration

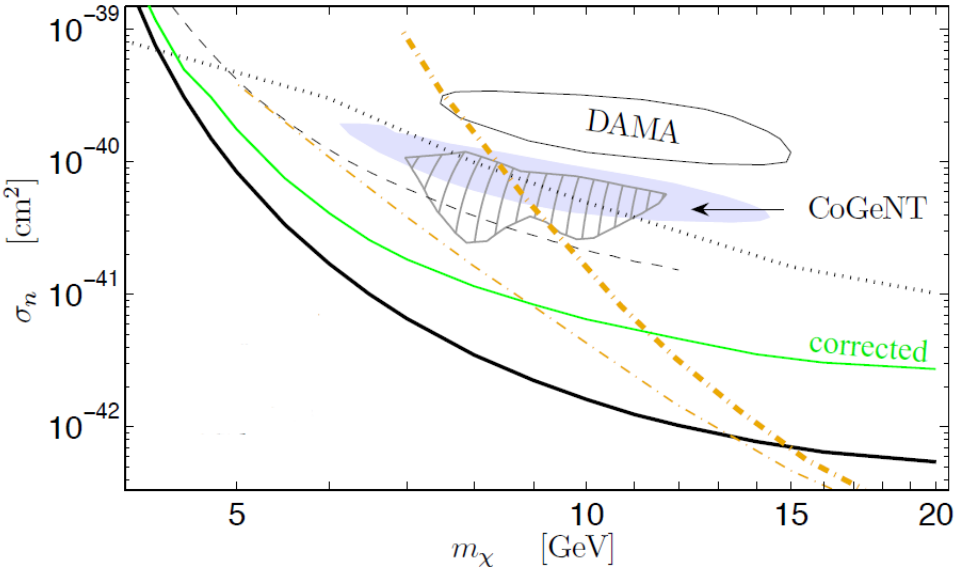

Figure 4.11: Curves indicate 90% CL exclusion limits on spin-dependent σ for elastic dark matter scattering, obtained by CDMS (dotted [182], and dashed [65]) and XENON100 (dash-dot [183]). The region consistent with assumption of a positive detection by CoGeNT is shown (hatched) [121], and (shaded) [52]. Also shown is the 3σ allowed region for the DAMA annual modulation signal (solid contour) [184]. Previously published (solid black curve) and corrected (solid green curve, labeled "corrected") 90% CL exclusion limits obtained from data.

of the meshes and 40 thin copper field shaping rings, equally spaced in the vertical coordinate, a uniform drift field of $\sim$ 530 V/cm is generated. Above the gate mesh, there is the anode. These two meshes, with the LXe/GXe interface in between, create the extraction field ($\sim$ 12 kV/cm biasing the anode at +4.5 kV). Other two meshes, both grounded, are used in order to close off the field lines: the top screening mesh, 5 mm above the anode, and the bottom screening grid, 12 mm below the cathode. The extraction properties are strongly connected to the LXe/GXe interface level. In order to keep it under control, a diving bell has been designed, figure 4.12. The diving bell, as for XENON10, has two main functions:

1. it keeps the liquid level at the desired height; to this aim a constant stream of gas is released through a small pipe that reaches out into LXe volume, to pressurize the system;

2. it allows to have LXe all around the TPC volume, thus giving a 4π coverage of the sensitive volume.

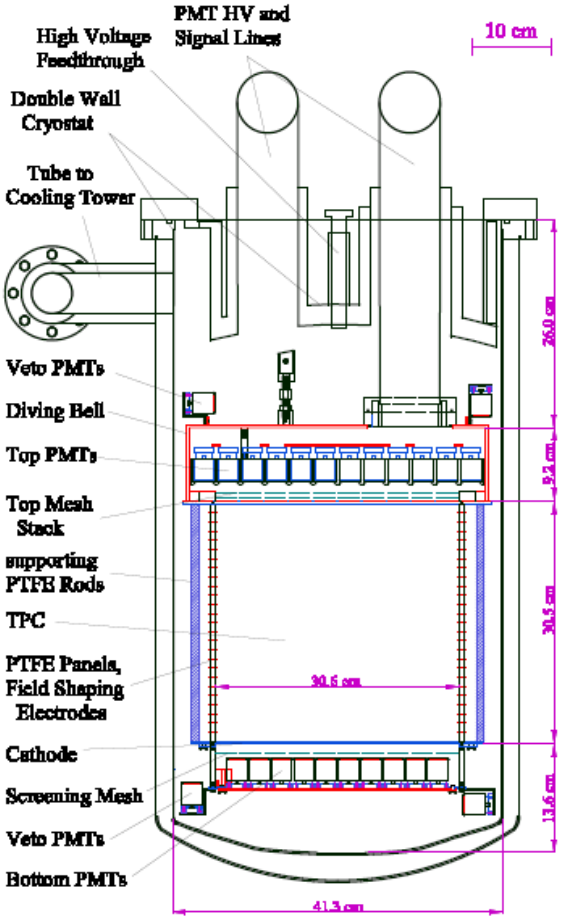

Figure 4.12: Schematic view of the XENON100 detector.

All around the TPC there is a 4 mm thick LXe layer, 99 kg in total, that acts as active veto. This veto is seen by dedicated PMTs placed around the TPC. In order to detect the S1 and S2 signals there are two arrays of Hamamatsu R8520-06-A1 1" square PMTs, on top and bottom of the TPC, figure 4.13.

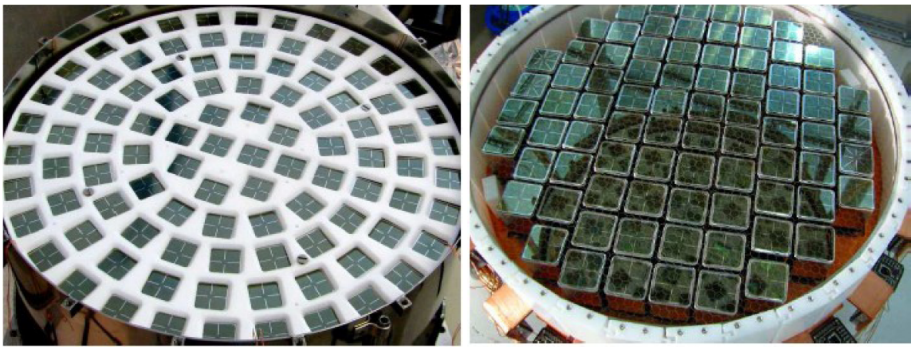

Figure 4.13: Top array (left), 98 PMTs, and bottom array (right), 80 PMTs.

Due to LXe refractive index (1.69 $\pm$ 0.02) [185] and the consequent total internal reflection, the S1 signal is seen mainly by the bottom PMT array. For this reason the bottom PMTs have a higher quantum efficiency than the top ones. The TPC is placed in a double walled 316Ti stainless steel cryostat which guarantees a thermal isolation from the environment. The whole detector structure has been placed in the same passive shield of XENON10, figure 4.3, with an addition of an outer layer of 20 cm of water, on top and on three sides of the shield, to further reduce the neutron background. To lower even more the external background the cryogenic and gas purification systems are placed far from the detector and connected to it through double walled pipes. As XENON10, also XENON100 uses a high temperature zirconium getter and a PTR. The cryogenic system is connected to the cryostats through a vacuum insulated pipe. The GXe from the detector can thus reach the cold-finger of the PTR where it is liquefied, figure 4.14. The liquid drops are collected by a funnel and flow back into the detector through a smaller diameter pipe at the center of the insulated pipe.

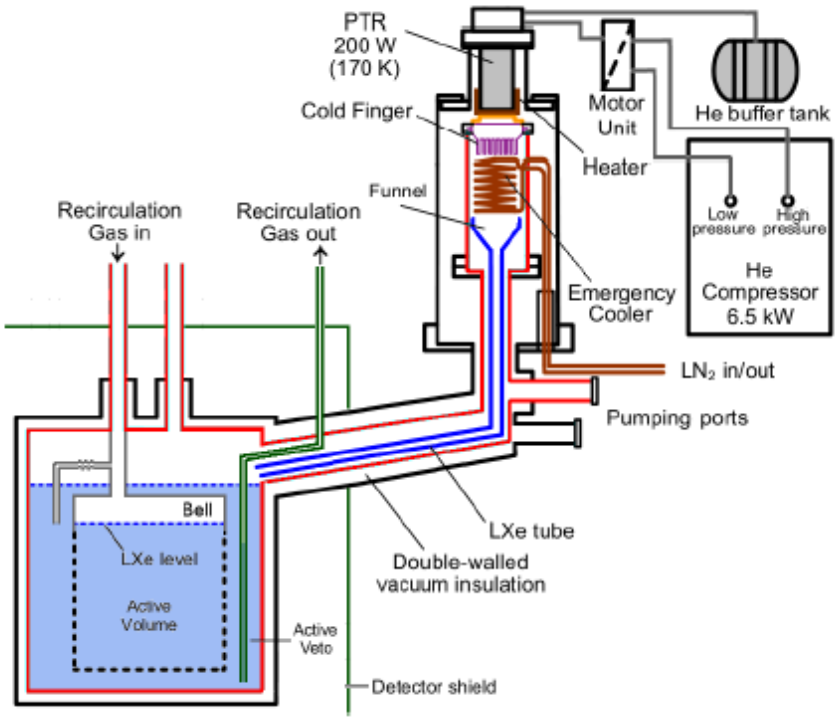

Figure 4.14: Schematic view of the detector and its cryogenic system.

Usually the commercial xenon comes with a certain amount of ^{85}Kr contamination. This element, through its beta decay, can produce a not negligible contributions to the background, thus reducing the sensitivity of the detector. For this reason a Kr distillation

column has been used, figure 4.15.

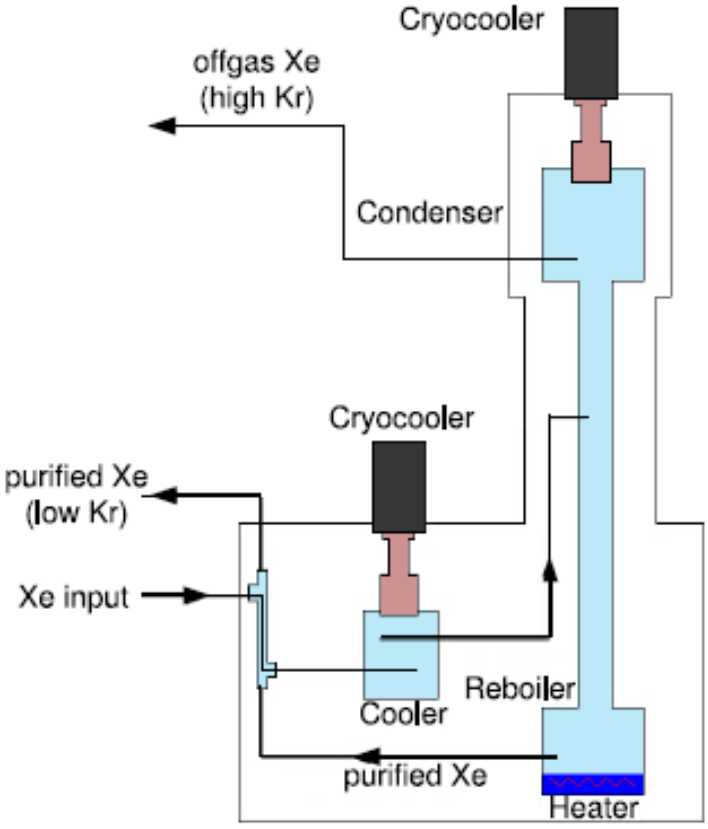

Figure 4.15: Schematic layout of the cryogenic distillation column used to separate krypton from xenon.

The column is based on the different boiling point of the Kr (120 K at 1 atm) and of the Xe (165 K at 1 atm). In this way the gas enriched in Kr reaches the top of the column and it is extracted while the gas with lower Kr concentration goes at the bottom of the column and then it is sent to the detector. The calibration of the detector to electromagnetic and nuclear recoils is made by using several sources. They are placed inside a thin copper tube all around the TPC. For the ER calibrations ^{60}Co and ^{232}Th have been used as well as a ^{137}Cs source to measure the electron lifetime. For what concern the nuclear recoils an ^{241}AmBe (α, n) source has been used. This source can also furnish inelastic scatters on the xenon nuclei that will provide additional gamma lines from xenon or fluorine: 40 keV (^{129}Xe), 80 keV (^{131}Xe), 110 keV (^{19}F in PTFE), 164 keV (^{131m}Xe), 197 keV (^{19}F), and 236 keV (^{129m}Xe).

4.3.1 Spin-independent results

The best results of XENON100, for the 2012, have been achieved using a dark matter science run over a period of 13 months that led to a 224.6 live-days dataset [8]. The analysis was carried out only on the data acquired in periods where the detector showed a stable behavior. For the analysis it was decided to use the *Profile Likelihood* [186] (PL) statistical method. Moreover, the *Maximum Gap method* [181] has been used as cross-check. The NR energy has been inferred using the S1 signal and the $\mathcal{L}_{eff}$ (Section 3.6), assuming $L_y = (2.28 \pm 0.04)$ pe/keV$_{ee}$, $S_{ee} = 0.58$ and $S_{nr} = 95$ with an electric field of 530 V/cm. Position reconstruction and S2/S1 discrimination, figure 4.16, have been used to lower the background.

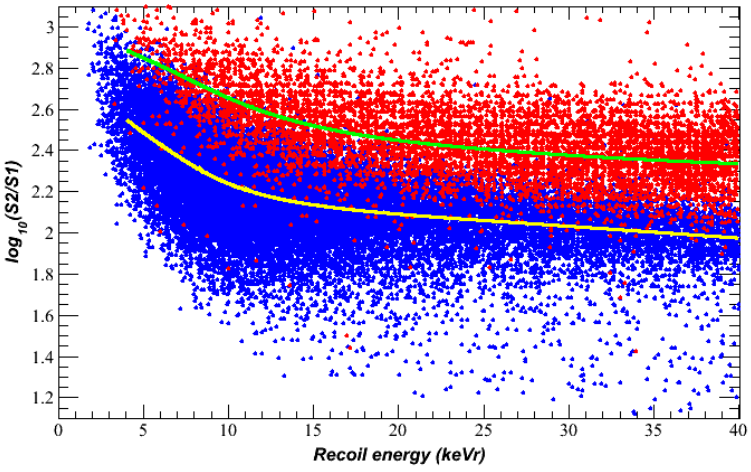

Figure 4.16: Discrimination parameter, $\log_{10}$S2/S1, as function of the recoil energy. The ER band (red points) is showed together with the NR band (blue points). Superimposed to the bands there are their medians, green and yellow solid lines for the ER and NR band, respectively.

In the $z-$coordinate the resolution has been 0.3 mm while in $x-y$ it has been < 3 mm. The total expected background, from MC simulations, has been (1.0 ± 0.2) events. For the analysis, a $S2 > 150$ pe threshold and an electron lifetime of 514 μs have been used. Dark matter runs were stopped only for LED calibrations of the PMTs and ER calibrations with ^{60}C and ^{232}Th sources. For the impurity monitoring, ^{136}Cs runs were used. For NR calibration, two runs of ^{241}AmBe have been done: at the beginning and at the end of the run, that showed a good agreement. To avoid any analysis bias, the DM runs have been blind in the region [2, 100] photoelectrons, keeping only the upper 90% of the ER band. To make a selection of the possible WIMP candidate events, several quality cuts and event selection criteria have been developed. Their acceptance, figure

4.17, has been evaluated on the NR calibrations with the exception of the quality cuts, since they are dependent on the status of the detector.

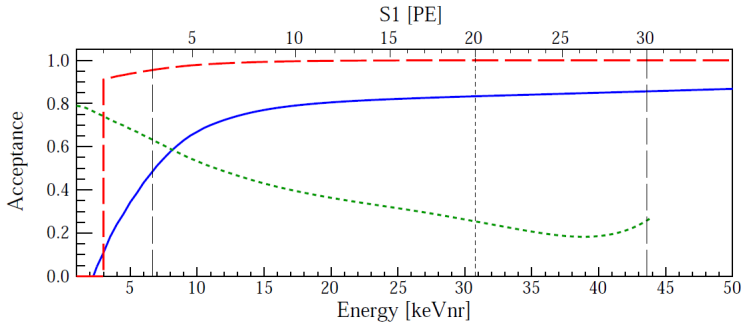

Figure 4.17: Cut acceptance (blue line), S2>150 PE threshold acceptance (red dashed line), NR discrimination cut (green line) [8].

The other cuts have been tested on the ER data or in the unblind part of the DM data. The benchmark region for the WIMP search has been defined as follows: 34 kg fiducial volume; [3, 20] pe window in S1 that corresponds to [6.6, 30.5] keV$_r$ energy window; below the 99.75% ER rejection line in S2/S1; S2 threshold > 150 pe. After unblinding the data, two events were left in the benchmark region inside the fiducial volume, figures 4.18 and 4.19.

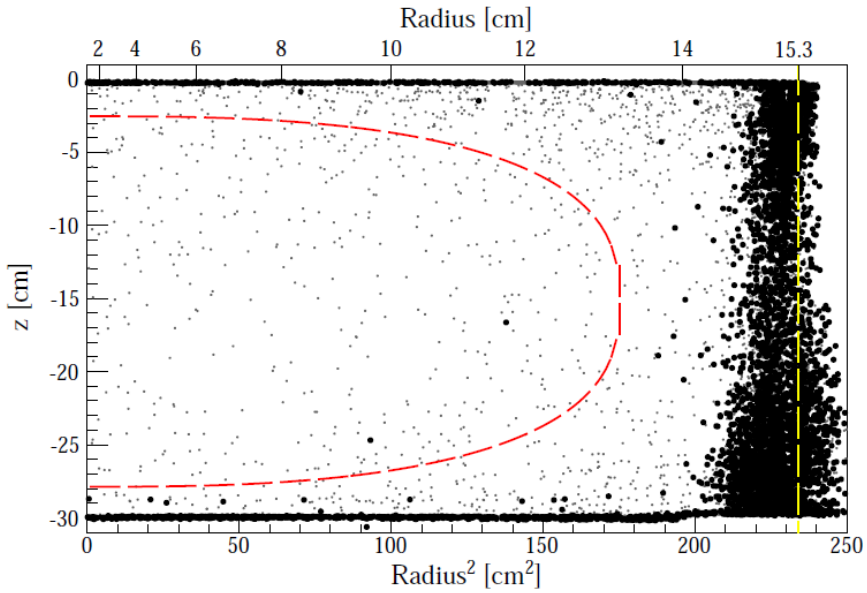

Figure 4.18: Spatial event distribution inside the TPC [8]. The 34 kg fiducial volume is indicated by the red dashed line. Gray points are above the 99.75% rejection line, black circles fall below.

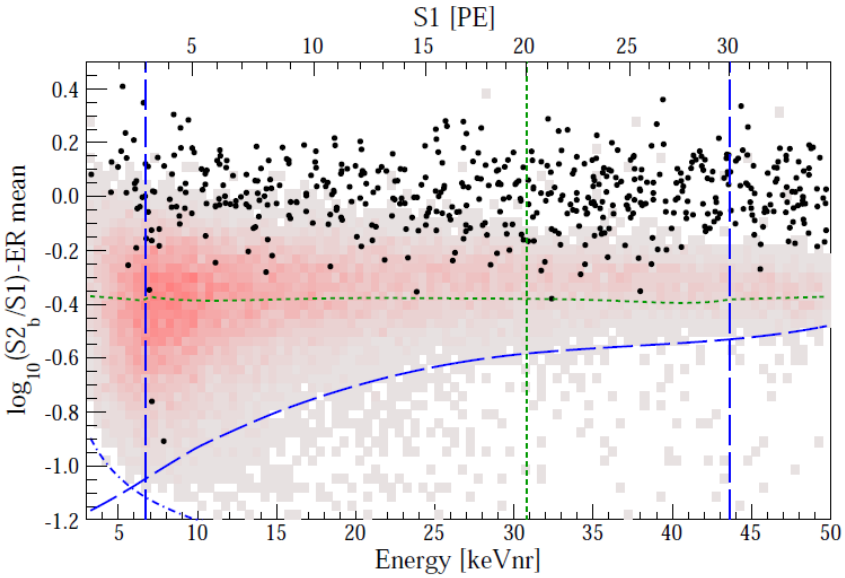

Figure 4.19: Event distribution, after the analysis, in the discrimination parameter space $\log_{10}(S2_b/S1)$ (flattened), in a 34 kg of FV (black points). A lower analysis threshold of 6.6 keV$_r$ has been considered. The negligible impact of the S2 > 150 pe threshold cut is indicated by the dashed-dotted blue line and the signal region is restricted by a lower border running along the 97% NR quantile. An additional strong $S2_b/S1$ discrimination cut at 99.75% ER rejection defines the benchmark WIMP search region from above (dotted green). The red dots indicate the NR band from the neutron calibration [8].

At the end of the analysis, cross section limits for WIMP-nuclei spin-independent (SI) elastic scatters, as function of the WIMP mass, have been evaluated (figure 4.20).

For the limits evaluation a halo density of $\rho_\chi = 0.3$ GeV/c^3, a local circular velocity $v_0 = 220$ km/s and galactic escape velocity $v_{esc} = 544$ km/s have been considered. The minimum for the sensitivity, $\sigma = 2.0 \cdot 10^{-45}$cm^2, has been found for a WIMP mass $m_\chi = 55$ GeV/c^2 [8].

4.3.2 Spin-dependent results

For spin-dependent (SD) interactions it is assumed that the WIMPs are a spin-1/2 or spin-1 fields, meaning that they couple to the quark axial current. The differential cross section [9] for this kind of interaction is given by:

$$\frac{\sigma_{SD}}{dq^2} = \frac{8G_F^2}{(2J+1)v^2} S_A(q) \tag{4.3}$$

where q is the momentum transfer, G_F is Fermi constant, v is the WIMP velocity relative to the target, J is the total angular momentum of the nucleus and $S_A(q)$ is the axial-

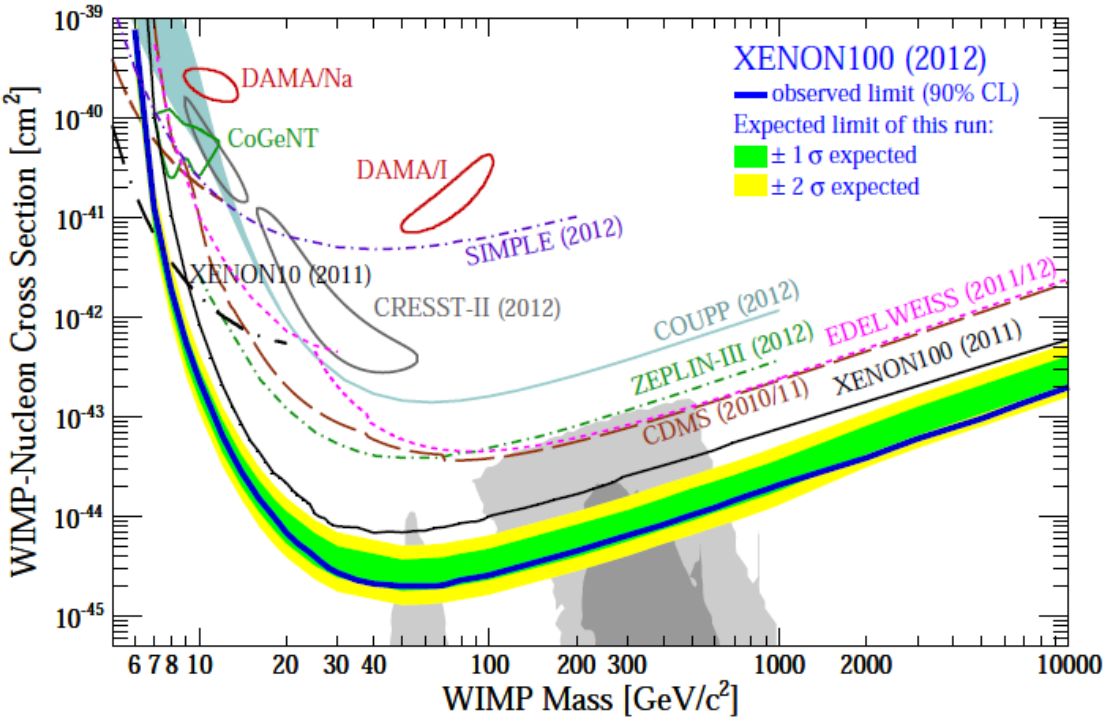

Figure 4.20: Result on SI WIMP-nucleon scattering from XENON100 [8]. The sensitivity is shown by the green/yellow band ($1\sigma/2\sigma$) and the resulting exclusion limit (90% CL) in blue. For comparison, other experimental limits (90% CL) and detection claims (2σ) are also shown together with the regions ($1\sigma/2\sigma$) preferred by supersymmetric (CMSSM) models [187].

vector structure function. In the limit of zero momentum transfer, the structure function reduces to the form:

$$S_A(0) = \frac{(2J+1)(J+1)}{\pi J}[a_p\langle S_p\rangle| + a_n\langle S_n\rangle|]^2, \tag{4.4}$$

where $\langle S_{p,n}\rangle = \langle J|\hat{S}_{p,n}|J\rangle$ are the expectation values of the total proton and neutron spin operators in the nucleus, and the effective WIMP couplings to protons and neutrons are defined in terms of the isoscalar $a_0 = a_p + a_n$ and isovector $a_1 = a_p - a_n$ couplings. Thus, WIMPs couple to the total angular momentum of nuclei and this means that only elements with an odd number of protons or neutrons have a significant sensitivity to this channel. For what concerns the xenon isotope abundance, in XENON100 there are 26.2% of ^{129}Xe and 21.8% of ^{131}Xe. In literature there are several calculations for the structure function S_A. The one used for the XENON100 limits [9] comes from the results of Menendez [188]. Considering the SD interactions, usually the results are given for $\sigma_{p/n}$: the cross section for the interaction with a single proton/neutron. Due to the

characteristics of ^{129}Xe and ^{131}Xe (even number of protons and odd number of neutrons) stronger limits are expected for σ_n (figure 4.21) than for σ_p (figure 4.22) since for both isotopes it results $|\langle S_p \rangle| \ll |\langle S_n \rangle|$.

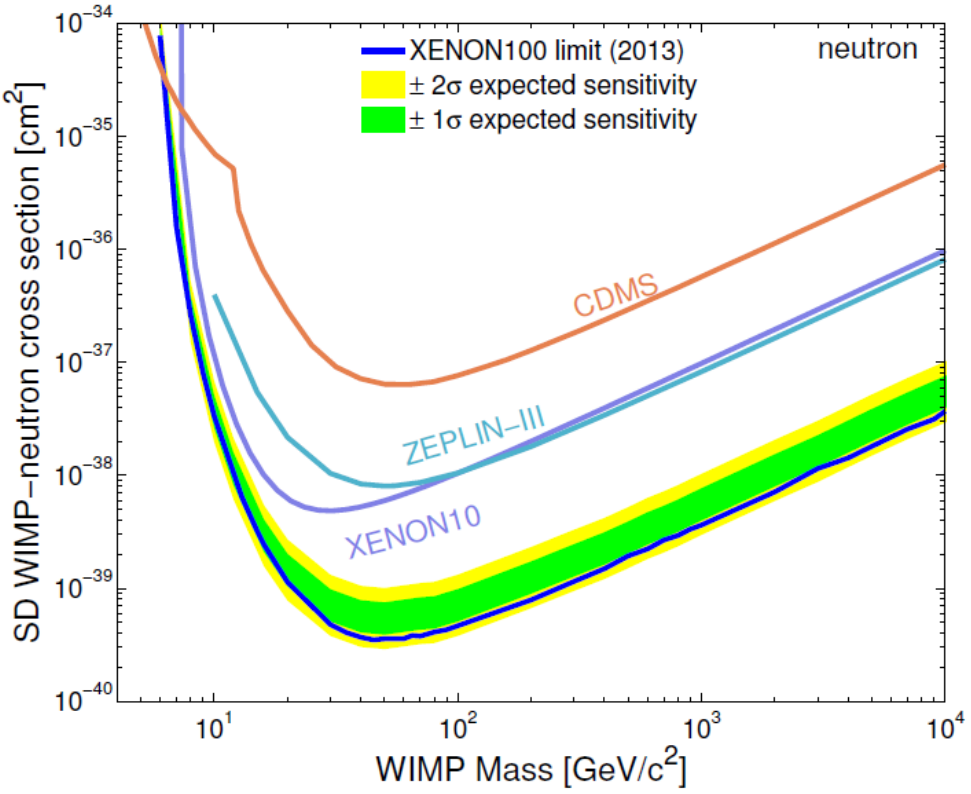

Figure 4.21: XENON100 90% CL upper limits on the WIMP SD cross section for interaction with neutrons [9] using Menendez [188]. The 1σ (2σ) uncertainty on the expected sensitivity is shown as a green (yellow) band. Also shown are results from XENON10 [176], CDMS [189], ZEPLIN-III [69].

Also for the SD analysis, as for the SI case, a Profile Likelihood approach has been used to evaluate cross section limits. The minimum WIMP-neutron cross section is $3.5 \cdot 10^{-40}$cm^2 at a WIMP mass of 45 GeV/c^2 [9] while, as explained, for WIMP-proton interactions the limits are weaker.

4.3.3 Solar axion and galactic ALP search results

The 224.6 live-days DM dataset has been used to search for solar axions and for non-relativistic galactic Axion Like Particles (ALPs) [37]. These particles can be detected through their different electromagnetic couplings with photons ($g_{A\gamma}$), electrons (g_{Ae}) and nuclei (g_{AN}). The g_{Ae} coupling can be tested using scatters off the electrons of the

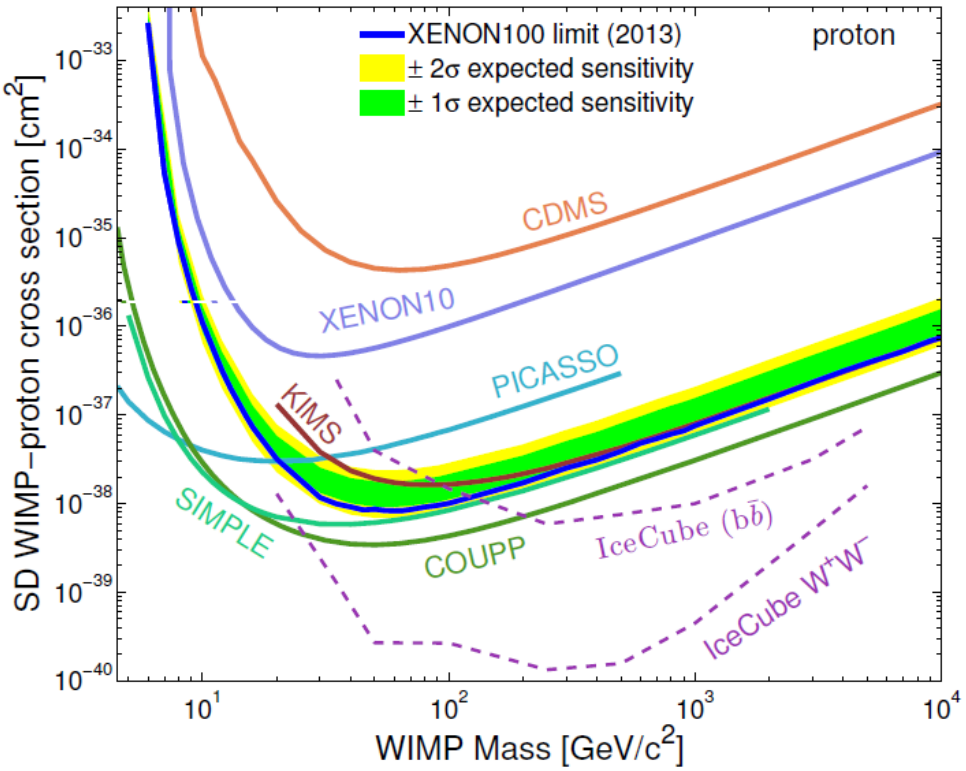

Figure 4.22: XENON100 90% CL upper limits on the WIMP SD cross section for interaction with protons [9] using Menendez [188]. The 1σ (2σ) uncertainty on the expected sensitivity is shown as a green (yellow) band. Also shown are results from XENON10 [176] (using Ressel and Dean [127]), CDMS [189], ZEPLIN-III [69] (using Toivanen et al. [190]), PICASSO [191], COUPP [192], SIMPLE [193], KIMS [194], IceCube [195].

Xe atoms through the axio-electric effect [196]. Thus, for this analysis, only the ER band has been considered after the application of all the quality cuts, figure 4.23, whose acceptance is shown in figure 4.24. The conversion from the energy deposition, E, to the observed signal in photoelectrons (pe), n^{exp}, is given by:

$$n^{exp}(E) = R(E) \cdot Q(E) \cdot f \cdot E \tag{4.5}$$

where $R(E)$ is scintillation efficiency relative to 32.1 keV$_{ee}$, $Q(E)$ is the quenching factor at non-zero field (measured at a field close to the one of XENON100) and $f = 3.76$ pe/keV$_{ee}$ is the derived XENON100 light yield at 31.2 keV$_{ee}$ and zero field [173]. The event rate with a given number of detected photons, n, is given by:

$$\frac{dR}{dn} = \int_0^\infty \frac{dR}{dE} \cdot \text{Poiss}(n|n^{exp}(E))dE \tag{4.6}$$

where dR/dE is the predicted spectrum and $n^{exp}(E)$ is defined in (4.5).

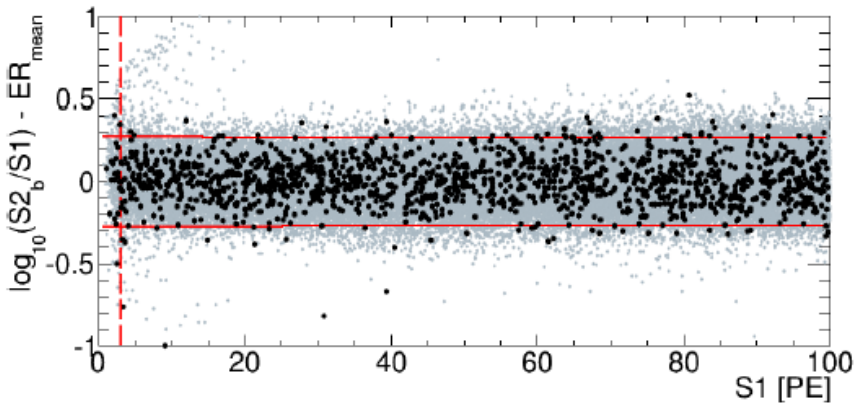

Figure 4.23: Events distributions for ER flattened band in $log_{10}(S2_b/S1)$ Vs $S1$ space. The black points are the observed events while the gray ones are the calibration events. The horizontal and vertical lines represent the applied cuts.

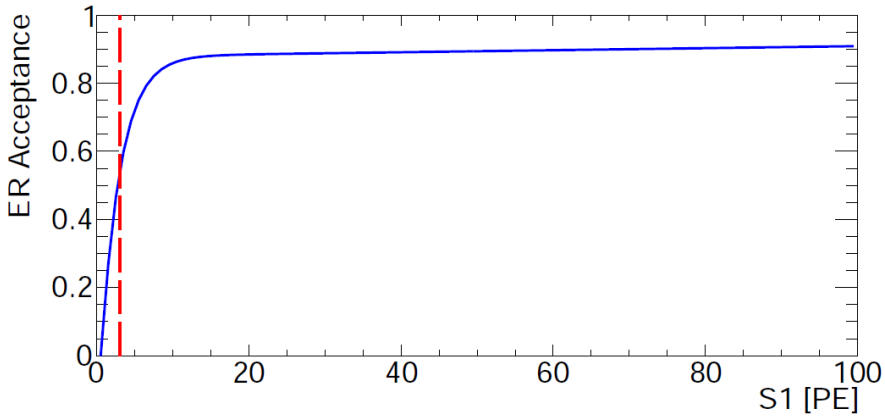

Figure 4.24: Combined cut acceptance for the Axions search analysis.

The background spectrum has been modeled on ^{60}C and ^{232}Th calibration data and scaled for the exposure time of the science data, figure 4.25. The survived events, after the application of the analysis cuts, are shown in figure 4.26. The axion search region has been considered between 3 and 30 pe. In figure 4.26, the solid gray line represents the background model (figure 4.25) while the black dots are the survived events. The blue dashed line is the expected solar axion spectrum assuming $m <$ 1 keV/c^2 for the axion mass and considering the available best limit on g_{Ae} from EDELWEISS-II [197] ($g_{Ae} = 2 \cdot 10^{-11}$). Since no excess of events have been observed, above the expected background, new limits on the g_{Ae} has been set (with a 90% CL), thus excluding values of the axion-electric couplings greater than $7.7 \cdot 10^{-12}$, figure 4.27 [37].

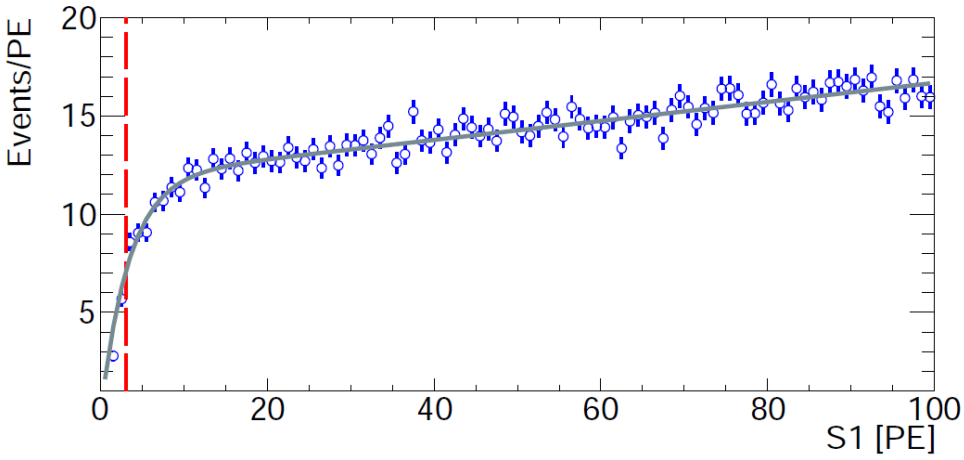

Figure 4.25: Background model (gray line), scaled to the correct exposure time. The model is based on the ^{60}Co and ^{232}Th calibration data (empty blue dots). The 3 pe threshold is indicated by the vertical red dashed line.

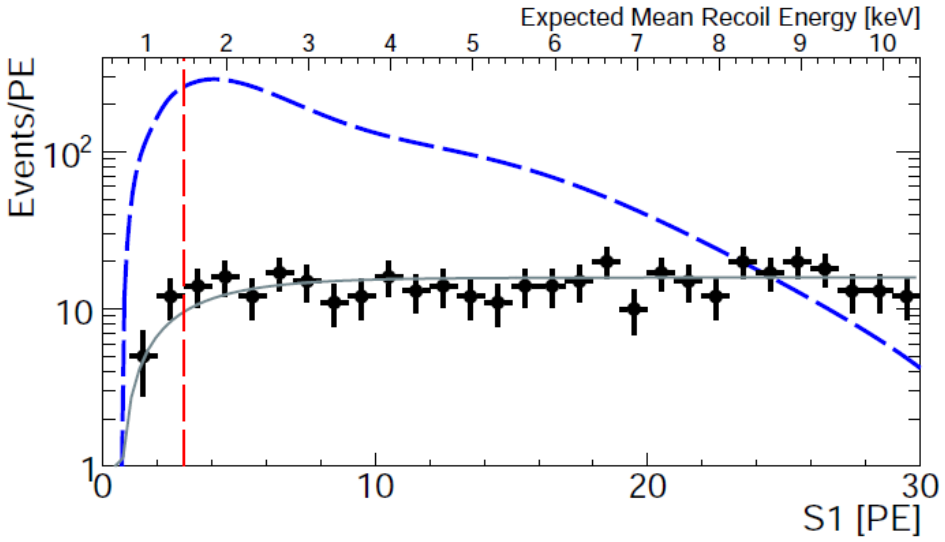

Figure 4.26: Expected Axion spectrum (blue dashed line) for $m <$ 1 keV/c^2 assuming $g_{Ae} = 2 \cdot 10^{-11}$. Also shown are: 3 pe S1 threshold (red dashed line), survived events (black dots) and background spectrum (gray line).

By translating this data into limits on the axion mass, they are excluded masses above 0.3 eV/c^2, DFSZ model [38], and above 80 eV/c^2, KSVZ model [39].
For what concerns the galactic axion-like particles (ALPs), the expected signal spectrum is shown in figure 4.28 assuming $g_{Ae} = 4 \cdot 10^{-12}$ and that ALPs constitute all the galactic dark matter.

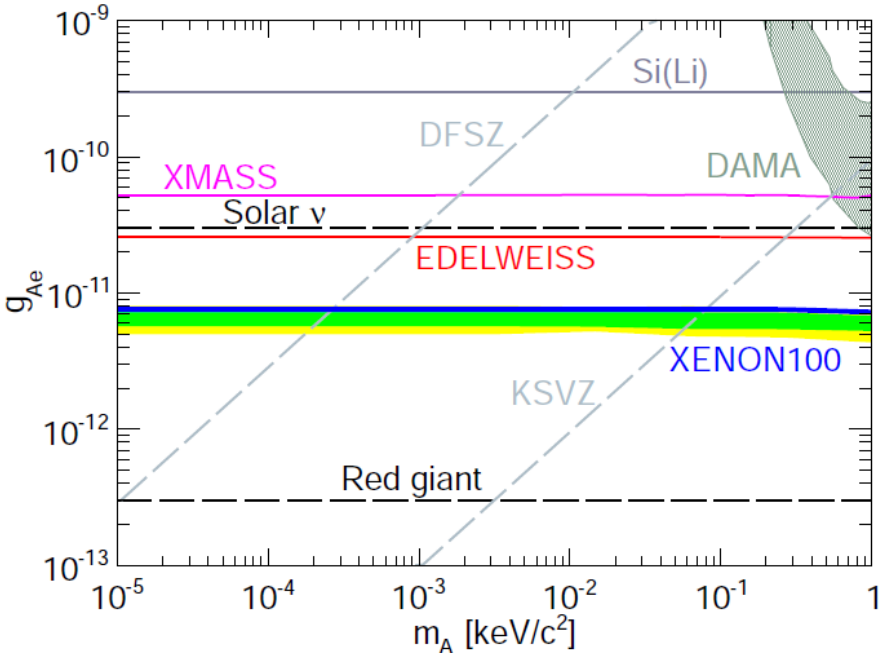

Figure 4.27: XENON100 limits (90% CL) on solar axions [37] (blue line). The expected sensitivity, based on the background hypothesis, is shown by the green/yellow bands ($1\sigma/2\sigma$). Limits by EDELWEISS-II [197], and XMASS [198] are shown, together with the limits from a Si(Li) [199]. Indirect astrophysical bounds from solar neutrinos [200] and red giants [201] are represented by dashed lines. The benchmark DFSZ [38] and KSVZ [39] models are represented by gray dashed lines .

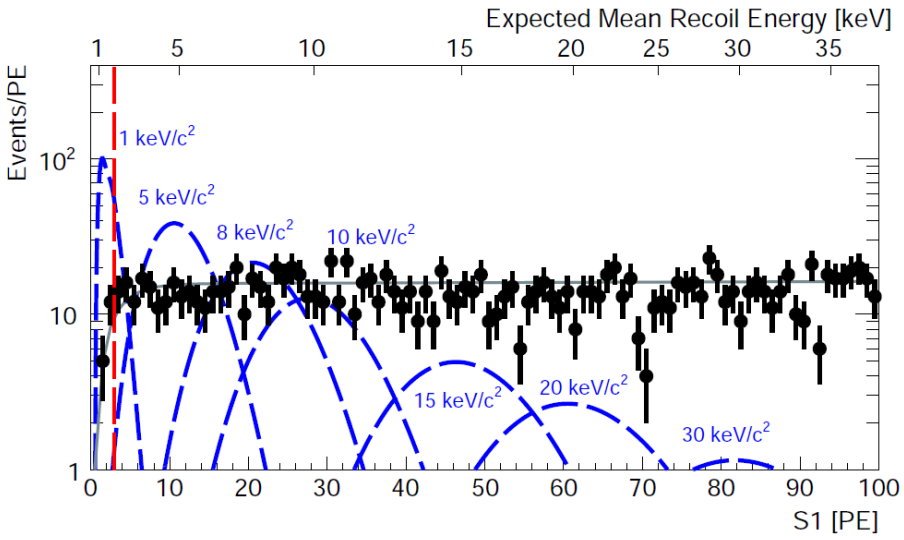

Figure 4.28: Event distribution in the galactic ALPs search region: [3, 100] pe (black dots). Also shown are: the background (gray), the S1 threshold (red dashed), the expected signal for various ALP masses, assuming $g_{Ae} = 4 \cdot 10^{-12}$, (blue dashed). The width of the mono-energetic signal is given by the energy resolution of the detector.

Also in this case, no excess of events, above the background, has been found. Thus, for ALPs with a mass in the range [5, 10] keV/c^2, XENON100 set the best upper limit excluding an axion-electron coupling $g_{Ae} > 1 \cdot 10^{-12}$ at the 90% CL [37]. The results are shown in figure 4.29, together with limits from other experiments and astrophysical bounds.

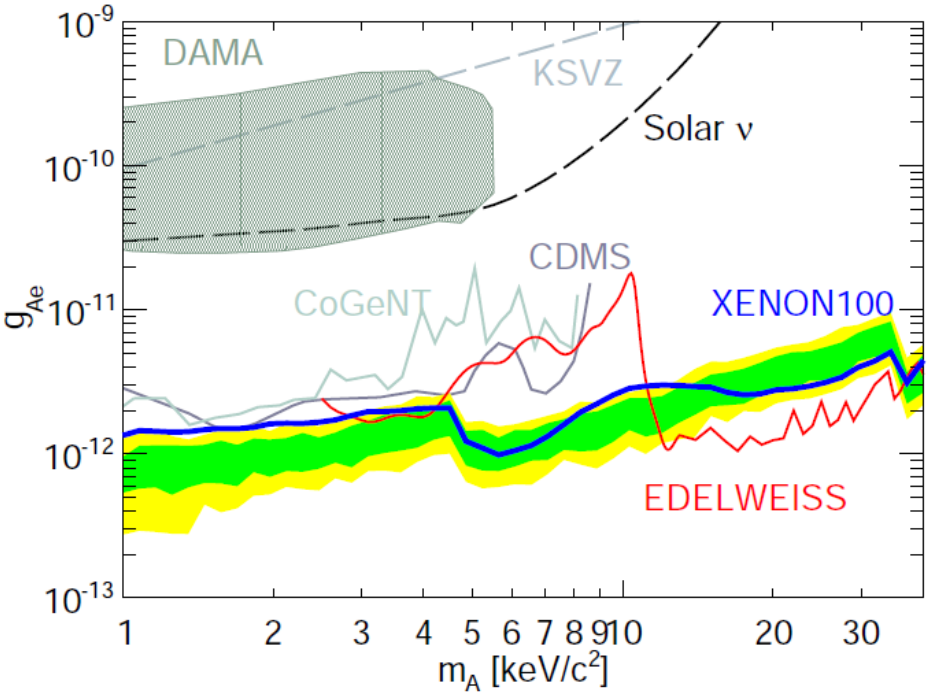

Figure 4.29: XENON100 limit (90% CL) on ALPs coupling to electrons as a function of the mass, under the assumption that ALPs constitute all the dark matter in our galaxy (blue line) [37]. The expected sensitivity is shown by the green/yellow bands ($1\sigma/2\sigma$). The contour area corresponds to a possible interpretation of the DAMA annual modulation signal as due to ALPs interactions, while the other curves are constraints set by CoGeNT (brown dashed line), CDMS (gray continuous line), and EDELWEISS-II (red line, extending up to 40 keV/c^2). Indirect astrophysical bound from solar neutrinos is represented as a dashed line. The benchmark KSVZ model is represented by a dashed gray line.

In figure 4.29, the steps in the sensitivity around 5 and 35 keV/c^2 reflect the photoelectric cross section due to the atomic energy levels. Below 5 keV/c^2 the obtained 90% CL is higher than expected deviating by as much as 2σ from the mean predicted sensitivity. This is due to a slight excess of events between 3 and 5 PE. A similar effect is responsible for the limit oscillating around the predicted sensitivity above 5 keV/c^2.

4.4 XENON1T design

XENON1T is the new detector of the XENON project and the first tonne-scale detector that will use double phase xenon as detection medium. It will be placed at the LNGS in the Hall B, figure 4.30 (top). The goal of the new detector is to improve the sensitivity to cross sections for dark matter interactions, down to $2 \cdot 10^{-47}$ cm^2, as shown in figure 4.30 (bottom).

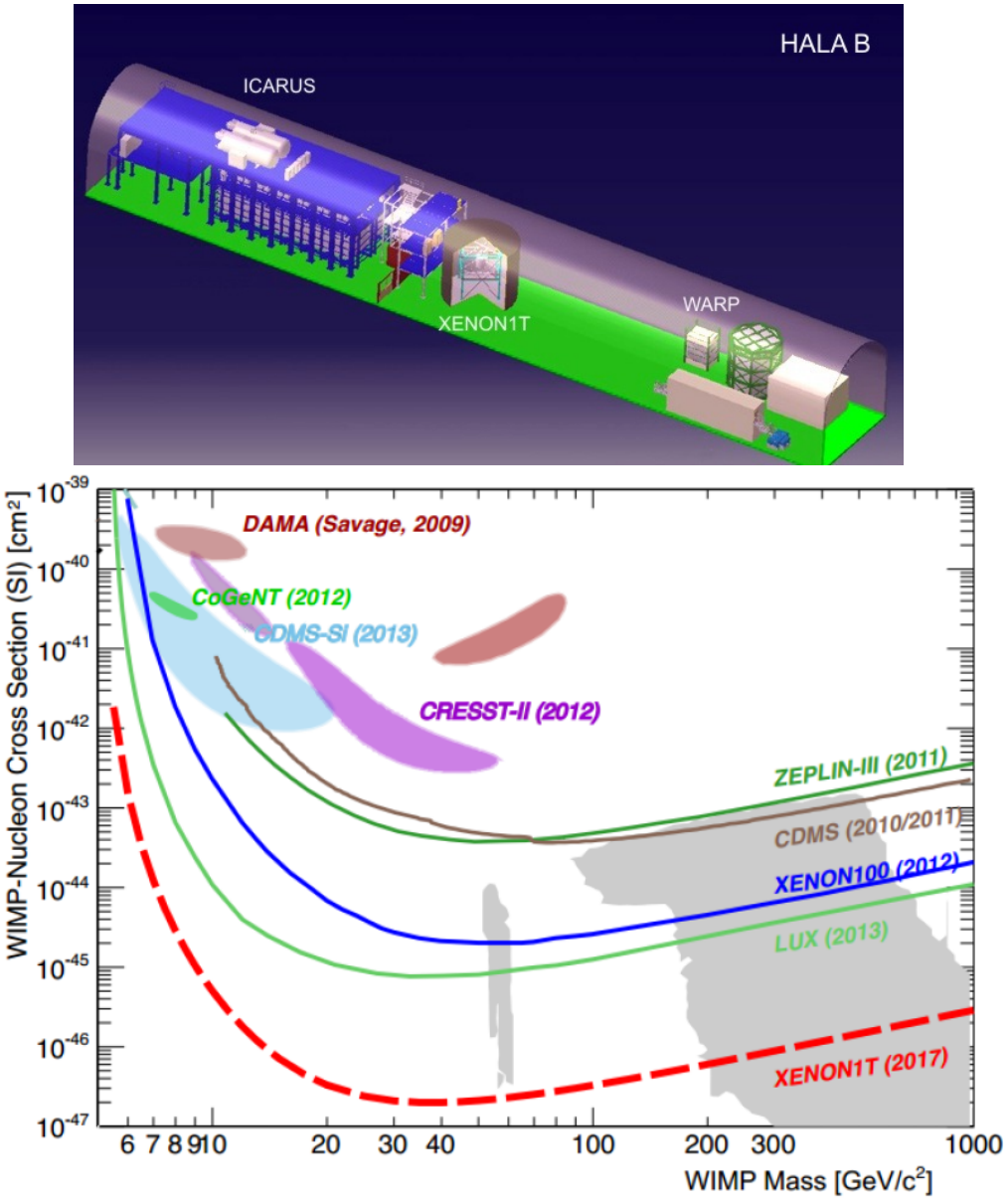

Figure 4.30: Top: HallB of the LNGS. Bottom: XENON1T expected sensitivity (red dashed line). As comparison are also shown limits from other experiments as LUX [10] and XENON100 [8].

To achieve such a result, it is mandatory to reduce the total background of at least two orders of magnitude with respect to XENON100. This can be done thanks to the size and characteristics of XENON1T and through the use of a water tank that will act as muon veto (Section 4.4.1). The detector will contain about 3 tonnes of LXe of which ∼2 will be used as sensitive volume. The sensitive volume will be enclosed in a TPC with a radius of 479 mm and a total height of about 967 mm. The details of the detector design, in particular the cryostats and the TPC, will be presented Chapter 5. Here I will briefly describe other ancillary systems, crucial for the experiment functioning and for the background reduction: the Muon Veto and the purification system.

4.4.1 Muon Veto design

At the depth of the LNGS, the flux of cosmic muons is $(3.31 \pm 0.03) \cdot 10^{-8} \mu$ cm^{-2}s^{-1} [202], with a mean energy of $\sim$ 270 GeV [203]. Such particles, together with their cascades, generated in the rock and concrete of the laboratory, can give both ER and NR backgrounds. The latter is more problematic since neutrons, produced in spallation processes on nuclei or in electromagnetic and hadronic showers, have an energy from 10 MeV up to tens of GeV and so they can penetrate even through large shields and mimic a WIMP-like signal. Due to this reason several efforts have been put in design a muon veto system that can tag and reject those events as background.
The Muon Veto for the XENON1T detector is made of a water tank with a cylindrical shape body, 4.8 m of radius and 9 m height, plus a truncated cone shape roof, for a total height of 10.5 m, that will be filled with water, figure 4.31. The Muon Veto system is based on the detection of the Cherenkov light emitted by particles that pass through the water. The light is seen by 84 PMTs (8" in diameter), model Hamamatsu R5912ASSY, whose quantum efficiency in the range [300, 600] nm is about 30%. The PMTs are arranged in two rings, one on top at 9 m from ground and one on the bottom of the water tank, each of which count 24 photomultipliers, and 4 equally spaced rings of 12 PMTs each, along the vertical wall of the tank. The detector will be placed at the center of the structure, figure 4.32, thus resulting surrounded by an equal thickness water layer in all directions. The inner surface of the water tank will be covered by a reflective foil, DF2000MA, which has a reflective efficiency close to 100% between 400 and 600 nm wavelengths. It acts also as a wavelength-shifter to better overlap the Cherenkov light spectrum with the high quantum efficiency region of the PMTs. To trigger a veto event there are two requirements that have to be satisfied: one regards the threshold, i.e. the level of the signal has to overcome a defined threshold, and another one concerning the length above the threshold, i.e. the signal has to stay above the threshold for a specific

amount of time.

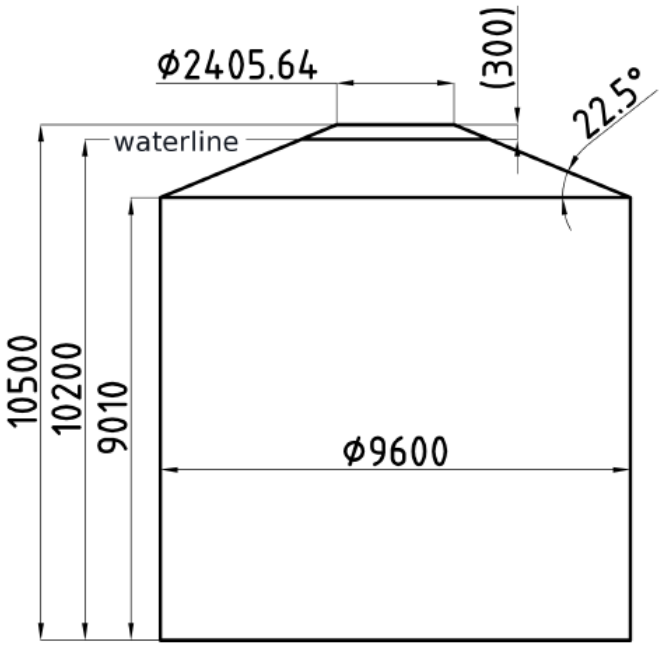

Figure 4.31: Schematic view of the XENON1T Muon Veto water tank.

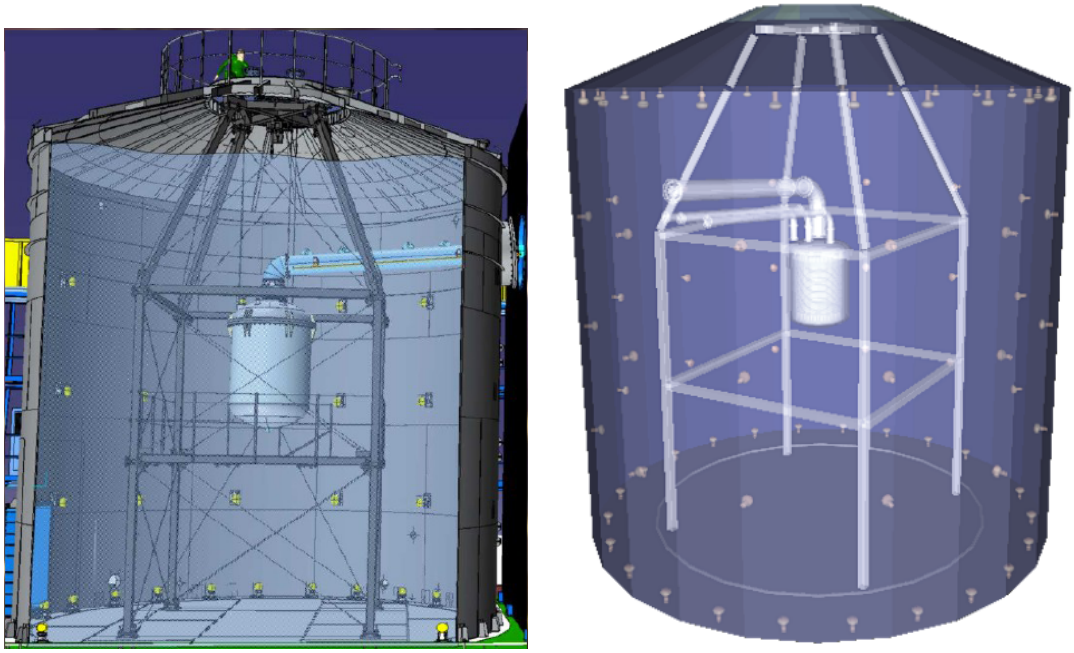

Figure 4.32: Left, design of the Muon Veto with the detector and its support structure at the center of the water tank. Right, MC simulation of the Muon Veto design [204].

To evaluate the trigger rate due to muon events, it is also necessary to consider the PMT dark counting rate and the flux of particles from radioactive decay of rock and concrete that surround the experiment. It is possible to reduce these contributions using a N-fold PMT coincidence, in a certain time window, with a certain threshold. After several MC simulations [204] it was established that using a 5-fold coincidence in 300 ns, a rate lower than 1 Hz can be reached, still having high efficiency in detecting single photoelectrons. Monte Carlo simulations determined that the efficiency of the Muon Veto, with respect to the muon-induced events, is 99.78% for events directly from muons and 72.2% for shower-induced events. The residual muon-induced neutron background, in XENON1T, is < 0.01 ev/y in 1 tonne FV, i.e. practically negligible. In figure 4.33 is shown the current status of the XENON1T Muon Veto water tank.

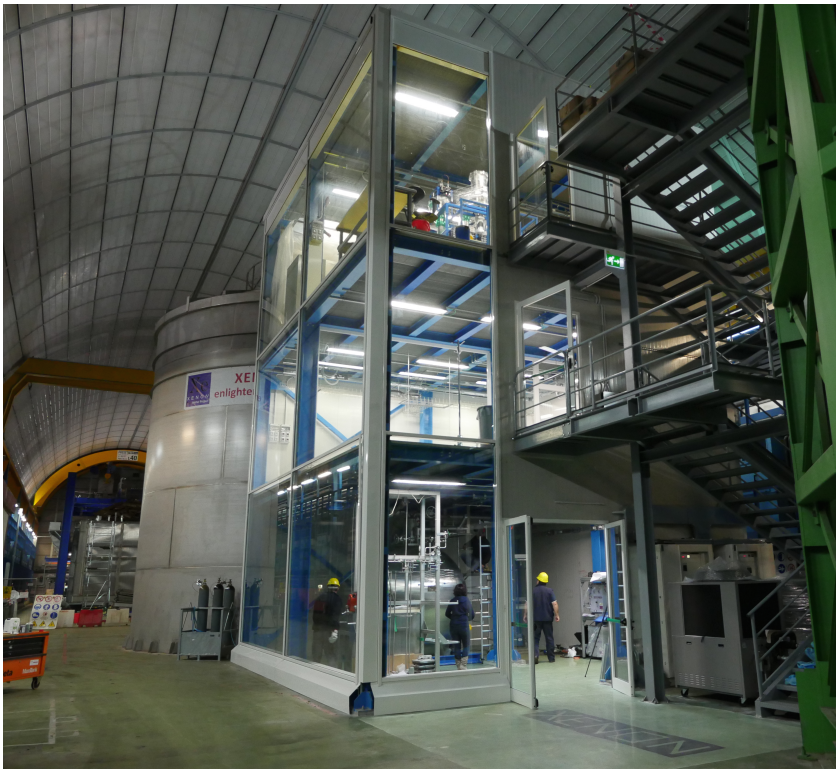

Figure 4.33: Photo of the XENON1T Muon Veto water tank and of the service building in the hall B at the LNGS.

4.4.2 LXe purification system

One of the most important goals for a dark matter experiment is to lower the background as much as possible. Indeed, it is important to place the detectors in a very low radioactive environment, use very low contaminated materials and veto techniques, but

this is not all what is possible to do. There is another important source of background called *intrinsic background* (Section 6.4), to which contribute the impurities naturally contained in the Xe, that requires proper techniques to be lowered. The most dangerous contaminations are ^{85}Kr (Section 6.4.1) and ^{222}Rn (Section 6.4.2). Since those impurities are uniformly distributed inside LXe, it is not possible to reduce their background using volume selection cuts. In this case LXe has to be purified. In order to have a sub-dominant contribution to the total background from the intrinsic one, the ^{85}Kr concentration has to be below 1 ppt. The xenon can be purified from ^{85}Kr using a distillation column, figure 4.34, that will exploit the different boiling temperature of this contaminant (120 K at 1 atm) and of the xenon (165 K at 1 atm).

Figure 4.34: XENON1T Kr distillation column (under construction).

The ^{222}Rn emanated from several sources in the detector is planning to be removed through a Mobile Radon Extraction Unit (MoREx) [205]. This contaminant, due to its long half life, can uniformly be distributed in the LXe volume. For the purpose of the XENON1T detector, the total ^{222}Rn activity has to be lower than 3 mBq, that corresponds to about 1 μBq/kg. Since the drift length is very large, about 97 cm (it is the TPC height), it is also important to have a very low level of electronegative impurities,

such as O_2 and H_2O, because they can absorb both electrons and the scintillation light (Section 3.4.3). In order to guarantee stable operation properties, the contamination of these elements has to stay below 1 part per billion (ppb) O_2 equivalent. The problem is that the strong Van Der Waals interactions of the xenon with the detector materials will extract such impurities from the detector materials, raising their concentration. To keep their concentration as low as possible, a continuous Xe gas circulation system and low outgassing materials, based on a high temperature metal getter (SAES), will be used (figure 4.35).

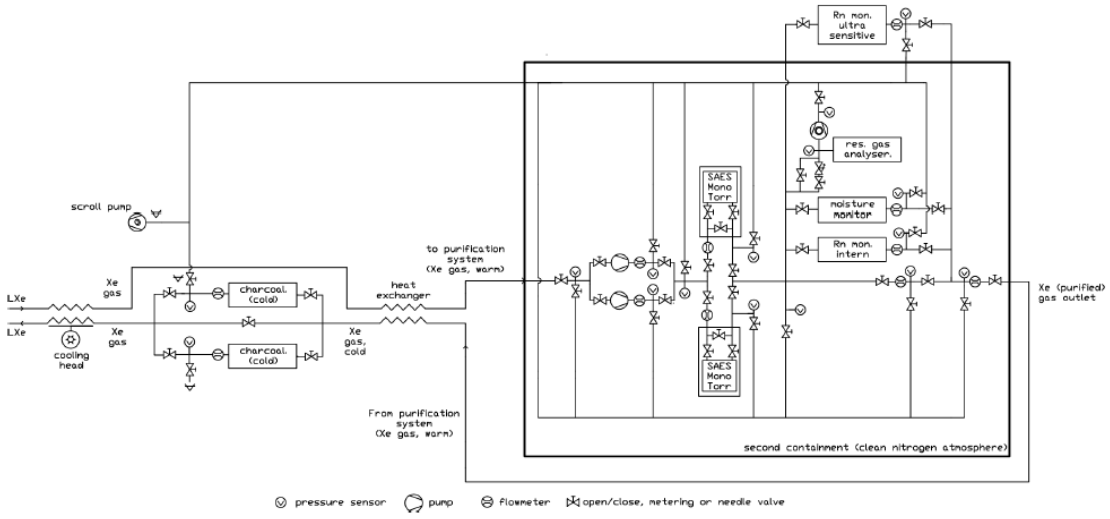

Figure 4.35: Schematic view of the XENON1T gas purification system.

4.5 XENON1T upgrade: XENONnT

The XENON project will then continue with its last phase: XENONnT. For this new generation detector, most of XENON1T systems will be used. For example, as it will be described in the next chapter, the XENON1T outer vessel is already realized to host this new detector that will increase the total amount of LXe to 7 tonnes, figure 4.36. XENONnT will require a larger TPC and more PMTs, 217 instead of 127 in the top array and 211 instead of 121 in the bottom one, than XENON1T. The foreseen sensitivity is about $3 \cdot 10^{-48}$ cm^2. About one order of magnitude below such a value, the neutrino coherent scattering becomes an irreducible background, figure 4.37. The NR from such process can mimic WIMP interactions, thus setting a limit on the sensitivity that detectors can reach. The only chance to go towards stronger limits will be to use new detection strategies such as, for example, directional ones.

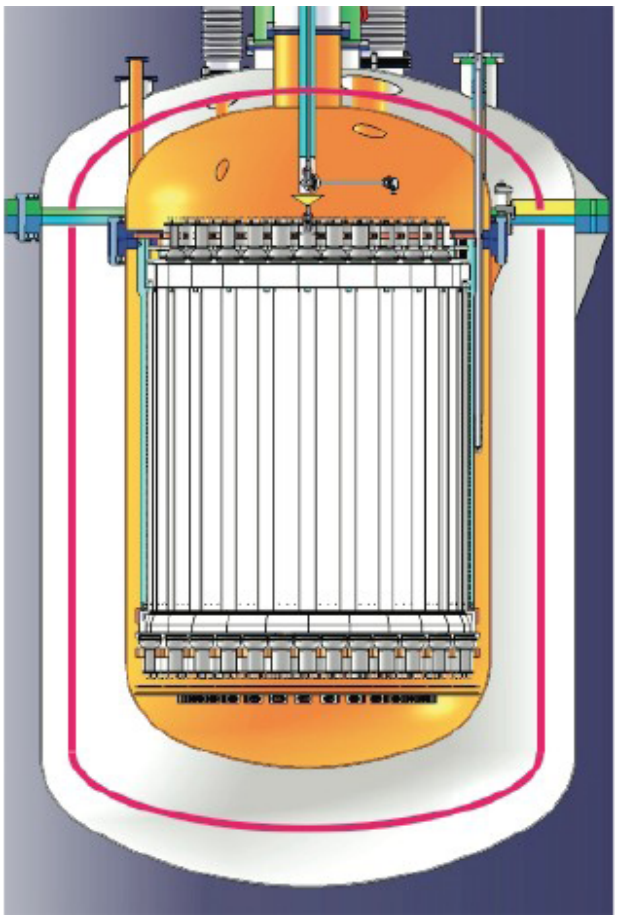

Figure 4.36: XENONnT outer and inner (red line) cryostats. The outer vessel will be the XENON1T one. Inside the cryostats, the XENON1T field cage is also shown.

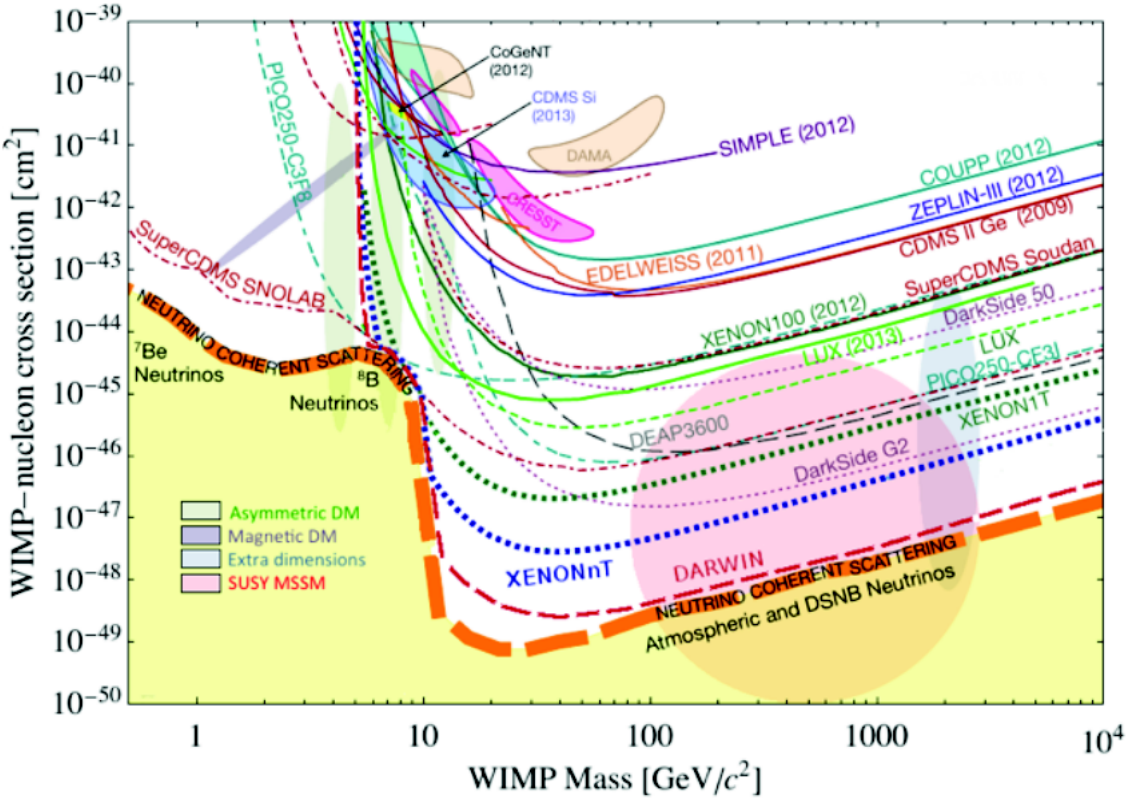

Figure 4.37: XENONnT sensitivity (blue dotted line) compared with the XENON1T expected one (green dotted line) and with the results from XENON100 225 live-days run [8] and from LUX [10]. Also shown are limits from other experiments and the neutrino coherent scattering bound (solid dashed orange line) that represents an irreducible source for the NR background.

Chapter 5

XENON1T Monte Carlo geometry simulation

The analysis of the design and materials chosen for the construction of a detector is essential to guarantee the achievement of an experiment purposes. A detailed Monte Carlo (MC) simulation is, hence, mandatory. This allows the analysis of some fundamental quantities such as, for example, the expected background from radioactive isotope contaminations of the detector materials. In this chapter the full MC simulation of the XENON1T detector geometry is described, with the aim of quantifying the internal and intrinsic backgrounds (Chapter 6) with the final goal of extrapolating the achievable sensitivity of the experiment as function of the WIMP mass (Chapter 7). The whole simulation has been realized with the GEANT4 toolkit, version 9.5.p01. The implemented geometry reproduces the CAD drawings of each component of the detector with very high accuracy. The accuracy of the simulation is verified by comparing the images of several components from the CAD drawings with the ones obtained by means of the simulation. In particular, the images from the simulation are done by using a proper software, Meshlab, or *geantinos* (fictitious particles used in GEANT4 to check the geometries).

5.1 Cryostats

Following the same work principles of XENON10 and XENON100, also in XENON1T the outermost part of the detector consists of a double vessel structure, figure 5.1. It will host about 3 tonnes of LXe 2 of which, called the *active volume*, will be enclosed in the field cage of the detector to constitute "the heart of the detector". Between the two vessels, named *Inner Cryostat* and *Outer Cryostat*, there is a vacuum jacket that

guarantees thermal isolation of LXe, during the detector operations, from the external environment. The two cryostats share the same geometry structure but with different dimensions: a central cylindrical body with two domes, one on the top and one on the bottom.

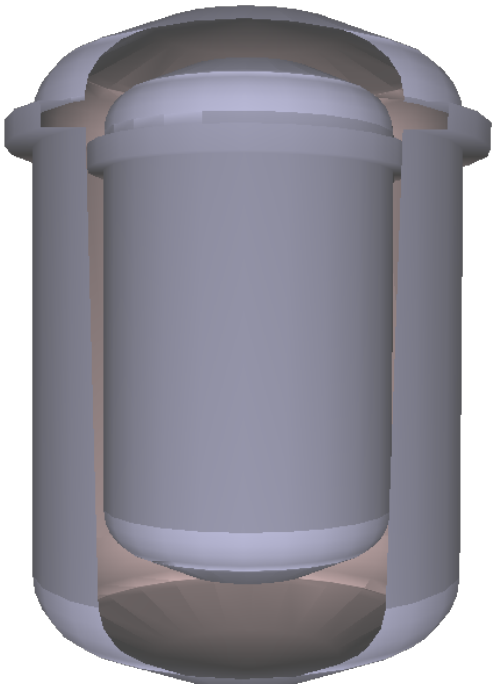

Figure 5.1: Inner and Outer cryostat geometries implemented in the simulation. Image from the GEANT4 code (Meshlab).

They are made of low radioactive stainless steel (SS) and their whole structure has a uniform thickness of 5 mm. In the MC code the two domes have been implemented as a union of two solids: a sphere and a torus. The cylindrical body of the inner cryostat has an outer diameter of 1110 mm and height of 1420 mm. The top and bottom domes have a bending outer radius of 893 mm. The outer cryostat is of greater size: the outer diameter of the central body is 1630 mm and the height is 1687 mm. Also in this case, both the top and bottom domes have the same bending outer radius equal to 1309 mm. For both cryostats, the bottom domes are directly connected to the cylindrical bodies while the top ones are attached through flanges, figures 5.2 and 5.3. Compared to figure 5.2, in figure 5.3 are absent the cryostats holes for the pipes connections, see later. This is due to some simplifications in the visualization software. While the size of the inner vessel are optimized for the current detector design, the dimensions of the outer vessel are such that it will be able to host also the upgrade XENONnT, Section 4.5. The flanges of both vessels are 90 mm height but they have different radial thickness: it is

100 mm for the outer cryostat and 62.5 mm for the inner one. The flanges have been implemented as rings with a rectangular section directly connected to the cryostat shells, on top of the cylindrical body.

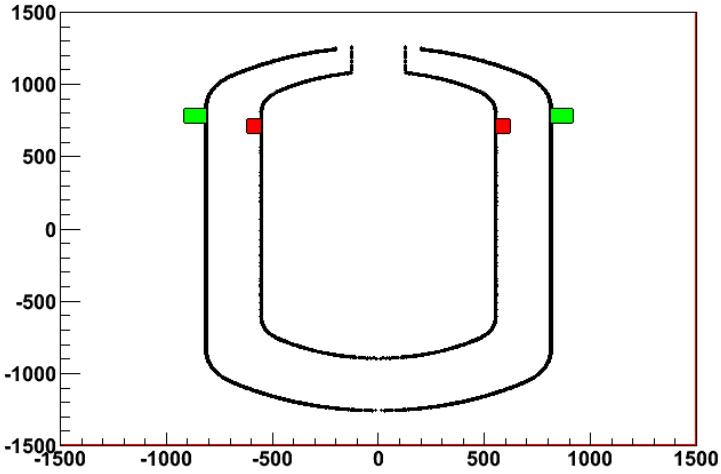

Figure 5.2: Frontal section of Inner and Outer cryostats (black), inner cryostat flange (red) and outer cryostat flange (green), as implemented in the simulation. Image done by using geantinos from the GEANT4 simulation code.

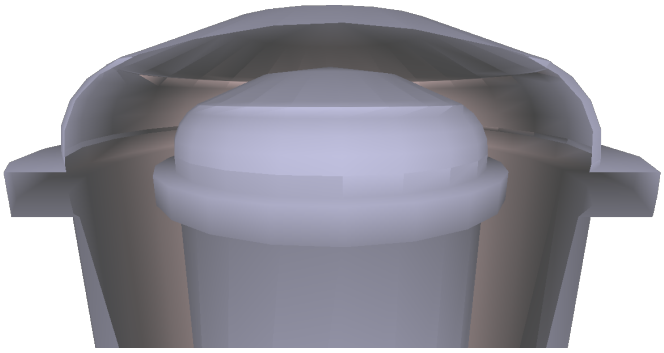

Figure 5.3: Frontal view of the inner and outer cryostat flange geometries implemented in the simulation. Image from the GEANT4 code (Meshlab).

In the real CAD drawings the flanges are divided into two parts, along the vertical coordinate. The top part is connected to the top domes of the cryostats while the bottom part is attached to the cylindrical bodies. The structural characteristics of cryostats shells and flanges are reported in table 5.1. On the surfaces of the top domes, there are few holes that allow the connection between the internal components of the detector and proper pipes for HV supply, monitoring, etc., figures 5.4 - 5.6.

Component	material	weight (kg)	height (mm)	thickness (mm)
Inner cryostat shell	SS316Ti	300.7	1987	5
Inner cryostat flange	SS316Ti	165.8	90	62.5
Outer cryostat shell	SS316Ti	569.4	2518	5
Outer cryostat flange	SS316Ti	391.3	90	100

Table 5.1: Summary of the main structural characteristics of the two cryostats.

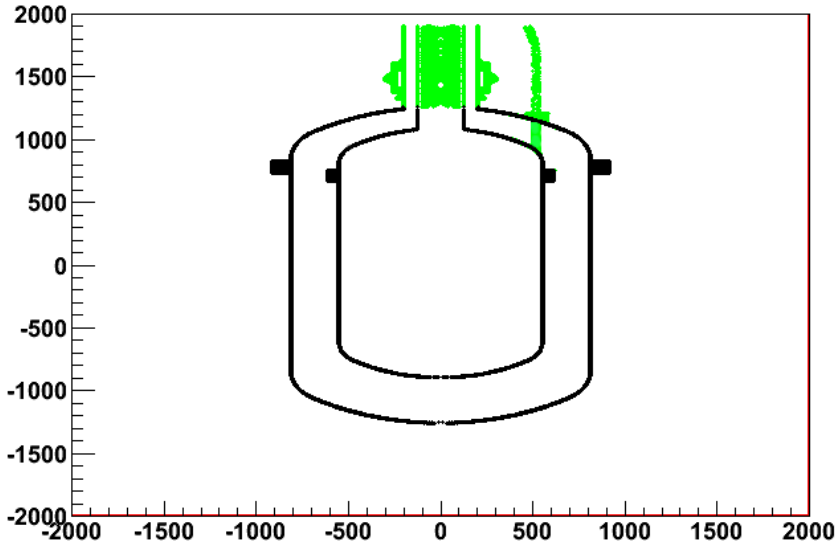

Figure 5.4: GEANT4 implementation of the pipes; image made by using geantinos.

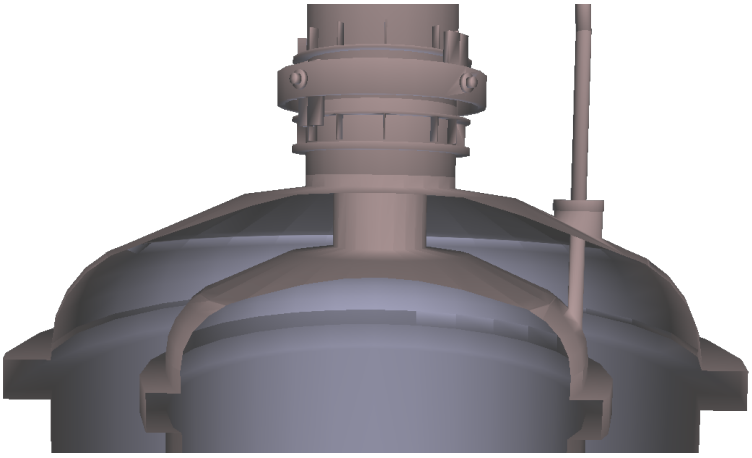

Figure 5.5: GEANT4 implementation of the pipes; image from Meshlab.

Those pipes have different dimensions: there is a smaller one, that contains all the connections for the HV feedthroughs, and a bigger central one that contains smaller

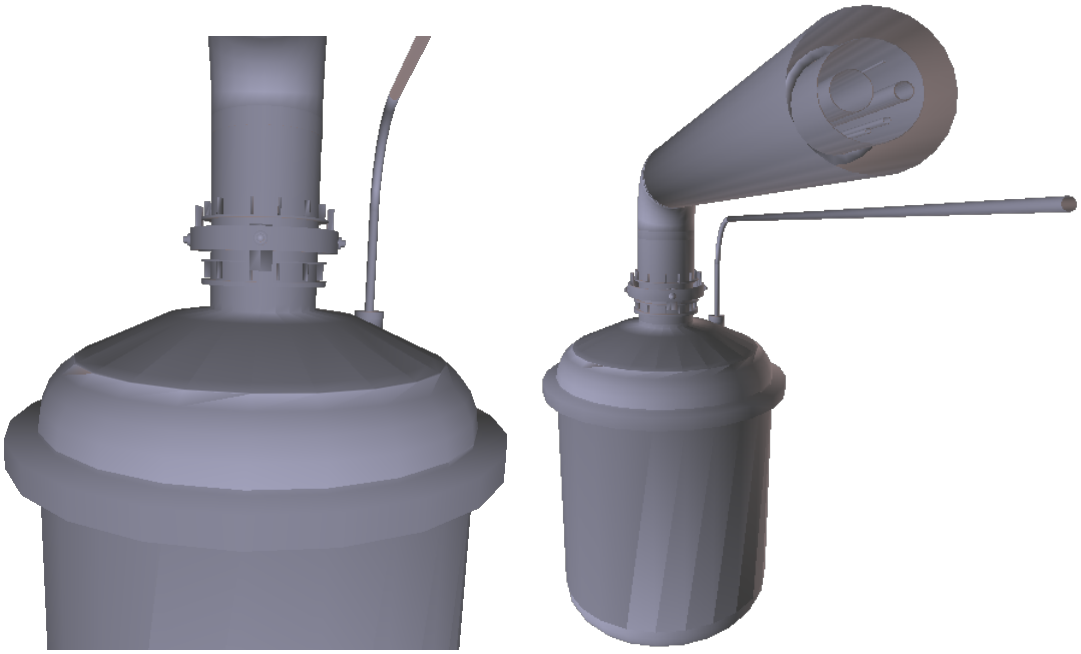

Figure 5.6: GEANT4 implementation of the pipes. Both images have been done by using the Meshlab software.

pipes for the gas recirculation and for signal and PMTs HV supply cables. Also the pipes are made of SS; they are under vacuum which also in this case is used as insulator from the external environment temperature.

5.2 Field cage

The double phase Time Projection Chamber (TPC, Section 4.1) is the most important element in the XENON1T detector because it will host the active LXe volume, about 2 tonnes, that is the target volume for the WIMP search. Due to its role, the TPC has been designed in order to maximize the chance to detect a dark matter interaction with a target nucleus. This requires, for example, a light tight region and good reflective properties. To satisfy the requirement of a light tight chamber, the TPC has been designed as made of 24 interlocking polytetrafluoroethylene (PTFE) panels, 5 mm thick, in an almost cylindrical shape, figure 5.7. The interlocking structure will avoid to lose light through the panels after the shrinkage that is, at LXe temperature, about 1.5%. In order to speed up the MC simulation, the geometry of the TPC has been implemented as a 5 mm thick PTFE empty cylinder, figure 5.8, with a radius of 479 mm and a total height of about 967 mm, with both quotes considered after the shrinkage. For the background estimation, this simplification causes no variation with respect to the real

case.

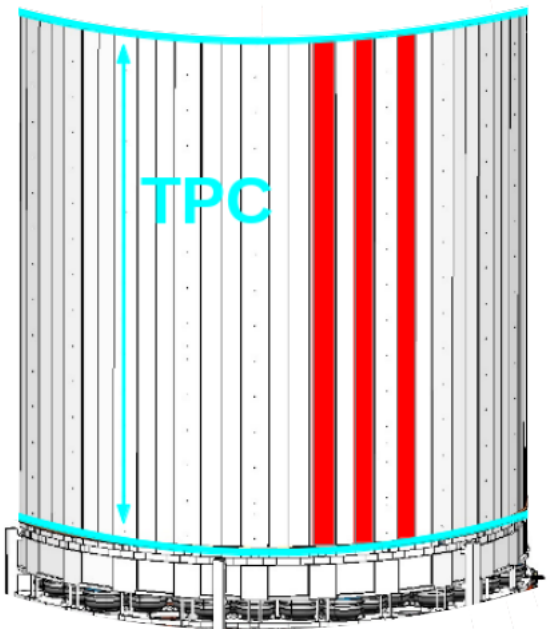

Figure 5.7: Interlocking PTFE panels of the TPC (white, enclosed in the cyan curves). Few panels have been emphasized in red. Image from the CAD drawings.

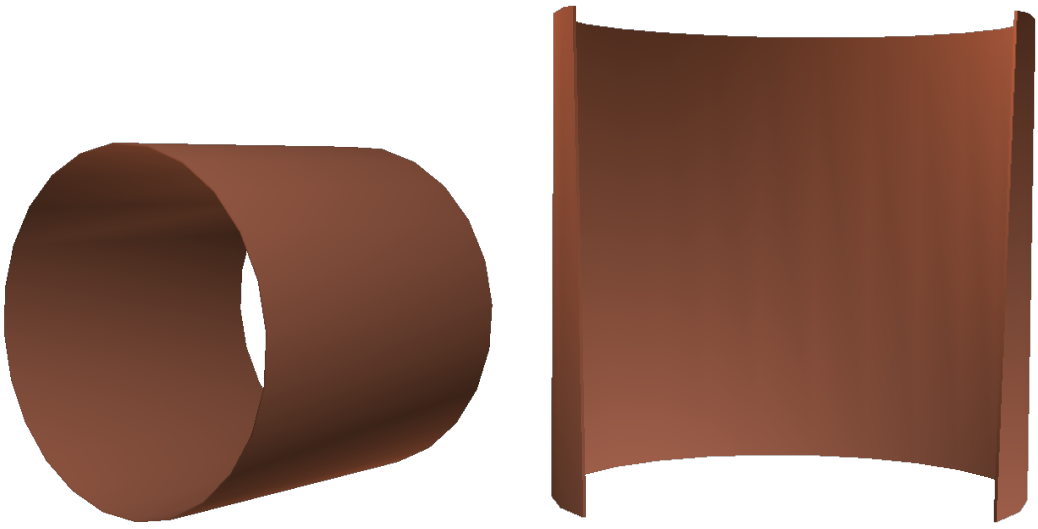

Figure 5.8: PTFE walls of the TPC as implemented in the simulation. Image done by using Meshlab from the GEANT4 simulation code.

In XENON1T the 2 tonnes of active volume will be enclosed laterally by PTFE walls and on top and bottom by the gate mesh and the cathode. This structure defines the drift region that is the region available for the drift of the charge carriers (electrons).

In order to drift these particles, an electric field is needed and so the cathode and gate mesh will be set at a proper tension. The former will be biased up to −100 kV while the latter will be grounded. The voltages will generate the electric drift field which will move the electrons towards the LXe/GXe interface, where they will be extracted into the GXe region by means of the extraction electric field. One of the most important requirements for the electric drift field is the uniformity along the whole drift region. In this way there will be no signal dependencies from the position inside the active volume. The uniformity of the drift field is reached through the use of the so called *field shaping rings*. These are 74 thin copper rings that are placed in contact with the external TPC walls and are equally spaced along the vertical axis. With this configuration, the copper rings will cover the whole vertical distance between the cathode and the gate mesh, i.e. the total available drift path. The rings are connected between them, the cathode and the gate mesh through a resistor chain. In this way they will automatically set themselves at the right tension giving a uniform drift field. The intensity of the electric field will be chosen in the commissioning phase of the experiment, from hundreds of V/cm up to 1 kV/cm. The copper rings have been implemented merging a central ring of square section, 5×5 mm^2, with two toroidal rings, one on top and one on bottom of the central ring, having a bending radius equal to half of the central ring side, figure 5.9. The total height of each ring is then 10 mm.

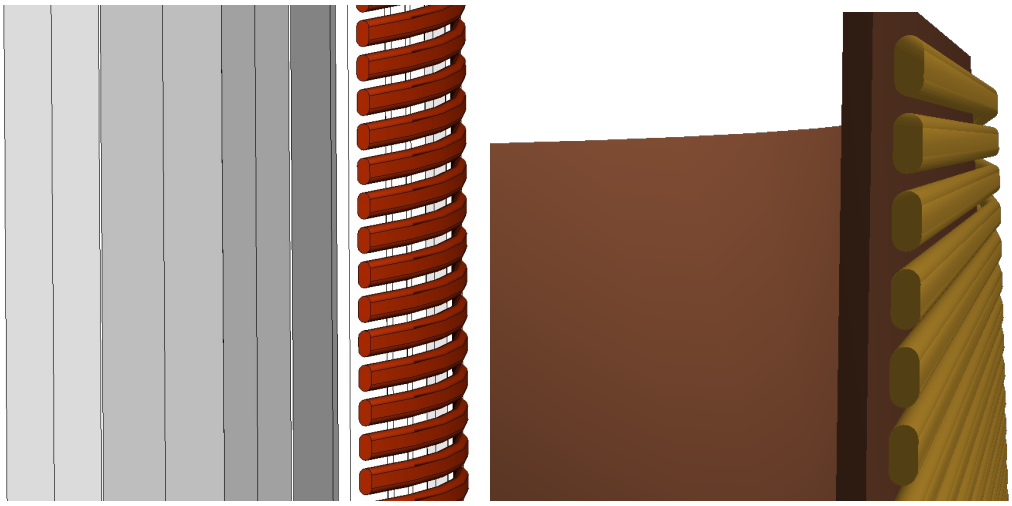

Figure 5.9: PTFE wall of the TPC with the copper rings around it. Left, copper rings (brown), TPC (white/gray); image from CAD drawings. Right, copper rings (dark yellow) and PTFE wall of the TPC (brown) as implemented in the simulation; image from the GEANT4 code (Meshlab).

To sustain the whole field cage structure (TPC PTFE walls plus field shaping rings)

24 PTFE pillars have been designed and implemented in the simulation, figure 5.10.

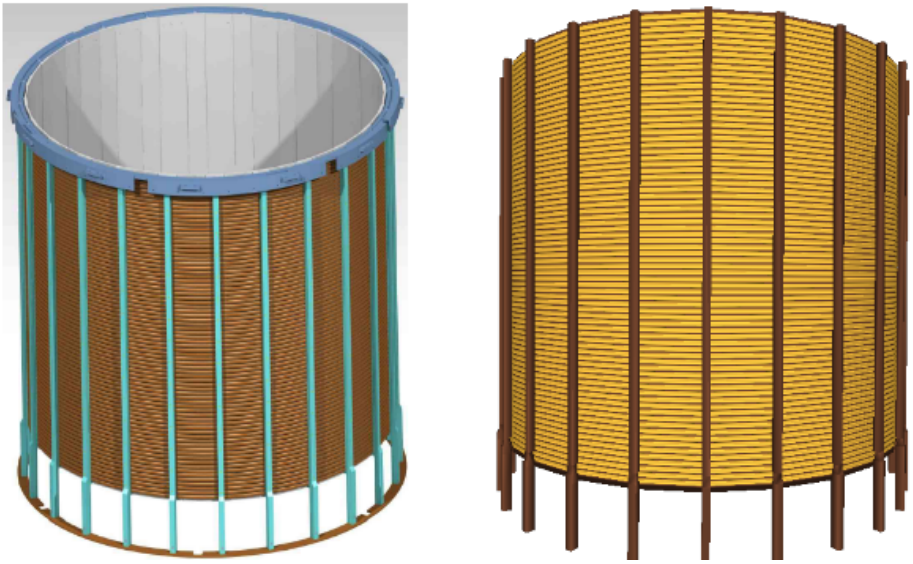

Figure 5.10: External view of the field cage with copper rings and PTFE pillars. Left, copper field shaping rings (brown) and PTFE pillars (cyan); image from CAD. Right, copper field shaping ring (yellow) and PTFE pillar (brown); image from Meshlab.

The pillars have been implemented as sum of several solids as parallelepipeds, trapezes, etc., and they are made of PTFE, figure 5.11.

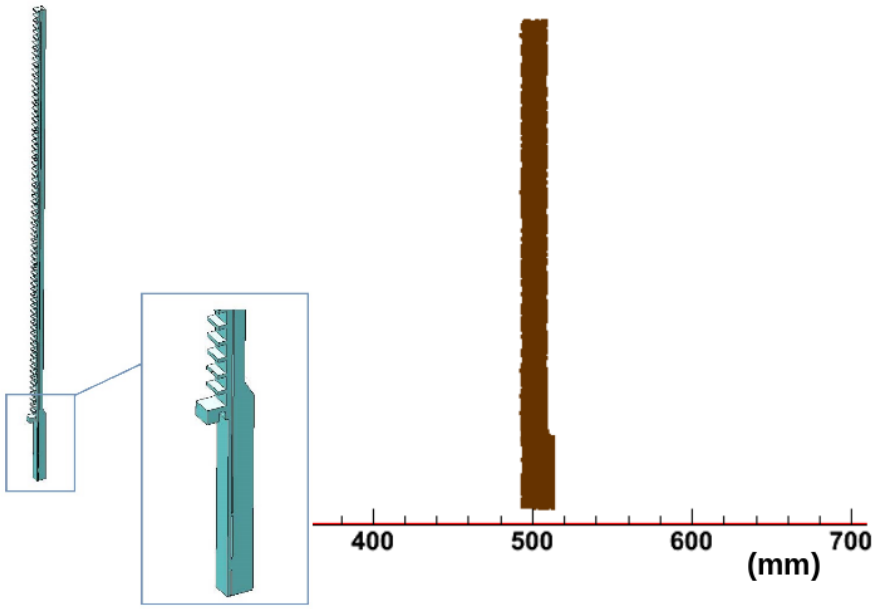

Figure 5.11: PTFE pillar structure. Left, image from the CAD drawings. Right, implementation in the simulation code; image from GEANT4 (geantinos).

To sustain the copper rings, the pillars are equipped with "teeth", left side in figure 5.11. However, in the MC implementation the teeth structure is absent. The reason is that in order to implement a solid with such elements, the "*G4SubtractionSolid*" or "*G4UnionSolid*" routine are mandatory but, due to the number of required subtractions or unions, we had several problems with the boolean operator. Since, between the two cases there are negligible differences, especially for what concern the mass, that is one of the main characteristics for the background estimation, the teeth were removed from the GEANT4 code. The pillars are placed on a copper ring on which they are distributed isotropically all around the PTFE walls, each one rotated by a 15^o angle with respect to the previous one, figure 5.12.

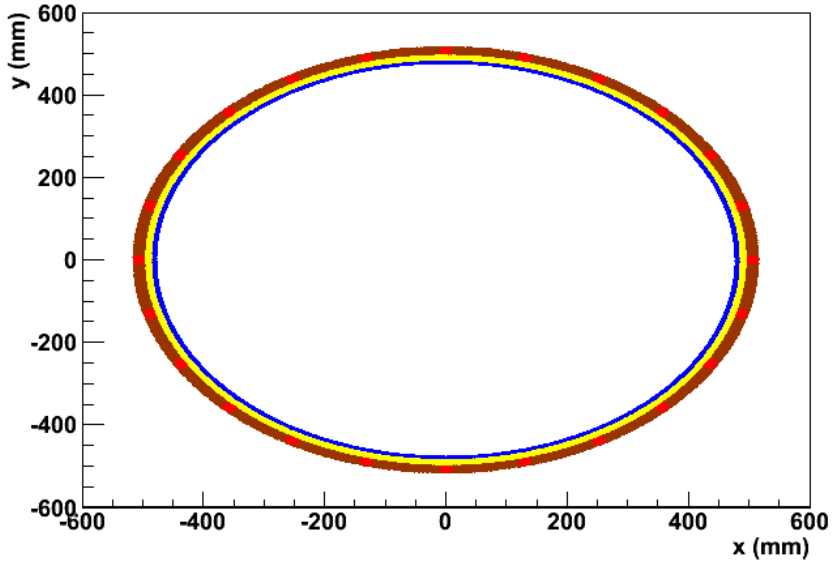

Figure 5.12: Top view of the implemented geometry of the field cage structure: PTFE walls (blue), field shaping rings (yellow), PTFE pillars (red), copper ring to sustain pillars (brown). Image from the GEANT4 code (geantinos).

The support ring of the pillars has been implemented as a rectangular section ring with a inner radius of 494 mm, a thickness of 20 mm and 5 mm height, figure 5.13. As said, the drift region is closed, on the bottom, by the cathode. Just below it there is a PTFE ring that follows the shape, with same radius and thickness, of the TPC walls. The PTFE ring acts as reflector for the UV light that doesn't hit the light sensor directly and connects the active region with the bottom PMT structure (Section 5.4), figure 5.14. Using this ring, the active region will be totally light tight on the bottom. It has been designed as made of 24 short panels, 69.1 mm height and 5 mm thick

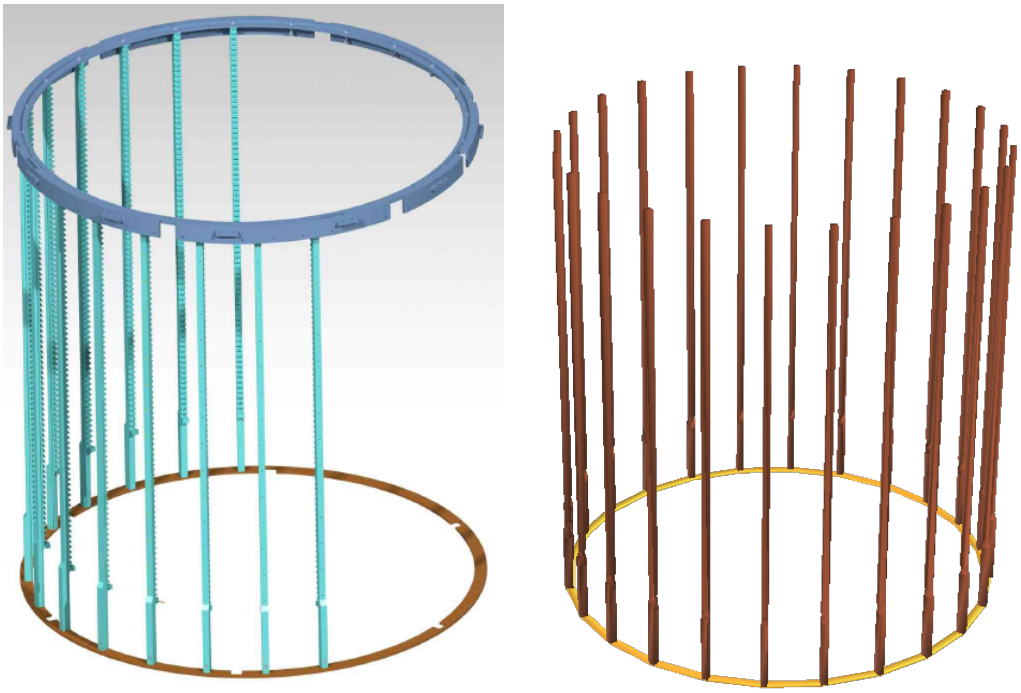

Figure 5.13: Left, PTFE pillars (cyan) and their copper ring (brown). Also shown is the L-shaped SS ring that sustain the bell (Section 5.5); image from the CAD drawings. Right, PTFE pillars (brown) and their copper ring (yellow); image done by using Meshlab from the GEANT4 simulation code.

As for the TPC, it has been implemented as an empty cylinder with the same radius of the TPC. In order to sustain the ring and also the cathode, 6 small PTFE pillars have been designed and implemented. In the MC code such small pillars are made of the union of two parallelepipeds, one for the main body and one for the "*hook*" that sustains the cathode electrode ring (Section 5.3), figure 5.14. The figure shows that the region below the TPC, from the cathode to the bottom reflector plate, Section 5.4, is light tight thanks to the PTFE ring. The 6 small pillars are placed isotropically all around the TPC, mounted on the same copper ring that sustains the 24 PTFE pillars. Each one of them is rotated by a 60^o angle with respect to the previous one, figure 5.15. Some of the characteristics of the field cage components are reported in table 5.2. As said, the drift region is enclosed by two meshes: the gate mesh, on top, and the cathode, on the bottom. The former has been designed and implemented in the MC simulation as made of hexagonal cells while the second one is made of an array of parallel wires (Section 5.6). The detailed study of their transparency, discussed in section 5.6, has demonstrated that it is not necessary to implement the detailed geometry of these components because a simplified exponential formula for the transparency, as function of the particle incident

angle with respect to the meshes, can be used. This allows to save memory and to speed up the simulations.

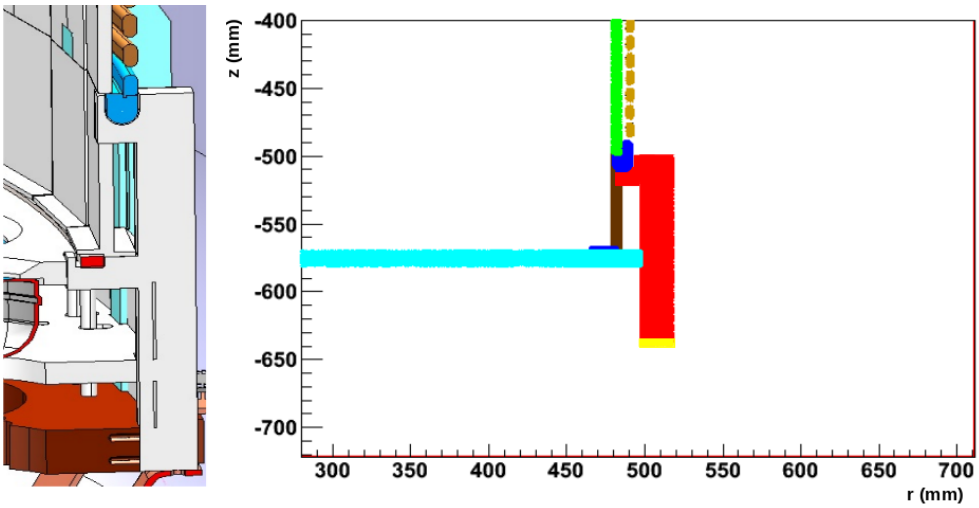

Figure 5.14: Right: bottom TPC (green), field shaping rings (dark yellow), PTFE ring below the TPC (brown), PTFE supports (red), support ring for the PTFE pillars (light yellow), cathode and bottom mesh electrode rings (blue) and the bottom PTFE reflector (cyan); image from GEANT4 (geantinos). Left, same geometry as right (different colors); image from the CAD drawings.

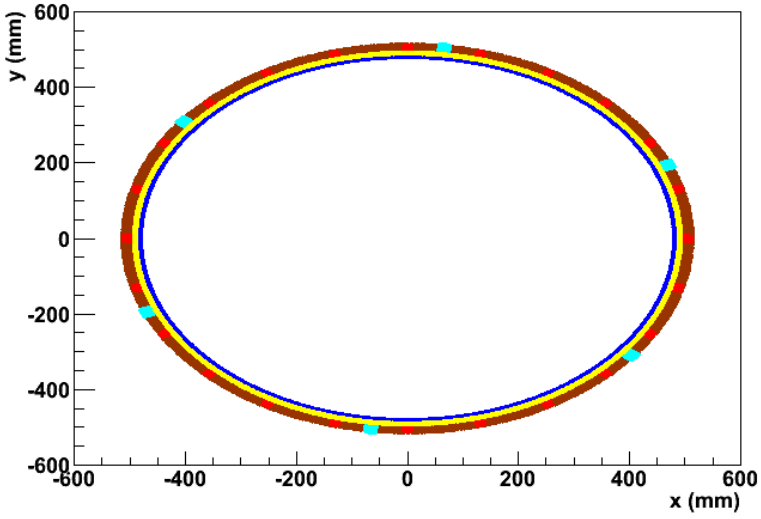

Figure 5.15: Top view of the field cage structure: TPC (blue), field shaping rings (yellow), PTFE pillars (red), copper ring to sustain pillars (brown) and cathode support pillars (cyan). Image done by using geantinos from the GEANT4 simulation code.

Component	material	weight (kg)	height (mm)	thickness (mm)
TPC	PTFE	32.5	968 (after shrinkage)	5
Ring below TPC	PTFE	2.1	69.1 (after shrinkage)	5
Cathode supports	PTFE	0.8 (for one component)	157.6 (after shrinkage)	20
Field shaping ring	Cu	90.7 (for all the 74 rings)	10	5
Field cage pillar	PTFE	13.5 (for all the 24 pillars)	1098 (after shrinkage)	15
Ring below Pillars	Cu	2.8	5	20

Table 5.2: Main characteristics of the field cage components.

As in XENON100 (Section 4.3), also XENON1T will use other three meshes: the anode and the top and bottom screening meshes. The *anode* will be placed 5 mm above the gate mesh. Exactly halfway between the stack of these two meshes there will be the LXe/GXe interface. Anode and gate mesh will create the extraction field and for this reason, the former will be biased at the proper voltage to have an extraction efficiency of the drifted electrons close, as much as possible, to 100%. Above the anode and below the cathode there will be the *Top* and *Bottom screening meshes*, needed to close the field lines and protect the PMTs. All the meshes will be connected to electrode rings, Section 5.3, in order to be sustained and biased at the proper voltage. To have a light tight region above the TPC, in the GXe region, a PTFE structure has been designed and implemented in the MC code. It acts as the PTFE ring below the TPC walls. It is made of a ring with orthogonal trapezoidal section, figure 5.16. It is 67.2 mm height, and its longer base has a inner radius of 481.3 mm and a thickness of 39 mm. Just above the top mesh electrode there is a PTFE plate, that is the first one in the PMT array structures, see section 5.4. From figure 5.16, it is clear that through the trapezoidal PTFE ring the GXe region is totally separated, and so light tight, from the rest of the detector. This will allow the best detection of light coming from the secondary scintillation signal (S2), Section 4.1.

5.3 Electrode rings

In order to bias the meshes to the proper voltage and also to give them the necessary stretch, each of them is welded onto an electrode ring, figure 5.17. The rings are made of SS and have different shapes, depending on the amount of mechanical tension they need to stand. Have a very well stretched meshes is mandatory since any inhomogeneities in the distance, for example between the gate mesh and the anode, will adversely affect the extraction field properties introducing a dependence of the S2 signal from the extraction point.

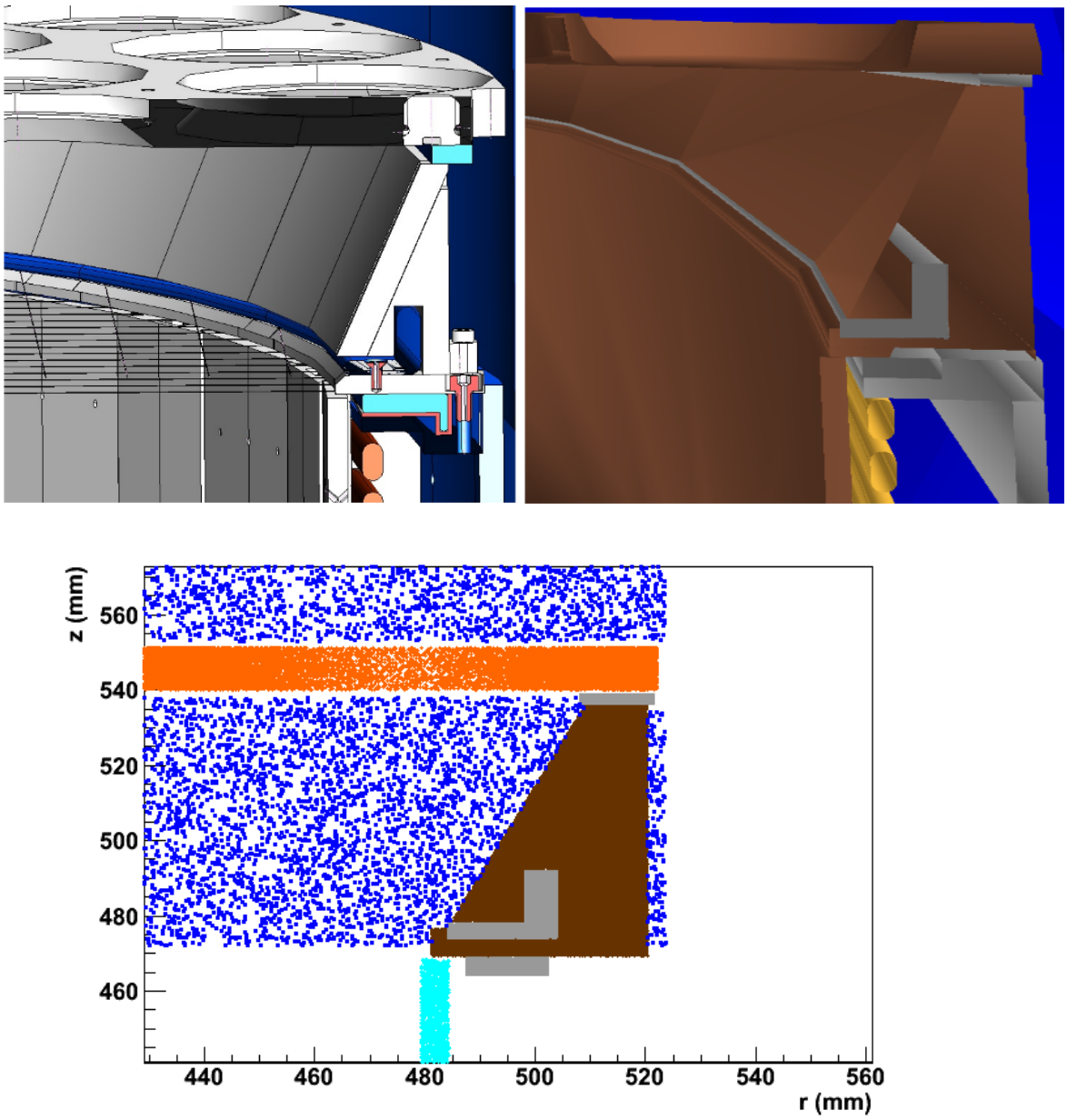

Figure 5.16: Top (left): top TPC structure; image from CAD drawings. Top (right): image done by using Meshlab from the GEANT4 simulation code. Bottom: top TPC structure implemented geometry. The components shown are: top reflector plate (orange, Section 5.4), GXe (blue dots), meshes electrodes (gray), PTFE structure around the GXe (brown), PTFE walls (cyan). Image from the GEANT4 code (geantinos).

For the top screening, bottom screening and the gate meshes, the electrode rings have been designed and implemented in the MC code as rings of rectangular section. The electrode ring of the top mesh has a inner radius of 508 mm; it is 13.5 mm a thick and 3 mm height. For the bottom mesh it has a inner radius of 465 mm, a thickness of

16.75 mm and a height equal to the top mesh one.

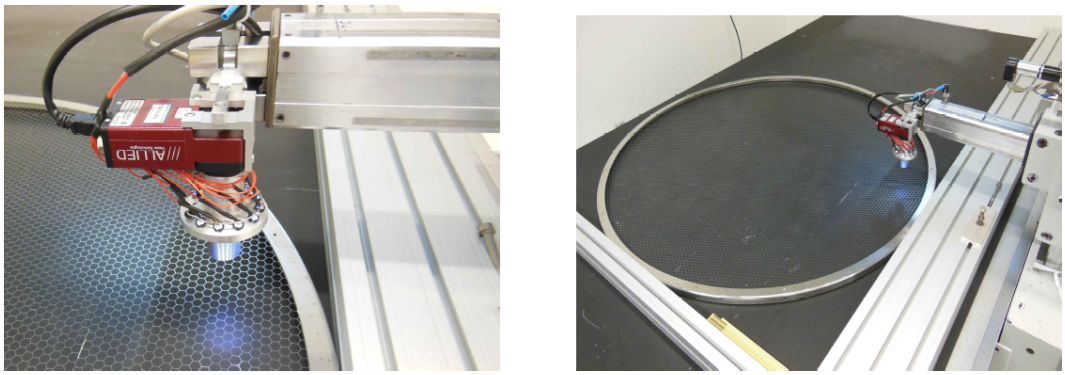

Figure 5.17: Mesh prototype during the welding on the proper electrode ring.

For what concerns the gate mesh, its electrode ring has a inner radius of 487.35 mm, a thickness of 15 mm and it is 5 mm height, figure 5.18.

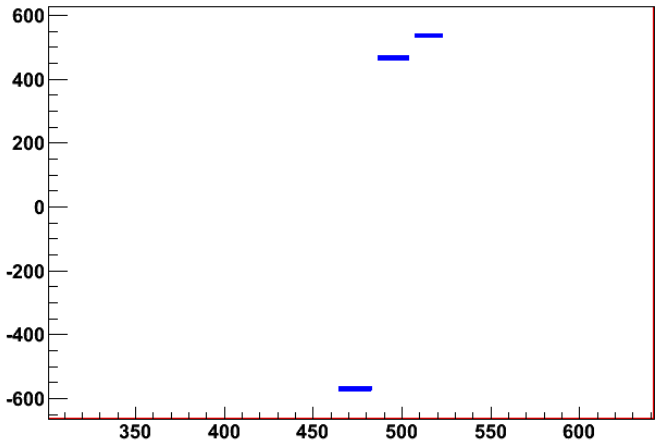

Figure 5.18: Frontal section of the bottom, gate and top mesh implemented geometries. Image from the GEANT4 code (geantinos).

The geometry of the anode and cathode electrode rings are totally different from the previous ones. The anode electrode ring is a L-shaped SS ring, figures 5.19 and 5.20 (left panels). It has been implemented in the MC as a union of two rings, both with a rectangular section. The first one has a inner radius of 484 mm, a thickness of 20 mm and a height of 4 mm while the dimensions of the second one are, respectively, 498 mm, 6 mm and 14 mm. Also the implementation of the cathode ring, figures 5.19 and 5.20 (right panels), required the union of several solids. It can be divided into two parts of similar shape but different dimensions. Both parts are a union of a torus and a square

section ring. For the bottom part, the square ring has a inner radius of 480.35 mm, a thickness of 11 mm and it is height 13.35 mm. For the top part, the dimensions are, respectively, 485 mm, 6.35 mm and 8.65 mm. The curvature of the two torus are half of the thickness of the ring to which they are connected.

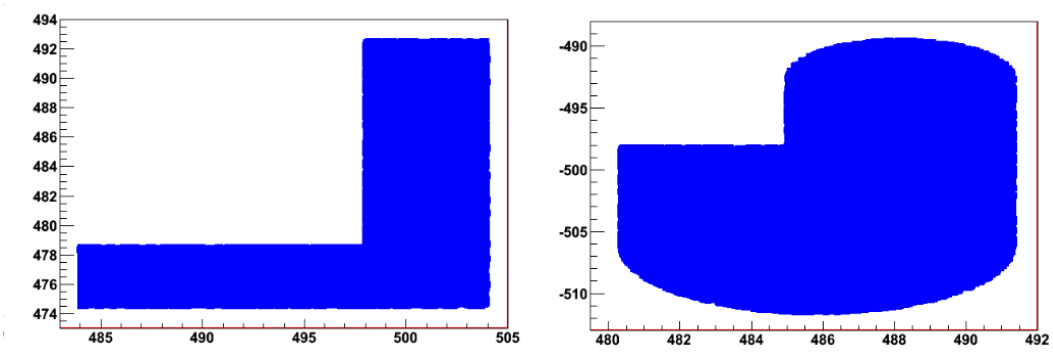

Figure 5.19: Left, frontal section of the anode ring implemented geometry. Right, frontal section of the cathode ring implemented geometry. Images from the GEANT4 code (geantinos).

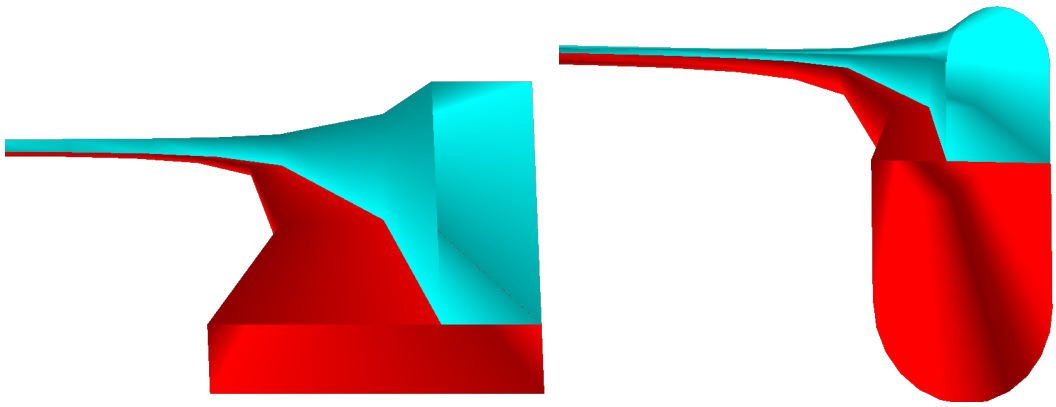

Figure 5.20: Frontal sections of the anode (left) and cathode (right) ring implemented geometries. Images from the GEANT4 code (Meshlab).

The meshes are welded onto their own electrode rings. This configuration has been also implemented in the MC simulation, figure 5.21. The main characteristics of the XENON1T electrodes are summarized in table 5.3.

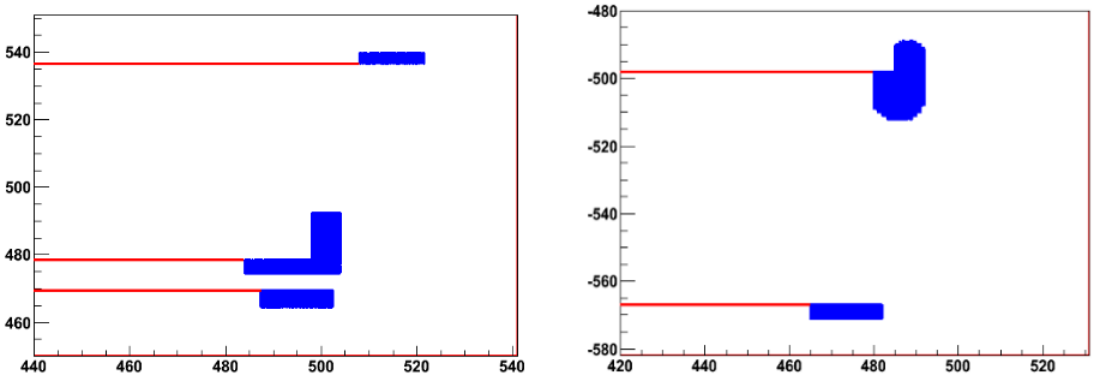

Figure 5.21: Left, top meshes (red) with their electrodes (blue). Right, bottom meshes (red) with their electrodes (blue). Images from the GEANT4 code (geantinos).

Component	material	weight (kg)	height (mm)	thickness (mm)
Bottom mesh electrode	SS	1.2	3	16.7
Cathode electrode	SS	4.5	—	—
Gate mesh electrode	SS	1.9	5	15
Anode electrode	SS	4.1	—	—
Top mesh electrode	SS	1.1	3	13.5

Table 5.3: Main characteristics of the SS electrode rings.

5.4 PMTs and their support structures

The XENON1T detector will be equipped with two arrays of photo-sensors: one on top, in the GXe region, and one on bottom, in LXe region, both inside the total light tight volume, to obtain the highest light detection efficiency. The PMTs are the 3" Hamamatsu R11410-21 characterized by a high quantum efficiency (36%) at the UV light emitted by the xenon. The PMTs, figure 5.22, consist of several parts: a quartz window, a photocathode and a bottom part made of ceramic. The interior of the PMTs is under vacuum and their total length is 114.1 mm. The top part consists of a torus plus a disk, while the central body is a cylinder. The voltage divider circuit is implemented as a simply disk made of Cirlex, 7 mm thick, that is placed 14 mm away from the PMT, In order to fix the PMTs in the desired configuration they are mounted onto proper support structures made of two PTFE plates with a copper plate between them, figure 5.23. The PMT windows are 5 mm inside the first PTFE plate that looks at the active region. These plates act also as reflectors for the photons that will not hit directly the

photomultipliers.

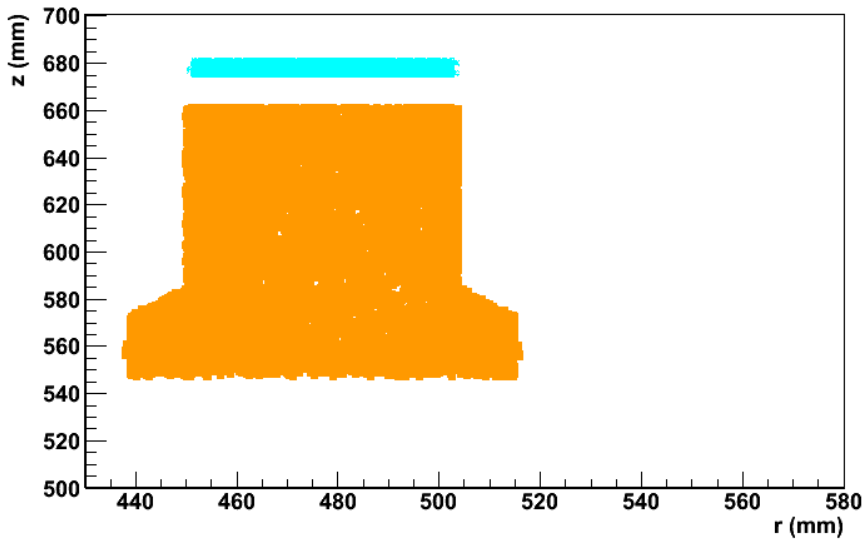

Figure 5.22: Implemented geometry of the PMT (orange) and its divider circuit (cyan). Image done by using geantinos from the GEANT4 simulation code.

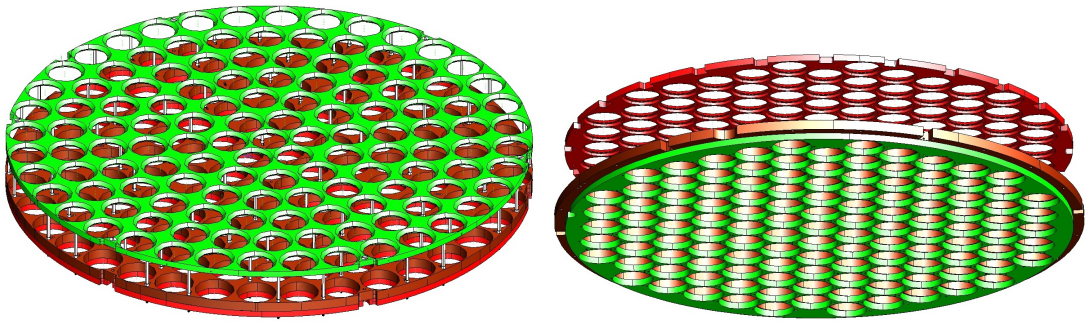

Figure 5.23: Top (left) and Bottom (right) PMT support structure design, image from the CAD drawings.

The holes in the reflector plate have a diameter that perfectly match the one of the PMT photocathodes, thus avoiding any loss of light through them. The top support structure is designed to host 127 PMTs placed in a concentric ring pattern, directly immersed in the GXe; in the bottom array there are 121 PMTs placed in a hexagonal pattern, directly immersed in LXe, figure 5.24. The outermost ring of the top PMT array slightly exceeds the PTFE walls radius; since the top array is used to reconstruct the x-y position of the interaction point, this configuration guarantees a good resolution also for events very close to the TPC edges.

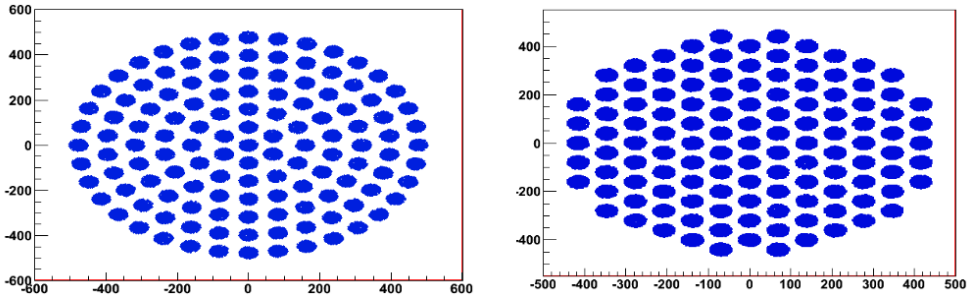

Figure 5.24: Top view of the top (left) and bottom (right) PMT arrays. Image from the GEANT4 code (geantinos).

In the bottom PMT support structure, the two PTFE plates have the same radius, 494.0 mm, and the same height, 12.7 mm. The copper ring has a larger radius, 515 mm (since the copper ring that sustains the TPC pillars is mounted on it, Section 5.2), and it is 19 mm height. The distance between the bottom reflector plate and the copper plate is 59.3 mm, while the other PTFE plate of the stack is directly connected to the copper one, figures 5.25 (right panel) and 5.26. For what concerns the top PMT support structure, all the plates have the same radius of 524 mm. The height of the first and the third plate, both made of PTFE, is 12.7 mm while the middle copper plate is 20 mm height. The distance between the first PTFE plate and the copper plate is 59.3 mm while the third plate is attached directly on the copper plate, figures 5.25 (left pane) and 5.27.

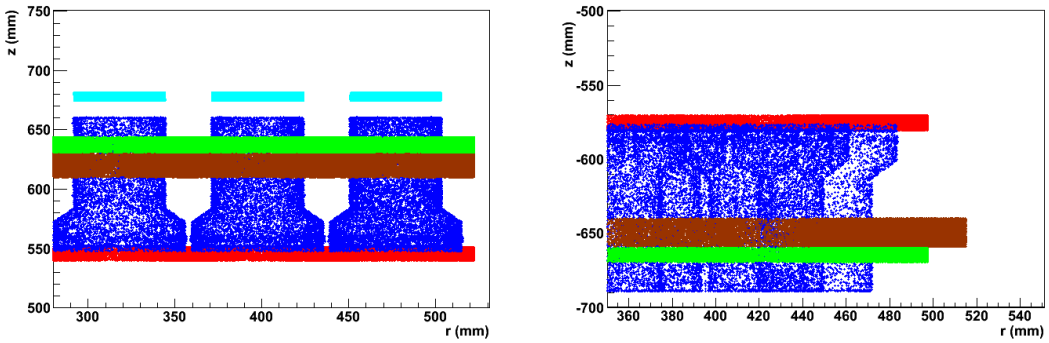

Figure 5.25: PMT support structure implemented geometries: PTFE reflector (red), copper plate (brown), PTFE plate (green), PMTs (blue) and PMT voltage divider circuits (cyan). Left for top array and right for bottom array. Image done by using geantinos from the GEANT4 simulation code.

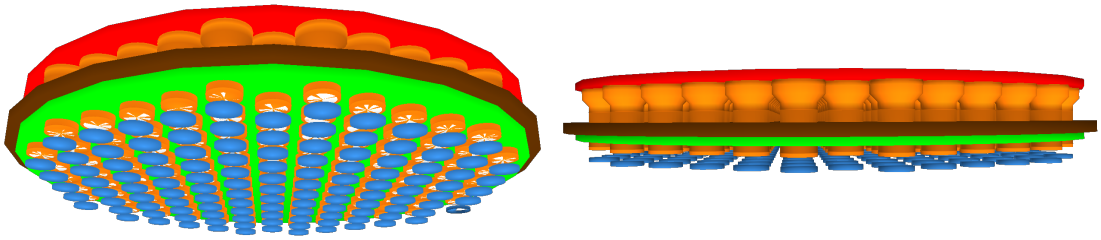

Figure 5.26: Bottom PMT support structure implemented geometry: voltage divider (blue disk), PMTs (orange), bottom reflector (red), copper plate (brown) and bottom PTFE plate (green). Image done by using Meshlab from the GEANT4 simulation code.

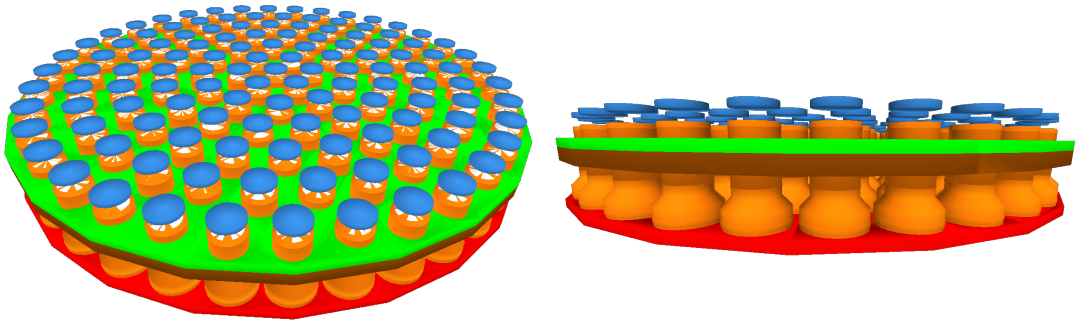

Figure 5.27: Top PMT support structure implemented geometry: voltage divider circuits (blue disk), PMTs (orange), top PTFE plate (green), copper plate (brown) and top reflector (red). Images from the GEANT4 code (Meshlab).

In table 5.4 are reported some properties of the PMT support structures.

Component	**material**	**weight (kg)**	**height (mm)**	**radius (mm)**
Top (bottom) reflector	PTE	6.3 (4.6)	12.7 (12.7)	524.0 (494.0)
Top (bottom) PTFE plate	PTFE	7.1 (4.3)	12.7 (12.7)	524.0 (494.0)
Top (bottom) copper plate	Cu	45.9 (44.6)	20.0 (19)	524.0 (515.0)

Table 5.4: Geometrical properties of the components forming the PMT support structures.

An overall view of the top and bottom PMT structures, with the other components in the top and bottom light tight regions are shown in figure 5.28 and figures 5.29 - 5.30, respectively.

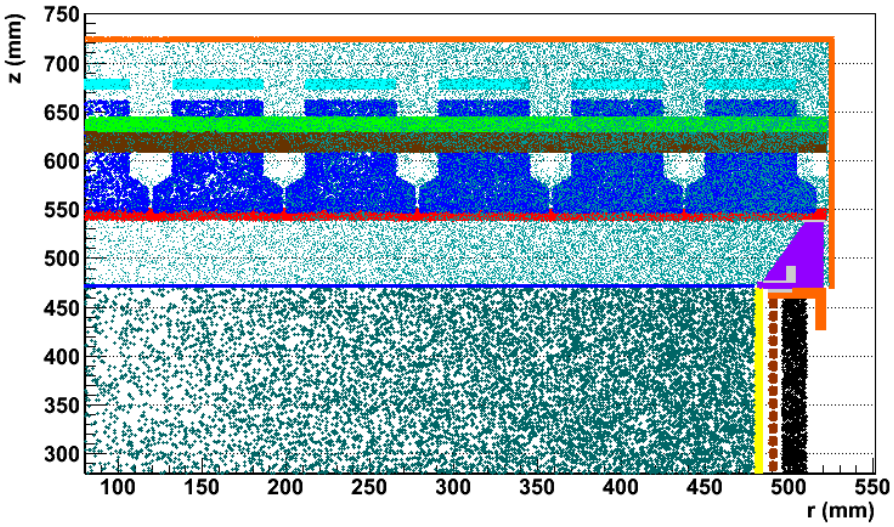

Figure 5.28: Frontal view of the top light tight region implemented geometry. The components shown are the same as in figure 5.25 (left) plus: LXe/GXe interface (solid blue horizontal line), PTFE trapezoid ring (violet), TPC (yellow), copper field shaping rings (brown), PTFE pillar (black), diving bell and its SS ring (orange, Section 5.5). The dots below and above the LXe/GXe interface line are the LXe and GXe volumes, respectively. Image from the GEANT4 code (geantinos).

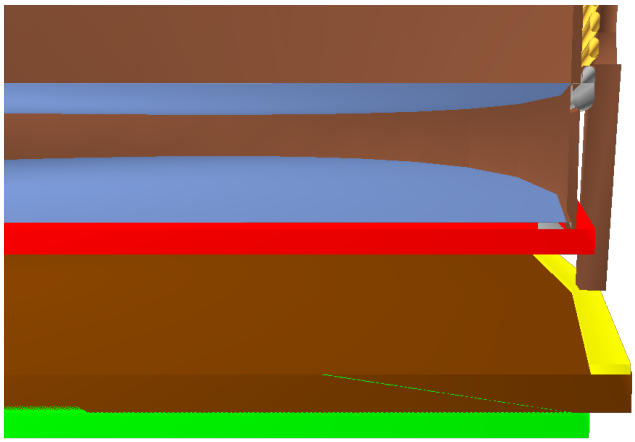

Figure 5.29: Frontal section of the bottom light tight region implemented geometry: PTFE TPC walls and PTFE ring below them (brown), cathode and bottom mesh electrodes (gray), field shaping rings (yellow), PTFE pillars (brown) and their support ring (light yellow), bottom reflector plate (red), copper (brown) and PTFE (green) bottom plates. Images from the GEANT4 simulation code (Meshlab).

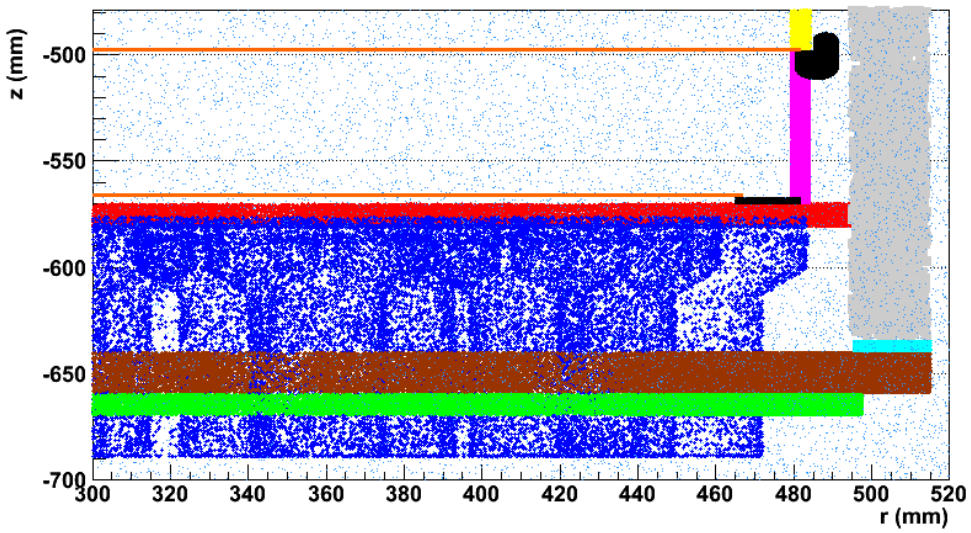

Figure 5.30: Same as figure 5.29 but image done by using geantinos.

5.5 Diving bell and bottom filler

The mutual distance between gate mesh, LXe/GXe interface and the anode is crucial for the extraction field properties and so for the S2 signal generation. For such a reason, the level of the interface between the meshes, as well as their stretch (Section 5.3), has to be kept under control. To this aim a diving bell has been designed, figure 5.31, and implemented in the MC code, figure 5.32.

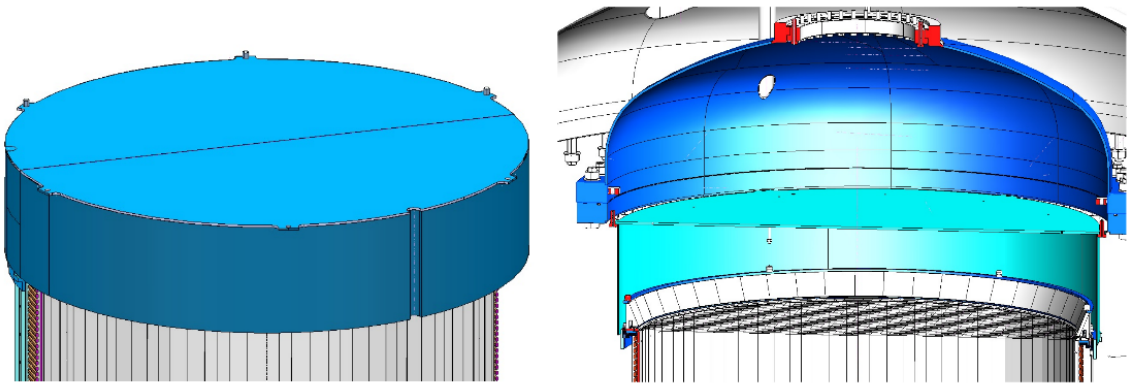

Figure 5.31: Diving bell, light blue. Left, outside view. Right, frontal section. Both picture are taken from the CAD drawings.

A prototype of the bell has been already constructed and tested, figure 5.33. The diving bell plays two main roles: it keeps under control the LXe/GXe interface level and it also guarantees a 4π coverage, of the sensitive volume, with LXe. In fact, the only

way to have a certain amount of liquid above the TPC, important to reduce external background, is to have a sealed volume on its top, i.e. a diving bell.

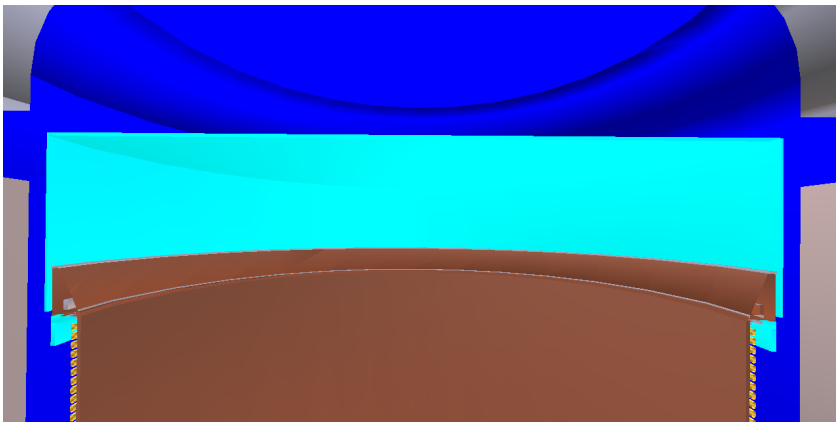

Figure 5.32: Frontal section of the diving bell (cyan) on top of the field cage. Image from the GEANT4 simulation code (Meshlab).

Figure 5.33: Prototype of the diving bell used for operational testing.

The bell keeps the liquid at a desired level using a stream of gas that pressurizes its internal volume. Adjusting the pressure of the gas, it is possible to push at a desired level the LXe/GXe interface. This is possible since the active volume is connected to the external LXe volume and thus lowering the level of the former will raise the volume of the latter outside the field cage. The gas is sent into the bell through a small pipe connected to the recirculation system and its pressure is controlled adjusting the open

end of the pipe. At the beginning of the design of the detector also the idea of not using the bell has been exploited (figure 5.34). After a MC study, the option with bell has been chosen.

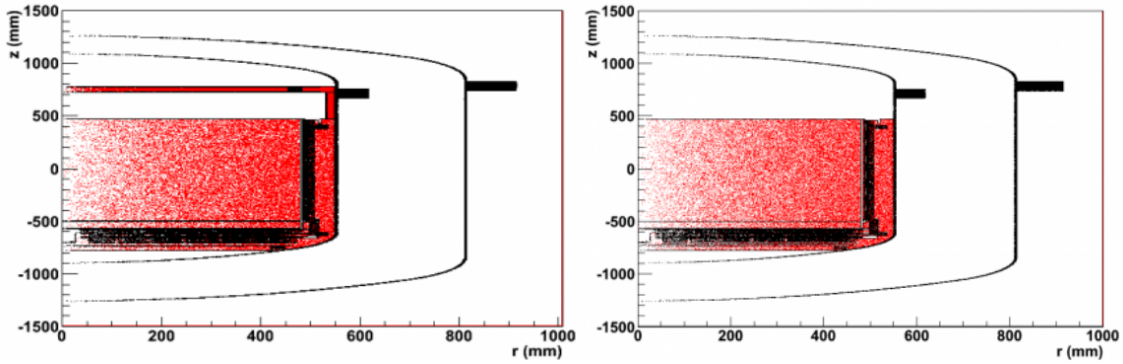

Figure 5.34: Overall frontal section of the XENON1T detector implemented geometry. Left, option with the diving bell. Right, option without the bell. In red is the LXe volume. Images done by using geantinos from the GEANT4 simulation code.

Figure 5.34 (left panel) clearly shows that the bell allows a total coverage of the active region, thus reducing the background inside the detector. The bell has a cylindrical shape and it is made of a SS top plate with thickness equal to 5 mm and radius of 523.5 mm and by a 3 mm thick lateral SS wall. Inside the bell there is xenon in gaseous phase. In the current MC implementation there is a 5 mm thick layer of LXe above the bell as well as some other amount all around it. The bell is mounted on a L-shaped, upside down, SS ring figure 5.35 - 5.37.

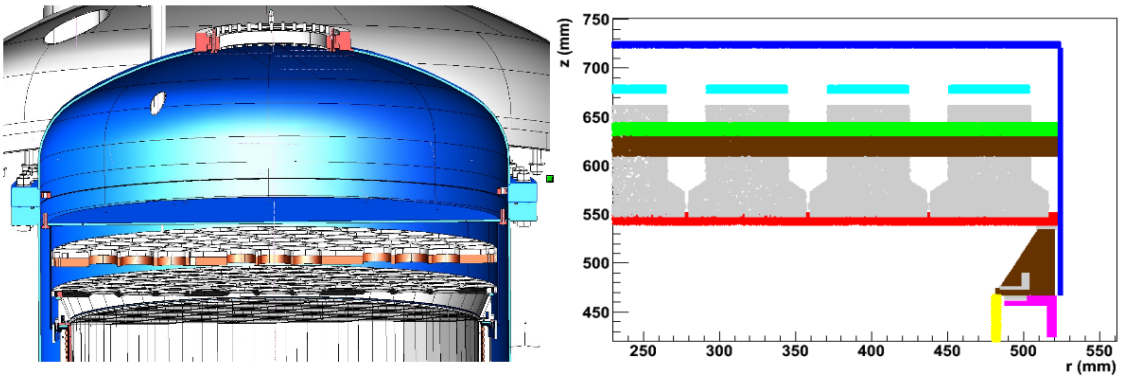

Figure 5.35: Frontal section of the diving bell with the top PMT structure inside. Left, image form CAD drawings. Right, MC implemented geometry; in magenta is the L-shaped SS ring on which the bell is welded and in yellow is the top part of the PTFE walls of the TPC. Image from the GEANT4 code (geantinos).

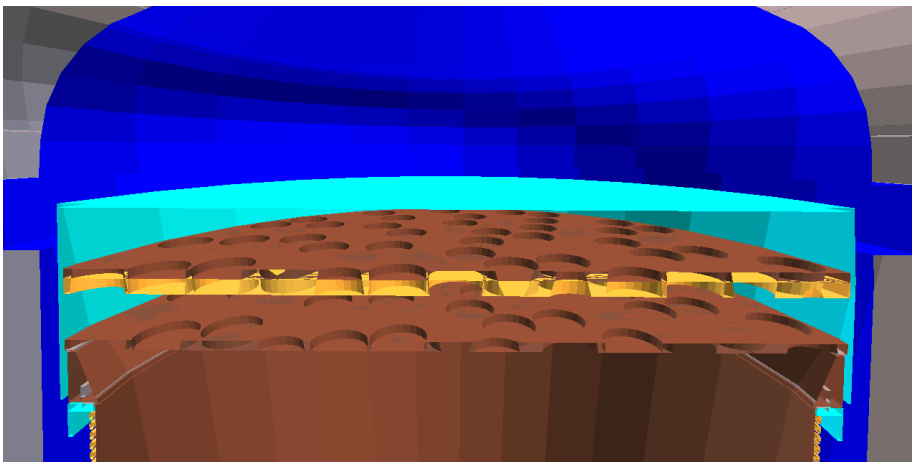

Figure 5.36: Frontal section of the bell with the top PMT support structure inside.

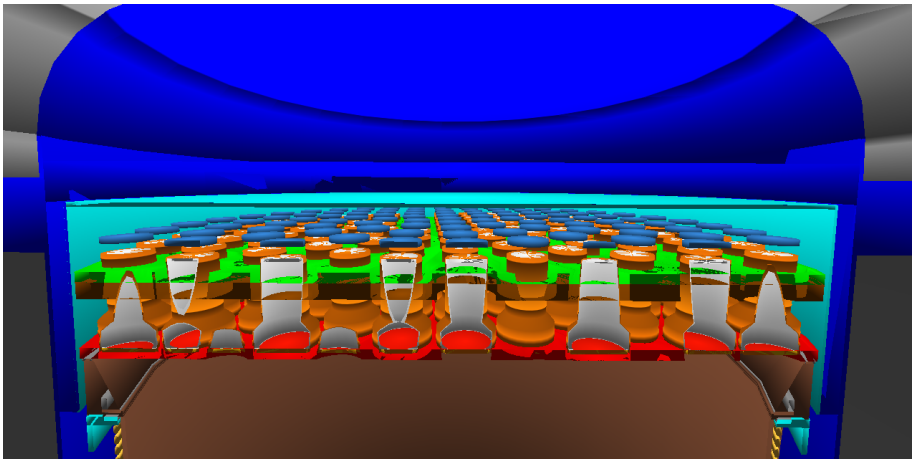

Figure 5.37: Frontal section of the bell with the top PMTs and their support structure inside.

In the bottom part of the inner cryostat, below the bottom PMT support structure, there is another component, the *bottom filler*, a hollow volume which can play two different roles: it can act just as a "filler", in such a case it will be evacuated and its only purpose is to reduce the total amount of Xe required to fill the detector, or it can work as reservoir for a certain amount of LXe. The filler has been implemented as union of two solids: a 5 mm thick SS lateral wall that follows the inner cryostat bottom shape and, on top, a 10 mm thick stainless steel plate that closes it, figure 5.38. In the current design there is vacuum inside and it is considered just as a "filler".

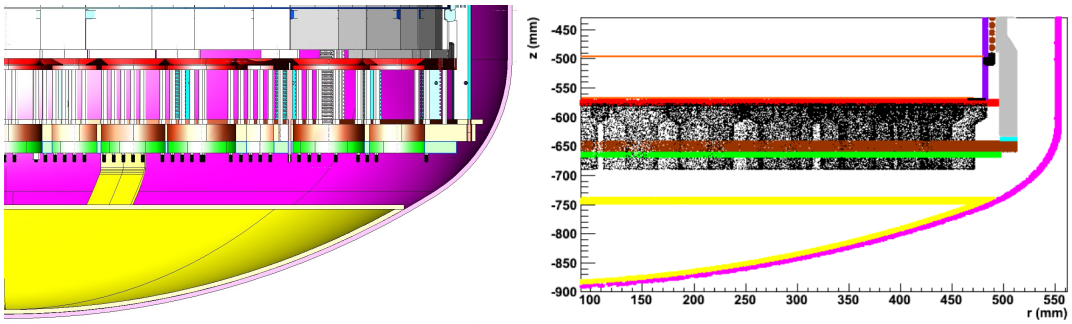

Figure 5.38: Left, design of the bottom TPC with the bottom filler (yellow); image from the CAD drawings. Right, bottom TPC and bottom PMT structure implemented geometries. The orange plates are the cathode and the bottom screening mesh. The black parts, starting from the top, are: the cathode electrode ring, the bottom mesh electrode ring and the bottom PMTs. The violet part above the cathode ring is the TPC while the one below it, is the other PTFE ring. Outside the TPC there are the field shaping rings (brown), the PTFE pillars (gray) and their support ring (cyan). The red and green plates are the bottom reflector and the bottom PTFE plate, respectively. The brown plate is the bottom copper plate. The last component in yellow, on the bottom of the inner cryostat (magenta), is the bottom filler. Image done by using geantinos from the GEANT4 code.

The total weight of the bottom filler is 90.4 kg. Some characteristics of the diving bell and of the bottom filler are reported in table 5.5.

Component	**material**	**weight (kg)**
Top plate	SS	34.4
Lateral bell wall	SS	20.0
L-shaped ring for the bell	SS	12.2
Bottom filler	SS	90.4

Table 5.5: Characteristics of the diving bell and of the bottom filler.

Finally, an external view of the whole field cage geometry is shown in figure 5.39.

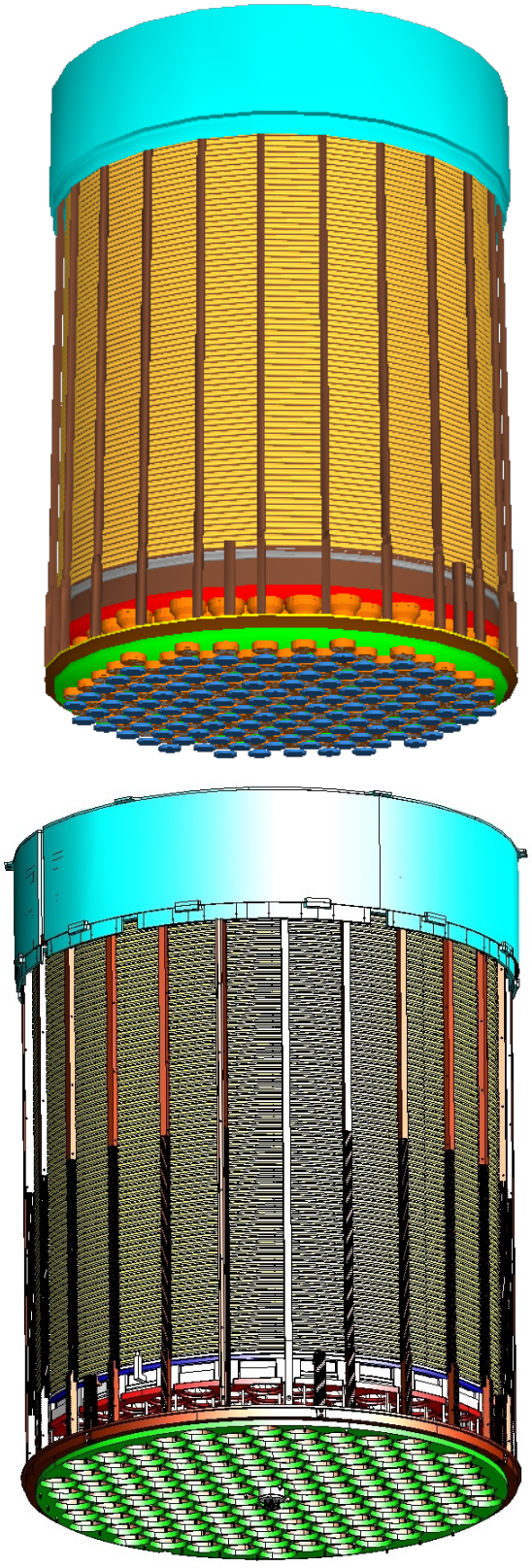

Figure 5.39: External view of the whole field cage geometry. Top, image obtained with Meshlab from the GEANT4 code. Bottom, image from CAD drawings.

5.6 XENON1T meshes transparency study

The transparency of the meshes is one of the needed ingredients to evaluate the detector light collection efficiency (Section 6.7.2). The five XENON1T meshes can be divided into three groups:

- top and bottom screening meshes, both with hexagonal cell pattern geometry;
- gate mesh and anode, still with hexagonal cell pattern geometry but with different dimensions with respect to the previous two meshes;
- cathode, with cylindrical wires pattern geometry.

All of them are made of stainless steel. In table 5.6 are summarized their geometrical properties.

Mesh	radius (mm)	pitch (mm)	wire diameter (mm)
Top/Bottom screening meshes	508/479.25	6.56	0.178
Anode/Gate mesh	479.25/479.25	3.63	0.127
Cathode	479.25	5.50	0.220

Table 5.6: XENON1T mesh geometry properties.

In figure 5.40 are shown the pitch and the wire diameter in the case of the hexagonal cells. For the cathode, the pitch is just the distance between the centers of two consecutive wires, figure 5.41 and 5.42.

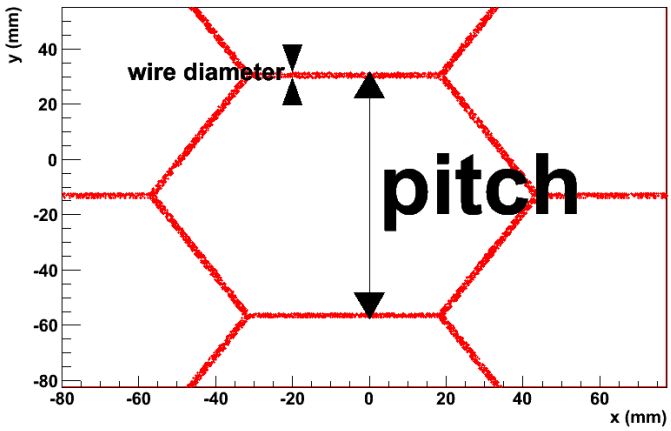

Figure 5.40: Pitch and wire diameter explanation for a hexagonal cell. Image from the GEANT4 code (geantinos).

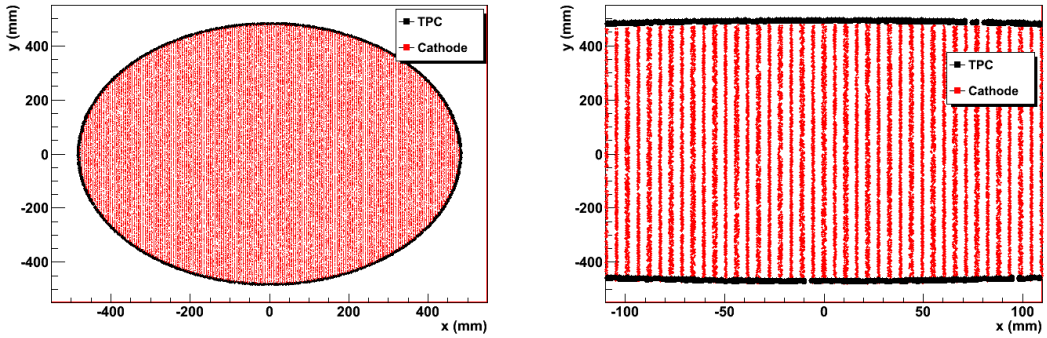

Figure 5.41: Left, cathode wires (red) and TPC contour (black). Right, zoom in the cathode structure. Image done by using geantinos from the GEANT4 simulation code.

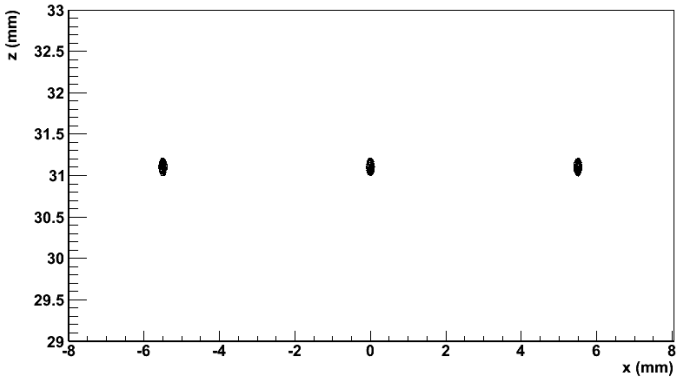

Figure 5.42: Example of the cathode wire pattern ($z-x$ plane). Image done by using geantinos from the GEANT4 simulation code.

The top and bottom screening meshes are shown in figure 5.43, left panel, while the anode and the gate mesh are shown in the right panel. Anode and gate mesh are shifted in the $x-y$ plane. Dedicated simulations showed that the extraction field is more efficient in the electrons extraction with this configuration. Due to the small dimensions of the hexagonal cells, each mesh contains thousands of them. In order to implement the geometry and reduce the CPU time, the **G4VPVParameterisation** GEANT4 class has been used. In this way it is possible to create multiple copies of a specific volume using a parameterisation of its geometry structure. A first estimation of the meshes transparency has been done by using only particles with orthogonal direction with respect to them. The goal has been the evaluation and comparison of the total simulated transparency with the geometrical one, table 5.7. The first value represents the ratio between the number of the generated particles and the number of the ones that

pass through the meshes without touching them.

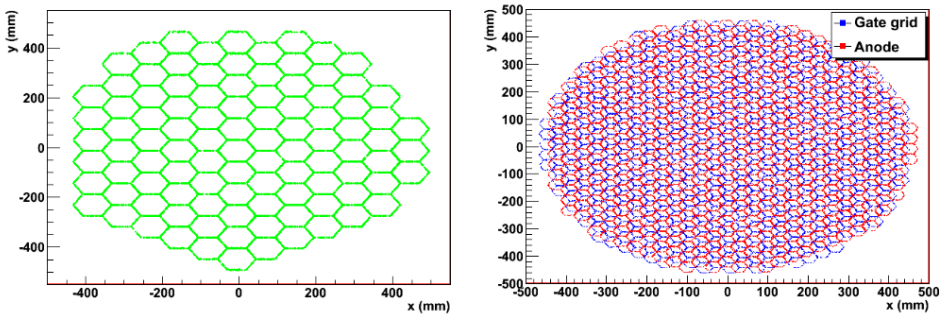

Figure 5.43: Mesh implemented geometries. Left, top/bottom screening mesh. Right, anode and gate mesh. The dimensions have been multiplied by a factor ten, with respect to the real ones, to speed up the simulation time. Images from the GEANT4 code (geantinos).

Mesh	**MC tot transparency (%)**	**Geometrical tot transparency (%)**
Top/Bottom screening meshes	94.6	94.5
Anode/Gate mesh (combined)	92.8 (86.0)	92.9 (86.3)
Cathode	95.95	96.00

Table 5.7: Transparency results. For anode and gate mesh it is also reported the combined transparency. This quantity is of fundamental importance because it is directly connected to the generation of the S2 signal.

A second study regarded particles with isotropic distribution of the trajectories. This permitted the analysis of the transparency as function of the angle of the incident particles, figure 5.44. In both the previous analysis, all the meshes have been considered totally opaque. The results from the transparency studies are very promising; indeed, all the meshes have very high transparency and this will guarantee to most of the photons to pass through the them and to be read by the light sensors. The mesh geometry simulations required massive CPU time, due to the large number of hexagonal cells. For this reason the simulated transparency has been compared with a simplified formula that could reproduce the proper value of the transparency as function of the incident angle. That "simplified" formula, as function of the particle incident angle, is given by:

$$t(\theta) = e^{-\frac{l(\theta)}{\lambda}}, \tag{5.1}$$

where l is the particle path length between the top and bottom mesh surfaces, θ is the particle incident angle with respect to the mesh and λ is a numerical factor defined as:

$$\theta = 0^o;\ t(0^o) = \text{geometrical transparency}. \tag{5.2}$$

Thus, λ is a factor that, for an incident particle with orthogonal direction with respect to the mesh, returns a transparency equal to the geometrical one, table 5.7.

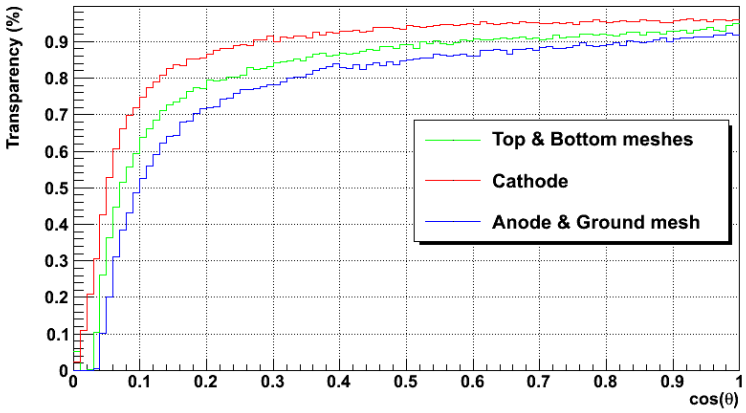

Figure 5.44: Mesh transparency as function of the angle of the incident particles: anode and gate mesh (blue curve), top and bottom screening meshes (green curve), cathode (red curve).

A comparison between the transparencies obtained with the two different methods is shown in figure 5.45. The excellent agreement between the transparency computed by using the simplified approach and the MC simulation demonstrates that there is no need to simulate the real geometry, thus considerably speeding up the simulation.

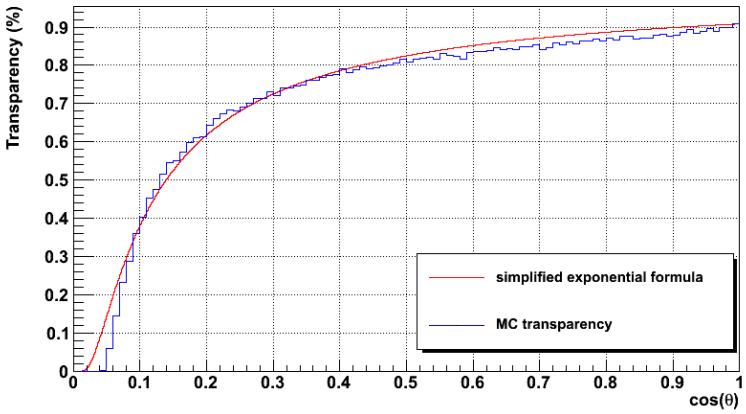

Figure 5.45: Example (for the gate mesh) of comparison between the simulated transparency, as function of the particle incident angle, and the simplified formula, equation (5.1).

Chapter 6

XENON1T background estimation

6.1 Introduction

For an experiment that looks for very rare events, such the interactions of dark matter particles, one of the most important requirements is to have a very low background. For what concerns the XENON1T detector, the goal is to have less than 1 background event per year inside the chosen *fiducial volume* (FV), Section 4.1. To lower the number of such events, besides all the passive and active shields, screening campaigns (Section 6.2) are also required to choose the materials with the lowest contaminations from radioactive nuclei. The most dangerous electromagnetic background comes from the γ emitted in the ^{238}U and ^{232}Th chains, and the decay of ^{60}Co, ^{40}K and ^{137}Cs. Using the implemented geometry, described in Chapter 5, MC simulations of the isotope decays have been run to study the background from the materials, also called **internal** (Sections 6.3 and 6.5). In each ^{60}Co decay, two different gammas are emitted: 1173 keV and 1332 keV. For what concerns ^{40}K a 1461 keV γ is emitted with a probability of 10.7%; for ^{137}Cs there is a 662 keV γ emitted with a probability of 94.6%, In the case of ^{238}U and ^{232}Th, for some materials there are evidences of disequilibrium for the chains. Thus, it is necessary to split them:

- ^{238}U : $^{238}\text{U} \rightarrow {}^{226}\text{Ra}$ and $^{226}\text{Ra} \rightarrow {}^{206}\text{Pb}$;
- ^{232}Th : $^{232}\text{Th} \rightarrow {}^{228}\text{Th}$ and $^{228}\text{Th} \rightarrow {}^{208}\text{Pb}$.

The ^{238}U and ^{232}Th chains are shown in figure 6.1; their spectra in figures 6.2 and 6.3

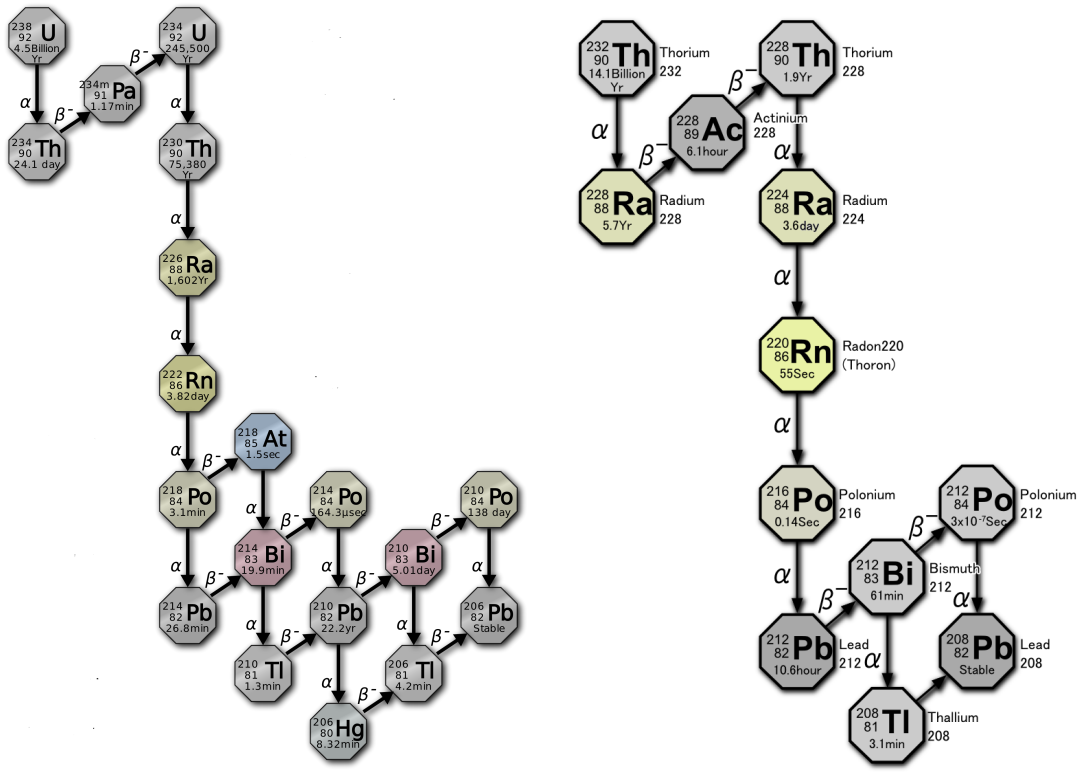

Figure 6.1: Left, ^{238}U decay chain. Right, ^{232}Th decay chain.

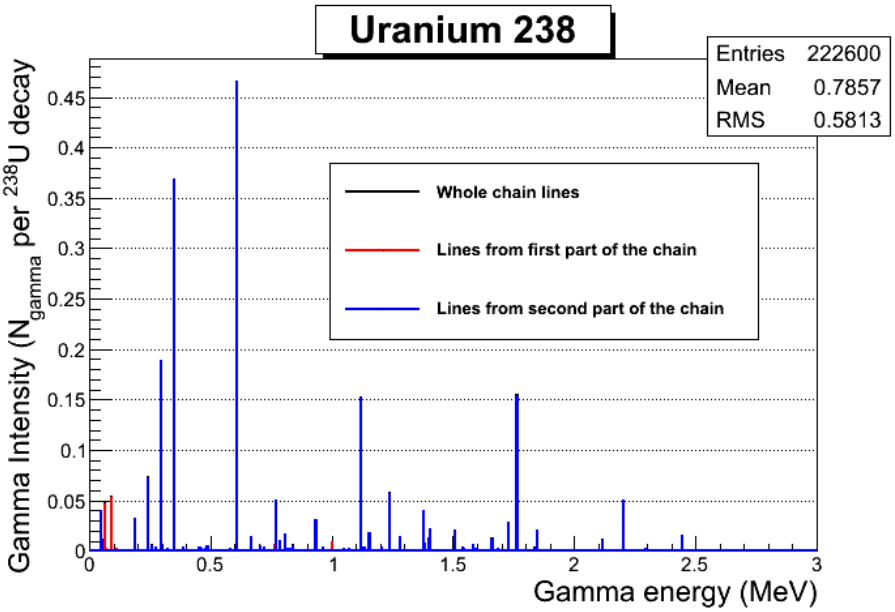

Figure 6.2: Gamma energy spectrum from the ^{238}U decay chain.

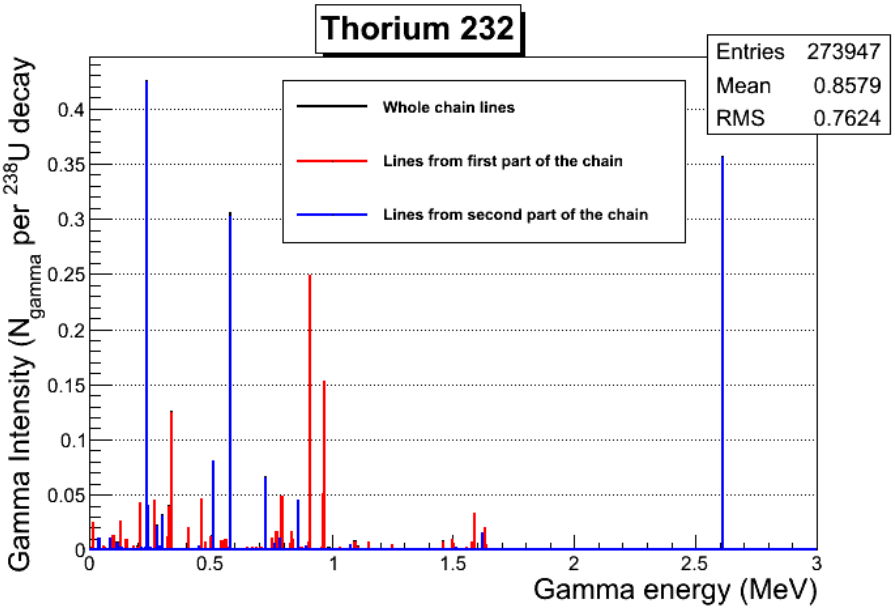

Figure 6.3: Gamma energy spectrum from the ^{232}Th decay chain.

A summary of the gamma production for the different isotopes, considered in the study of the background level, is shown in table 6.1. In the table, for ^{238}U and ^{232}Th, the γ production is considered as gammas emitted for each disintegration of the parent element in the chain. Besides the internal background, there is also the so called **intrinsic** background; its study and characterization are presented in sections 6.4 and 6.5. The intrinsic background is much harder to reduce since its due to solar neutrinos or to radioactive isotopes that are uniformly distributed in LXe. Thus, for such radionuclides it is not possible to use any position cut in the analysis to reduce their contribution. The goal of the study presented in this chapter is to estimate the total amount of background, internal plus intrinsic, for the XENON1T experiment. Electromagnetic recoils (ER), from γ and e^-, can represent a background for the WIMP search because of statistical leakage from the ER to the NR band (Sections 4.2 and 4.3); the separation of the two bands in the discrimination parameter is shown indeed in figure 4.16. Besides, also NR from neutron elastic scattering are dangerous since they mimic the same process as WIMP interactions. In the analysis of the results of the Monte Carlo simulations, the dangerous events have been chosen as those that satisfy the following requirements:

- a single scatter interaction;
- in the chosen fiducial volume;
- with energy released in the WIMP search region.

Isotope	**γ/decay**	**energy (keV)**
$^{238}\mathrm{U} \rightarrow {}^{226}\mathrm{Ra}$	0.14	figure 6.2
$^{226}\mathrm{Ra} \rightarrow {}^{206}\mathrm{Pb}$	2.09	figure 6.2
$^{232}\mathrm{Th} \rightarrow {}^{228}\mathrm{Th}$	1.27	figure 6.3
$^{228}\mathrm{Th} \rightarrow {}^{208}\mathrm{Pb}$	1.47	figure 6.3
$^{60}\mathrm{Co}$	2	1173, 1332
$^{40}\mathrm{K}$	0.107	1461
$^{137}\mathrm{Cs}$	0.946	662

Table 6.1: γ production from each isotope considered in the background study.

Due to their characteristics, WIMPs are not expected to give more than one scatter in the LXe fiducial volume. The capability to distinguish two scatters is related to the width of the S2 signals and the peak separation efficiency of the S2 peak finder algorithm. Based on the XENON100 performances [173], a multiple scatter event is considered as a single scatter if the interactions happen inside 3 mm along the Z axis. For what concerns the fiducial volume, 1 tonne has been considered as reference. It is defined as a super-ellipsoid, centered in the middle of the active region, with radius and semi-height equal to 40 cm. In this way a minimum distance of 4 cm from the borders of the TPC is guaranteed. It is defined as:

$$\left(\frac{|z|(\mathrm{mm})}{400}\right)^3 + \left(\frac{R^2(\mathrm{mm})^2}{160000}\right)^3 < 1. \tag{6.1}$$

However, also other fiducial volumes have been considered in the analysis. Having a different response to ER with respect to NR, the keV_{ee} and keV_r units are used (Section 3.6). With the typical velocities from the standard galactic halo model, WIMPs are expected to produce NR in xenon with kinetic energies below 100 keV_r which translates in an ER energy region below 20 keV_{ee}. In particular, the reference energy region for WIMP search will be [5, 50] keV_r that corresponds to [2, 12] keV_{ee} for ER. Having the total background spectra, ER and NR, it is then possible to evaluate the sensitivity (Chapter 7). In order to do that, we have to convert the two spectra, together with the WIMP ones, on a common scale; the procedure is shown in Section 6.7.

6.2 Material screening campaigns

The material contaminations have been measured using a variety of complementary techniques and dedicated measurements: Ge detectors and mass spectroscopy techniques.

For the gamma spectrometry with Ge, XENON has access to a dedicated screening facility underground at LNGS, the GATOR detector [206]; moreover, other screening facilities have been used at LNGS and Heidelberg. In particular, Ge detectors are sensitive to most of the dangerous radiogenic nuclides: ^{40}K, ^{60}Co, ^{232}Th chain, ^{137}Cs and the second part of the ^{238}U chain, from ^{226}Ra on. The main exception is indeed the first part of the ^{238}U chain, where very few and low energy gammas are emitted. The estimation of the activity of this part of the chain is anyway very important, since it is responsible for the production of neutrons from spontaneous fission. For this reason we also used various mass spectrometry techniques that allow to directly count the amount of primordial nuclides (^{238}U, ^{232}Th). With the results from the screening campaign, it is possible to evaluate the expected number of background events from materials (section 6.3). A summary of the material contaminations, together with their masses, is presented in table 6.2. The values reported as upper limits have been used as detected values and then we set them to zero, to get respectively the maximum and the minimum estimation of the background rate. For the estimation of the PMT contaminations two strategies have been followed: for the ER background the values obtained from measurements in Ge of the whole PMT have been used; for the estimation of the NR background, since the neutron yield depends also on the particular material, the measurements of the PMT raw components (last four rows in table 6.2) have been considered.

Summary of material properties and contaminations

Component	Material	Mass (kg)	Contamination (mBq/kg or mBq/PMT(PMT base))							
			^{238}U	^{235}U	^{226}Ra	^{232}Th	^{228}Th	^{60}Co	^{40}K	^{137}Cs
Cryostat shells	SS	870	2.4 ± 0.7	$(1.1 \pm 0.3)\cdot10^{-1}$	$< 6.4 \cdot 10^{-1}$	$(2.1 \pm 0.6)\cdot10^{-1}$	$< 3.6 \cdot 10^{-1}$	9.7 ± 0.8	< 2.7	$< 6.4 \cdot 10^{-1}$
Cryostat flanges	SS	557	1.4 ± 0.4	$(6 \pm 2)\cdot10^{-2}$	< 4.0	$(2.1 \pm 0.6)\cdot10^{-1}$	4.5 ± 0.6	37.3 ± 0.9	< 5.6	< 1.5
PMT		248 (PMTs)	8 ± 2	$(3.6 \pm 0.8)\cdot10^{-1}$	$(5 \pm 1)\cdot10^{-1}$	$(5 \pm 1)\cdot10^{-1}$	$(5.0 \pm 0.6)\cdot10^{-1}$	$(7.1 \pm 0.3)\cdot10^{-1}$	13 ± 2	$< 1.8 \cdot 10^{-1}$
PMT bases	Cirlex	248 (PMT bases)	$(8.20 \pm 0.27)\cdot10^{-1}$	$(7.1 \pm 1.6)\cdot10^{-2}$	$(3.2 \pm 0.2)\cdot10^{-1}$	$(2.04 \pm 0.25)\cdot10^{-1}$	$(1.53 \pm 0.13)\cdot10^{-1}$	$< 5.2 \cdot 10^{-3}$	$(3.55 \pm 0.81)\cdot10^{-1}$	$< 9.8 \cdot 10^{-3}$
Field cage[1]	PTFE	91.5	< 1.9	$< 8.7 \cdot 10^{-2}$	$< 1.2 \cdot 10^{-1}$	$< 1.1 \cdot 10^{-1}$	$< 6.5 \cdot 10^{-2}$	$< 2.7 \cdot 10^{-2}$	$< 3.4 \cdot 10^{-1}$	$(1.7 \pm 0.3)\cdot10^{-1}$
Copper components	Cu	184	$(7 \pm 2)\cdot10^{-2}$	$(3.4 \pm 1.0)\cdot10^{-3}$	$(7 \pm 2)\cdot10^{-2}$	$(2.1 \pm 0.7)\cdot10^{-2}$	$(2.1 \pm 0.7)\cdot10^{-2}$	$(2 \pm 1)\cdot10^{-3}$	$(2.3 \pm 0.6)\cdot10^{-2}$	$< 1.4 \cdot 10^{-1}$
Bottom filler	SS	90.4	11 ± 3	$(5 \pm 2)\cdot10^{-1}$	1.2 ± 0.3	1.2 ± 0.4	2.0 ± 0.4	5.5 ± 0.5	< 1.3	$< 5.8 \cdot 10^{-1}$
SS components[2]	SS	36.7	2.4 ± 0.7	$(1.1 \pm 0.3)\cdot10^{-1}$	$< 6.4 \cdot 10^{-1}$	$(2.1 \pm 0.6)\cdot10^{-1}$	$< 3.6 \cdot 10^{-1}$	9.7 ± 0.8	< 2.7	$< 6.4 \cdot 10^{-1}$
Bell lateral wall	SS	20.0	50 ± 25	$(5.0 \pm 2.5)\cdot10^{-1}$	3.6 ± 1.8	$(8.1 \pm 4.1)\cdot10^{-1}$	1.8 ± 0.9	7.0 ± 3.5	5.7 ± 2.8	$< 5.8 \cdot 10^{-1}$
Middle SS[3]	SS	22.7	1.4 ± 0.4	$(6 \pm 2)\cdot10^{-2}$	< 4.0	$(2.1 \pm 0.6)\cdot10^{-1}$	4.5 ± 0.6	37.3 ± 0.9	< 5.6	< 1.5
PMT Stem	Al_2O_3	248 (PMTs)	2.4 ± 0.4	$(1.1 \pm 0.2)\cdot10^{-1}$	$(2.6 \pm 0.2)\cdot10^{-1}$	$(2.3 \pm 0.3)\cdot10^{-1}$	$(1.1 \pm 0.2)\cdot10^{-1}$	$< 1.8 \cdot 10^{-2}$	1.1 ± 0.2	$< 2.2 \cdot 10^{-2}$
PMT Window	Quartz	248 (PMTs)	< 1.2	$< 2.4 \cdot 10^{-2}$	$(6.5 \pm 0.7)\cdot10^{-2}$	$< 2.9 \cdot 10^{-2}$	$< 2.5 \cdot 10^{-2}$	$< 6.7 \cdot 10^{-3}$	$< 1.5 \cdot 10^{-2}$	$< 6.8 \cdot 10^{-3}$
PMT SS	SS	248 (PMTs)	$(2.6 \pm 0.8)\cdot10^{-1}$	$(1.1 \pm 0.4)\cdot10^{-2}$	$< 6.5 \cdot 10^{-2}$	$< 3.9 \cdot 10^{-2}$	$< 5.0 \cdot 10^{-2}$	$(8.0 \pm 0.7)\cdot10^{-2}$	$< 1.6 \cdot 10^{-1}$	$< 1.9 \cdot 10^{-2}$
PMT Body	Kovar	248 (PMTs)	$< 1.4 \cdot 10^{-1}$	$< 6.4 \cdot 10^{-3}$	$< 3.1 \cdot 10^{-1}$	$< 4.9 \cdot 10^{-2}$	$< 3.7 \cdot 10^{-1}$	$(3.2 \pm 0.3)\cdot10^{-1}$	< 1.1	$< 1.2 \cdot 10^{-1}$

Table 6.2: Summary of the XENON1T material contaminations. For component description see Chapter 5.
Field cage[1]: TPC walls, PTFE plates of the PMT support structures, PTFE ring below the TPC, teflon pillars and cathode pillars, trapezoidal section ring on top of the TPC.
SS components[2]: top bell plate, top and bottom electrode rings.
Middle SS[3]: L-shaped ring, anode, gate and cathode electrode rings.

6.3 ER background from materials

Considering the contaminations given in table 6.2, decays from each component have been simulated. The events were generated from the proper isotope, confining its origin uniformly inside the volume of that component. The dangerous events are given by those γ produced by the isotope decay, that reach the internal volume of the active region, produce a low energy Compton scatter and leave the detector without other interactions. Given the small probability for such an event to occur, a huge number of generated events is needed; using the large amount of CPU available on the GRID, $\mathcal{O}(3 \cdot 10^9)$ decays for each component and isotope have been generated. Applying the selection cuts, mentioned in the introduction of the chapter, the number of survived events N_R is obtained; then the background rate is evaluated by scaling N_R for the effective lifetime T of the MC simulation:

$$T = N_G/(M_C \cdot A_C), \tag{6.2}$$

where N_G is the number of generated events, M_C is the mass and A_C the specific activity of the components given in table 6.2. Then, the rate R of events per unit of time, mass and energy is given by:

$$R = N_R/(T \cdot M_{FV} \cdot \Delta E), \tag{6.3}$$

where M_{FV} is the considered fiducial mass of LXe and ΔE is the width of the considered energy range for the ER. In the evaluation of the background rate, equation (6.3), there are two variables that are affected by errors: the activity, A_C, and the number of survived events, N_R. For what concerns the former, the errors are reported in table 6.2 while for the latter it is considered as a result of a Poissonian process thus the errors are evaluated as $\sqrt{N_R}$. In order to evaluate the error on R, the two contribution are considered as independent. Since the other terms in equation (6.3) can be treated as constant, R can be re-write as:

$$R = \frac{N_R}{M_{FV} \cdot \Delta E} \cdot \frac{M_C \cdot A_C}{N_G} = \alpha N_R A_C; \tag{6.4}$$

where

$$\alpha = \frac{1}{M_{FV} \cdot \Delta E} \cdot \frac{M_C}{N_G}$$

The error on R can be then evaluated through:

$$\delta_R = \sqrt{\sum_{x_i} \left(\frac{\partial R}{\partial x_i} \delta_{x_i} \right)^2}; \quad x_i = A_C,\ N_R \tag{6.5}$$

where δ_{x_i} are the errors on A_C and N_R. From equation (6.5) it results:

$$\delta_R = \alpha \sqrt{\left(N_R \delta_{A_C} \right)^2 + \left(A_C \delta_{N_R} \right)^2} \tag{6.6}$$

Equation (6.6) represents the error on the background rate for each isotope from each material. To obtain the error on the background from each component, summed over all the isotopes, the various δ_R have been summed in quadrature.
After the analysis of the simulation outputs we obtained the energy spectra from the electromagnetic recoils from each material, summed over all the isotopes, in a 1 tonne fiducial volume; the spectra, obtained considering the central value for the background rate, are shown in figures 6.4 and 6.5.

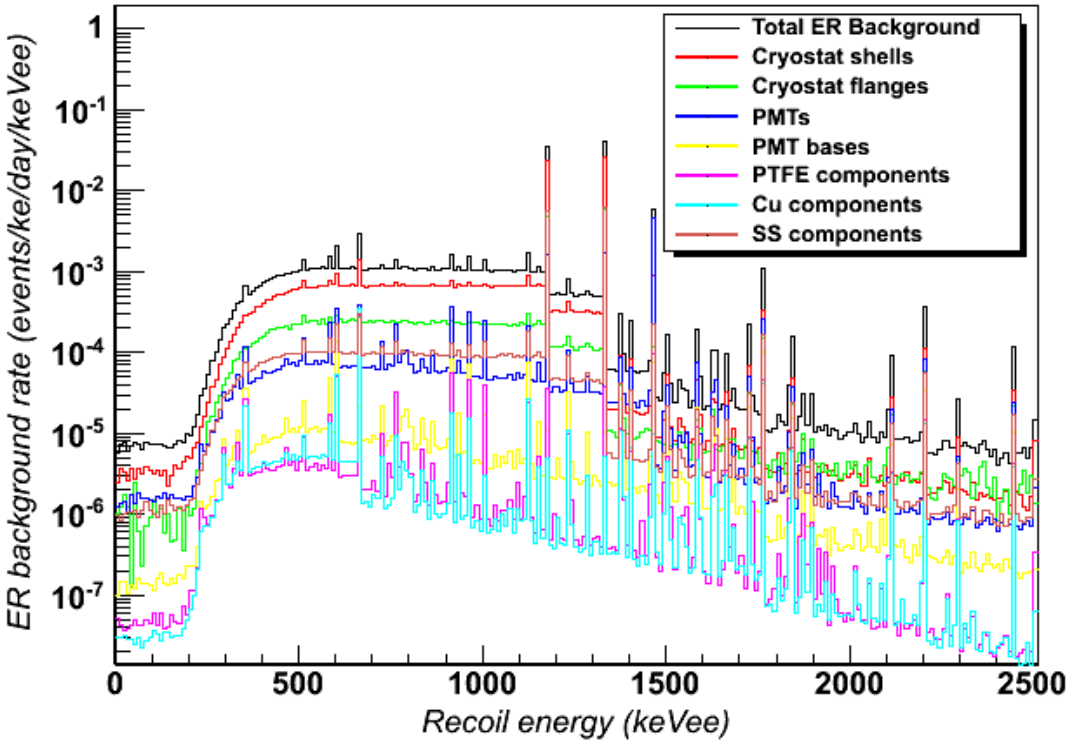

Figure 6.4: Energy spectra of the ER background in 1 tonne fiducial volume. Each curve corresponds to the background from a specific material, summed over all the isotopes.

From figures 6.4 and 6.5 it is possible to see that, for the chosen fiducial volume, the spectra are flat in the [1, 200] keV_{ee} window. This feature allows to estimate the background in [2, 12] keV_{ee} using a wider energy region, i.e. using more statistics, and then re-scale the value to the proper energy range. Going towards larger fiducial volumes this flat behavior is not longer true and it is mandatory to use directly the proper energy region. The spectra in figure 6.4 are given by Compton scattering together with various photo-absorption lines: 1460 keV_{ee} from ^{40}K, 1173 and 1333 keV_{ee} from ^{60}Co, etc. The positions of the electromagnetic recoils inside the TPC, considering the energy region

[2, 12] keV$_{ee}$, are shown in figure 6.6.

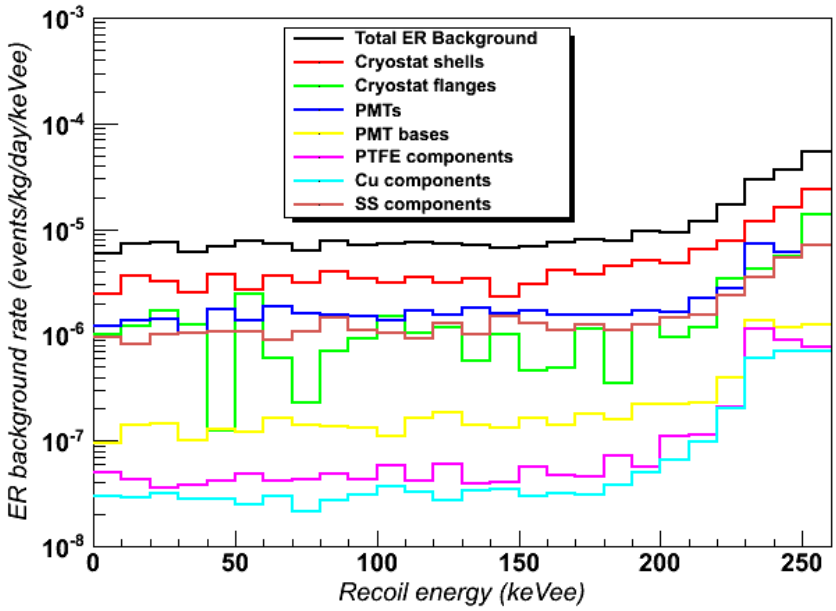

Figure 6.5: Same as figure 6.4 but with a zoom in the [0, 250] keV$_{ee}$ energy region; to have a more readable image, the number of bins with respect to the spectra in figure 6.4 have been reduced.

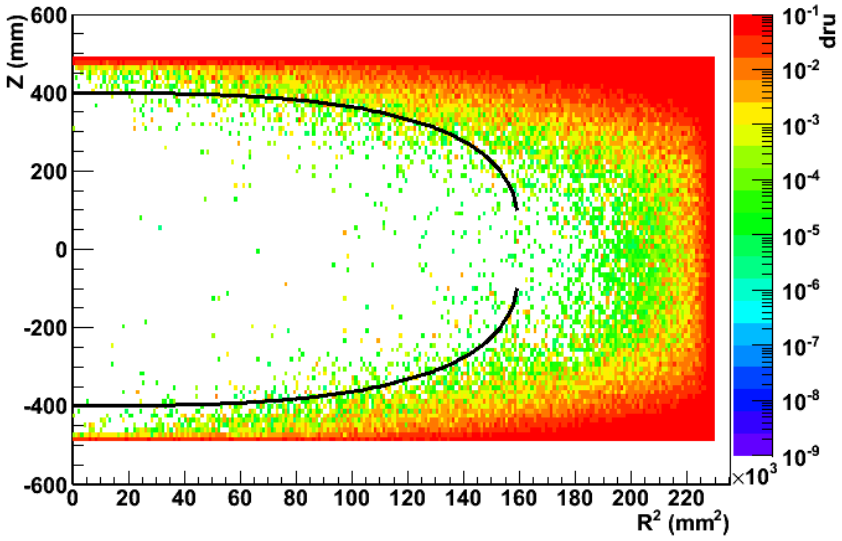

Figure 6.6: Electromagnetic background events distribution inside the XENON1T TPC, considering the [2, 12] keV$_{ee}$ energy region. The two black curves represent the 1 tonne fiducial volume. The dru is given by: 1 dru = 1 ev/kg/day/keV$_{ee}$.

The choice of the FV for dark matter search results from a compromise between the increase of the number of WIMP interactions and of the background events when including in the analysis also the outer layers of the active volume. It is then very useful to understand the behavior of the background as function of the fiducial volume: the results are shown in figures 6.7 and 6.8.

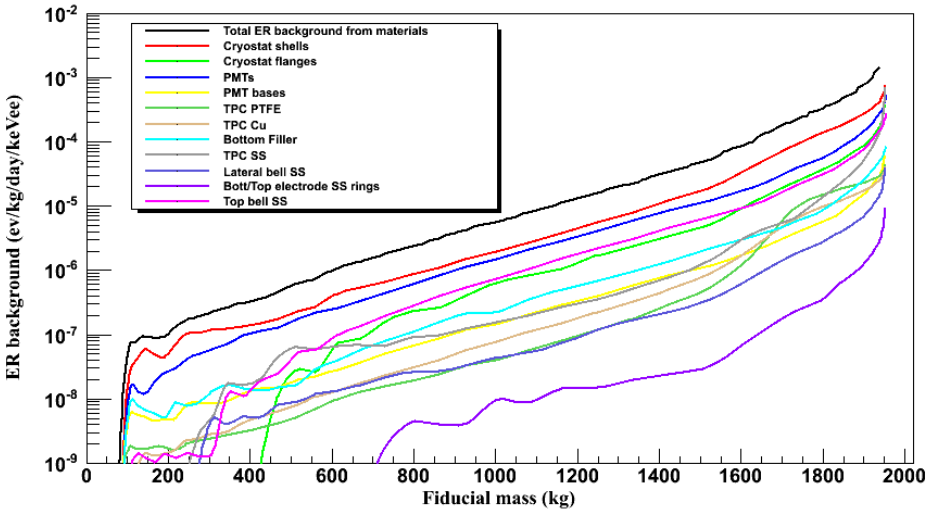

Figure 6.7: ER background from materials, as function of the fiducial volume, in the [2, 12] keV$_{ee}$ energy region.

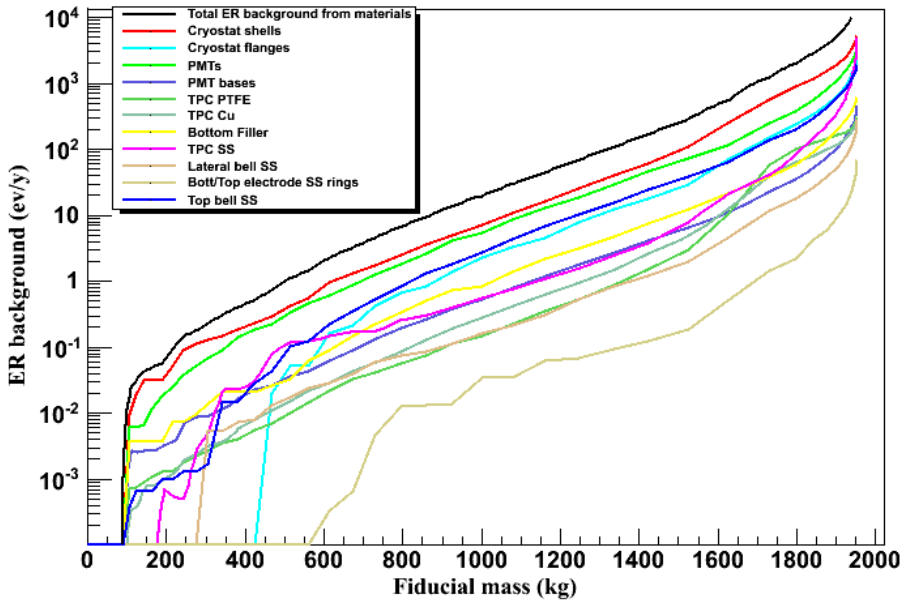

Figure 6.8: ER background from materials, in units of events per year (ev/y), as function of the fiducial volume, in the [2, 12] keV$_{ee}$ energy window.

Using the spectra in figure 6.4, the total ER background from each detector material, summing the contribution from the various isotopes, have been evaluated. The results are reported in table 6.3. Using the value shown in the table, the total amount of internal ER background, in the [2, 12] keV_{ee} energy region, is:

$$(\mathbf{7.3 \pm 0.3}) \cdot \mathbf{10^{-6}\ events/kg/day/keV}_{ee}, \tag{6.7}$$

or

$$\mathbf{27 \pm 1\ ev/y}, \tag{6.8}$$

considering a 1 tonne fiducial volume. A lower bound for the background level can be evaluated setting equal to zero all the contaminations that are reported as upper limits in table 6.2. In such a case, the total amount of background is:

$$(\mathbf{6.7 \pm 0.3}) \cdot \mathbf{10^{-6}\ ev/kg/day/keV}_{ee}, \tag{6.9}$$

or

$$\mathbf{25 \pm 1\ ev/y}, \tag{6.10}$$

Thus, the total amount of background from materials is in the range:

$$[\mathbf{6.7}^{\pm\mathbf{0.3}},\ \mathbf{7.3}^{\pm\mathbf{0.3}}] \cdot \mathbf{10^{-6}\ ev/kg/day/keV}_{ee}, \tag{6.11}$$

or

$$[\mathbf{25}^{\pm\mathbf{1}},\ \mathbf{27}^{\pm\mathbf{1}}]\ \mathbf{ev/y}\ \text{(in 1 tonne FV)}. \tag{6.12}$$

The contributions to the total amount of background from each component are shown in figure 6.9.

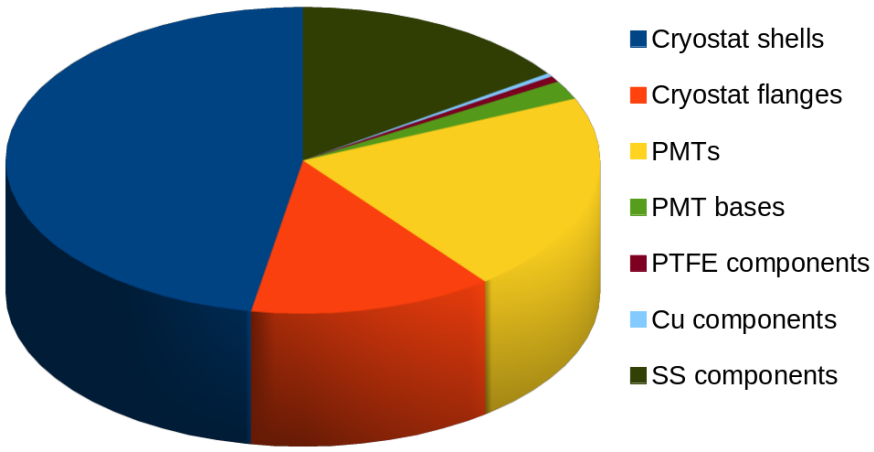

Figure 6.9: Contributions to the ER background from the various components of the detector.

Summary of material properties and contaminations

Component	ER background									
	(events/kg/day/keV$_{ee}$)									(events/year)
	^{238}U	^{226}Ra	^{232}Th	^{228}Th	^{60}Co	^{40}K	^{137}Cs	Total	%	Total
Cryostat shells	$< 1.1{\cdot}10^{-8}$	$(1.36 \pm 0.12){\cdot}10^{-7}$	$(1.44 \pm 0.49){\cdot}10^{-8}$	$(5.94 \pm 0.70){\cdot}10^{-8}$	$(3.15 \pm 0.29){\cdot}10^{-6}$	$(6.29 \pm 0.60){\cdot}10^{-8}$	$(5.5 \pm 2.1){\cdot}10^{-9}$	$\mathbf{(3.43 \pm 0.29){\cdot}10^{-6}}$	47.2	**12.5 ± 1.0**
Cryostat flanges	$< 6.5{\cdot}10^{-9}$	$(1.30 \pm 0.28){\cdot}10^{-7}$	$< 1.4{\cdot}10^{-9}$	$(1.34 \pm 0.41){\cdot}10^{-7}$	$(6.9 \pm 1.1){\cdot}10^{-7}$	$(1.31 \pm 0.39){\cdot}10^{-8}$	$< 5.5{\cdot}10^{-9}$	$\mathbf{(9.7 \pm 1.2){\cdot}10^{-7}}$	13.3	**3.53 ± 0.44**
PMT	$(2.4 \pm 1.4){\cdot}10^{-8}$	$(1.79 \pm 0.37){\cdot}10^{-7}$	$(8.1 \pm 1.7){\cdot}10^{-8}$	$(1.17 \pm 0.15){\cdot}10^{-7}$	$(3.94 \pm 0.19){\cdot}10^{-7}$	$(7.33 \pm 1.15){\cdot}10^{-7}$	$(5.96 \pm 0.67){\cdot}10^{-9}$	$\mathbf{(1.53 \pm 0.13){\cdot}10^{-6}}$	21.1	**5.60 ± 0.46**
PMT bases	$< 1.7{\cdot}10^{-8}$	$(8.05 \pm 0.76){\cdot}10^{-8}$	$(2.36 \pm 0.35){\cdot}10^{-8}$	$(2.39 \pm 0.26){\cdot}10^{-8}$	$(2.03 \pm 0.07){\cdot}10^{-9}$	$(1.23 \pm 0.28){\cdot}10^{-8}$	$(2.29 \pm 0.31){\cdot}10^{-10}$	$\mathbf{(1.45 \pm 0.10){\cdot}10^{-7}}$	2.0	**0.53 ± 0.03**
Field cage$^{(1)}$	$(3.3 \pm 1.5){\cdot}10^{-9}$	$(1.66 \pm 0.08){\cdot}10^{-8}$	$(7.09 \pm 0.43){\cdot}10^{-9}$	$(4.36 \pm 0.26){\cdot}10^{-9}$	$(4.7 \pm 1.2){\cdot}10^{-9}$	$(8.03 \pm 0.25){\cdot}10^{-9}$	$(2.98 \pm 0.60){\cdot}10^{-9}$	$\mathbf{(4.70 \pm 0.19){\cdot}10^{-8}}$	0.6	**0.17 ± 0.01**
Copper components	$(2.5 \pm 1.3){\cdot}10^{-10}$	$(1.94 \pm 0.56){\cdot}10^{-8}$	$(2.46 \pm 0.83){\cdot}10^{-9}$	$(3.1 \pm 1.0){\cdot}10^{-9}$	$(6.6 \pm 3.3){\cdot}10^{-10}$	$(8.8 \pm 2.3){\cdot}10^{-10}$	$(4.77 \pm 0.44){\cdot}10^{-9}$	$\mathbf{(3.15 \pm 0.58){\cdot}10^{-8}}$	0.4	**0.12 ± 0.02**
Bottom Filler	$< 1.1{\cdot}10^{-8}$	$(9.5 \pm 3.1){\cdot}10^{-9}$	$(5.31 \pm 2.17){\cdot}10^{-9}$	$(2.95 \pm 0.70){\cdot}10^{-8}$	$(9.05 \pm 1.14){\cdot}10^{-8}$	$(1.81 \pm 0.28){\cdot}10^{-9}$	$< 3.9{\cdot}10^{-10}$	$\mathbf{(1.37 \pm 0.14){\cdot}10^{-7}}$	1.9	**0.50 ± 0.05**
Middle SS$^{(2)}$	$< 1.4{\cdot}10^{-9}$	$(1.10 \pm 0.39){\cdot}10^{-8}$	$< 1.5{\cdot}10^{-10}$	$< 3.3{\cdot}10^{-9}$	$(1.06 \pm 0.22){\cdot}10^{-7}$	$(2.31 \pm 0.64){\cdot}10^{-9}$	$< 3.9{\cdot}10^{-10}$	$\mathbf{(1.22 \pm 0.23){\cdot}10^{-7}}$	1.7	**0.44 ± 0.08**
Lateral Bell	$< 5.1{\cdot}10^{-8}$	$(1.61 \pm 0.92){\cdot}10^{-8}$	$< 5.9{\cdot}10^{-10}$	$(6.6 \pm 3.7){\cdot}10^{-9}$	$(5.1 \pm 2.6){\cdot}10^{-8}$	$(4.9 \pm 2.6){\cdot}10^{-9}$	$< 3.9{\cdot}10^{-10}$	$\mathbf{(7.9 \pm 2.9){\cdot}10^{-8}}$	1.1	**0.29 ± 0.10**
Bottom/Top Ring	$< 2.5{\cdot}10^{-9}$	$< 6.6{\cdot}10^{-10}$	$< 1.5{\cdot}10^{-10}$	$< 2.6{\cdot}10^{-10}$	$< 3.6{\cdot}10^{-9}$	$< 2.6{\cdot}10^{-10}$	$< 3.9{\cdot}10^{-10}$	$\mathbf{(1.4 \pm 1.2){\cdot}10^{-9}}$	0.02	**0.005 ± 0.004**
Top Bell Plate	$< 2.5{\cdot}10^{-9}$	$(2.59 \pm 0.24){\cdot}10^{-8}$	$(4.5 \pm 1.4){\cdot}10^{-9}$	$(1.09 \pm 0.10){\cdot}10^{-8}$	$(7.18 \pm 0.66){\cdot}10^{-7}$	$(1.69 \pm 0.12){\cdot}10^{-8}$	$(2.75 \pm 0.63){\cdot}10^{-9}$	$\mathbf{(7.80 \pm 0.66){\cdot}10^{-7}}$	10.7	**2.85 ± 0.24**
Total	$(3.1 \pm 1.4){\cdot}10^{-8}$	$(6.24 \pm 0.50){\cdot}10^{-7}$	$(1.40 \pm 0.18){\cdot}10^{-7}$	$(3.91 \pm 0.45){\cdot}10^{-7}$	$(5.21 \pm 0.32){\cdot}10^{-6}$	$(8.56 \pm 1.16){\cdot}10^{-7}$	$(2.22 \pm 0.24){\cdot}10^{-8}$	$\mathbf{(7.27 \pm 0.34){\cdot}10^{-6}}$	100	**26.5 ± 1.3**
%	0.4	8.6	1.9	5.4	71.6	11.8	0.3	100		100

Table 6.3: Summary of the total material background. The ev/y background is evaluated for 1 tonne fiducial volume.
Field cage$^{(1)}$: TPC walls, PTFE plates of the PMT support structures, PTFE ring below the TPC, teflon pillars and cathode pillars, trapezoidal section ring on top of the TPC.
Middle SS$^{(2)}$: L-shaped ring, gate, anode and cathode electrode rings.
The upper limits have been evaluated considering 3 survived events for the isotopes that gives less than 3 events after the analysis of the simulations (to quantify the total background, the real number of survived events has been considered).
In table 6.2 are reported the contaminations used for the present study.

The highest contribution comes from the cryostat shells, about half of the total ER background from materials, mainly from ^{60}Co; the PMTs contribute about 20% and the other SS components give about 15%. The contribution from PTFE and Copper is about 1%. The amount of events from material contaminations are acceptable for the XENON1T aim because, as it will be shown in sections 6.4 and 6.5, it is still smaller than the background from the intrinsic sources.

6.3.1 Trigger rate

From the same simulations used for the estimation of the internal background, it is possible to quantify the expected trigger rate due to the electromagnetic recoils in the whole LXe volume without considering any energy or volume cuts. For this analysis we considered both single and multiple scatters, with the only requirement of having a S2 signal greater than 150 pe (that is the current threshold for the XENON100 signals). Considering the contaminations of the materials already described in this section, the value for the trigger rate from electromagnetic recoils, due to the internal background, is shown in table 6.4.

Component	**Trigger rate (Hz)**
Cryostat shells	0.786
Cryostat flanges	0.504
PMT (bases)	0.206
PMT bases	0.032
TPC + other PTFE components	0.038
Copper components	0.007
SS components	0.559
Total	**2.13**

Table 6.4: Expected trigger rate, from internal background, for the XENON1T detector.

The final value of the event rate is totally acceptable for the data acquisition system of the XENON1T experiment.

6.4 Intrinsic ER background

The **intrinsic background** is another source of dangerous events. It is due to some radioactive isotopes that are uniformly distributed in LXe (^{85}Kr, ^{222}Ra and ^{136}Xe) and to some other physics processes such as solar neutrino recoils. The first three isotopes

are found naturally in the Xe and to lower their contribution it is necessary to reduce their concentration using proper purification (for ^{85}Kr and ^{222}Ra) and depletion (for ^{136}Xe) techniques. For the neutrinos, the only chance to reduce their contribution to the electromagnetic background is to increase the rejection power for the ER band.
For what concerns the values reported for the background rates in the energy region of interest, the errors have been assumed to be 20% mainly due to the available data and knowledge about the low energy part of the recoil spectra. In drawing the recoil spectra, we considered only the central values of the background rates.

6.4.1 ^{85}Kr

The Kr is naturally found mixed with the Xe and its typical contamination, $^{\text{nat}}$Kr/Xe, is at level of part per million (ppm). What is dangerous is the isotope ^{85}Kr, mainly produced in nuclear reprocessing plants. Its relative isotopic abundance in Europe has been determined, by low level counting, to be $2 \cdot 10^{-11}$ g/g [207]. ^{85}Kr is a beta emitter characterized by a half life of $T_{1/2} = 10.76$ y and an end-point energy of 687 keV$_{ee}$. The low energy part of its spectrum is the most dangerous since it overlaps with the WIMP search energy region, figures 6.13 and 6.14 (blue curve). Since this element is uniformly distributed in the Xe it is not possible to reduce its contribution to the background through volume fiducialization. A new high through-put and high separation cryogenic distillation column will be used to reduce the $^{\text{nat}}$Kr concentration to 0.2 ppt [mol/mol], that is the goal from the Xe purification for XENON1T (during the XENON100 operations the concentration was 19 ± 4 ppt [8]). From such an amount of ^{85}Kr, the total activity for this impurity is of $3.75 \cdot 10^{-5}$ mBq/kg. Using such a contamination, the background rate from ^{85}Kr is:

$$(\mathbf{7.6 \pm 1.5}) \cdot \mathbf{10^{-6}}\ \mathbf{ev/kg/day/keV}_{ee}, \tag{6.13}$$

in [2,12] keV$_{ee}$, very close to the value from the materials.

6.4.2 ^{222}Rn

The ^{222}Rn is part of the ^{238}U decay chain. As the Kr, also Rn can fill uniformly the LXe volume, especially thanks to its half life (3.8 days). It can emanate from detector materials and getter, or diffuse through the seals. Looking at its decay chain, figure 6.10, until the long-lived ^{210}Pb ($T_{1/2} = 22$ y) there are two β emitters: the ^{214}Pb and, its daughter, ^{214}Bi. The latter is not dangerous since it is possible to tag its β decay using the α decay of the ^{214}Po, its daughter, that happens about 160 μs after its parent decay.

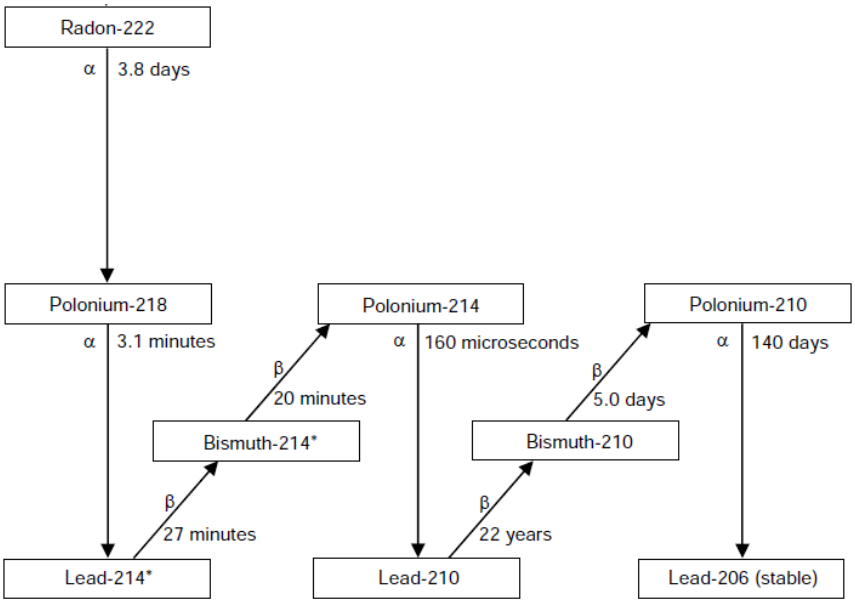

Figure 6.10: ^{222}Rn decay chain.

More dangerous is the ^{214}Pb decay into the ^{214}Bi, with an end-point of 1023 keV$_{ee}$. In particular its decay into the Bi ground state is the most dangerous (6.6% branching ratio from GEANT4 code) because in this case there are not other γ emitted. However, also the decays in other energy levels can be dangerous if the following γ is not tagged. This can happen especially close to the TPC walls where there is a finite probability that the accompanying γ can exit the detector without depositing energy and being detected. This is responsible for the slightly higher background rate from ^{222}Rn seen at larger fiducial masses in figure 6.15 (red curve). To reduce the ^{222}Rn concentration, XENON1T is foreseen to be equipped with a radon removal system, aiming at the constant purification of the LXe target from emanated radon during detector operation, through the use of either adsorption or cryogenic distillation techniques. The goal for XENON1T will be to reach a ^{222}Rn contamination of 1 μBq/kg, a reduction of a factor $\sim$ 50 with respect to the current values reached in XENON100. Considering such a contamination, the ER background in 1 tonne fiducial volume and in [2,12] keV$_{ee}$ is

$$(\mathbf{9 \pm 2}) \cdot \mathbf{10^{-6}}\ \mathbf{ev/kg/day/keV}_{ee} \tag{6.14}$$

The ^{222}Rn recoil spectrum is shown in figures 6.13 and 6.14 (red curve).

6.4.3 Solar neutrinos

Solar neutrinos can scatter elastically off the electrons of the medium, producing electron recoils in the low energy region. For the background estimation we considered neutrinos

from the pp chain and the ^{7}Be lines, taking into account neutrino oscillation $\nu_e \rightarrow \nu_x$ and the reduced cross section for ν_x [208]. The resulting recoil energy spectrum is shown in figure 6.13 and 6.14 (green curve). Most of the interactions (92%) come from pp neutrinos, ^{7}Be contributes with 7%, pep and all the others sources with less than 1%. The differential rate can be parameterized as:

$$(9.155 - 0.036 \cdot E_R/\mathrm{keV}_{ee}) \cdot 10^{-6}\ \mathrm{ev/kg/day/keV}_{ee}, \tag{6.15}$$

where E_R is the recoil energy. The average background rate in the energy region [2,12] keV_{ee} is

$$\mathbf{(9 \pm 2) \cdot 10^{-6}\ ev/kg/day/keV}_{ee}. \tag{6.16}$$

This source of background of course cannot be reduced, the only way to mitigate its impact is to improve the discrimination of NR from ER, figure 4.16.

6.4.4 $2\nu2\beta$ decay

The $2\nu2\beta$ decay is due to the ^{136}Xe isotope. Its typical abundance is about 8.9% in the natural Xe; it has a $Q-$value of 2458 keV_{ee} and a $\mathrm{T}_{1/2} = 2.23 \cdot 10^{3}$ y [209]. As for the solar neutrinos, also in this case a parameterisation of the energy spectrum has been considered, figure 6.13 and 6.14 (brown curve), using the Primakoff-Rosen approximation [210]:

$$\frac{dN}{dK} \sim K(T_0 - K)^5\Big(1 + 2K + \frac{4}{3}K^2 + \frac{1}{3}K^3 + \frac{1}{30}K^4\Big). \tag{6.17}$$

In equation (6.17) K is the total kinetic energy of the electrons, T_0 is the $Q-$value of the decay (2458 keV_{ee}) and all the quantities are expressed in units of the electron mass. In order to check the goodness of the previous formula, we also compared this parameterisation with a simulation made with the code DECAY0 [211], a specific tool to generate the energy spectrum of the electrons coming from the double beta decay. We generated $1 \cdot 10^{5}$ events obtaining a full agreement, figure 6.11, with the result of equation (6.17).

This agreement is of particularly importance since DECAY0 does not use the Primakoff-Rosen approximation [212], hence it is an independent calculation.
At low energies, the spectrum parameterisation can be expressed as:

$$(3.5 \ \cdot \ E_R/\mathrm{keV}_{ee})\ 10^{-6}\ \mathrm{ev/kg/day/keV}_{ee}, \tag{6.18}$$

where E_R is the recoil energy. The average background rate in the energy region [2, 12] keV_{ee} is

$$\mathbf{(3 \pm 1) \cdot 10^{-6}\ ev/kg/day/keV}_{ee}. \tag{6.19}$$

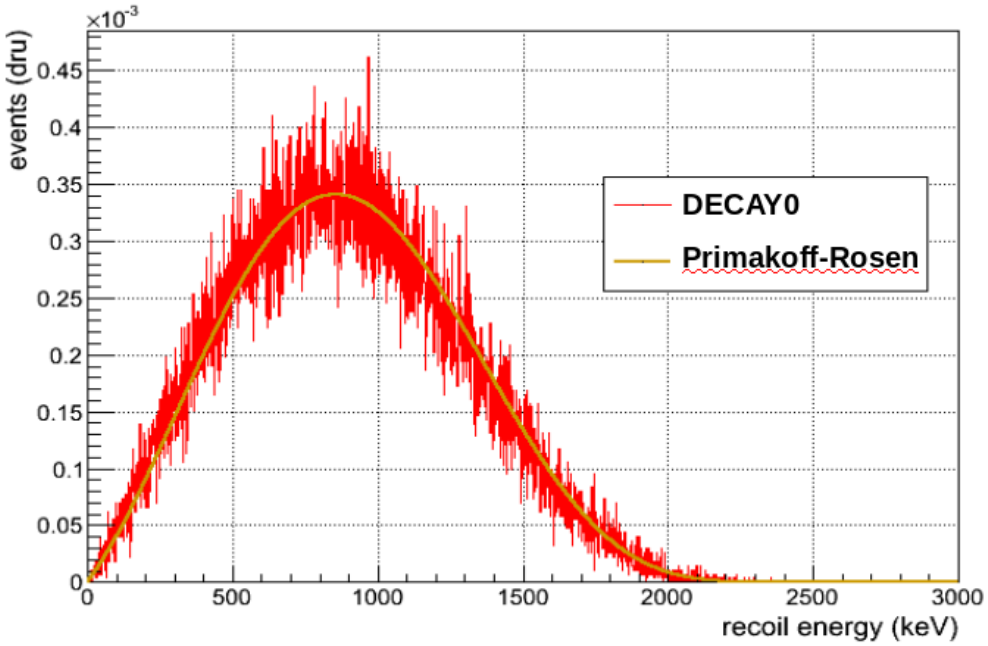

Figure 6.11: Comparison between the parameterized energy recoil spectrum (dark yellow) and the output of the DECAY0 code (red plot).

6.5 Summary of the ER backgrounds

A summary of the various contributions to the total electromagnetic background is shown in table 6.5 and figure 6.12.

Source	**background (ev/kg/day/keV$_{ee}$)**	**background (ev/y)**	**% contribution**
materials	$(7.27 \pm 0.34) \cdot 10^{-6}$	26.5 ± 1.3	20.5
^{222}**Rn**	$(8.88 \pm 1.78) \cdot 10^{-6}$	32.4 ± 6.5	25.1
^{85}**Kr**	$(7.64 \pm 1.53) \cdot 10^{-6}$	27.9 ± 5.6	21.6
solar neutrinos	$(8.89 \pm 1.78) \cdot 10^{-6}$	32.4 ± 6.5	25.2
$2\nu2\beta$ **decay**	$(2.70 \pm 0.54) \cdot 10^{-6}$	9.9 ± 2.0	7.6
Total	$\mathbf{(3.54 \pm 0.30) \cdot 10^{-5}}$	$\mathbf{129 \pm 11}$	**100**

Table 6.5: Summary of the total intrinsic and internal ER background. The ev/y background is evaluated for a 1 tonne of fiducial volume. The errors on the intrinsic sources are 20% due to the uncertainties about the knowledge on the low energy part of the recoil energy spectra.

In figures 6.13 and 6.14 are shown the recoil spectra of the intrinsic and internal background sources. As already done in the case of the internal background, also for the intrinsic one its behavior, as function of the fiducial mass, has been studied. The results

are shown in figures 6.15-6.17.

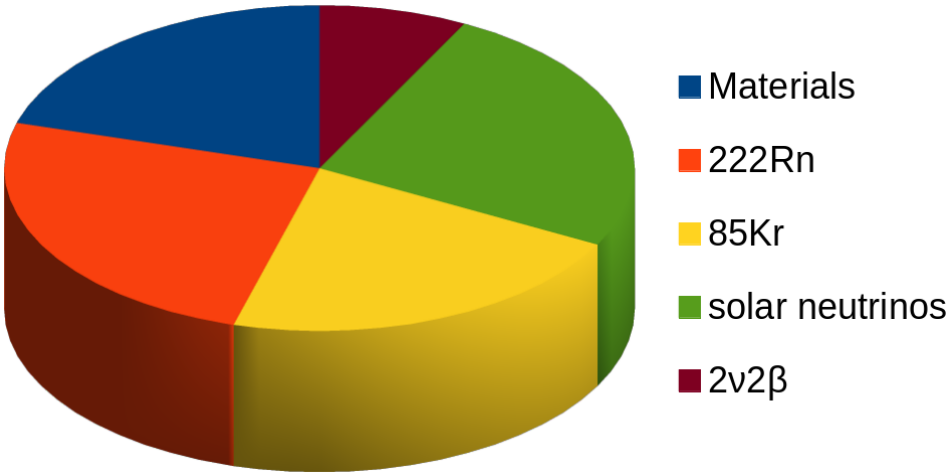

Figure 6.12: Contributions to the total ER background from materials and from the various intrinsic sources in [2, 12] keV$_{ee}$ and 1 tonne FV.

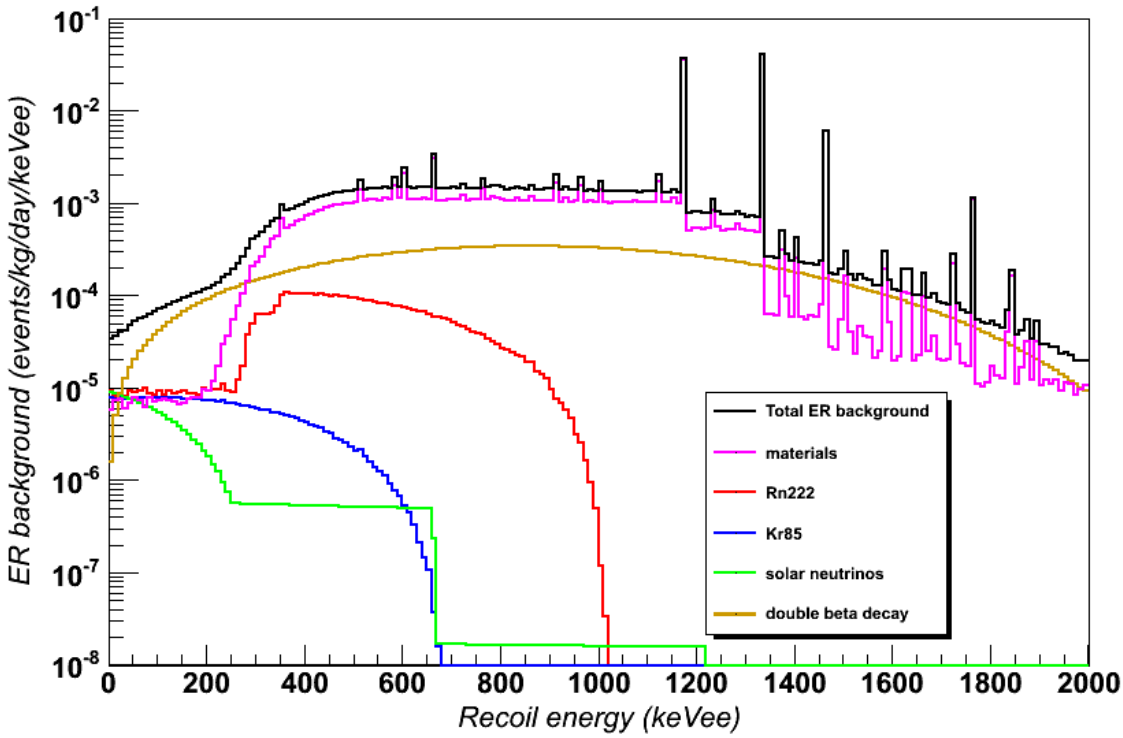

Figure 6.13: Total ER spectrum (black curve) and spectra from materials and from each intrinsic contamination, in 1 tonne fiducial volume.

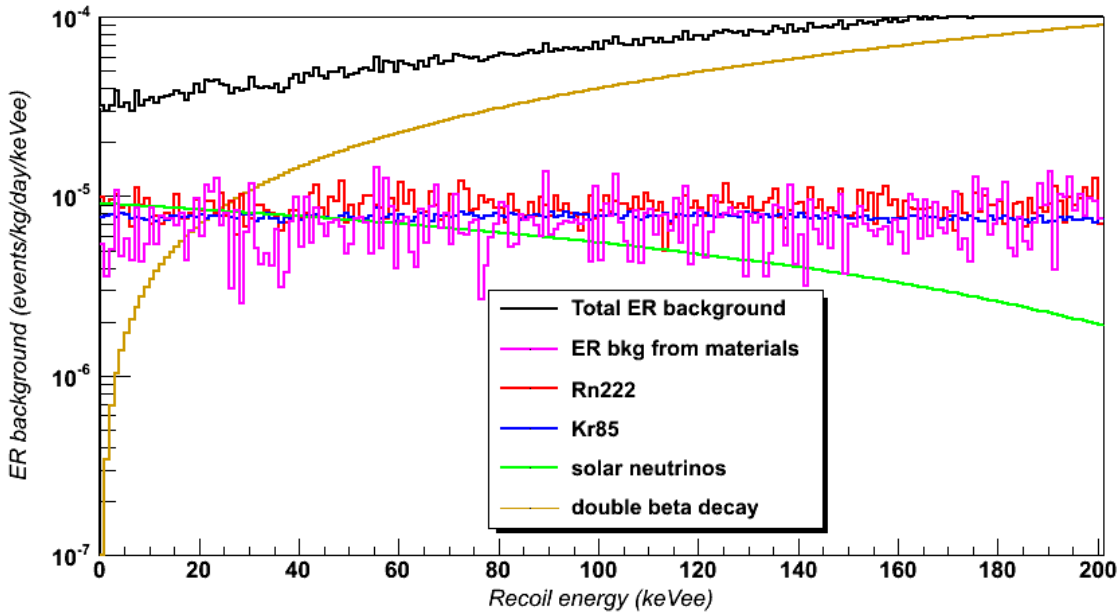

Figure 6.14: Same as figure 6.13 but with a zoom in the region [0, 200] keV_{ee}.

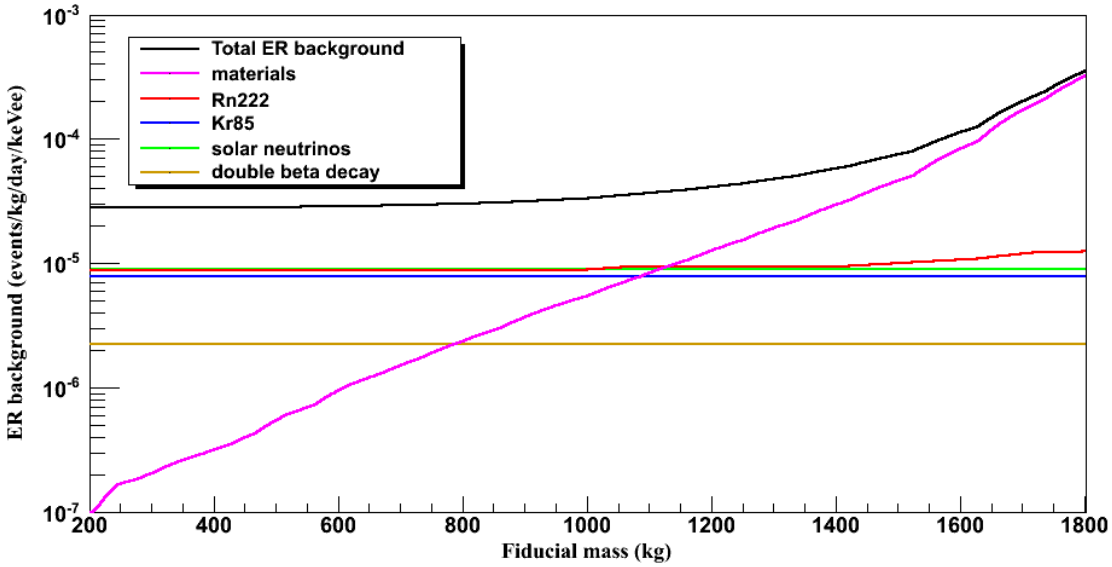

Figure 6.15: Electromagnetic background, as function of the fiducial mass, in the [2, 12] keV_{ee} energy region. As expected, the background from the intrinsic sources does not depend on the mass with the exception of the slightly rise of the ^{222}Rn at higher fiducial masses due to the finite probability of the γ, from the decay into ^{214}Bi, to escape through the TPC walls without being tagged.

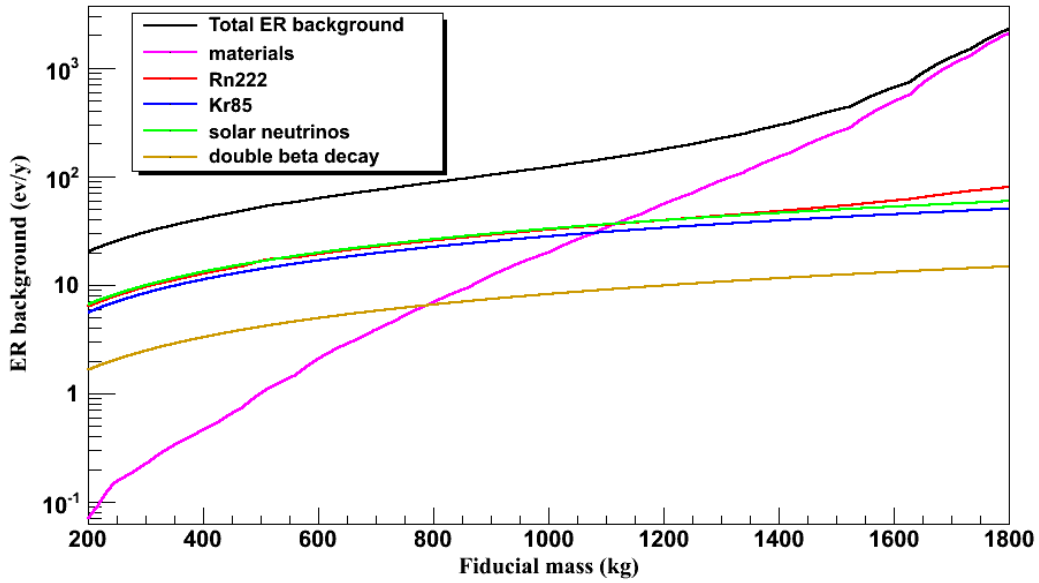

Figure 6.16: Electromagnetic background as function of the fiducial mass (ev/y), in the [2, 12] keV$_{ee}$ energy window.

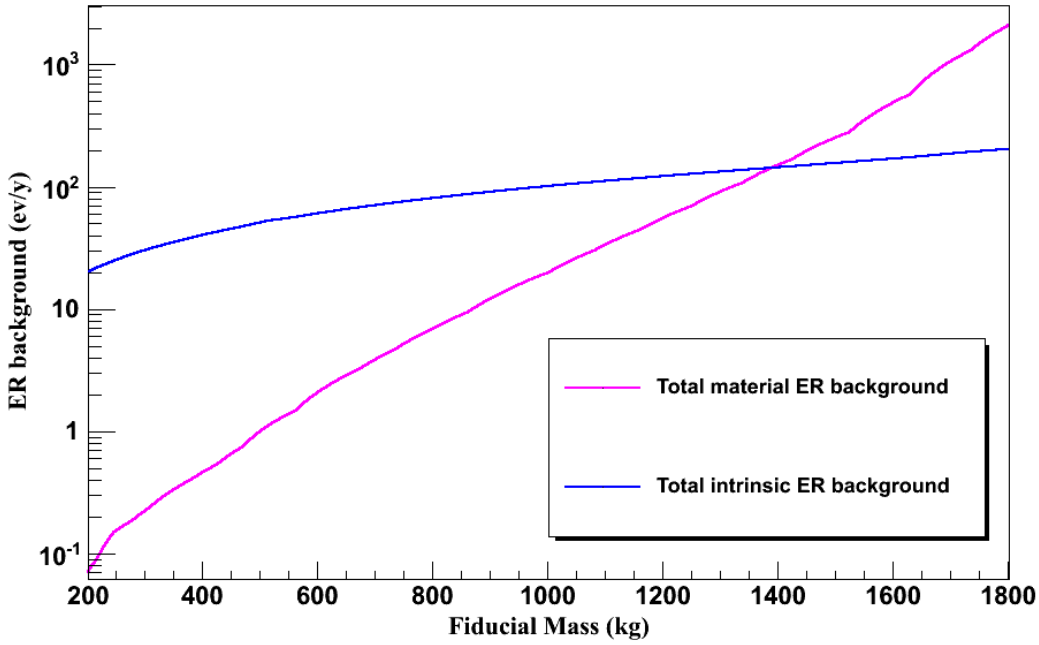

Figure 6.17: Comparison between intrinsic (blue line) and material (magenta line) total ER background, as function of the fiducial volume, in the [2, 12] keV$_{ee}$ energy region.

From the analysis of the internal and intrinsic ER backgrounds it is, finally, possible

to conclude that:

- in [2, 12] keV$_{ee}$ and in 1 tonne fiducial volume the main contributions to the ER background come from ^{222}Rn, solar neutrinos and ^{85}Kr (figures 6.12 - 6.16);
- for energies above 300 keV$_{ee}$, in 1 tonne fiducial volume, the detector materials give the highest contribution (figure 6.13).
- in [2, 12] keV$_{ee}$ and for fiducial volumes larger than 1400 kg, the background from detector materials becomes dominant (figure 6.17);
- in the energy range [20, 300] keV$_{ee}$, in 1 tonne fiducial volume, the $2\nu2\beta$ decay of the ^{136}Xe becomes dominant (figures 6.13 and 6.14).

6.6 Nuclear recoil background

Neutrons can produce single NR via elastic scattering with xenon nuclei and generate a signal which is, on an event-by-event basis, indistinguishable from that of WIMPs. Moreover, fast neutrons are more penetrating than γ-rays in LXe (Section 3.2), their mean free path being of the order of tens of cm, so either it is more difficult to shield them and also their probability to have a single scatter in the LXe active volume is higher than γ. It is therefore crucial to minimize and accurately characterize this potentially dangerous background. The presence of ^{238}U, ^{235}U and ^{232}Th in the detector materials generates radiogenic neutrons in the MeV energy range through spontaneous fission (SF), mainly from ^{238}U and (α, n) reactions induced by the α emitted along the chains. Additionally, cosmogenic neutrons, with energies extending to tens of GeV, are produced by muons along their path through the rock into the underground laboratory and through the materials that surround the detector.

6.6.1 Radiogenic neutrons from the materials

The radiogenic neutron production rates and energy spectra have been calculated with the SOURCES-4A software [213], modified by the group of the University of Sheffield in order to extend the cross sections for (α, n) reactions from 6.5 MeV to 10 MeV, based on available experimental data [214]. The calculation was performed with the assumption that the α-emitters are uniformly distributed within a homogeneous material. The systematic uncertainty on the neutron production rate of the SOURCES-4A code is 17%. A cross-check of the calculations of the neutron production was performed [215] with an independent software described in [216], showing agreement in neutron rates to within 20%. The neutron production rates for all the materials considered in the

background estimation are presented in table 6.6, considering also chain disequilibrium. The neutron yield from SF ($1.1 \cdot 10^{-6}$ neutrons per each Uranium decay) is included in the ^{238}U column.

Material	**Neutron yield (neutron/decay)**				
	^{238}U	^{235}U	^{226}Ra	^{232}Th	^{228}Th
Stainless Steel	$1.1 \cdot 10^{-6}$	$4.11 \cdot 10^{-7}$	$3.11 \cdot 10^{-7}$	$1.81 \cdot 10^{-9}$	$2.01 \cdot 10^{-6}$
PTFE (CF_2)	$7.41 \cdot 10^{-6}$	$1.31 \cdot 10^{-4}$	$5.51 \cdot 10^{-5}$	$7.31 \cdot 10^{-7}$	$1.01 \cdot 10^{-4}$
Copper	$1.11 \cdot 10^{-6}$	$3.31 \cdot 10^{-8}$	$2.51 \cdot 10^{-8}$	$3.01 \cdot 10^{-11}$	$3.61 \cdot 10^{-7}$
Ceramic (Al_2O_3)	$1.21 \cdot 10^{-6}$	$1.31 \cdot 10^{-5}$	$6.01 \cdot 10^{-6}$	$9.21 \cdot 10^{-9}$	$1.41 \cdot 10^{-5}$
Quartz (SiO_2)	$1.21 \cdot 10^{-6}$	$1.91 \cdot 10^{-6}$	$8.81 \cdot 10^{-7}$	$6.81 \cdot 10^{-9}$	$1.91 \cdot 10^{-6}$
Kovar	$1.11 \cdot 10^{-6}$	$1.31 \cdot 10^{-7}$	$1.21 \cdot 10^{-7}$	$3.01 \cdot 10^{-11}$	$1.01 \cdot 10^{-6}$
Cirlex ($C_{22}H_{10}N_2O_5$)	$1.31 \cdot 10^{-6}$	$2.21 \cdot 10^{-6}$	$3.51 \cdot 10^{-6}$	$4.11 \cdot 10^{-8}$	$2.41 \cdot 10^{-6}$

Table 6.6: Neutron production rates for the material of the XENON1T experiment. The results are expressed as neutrons emitted for each disintegration of the parent element in the chain.

The highest (α, n) yields are from light materials like PTFE and the ceramic of the PMT stem because of the high Coulomb barrier of heavy nuclei, which suppresses the (α, n) interaction; for heavy nuclei the neutron production is almost entirely due to SF. Among the various contaminants, we note that the neutron emission from the first part of the ^{232}Th chain is negligible. In figures 6.18 and 6.19 are shown the neutron energy spectra for two materials: PTFE (low Z) and Copper (high Z). For each detector component listed in table 6.2, 10^7 neutrons have been generated with the proper energy spectrum. We have selected the events that mimic a WIMP signal, i. e. those with a single elastic scatter in the active volume; then the results have been scaled for the neutron yield of the material, table 6.6, and the contamination, table 6.2, of the component. The energy spectrum of the total NR background from the materials, in a 1 tonne fiducial volume, is shown in figure 6.20. Considering, for instance, the [5, 50] keV$_r$ energy range (which allows to contain about 70% of the NR from a 100 GeV/c^2 WIMP) the background rate is:

$$\mathbf{0.5 \pm 0.1\ ev/y}\ \text{in (1 tonne FV)} \tag{6.20}$$

Thanks to the number of simulated events, the statistical error is negligible. The only source of uncertainty is due to the systematic error on the neutron production rate that is about 20%, as said at the beginning of this subsection. Figure 6.20 has been done considering the central value for the background rate.

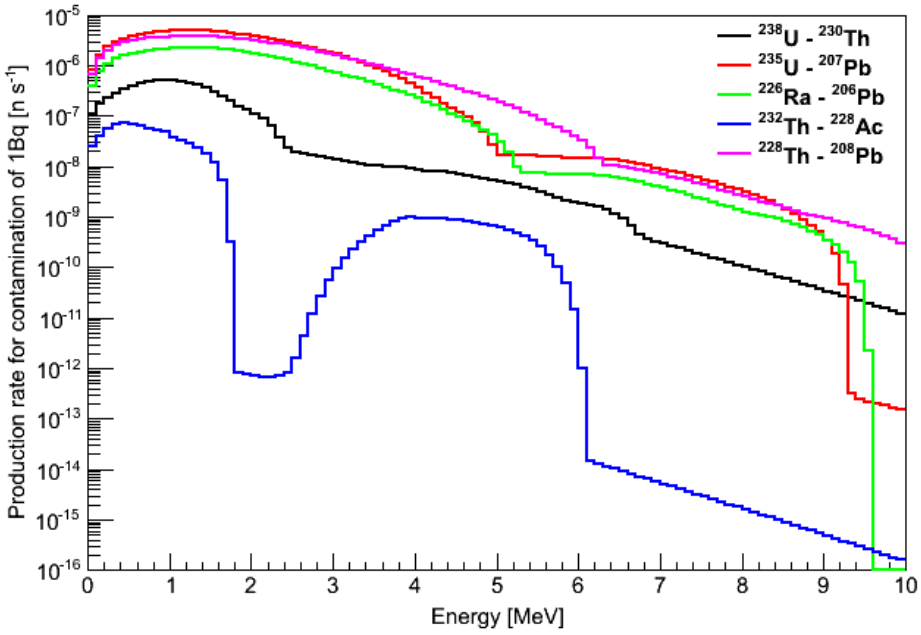

Figure 6.18: Differential rate of the neutrons produced from SF and (α, n) reaction in PTFE, for a contamination of 1 Bq.

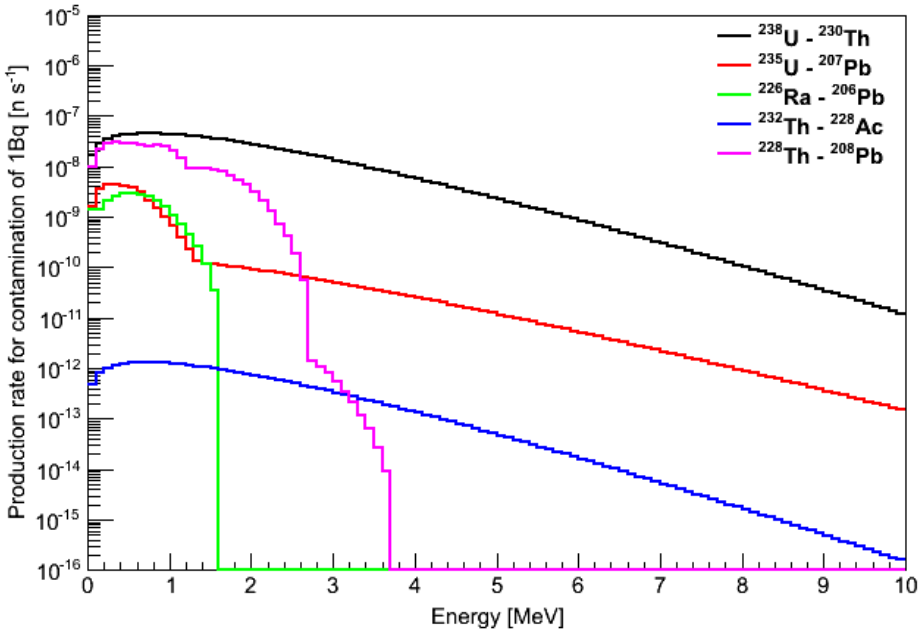

Figure 6.19: Differential rate of the neutrons produced from SF and (α, n) reaction in Copper, for a contamination of 1 Bq.

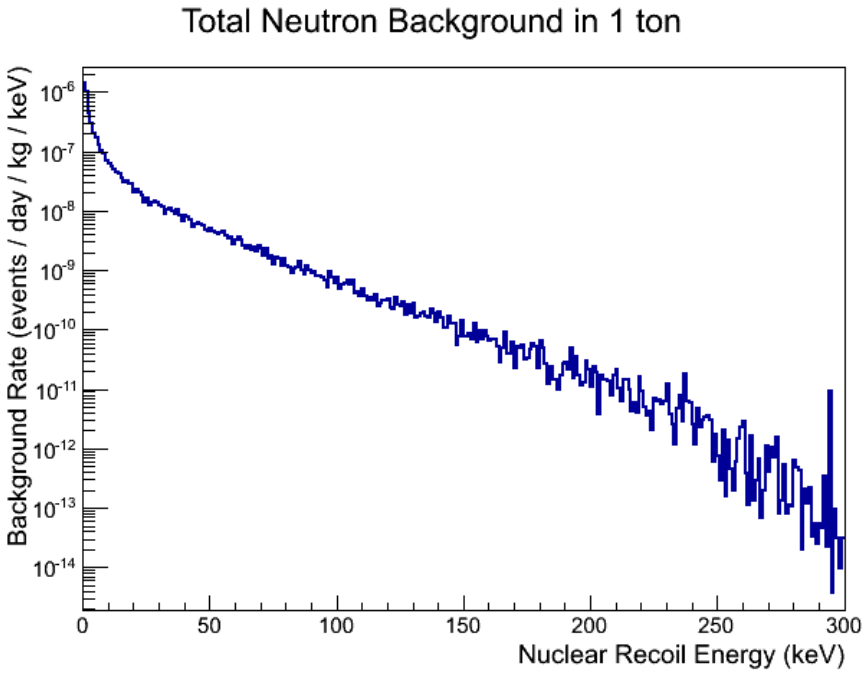

Figure 6.20: Energy spectrum of the nuclear recoil background events from the neutrons of the detector materials, in the 1 tonne fiducial mass.

The largest fraction of background events comes from the Cryostat SS (28%), then the PMTs (23%, mostly from the ceramic stem), PTFE (18%), PMT bases (12%), SS of the TPC (10%) and of the Bottom Filler (8%), figure 6.21.

Figure 6.21: Fraction of NR background events from the various detector components.

The position of the NR background events inside the LXe active volume, in the [5, 50] keV$_r$ energy region is shown in figure 6.22 and the background rate, as function of the fiducial mass, is shown in figure 6.23 for three choices of the energy region of interest.

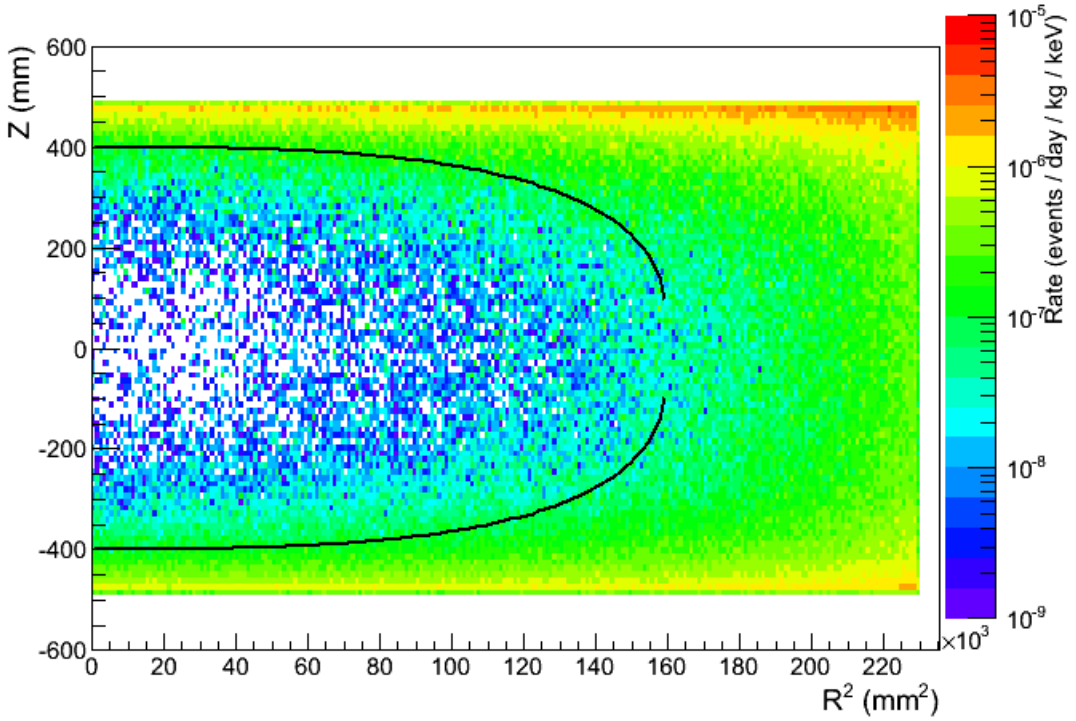

Figure 6.22: Spatial distribution, in the LXe active volume, of the NR background events in the [5, 50] keV$_r$ energy range. The black lines represent the 1-t fiducial volume.

6.6.2 Muon-induced neutrons

The contribution from cosmogenic neutrons, produced by the interaction of high energy muons in the Gran Sasso rock, is negligible. Indeed, thanks to the Muon Veto system of XENON1T [204] (Section 4.4.1), the background from muon induced neutrons is below 0.01 ev/y in 1 tonne fiducial volume inside the WIMP search energy region. Therefore this potential source of background will not be considered in the estimation of the sensitivity.

6.7 Conversion from energy to S1 and S2 signals

To evaluate the sensitivity of the XENON1T experiment, Chapter 7, the total background spectrum (ER+NR) together with the WIMP recoil spectra are needed. Since

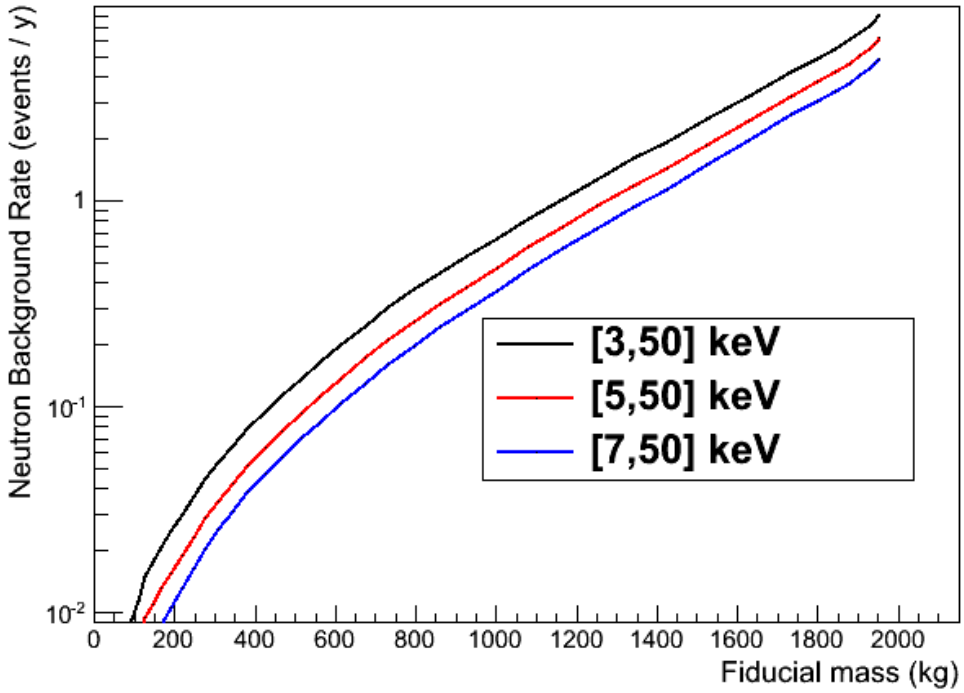

Figure 6.23: NR background rate as function of the fiducial mass calculated in the [3, 50] keV$_r$ (black line), [5, 50] keV$_r$ (red) and [7, 50] keV$_r$ (blue) energy ranges.

nuclear and electromagnetic recoils show different scintillation and ionization yields (Section 3.6), they have to be converted on a common scale. Thus, the ER and NR background spectra, as well as the WIMP recoil spectra, are converted from energy into light (S1) and charge (S2) signals. The conversion has been divided into two steps: photons and electrons production, from the released energy, and their conversion into S1 and S2 signals (photoelectrons, pe).

6.7.1 Generation of photons and electrons

ER

For what concerns the electromagnetic recoils, the Noble Element Simulation Technique (NEST) package for GEANT4 [217, 218] has been used. The first step is to evaluate the number of produced quanta, N_{quanta}. It is calculated from the deposited energy using 73 quanta/keV$_{ee}$ as conversion factor for the whole energy spectrum. Then it is smeared with a Gaussian distribution using 0.03 as Fano Factor, F, (taken from the NEST code):

$$N_{quanta} = \text{Gauss}(73 \cdot E,\ \sqrt{73 \cdot E \cdot F}), \tag{6.21}$$

where E is the deposited energy in keV_{ee}. The mean number of produced photons given the energy, $\langle N_{phot} \rangle$, is taken in particular from the data available in the NEST web site [219]. The data are computed for the energy released by the electrons and are presented for various electric field, figure 6.24. In this study, a value of 530 V/cm for electric field has been considered. To take into account the anti-correlation between light and charge, first the fraction of light over quanta is estimate:

$$f_{light} = \langle N_{phot} \rangle / N_{quanta}; \tag{6.22}$$

then the number of photons has been sampled using a binomial distribution:

$$N_{phot} = \text{Binomial}(N_{quanta},\ f_{light}). \tag{6.23}$$

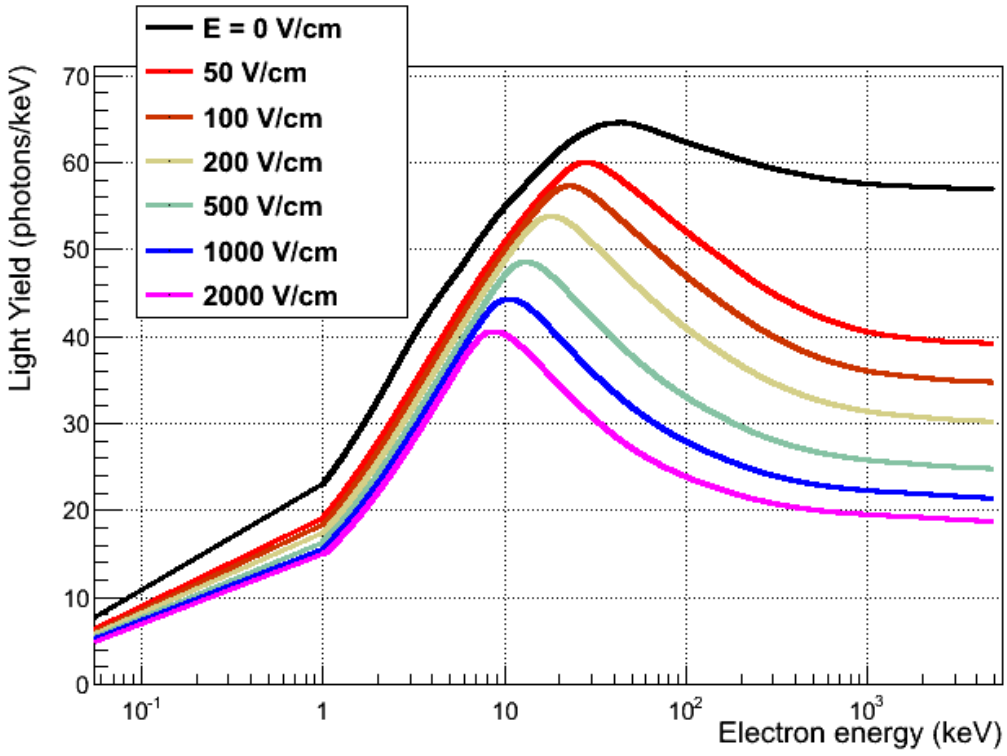

Figure 6.24: Photon yield as function of the released energy for electromagnetic recoils, from NEST [217, 218].

The number of electrons is consequently calculated as the difference between quanta and photons.

$$N_{e^-} = N_{quanta} - N_{phot}. \tag{6.24}$$

NR

For what concerns the nuclear recoils, the mean number of produced photons, figure 6.25, is given by:

$$\langle N_{phot} \rangle = E \cdot \mathcal{L}_{eff}(E) \cdot Ph^{122\ \mathrm{keV}_{ee}} \cdot S_{NR}, \tag{6.25}$$

where E is the released energy, $\mathcal{L}_{eff}$ is given in figure 3.19, $Ph^{122\ \mathrm{keV}_{ee}} = 63.4$ photons/keV$_{ee}$ is the photon yield of a 122 keV$_{ee}$ γ at zero field (taken from NEST [217, 218]) and $S_{NR} = 0.95$ [220] is the quenching due to the electric field (assumed independent on the energy).

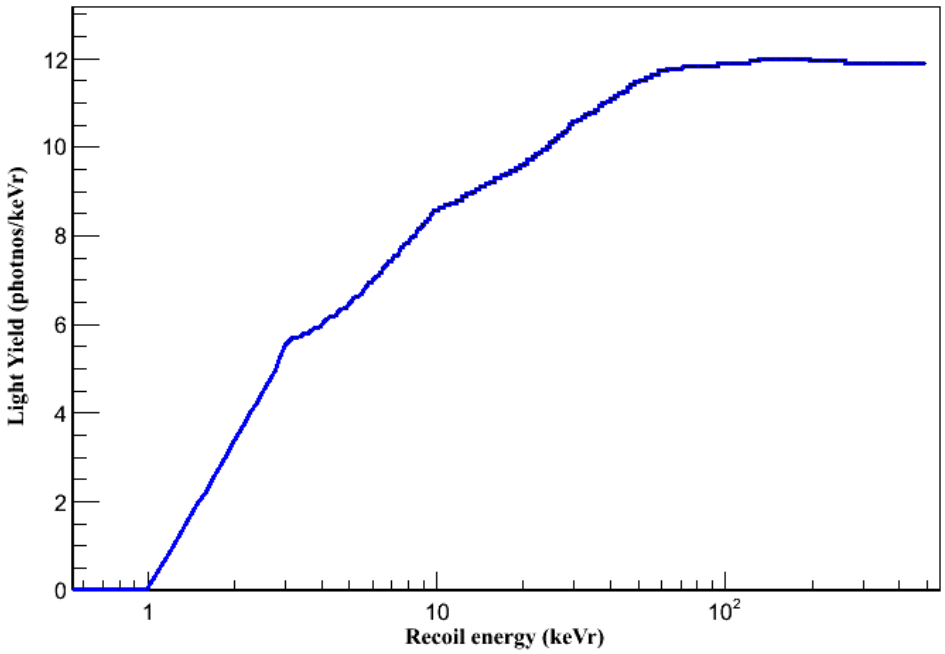

Figure 6.25: Light yield, as function of the recoil energy, for NR. The curve has been obtained from XENON100 AmBe calibration data [221].

The mean number of generated electrons is given by:

$$\langle N_{e^-} \rangle = E \cdot Q_y(E), \tag{6.26}$$

where $Q_y(E)$ is the charge yield measured in XENON100 through a comparison of data and MC for the AmBe calibration [221], figure 6.26.

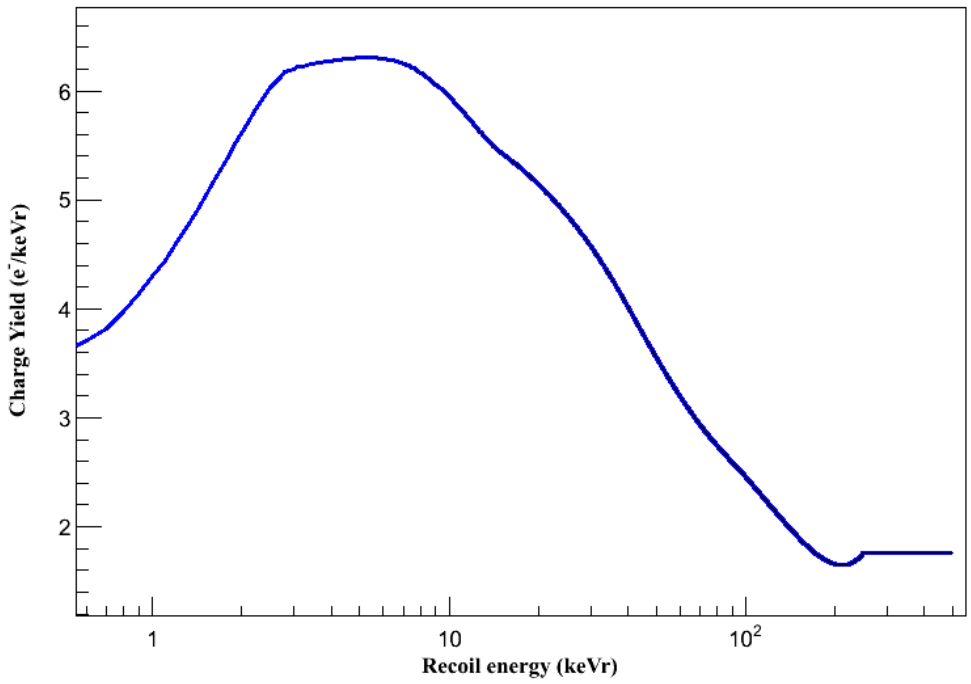

Figure 6.26: Charge yield, as function of the recoil energy, for NR. The curve has been obtained from XENON100 AmBe calibration data [221].

To sample light and charge in an anti-correlated way, the total mean number of quanta produced have been evaluated:

$$\langle N_{quanta} \rangle = \langle N_{phot} \rangle + \langle N_{e^-} \rangle \tag{6.27}$$

The final number of generated quanta produced is thus given by a Gaussian smearing with a Fano factor of 0.03:

$$N_{quanta} = \text{Gauss}(\langle N_{quanta} \rangle,\ \sigma(= \sqrt{\langle N_{quanta} \rangle \cdot F})). \tag{6.28}$$

From the total number of quanta, the number of photons is obtained through a binomial sampling:

$$N_{phot} = Binomial(N_{quanta},\ \langle N_{phot} \rangle / \langle N_{e^-} \rangle) \tag{6.29}$$

Thus, the number of electrons is simply:

$$N_{e^-} = N_{quanta} - N_{phot}. \tag{6.30}$$

6.7.2 Light Collection Efficiency (LCE)

The light collection efficiency represents the efficiency in detecting photons. A high value for the LCE means that the majority of photons are collected, giving a better

energy and position reconstruction. To characterize the light collection property of the TPC, a LCE map is required. Thus, extensive MC simulations have been performed, generating $\mathcal{O}(10^9)$ photons uniformly in the whole volume of the TPC. An absorption length in LXe of 50 m, a PTFE reflectivity of 99% and the transparency of the various meshes described in Section 5.6 have been considered. The resulting map, used for the conversion from energy to S1 signals of the background and WIMPs spectra, is shown in figure 6.27. Each spot of the map is simply given by the ratio between the number of detected photons (defined as those that reach the PMT photocathode) and the number of the generated ones. The top and bottom edges of figure 6.27 represent the position of the gate mesh and of the cathode, respectively.

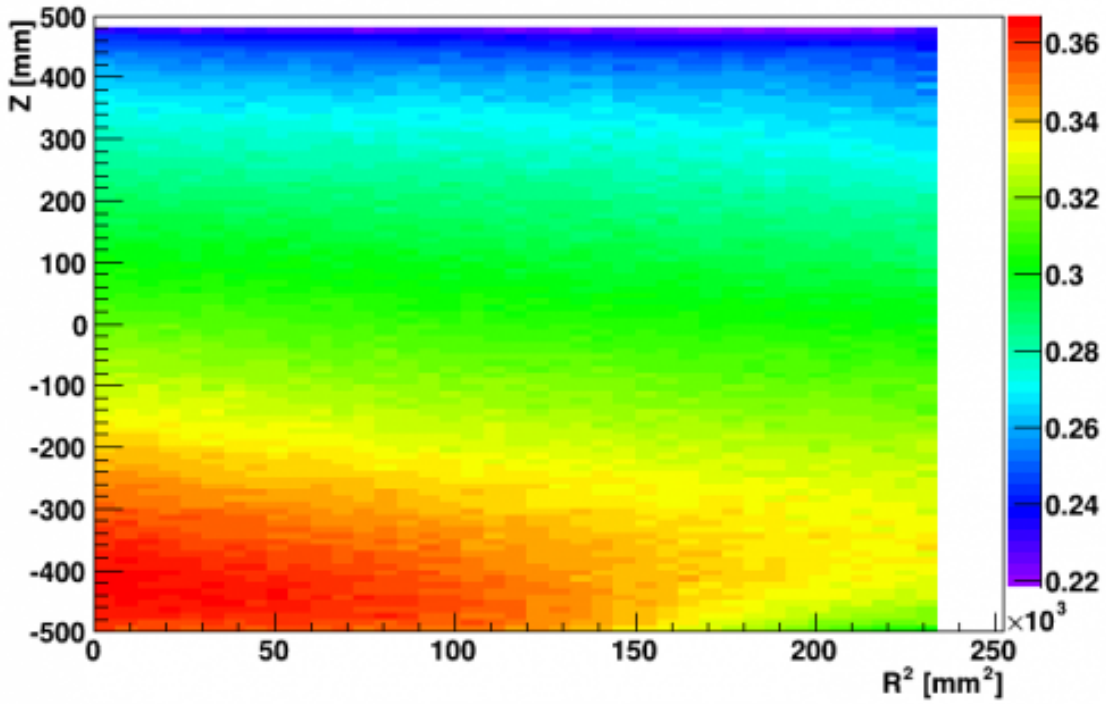

Figure 6.27: LCE map of the XENON1T TPC.

It is clear that the highest value for the LCE is reached in regions at the center of the TPC and close to the bottom PMT array. This happens for two reasons: because of total internal reflection at the LXe/GXe interface most of the light is detected by the bottom PMT array; photons produced at the center of the TPC can; on average; reach the PMTs with less reflections on the PTFE walls thus, having a lower probability of being absorbed. Integrating, over the radius, the LCE map it is possible to obtain such a quantity as function the z coordinate, figure 6.28. At the end of the analysis, the LCE

averaged over the whole TPC resulted equal to 38%.

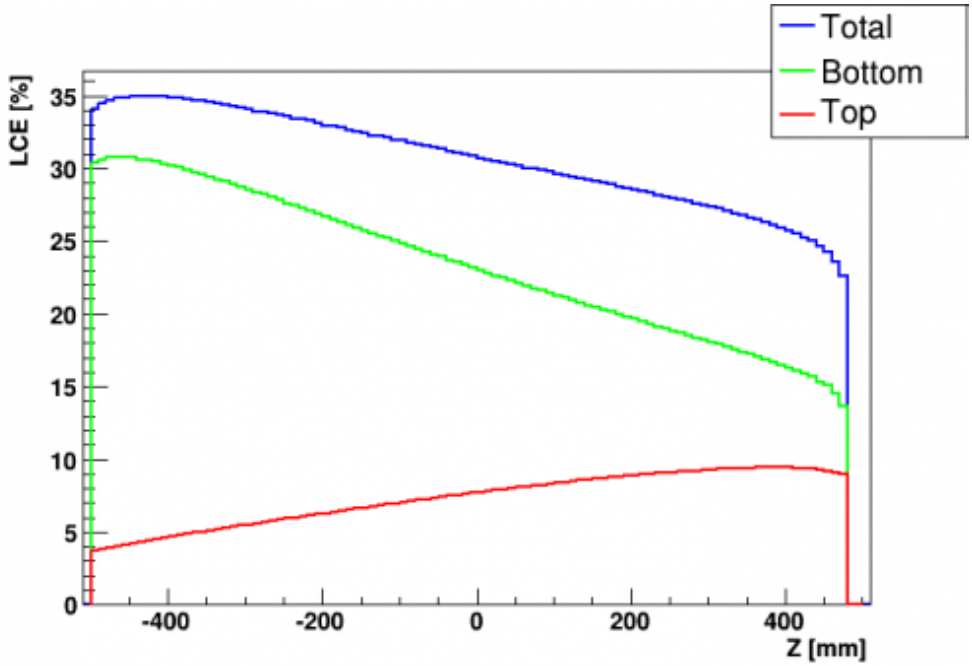

Figure 6.28: LCE as function of the z coordinate in the XENON1T TPC. The total contribution from the top and bottom PMT arrays is shown (blue curve), together with the separate ones from the top array (red curve) and the bottom array (green curve).

6.7.3 Generation of S1 and S2 signals

S1

Photons are thus converted into S1 signal applying the position-dependent LCE (Section 6.7.2.) whose value, averaged over the whole TPC, is 38%. This corresponds to the S1-yield, $S1_y$, through:

$$S1_y = Ph^{122\ \mathrm{keV}_{ee}} \cdot LCE \cdot QE \cdot CE, \tag{6.31}$$

where $Ph^{122\ \mathrm{keV}_{ee}}$ is the number of photons emitted by a 122 keV_{ee} gamma at zero electric field (63.4 photons/keV_{ee}), QE and CE are the quantum and the collection efficiency of the PMTs (36% and 90% respectively). Thus the S1-yield is 7.8 photoelectrons/keV_{ee} for a 122 keV_{ee} γ at zero electric field, corresponding to 4.6 pe/keV_{ee} at the operation field of 530 V/cm. Changing the transparency of the meshes (Section 5.6), for example using for all of them a wired pattern geometry with the only exception of the anode, it is possible to increase such a value for the S1-yield from 4.6 pe/keV_{ee} up to 5.6 pe/keV_{ee}, considering the XENON1T operation field. Unfortunately, this would affect the extraction field properties, thus making this option not very suitable. To take into account the

fluctuations, the final number of detected photoelectrons is given by a binomial sampling considering $n = N_{phot}$ and $p = DE$:

$$DP = \text{Binomial}(N_{phot},\ DE), \tag{6.32}$$

where DP is the final number of detected photoelectrons and DE is the photon detection efficiency of the PMTs given by:

$$DE = LCE \cdot QE \cdot CE, \tag{6.33}$$

Then a Gaussian smearing is applied to reproduce the response of the PMTs.

$$S1 = \text{Gauss}(DP,\ 0.5 \cdot \sqrt{DP}). \tag{6.34}$$

The resulting distribution of the S1-yield is shown in figures 6.29 and 6.30 (top panels) for low energy electrons and NR, respectively.

S2

For what concerns the S2-yield, the generated electrons are first accounted for the survival probability during their drift towards the anode:

$$Prob = e^{-t/e_{life}}, \tag{6.35}$$

then

$$N_{e^-}^{surv} = \text{Binomial}(N_{e^-},\ Prob), \tag{6.36}$$

where t is the time the e^- requires to go from its creation position to the anode, N_{el} is the number of generated electrons, $Prob$ is the survival probability and e_{life} is the electron lifetime (assumed equal to 500 μs). Then the S2 signal is generated assuming a Gaussian smearing of (20±7) pe/e- [222]:

$$S2 = \text{Gauss}(N_{e^-}^{surv} \cdot 20,\ 7 \cdot \sqrt{N_{e^-}^{surv}}); \tag{6.37}$$

The distribution of the S2-yield is shown in figures 6.29 and 6.30 (bottom panels) for low energy electrons and NR, respectively. After the conversion of the deposited energy into detector signals, the ER and NR backgrounds can be shown together in the same scale. In figure 6.31 the total background (black line), in 1 tonne fiducial volume, is presented as function of S1 together with the separate contribution of ER and NR. Below 10 pe the dominant background comes from neutrons, while above it is mostly due to the ER. For comparison in green is superimposed the NR spectrum given by a WIMP with mass 100 GeV/c^2 and cross section $\sigma = 2 \cdot 10^{-47}$ cm^2, assuming galactic halo properties as in [8].

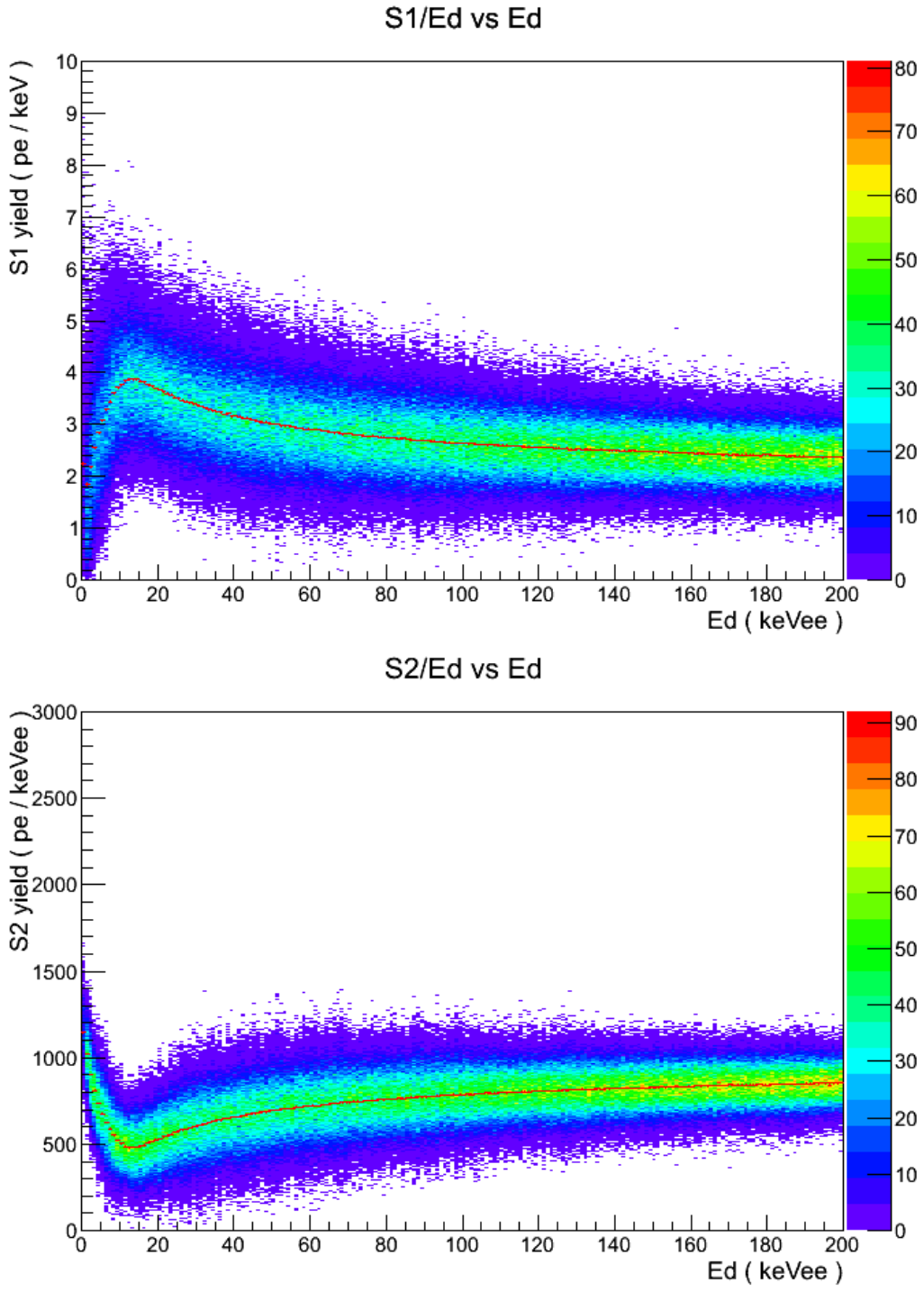

Figure 6.29: Distribution of the S1 (top) and S2 (bottom) yield for low energy electrons.

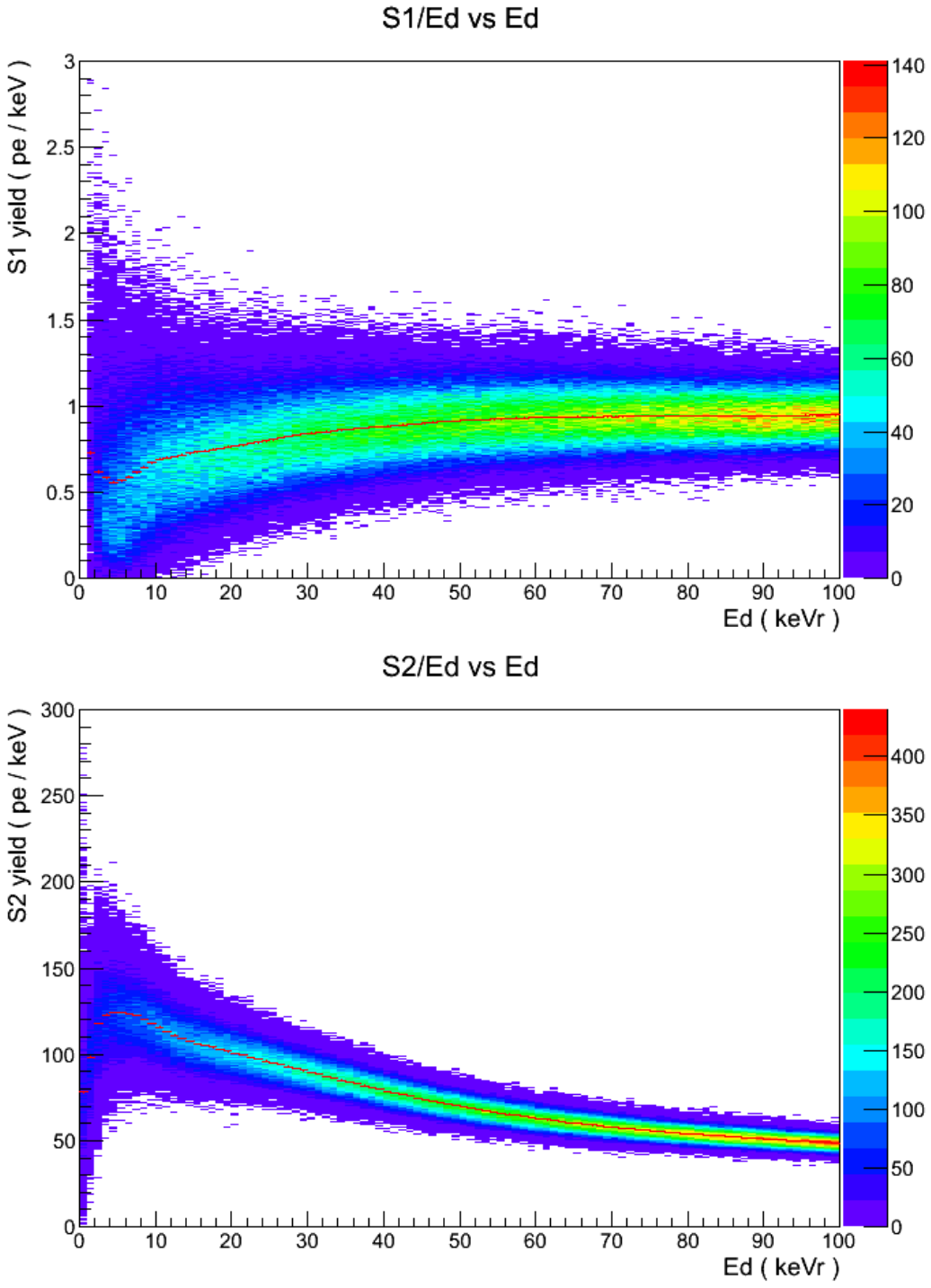

Figure 6.30: Distribution of the S1 (top) and S2 (bottom) yield for nuclear recoils.

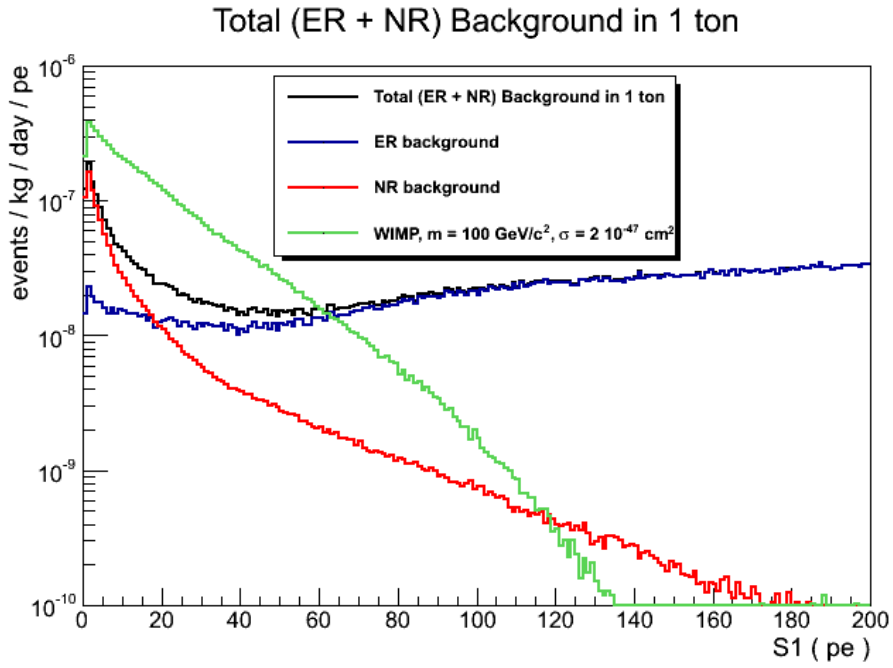

Figure 6.31: Background spectra as function of S1: in blue the ER, in red the NR, in black their sum. The green curve represents the NR spectrum given by a WIMP with mass 100 GeV/c^2 and cross section $\sigma = 2 \cdot 10^{-47}$ cm^2.

Chapter 7

XENON1T sensitivity

In direct dark matter search the sensitivity is usually presented as the ultimate cross section, as function of the WIMP mass, that a detector is able to detect. When a DM experiment does not see any candidate event, or the observed ones are compatible with the background-only hypothesis, it can only set the upper limits on the WIMP-nucleon cross section. Thus, the sensitivity curve is given by the interpolation of the upper limits obtained for the different values of the WIMP masses. In addition to the data from experiments already in operation, it is also possible to analyze the sensitivity of an experiment under construction, as XENON1T, using Montecarlo simulations based on the detector characteristics (Chapter 5 and Chapter 6).
In 2012, XENON100 [8] set the most stringent limit on the spin-independent WIMP-nucleon elastic scattering cross section for WIMP masses above 8 GeV/c^2, with a minimum of 2×10^{-45} cm^2 at 55 GeV/c^2, with a 90% confidence level. This result has been the best limit until LUX results [10] (figure 1.30) in October 2013, when the minimum of the cross section was lowered to 7.6×10^{-46} cm^2 at a WIMP mass of 33 GeV/c^2, with a 90% confidence level. In section 6.7 it has been shown the conversion of the total background (ER+NR) spectrum from energy into S1 and S2 signals. To evaluate the sensitivity of the experiment, also the WIMP recoil spectra have to be converted. They are evaluated assuming a certain WIMP velocity distribution and a proper halo model; the calculations are presented in section 7.1. Having all the spectra, background and WIMP, expressed in the same scale, the sensitivity of XENON1T, for spin-independent WIMP-nucleon interactions, is evaluated using the **Maximum Gap method** (Sections 7.2 - 7.6). The analysis has been carried out assuming different values for some detector operational parameters.

7.1 WIMPs expected rates

It is usually assumed that WIMPs follow a Maxwellian velocity distribution:

$$f(\mathbf{v}, \mathbf{v}_E(t)) \propto e^{-(\mathbf{v}+\mathbf{v}_E(t))^2/v_0^2} \tag{7.1}$$

where $\mathbf{v}_E$ is the Earth velocity. This term is composition of the Earth motion around the Sun and of its revolution around the center of the galaxy, thus it is time dependent:

$$\mathbf{v}_E(t) = \mathbf{v}_\odot + \mathbf{v}_\oplus(t) \tag{7.2}$$

where $\mathbf{v}_\odot$ is the velocity of the Sun in the galactic reference frame.
The general form for the expected differential DM recoil energy spectrum is given by [224]:

$$\frac{dR}{dE_R} = R_0 \; S(E_R) \; F^2(E_R) \; I \tag{7.3}$$

where E_R is the recoil energy of the target nucleus, R_0 is the total event rate, $F(q)$ is the form factor, I takes into account for the spin-independent and spin-dependent factors and $S(E_R)$ represents the effect of the detector efficiency, the relative motion between Earth and WIMP halo and other parameters that depend on the experiment. For incoming particles of number density n and velocity v, the scatter rate off a single target, per unit mass (kg), can be described as:

$$dR = \frac{N_A}{A} \; \sigma \; v \; dn, \tag{7.4}$$

where N_A is the Avogadro number ($6.022{\cdot}10^{26}$ kg^{-1}) and A is the atomic mass (a.m.u.) of the target. The total event rate per unit mass is given by:

$$R = \frac{N_A}{A} \; \sigma_0 \int v \; dn \equiv \frac{N_A}{A} \; \sigma_0 \; n_0 \; \langle v \rangle \tag{7.5}$$

where σ_0 is the *zero momentum transfer* cross section and dn is the differential dark matter particle density given by:

$$dn = \frac{n_0}{k} \; f(\mathbf{v}, \mathbf{v}_E) \; d^3\mathbf{v}. \tag{7.6}$$

The variable k is the normalization constant such that the integrated particle density with velocity in $[0, v_{esc}]$ is equal to the mean WIMP number density $n_0 = \rho_\chi / M_\chi$, where ρ_χ and M_χ are the WIMP density and mass, respectively. Thus, k is given by:

$$k = \int_0^{2\pi} d\phi \int_{-1}^{+1} d(\cos\theta) \int_0^{v_{esc}} v^2 f(\mathbf{v}, \mathbf{v}_E) \; dv, \tag{7.7}$$

where v_{esc} is the galactic escape velocity. For $v_{esc} = \infty$, the integrals return $k = k_0 = (\pi v_0^2)^{3/2}$ while for a finite escape velocity it results:

$$k = k_1 = k_0 \left[erf\left(\frac{v_{esc}}{v_0}\right) - \frac{2}{\pi^{1/2}} \frac{v_{esc}}{v_0} e^{-v_{esc}^2/v_0^2} \right]. \tag{7.8}$$

Assuming $v_{esc} = \infty$ and $v_E = 0$, the total event rate per unit of mass, equation (7.5), is given by:

$$R_0 = \frac{2}{\sqrt{\pi}} \frac{N_0}{A} \frac{\rho_\chi}{M_\chi} \sigma_0 v_0. \tag{7.9}$$

With $\rho_\chi = 0.4$ GeV/c^{2}cm^{-3} [223] and $v_0 = 230$ km/s, it is possible to express R_0 in units of events/kg/day:

$$R_0 = \frac{503}{M_\chi M_t} \left(\frac{\sigma_0}{1\text{pb}}\right) \left(\frac{\rho_\chi}{0.4 \text{ GeVc}^{-2}\text{cm}^{-3}}\right) \left(\frac{v_0}{230\text{km/s}}\right) \tag{7.10}$$

where M_t is the mass of the target nucleus (in GeV/c^2). By using equation (7.9), it is possible to re-write the equation (7.5) as:

$$R = R_0 \frac{\sqrt{\pi}}{2} \frac{\langle v \rangle}{v_0} = R_0 \frac{k_0}{k} \frac{1}{2\pi v_0^4} v \int f(\mathbf{v}, \mathbf{v}_E) d^3v. \tag{7.11}$$

The differential form of the equation (7.11) is given by:

$$dR = R_0 \frac{k_0}{k} \frac{1}{2\pi v_0^4} v f(\mathbf{v}, \mathbf{v}_E) d^3v. \tag{7.12}$$

Integrating equation (7.12), under different assumptions on v_e and v_{esc}, the total event rate becomes:

$$\frac{R(0, v_{esc})}{R_0} = \frac{k_0}{k_1} \left[1 - \left(1 + \frac{v_{esc}^2}{v_0^2}\right) e^{-v_{esc}^2/v_0^2}\right]; \tag{7.13}$$

$$\frac{R(v_{esc}, \infty)}{R_0} = \frac{1}{2} \left[\pi^{1/2} \left(\frac{v_E}{v_0} + \frac{1}{2} \frac{v_0}{v_E}\right) erf\left(\frac{v_E}{v_0}\right) + e^{-v_E^2/v_0^2}\right]; \tag{7.14}$$

$$\frac{R(v_E, v_{esc})}{R_0} = \frac{k_0}{k_1} \left[\frac{R(v_{esc}, \infty)}{R_0} - \left(\frac{v_{esc}^2}{v_0^2} + \frac{1}{3} \frac{v_E^2}{v_0^2} + 1\right) e^{-v_{esc}^2/v_0^2}\right]. \tag{7.15}$$

The expcted WIMP differential recoil energy spectrum is evaluated using almost the same procedure as done for the total event rate. The recoil energy, E_R, of the target nucleus hit by a dark matter particle with energy $E = \frac{1}{2} M_\chi v^2$ and scattered at an angle θ, figure 7.1, is given by: $E_R = Er(1 - \cos\theta)/2$, where $r = \frac{4 M_\chi M_t}{(M_\chi + M_t)^2}$. Assuming an isotropic scatter process, meaning that E_R is uniformly distributed in the range $0 \leq E_R \leq Er$, the differential rate is given by:

$$\frac{dR}{dE_R} = \int_{E_{min}}^{E_{max}} \frac{1}{Er} dR(E) = \frac{1}{E_0 r} \int_{v_{min}}^{v_{max}} \frac{v_0^2}{v^2} dR(v), \tag{7.16}$$

where E_{min} is the smallest particle energy that can give a recoil of energy E_R; $E_0 = \frac{1}{2} M_\chi v_0^2 = (v_0/v)^2 E$ is the most probable kinetic energy of the WIMPs and v_{min} is the velocity corresponding to E_{min}:

$$v_{min} = \sqrt{2E_{min}/M_\chi} = v_0 \sqrt{E_R / r E_0}. \tag{7.17}$$

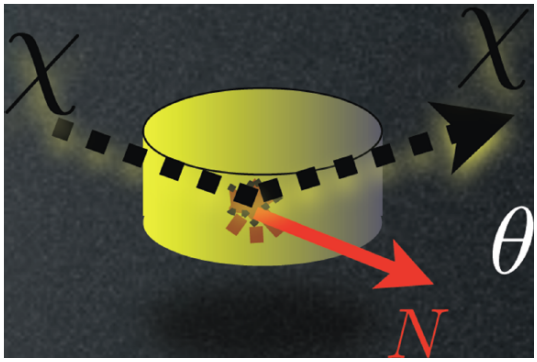

Figure 7.1: Representation of a WIMP scattering process.

Combining equations (7.12) and (7.16), the differential recoil energy spectrum can be expressed as:

$$\frac{dR(v_E, v_{esc})}{dE_R} = \frac{R_0}{E_0 r}\frac{k_0}{k}\frac{1}{2\pi v_0^2}\int_{v_{min}}^{v_{max}} \frac{1}{v} f(\mathbf{v}, \mathbf{v}_E) d^3v \tag{7.18}$$

To correctly evaluate the integral on the velocity, it has to be considered that the WIMP velocity in the galactic reference frame, v', cannot exceed v_{esc} otherwise DM particles would escape from the galaxy. The velocity v' is composition of the WIMP velocity relative to the target, $\mathbf{v}$, and velocity of the target itself: $\mathbf{v}' = \mathbf{v}_E + \mathbf{v}$. Its module is given by: $v'^2 = v^2 + v_{esc}^2 + 2vv_{esc}\cos\theta$. It means that: $(\mathbf{v} - \mathbf{v}_e)^2 \leq \mathbf{v}'^2 \leq (\mathbf{v} + \mathbf{v}_e)^2$, thus setting a certain value for v, v' results function of $\cos\theta$. It should be noted that the integral in equation (7.18) is evaluated on the WIMP relative velocity, $\mathbf{v}$. The maximum value of v is reached when the Earth moves in the opposite direction with respect to the incoming WIMP when the latter has $v' = v_{esc}$: $v_{max} = v' + v_{esc}$. Now, two cases have to be considered:

- if $v \leq v_{esc} - v_E$, then it is possible to integrate equation (7.18) without any condition on $\cos\theta$, since it always results $v' \leq v_{esc}$:
  $v'^2 = (v + v_E)^2 \leq (v_{esc} - v_E + v_E)^2 \leq v_{esc}^2$;
- if $v_{esc} - v_E \leq v \leq v_{esc} + v_E$, then it has to be set a condition on $\cos\theta$: $v'^2 = v^2 + v_E^2 + 2vv_E\cos\theta \leq v_{esc}^2 \Rightarrow \cos\theta \leq (v_{esc}^2 - v^2 - v_E^2)/2vv_E$.

The integral on the velocity becomes:

$$\int_{v_{min}}^{v_{max}} \frac{1}{v} f(\mathbf{v}, \mathbf{v}_E) d^3v = \int_0^{2\pi} d\phi \int_{-1}^{c_{max}} d(\cos\theta) \int_{v_{min}}^{v_{max}} \frac{1}{v} f(\mathbf{v}, \mathbf{v}_E) dv =$$

$$= 2\pi \left[\int_{-1}^{1} d(\cos\theta) \int_{v_{min}}^{v_{esc}-v_E} + \int_{-1}^{(v_{esc}^2 - v^2 - v_E^2)/2vv_E} d(\cos\theta) \int_{v_{esc}-v_E}^{v_{esc}+v_E} \right] \frac{1}{v} f(\mathbf{v}, \mathbf{v}_E) dv \tag{7.19}$$

The lower bound of the integral on cosθ can be leaved equal to -1 since the physical condition $v' \geq 0$ is always satisfied. Besides the conditions on cosθ, it has to be considered also a condition on v_{min} to assure that $v_{min} \leq v_{esc} - v_E$. If this relation is not satysfied, one should consider only the second part of the last integral in equation (7.19), substituting the lower bound of the velocity integral with v_{min}, otherwise the integral is evaluated with the wrong condition on the cosθ. Thus, the integral on the velocity can be written as:

$$\int_{v_{min}}^{v_{max}} v f(\mathbf{v}, \mathbf{v}_E) d^3v \; = 2\pi$$

$$\times \begin{cases} \left[\int_{-1}^{1} \int_{v_{min}}^{v_{esc}-v_E} + \int_{-1}^{(v_{esc}^2 - v^2 - v_E^2)/2vv_e} \int_{v_{esc}-v_E}^{v_{esc}+v_E} \right] \frac{1}{v} f(\mathbf{v}, \mathbf{v}_E) d(\cos\theta) \; dv & 0 \leq v_{min} \leq v_{esc} - v_E \\ \int_{-1}^{(v_{esc}^2 - v^2 - v_E^2)/2vv_E} \int_{v_{min}}^{v_{esc}+v_E} \frac{1}{v} f(\mathbf{v}, \mathbf{v}_E) d(\cos\theta) dv & v_{esc} - v_E \leq v_{min} \leq v_{esc} + v_E \\ 0 & v_{min} \geq v_{esc} + v_E \end{cases} \tag{7.20}$$

Using the conditions on cosθ and v_{min}, it is possible to integrate equation (7.18). The expected DM differential energy spectrum, for various assumptions about v_E and v_{esc}, is thus given by:

$$\frac{dR(0,\infty)}{dE_R} = \frac{R_0}{E_0 r} e^{-E_R/E_0 r}; \tag{7.21}$$

$$\frac{dR(0, v_{esc})}{dE_R} = \frac{k_0}{k_1} \left[\frac{dR(0,\infty)}{dE_R} - \frac{R_0}{E_0 r} e^{-v_{esc}^2/v_0^2} \right]; \tag{7.22}$$

$$\frac{dR(v_E,\infty)}{dE_R} = \frac{R_0}{E_0 r} \frac{\pi^{1/2}}{4} \frac{v_0}{v_E} \left[erf\left(\frac{v_{min}+v_E}{v_0} \right) - erf\left(\frac{v_{min}-v_E}{v_0} \right) \right]; \tag{7.23}$$

$$\frac{dR(v_E, v_{esc})}{dE_R} = \frac{k_0}{k_1} \left[\frac{dR(v_E,\infty)}{dE_R} - \frac{R_0}{E_0 r} e^{-v_{esc}^2/v_0^2} \right]. \tag{7.24}$$

7.1.1 The nuclear form factor

The DM recoil spectra evaluated in the previous section have been obtained assuming zero momentum transfer. In this case it is possible to neglect the correction to the cross section due to the nucleus shape. Indeed, it is possible to express the cross section as: $\sigma = \sigma_0 F^2(qr_n)$, where σ_0 is the WIMP-target cross section at zero momentum transfer and $F(q)$ is the nuclear form factor that takes care of the nucleus shape (when the corrections are neglected, $F(qr_n) = 1$). F is function of the dimensionless quantity $qr_n/\hbar$, where $r_n = a_n A^{1/3} + b_n$ is the effective nuclear radius. With $\hbar = 197.3$ MeV fm, the dimensionless quantity is given by:

$$qr_n = 6.92 \cdot 10^{-3} A^{1/2} E_R^{1/2} (a_n A^{1/3} + b_n), \tag{7.25}$$

with E_R in keV and a_n/b_n in fm. In the plane wave approximation, the form factor is the Fourier transform of $\rho(r)$, the density distribution of scattering centers. Considering an isotropic density, it can be expressed as:

$$F(q) = \int \rho(r) e^{i\mathbf{q}\cdot\mathbf{r}} d^3r = \frac{4\pi}{q} \int_0^\infty r \, \sin(qr)\rho(r)dr. \tag{7.26}$$

For the expression of $\rho(r)$ it is possible to distinguish between spin-independent (SI) and spin-dependent (SD) interactions [224]: in the SI case, one can consider a solid sphere approximation thus considering the interaction with the whole nucleus, while for SD it is used the thin shell approximation assuming interactions with a single outer shell nucleon. The respective form factors are given by:

$$F(qr_n) = 3\left(\frac{\sin(qr_n)}{(qr_n)^3} - \frac{\cos(qr_n)}{(qr_n)^2}\right) \tag{7.27}$$

for the solid sphere and

$$F(qr_n) = \frac{\sin(qr_n)}{qr_n} \tag{7.28}$$

for the thin shell approximation. In figures 7.2 and 7.3 they are shown the form factors, as function of the energy, for different target materials. For the spin-independent calculations, Helm profile for $\rho(r)$ [226] has the advantage to give an analytic expression for the form factor:

$$F(qr_n) = 3\frac{j_1(qr_n)}{qr_n} e^{-(qs)^2/2}, \tag{7.29}$$

where $j_1(x) = \sin(x)/x^2 - \cos(x)/x$ is the first order Spherical Bessel Function and s is a measure of the nuclear skin thickness.

7.1.2 Spin corrections

With the final goal of the evaluation of the differential recoil energy spectrum, also the spin properties of the interactions have to be considered. The total zero-momentum WIMP-nucleus cross section can be written as:

$$\sigma_0 = 4G_F^2 \mu_N^2 C, \tag{7.30}$$

where G_F is the Fermi coupling constant, $\mu_N = M_t M_\chi/(M_t + M_\chi)$ is the WIMP-target reduced mass in the center-of-momentum frame, and C C is a dimensionless number that carries all the particle-physics model information. Concerning the SD case, one has:

$$C_{SD} = \frac{8}{\pi}\Lambda^2 J(J+1), \tag{7.31}$$

with

$$\Lambda = \frac{[a_p\langle S_p\rangle + a_n\langle S_n\rangle]}{J}, \tag{7.32}$$

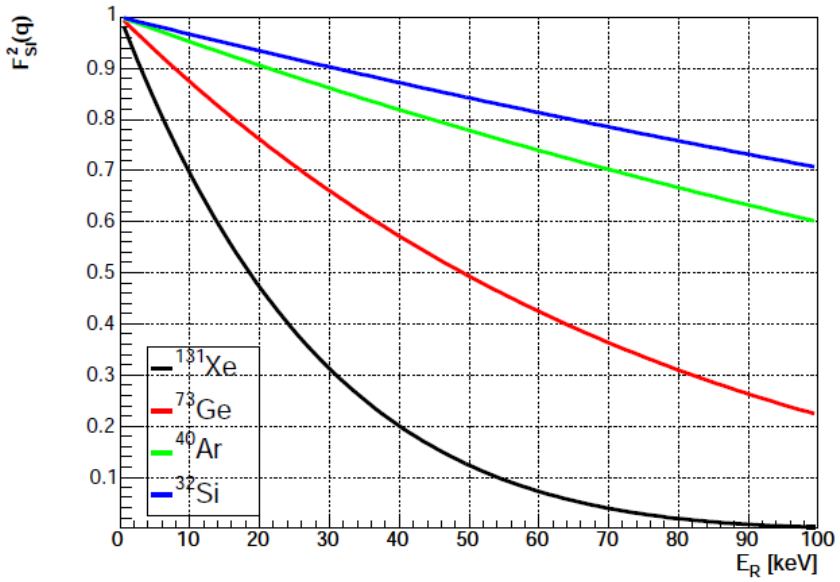

Figure 7.2: Form factor, as function of the energy, for SI interactions [225].

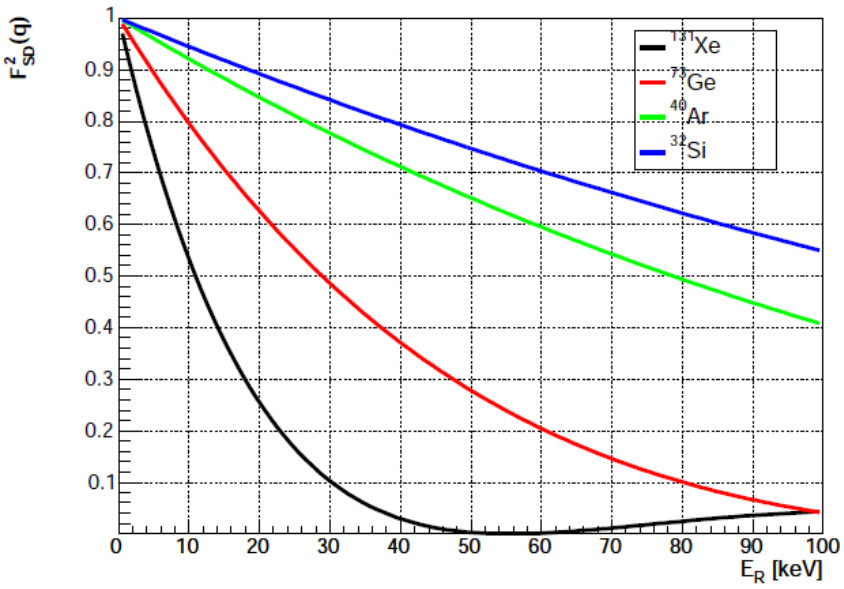

Figure 7.3: Form factor, as function of the energy, for SD interactions [225].

where J is the total nuclear spin, $a_n(p)$ is the WIMP-neutron(proton) coupling and $\langle S_p(n) \rangle$ is the expectation value of the proton(neutron) spin in the nucleus. The contributions from protons and neutrons can be separated, thus allowing to derive experimental limits independent of the adopted WIMP model. The contributions are given by

[227]:

$$C_{SD}^{p,n} = \frac{8}{\pi}[a_{p,n}\langle S_{p,n}\rangle]^2 \frac{J+1}{J}. \tag{7.33}$$

Thus, the cross section at zero momentum transfer, for protons and neutrons, in the SD case is given by:

$$\sigma_0^{p,n} = 4G_F^2 \mu_N^2 C_{SD}^{p,n}, \tag{7.34}$$

with, from equation (7.30), $\sigma_0 = (\sqrt{\sigma_0^p} + \sqrt{\sigma_0^n})^2$. Assuming that the total WIMP-nucleus cross section is dominated by the proton (neutron) contribution, limits on σ_0, from a certain target material, can be converted onto limits on the single proton (neutron) cross section:

$$\sigma_{p,n}^{lim} = \sigma_0^{lim} \frac{\mu_{p,n}^2}{\mu_N^2} \frac{1}{C_{SD}^{p,n}/C_{p,n}}, \tag{7.35}$$

where $C_{p(n)}$ is the proton (neutron) cross section enhancement factor. In the particular case of free nucleons the factor is given by: $C_{p,n} = 6a_{p,n}^2/\pi$. It is clear that the use of the ratios $C_{SD}^{p,n}/C_{p,n} = 4/3\langle S_{p,n}\rangle^2(J+1)J$ ensures the cancellation of the WIMP-dependent $a_{p,n}^2$ terms contained within the WIMP-target cross section and, hence, ensures WIMP model-independence. This allows to compare limits derived by different experiments which use different target materials. Also, it is possible a direct comparison between experimental results and theoretical calculations from a specific (e.g., SUSY) model that gives predictions for $\sigma^{p,n}$.

For what concerns the SI case, one has:

$$C_{SI} = \frac{1}{\pi G_F^2}[Zf_p + (A-Z)f_n]^2, \tag{7.36}$$

where $f_n(p)$ is the WIMP-neutron(proton) coupling and Z and A-Z are numbers of protons and neutrons. In most instances, $f_n \simeq f_p$, then:

$$C_{SI} = \frac{1}{\pi G_F^2}(Af_p)^2. \tag{7.37}$$

Thus, for SI interactions and assuming equal coupling to protons and neutrons, the WIMP-nucleon cross section is proportional to the square of the atomic mass of the target nucleus, A^2, giving higher interactions in more massive targets.

7.1.3 Modulation of the WIMP signal

During its revolution around the Sun, the relative velocity of the Earth with respect to the dark matter halo changes. This results in a modulation of the potential signal that can be seen in a detector since, as shown in the previous section, the event rate depends on the relative velocity between the detector and the WIMPs. Moreover, a modulation

of the signal is a clear signature for dark matter interactions since the background, for example from radioactive nuclides on the Earth, is constant over the whole year. The relative velocity of an earth-based detector to the galactic halo as a function of time in the year, $v(t)$, is given by:

$$v(t) = v_{\odot} + v_E \cos\theta \cos[2\pi(t - t_0)], \tag{7.38}$$

where θ is the inclination of the Solar system plane to the direction of motion of the Sun, t_0 is the time when the Earth's velocity relative to the halo is the highest (around June 2nd), $v_E \equiv 30$ km/s is the rotational velocity of the Earth and $v_{\odot} \equiv 220$ km/s is the Sun's velocity relative to the Galactic halo. In figure 7.4 it is shown the expected differential event rates, as given in equation (7.24), for June and December together with their average and difference.

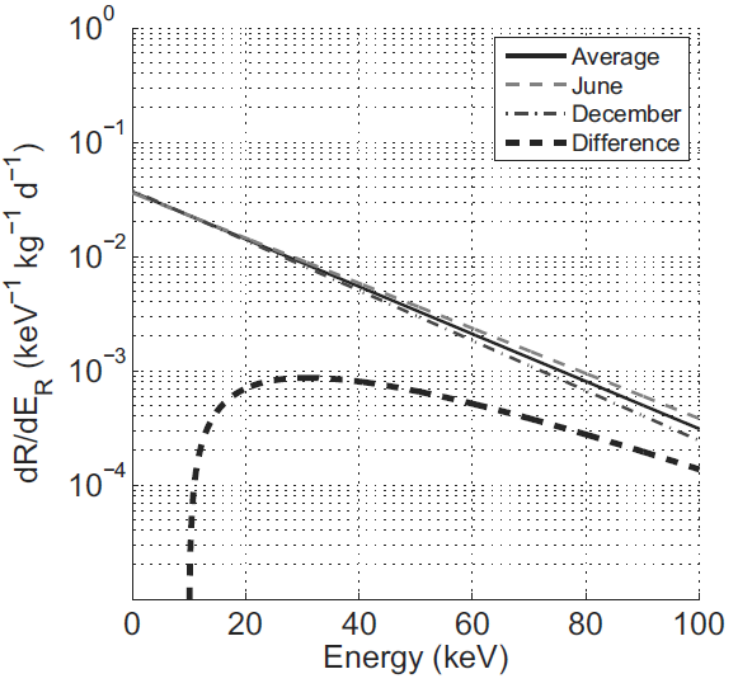

Figure 7.4: Expected WIMP recoil spectra in June (dashed) and December (dash-dotted); also shown are their difference and average. The curves have been computed assuming: $\sigma_0 = 10^{-5}$ pb, $M_{\chi} = 100$ GeV/c^2, $v_0 = 230$ km/s, $v_s = 230$ km/s, $v_E = 30$ km/s and $v_{esc} = 600$ km/s.

7.1.4 Expected WIMP recoil spectra for spin-independent interactions

Having all the needed quantities in equation (7.3), it is possible to evaluate the expected differential energy spectrum, equation 7.24, for WIMPs of different masses, figure 7.5.

From the table we have that for a DM candidate with a mass of 5 GeV/c^2, there are 0 expected events inside the [5, 50] keV$_r$ energy region. The only chance to detect such a particle is that the Poissonian fluctuations, of the number of produced photons, push the amount of emitted light above the detection threshold even for an energy released below 5 keV$_r$.

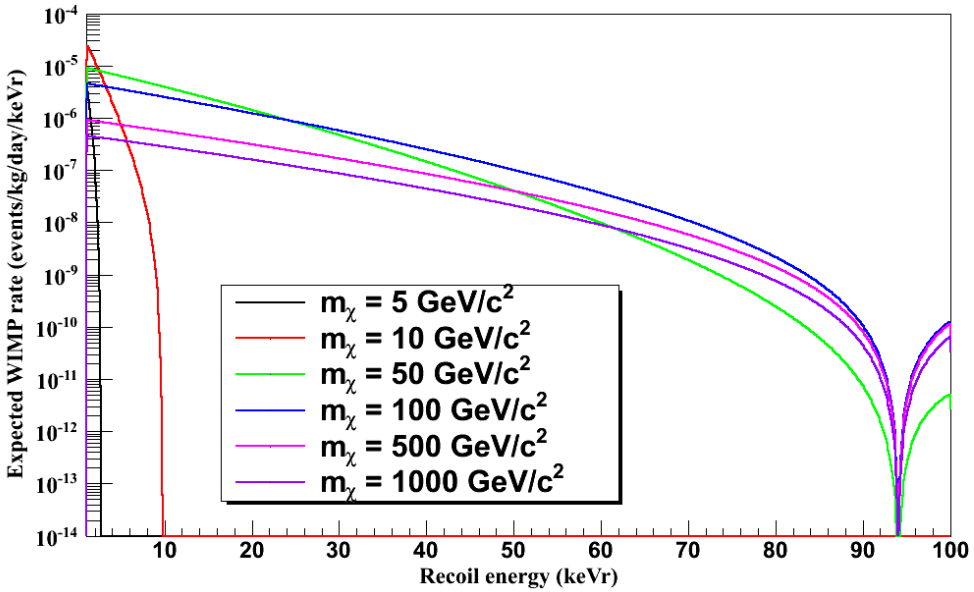

Figure 7.5: WIMP recoil spectra, as function of the energy, for different WIMP masses. The spectra have been computed considering $\sigma = 1 \cdot 10^{-46}$ cm^2.

From the figure it is possible to extract, for the fixed assuming a certain value for the cross section, the mean number of expected NR events from WIMPs. The results are presented in table 7.1.

m$_\chi$ (GeV/c^2)	**expected recoil events (events in 2 tonne-years)**
5	0
10	0.5
50	45.2
100	34.2
500	8.4
1000	4.3

Table 7.1: Expected WIMP scatters inside 1 tonne fiducial volume of LXe. The events have been evaluated from the spectra in figure 7.5 considering: $\sigma = 1 \cdot 10^{-46}$ cm^2, [5, 50] keV$_r$ energy region and 2 years of exposure.

7.2 The Maximum Gap method

The **Maximum Gap** is an unbinned statistical method [181] used to quote upper limits, with a certain confidence level (CL), of the σ for WIMP-nucleon scatterings when:

- there are no clear evidences for a signal event;
- there is the possibility for the existence of an unknown background;
- the observed events are compatible with the background-only hypothesis.

From the DM theory it is possible to obtain the shape of the expected WIMP recoil energy spectra, section 7.1, but not their normalization, i.e. the σ. From the published results on DM search (Chapter 1), it is known that the number of expected recoil events from WIMPs is very small thus, also a very low background could account for all the observed events. Furthermore, from the theory we know that the energy released in DM scattering processes is at most of hundred of keV_r and so very close to the energy threshold of the detectors. In such a situation, unknown backgrounds, connected for example to the noise of the electronic components of the experiment, could contribute significantly to the observed low energy events. The procedure to use the Maximum Gap method can be schematically summarized as in figure 7.6.

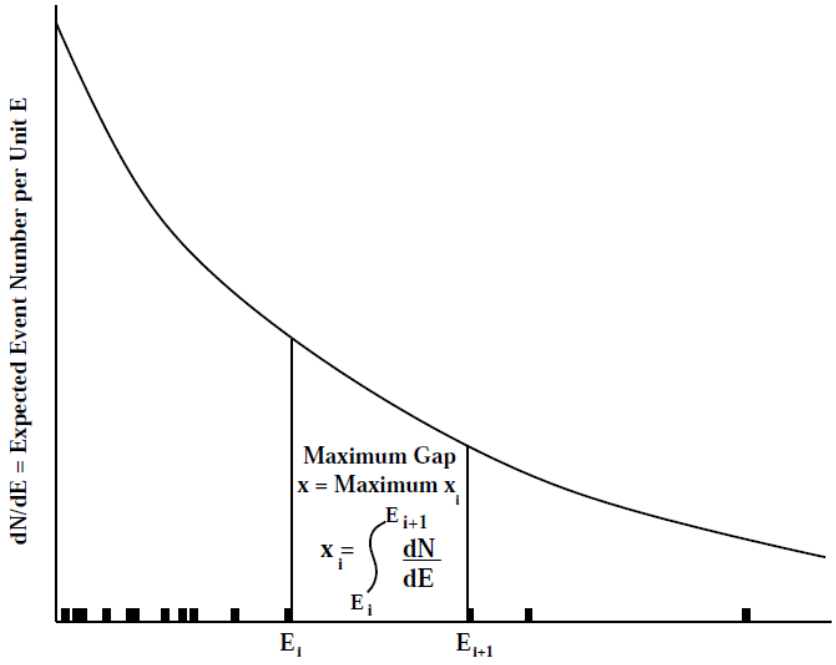

Figure 7.6: Explanation of the Maximum Gap method: dN/dE is the expected event spectrum, as function of a generic 1-D variable, of the process for which one wants to evaluate the upper limit on the cross section; the black squares are the observed events.

The dN/dE curve represents the expected signal spectrum for which one wants to evaluate the cross section, while the black rectangles are the observed events. On the x-axis there is the energy of the recoils, but any other 1-D variable can be used. Assuming a certain value for the cross section, between each two consecutive events there is a "gap" given by:

$$x_i = \int_{E_i}^{E_{i+1}} \frac{dN}{dE} dE, \tag{7.39}$$

where $E_{i,i+1}$ are the energies of any two adjacent events. The gap sizes x_i represent the number of expected signal events, for the hypothesized value of the σ, in energy intervals where no events have been observed. Given a certain distribution for the data, the "maximum gap" is the largest gap between them. Being XENON1T still under construction, MC simulations are required to generate the observed events. The procedure to apply the method can be summarized as follows. Suppose to have, as result of a simulated experiment, a certain number of events that are distributed following a certain 1-D variable, like the recoil energy or the number of photoelectrons of the S1 signal. Then, it is assumed that all the events are due only to the background, being interested in upper limits in the background-only hypothesis. Between each two adjacent events we evaluate, using the signal spectrum, the size of the gap and then we look for the largest one. The gaps are evaluated on the signal spectrum because one wants to quote upper limits for the signal cross section. Thus, the gaps represent the number of signal events that we were expecting to observe, for the assumed value of the σ, between two adjacent background events. Knowing the maximum gap and having observed 0 events in it, we want to know the value of the σ for which we would observed 0 events with a certain probability. The value of the probability defines the CL of the upper limit. Finally, the Maximum Gap method returns the value of the cross section that is the upper limit on this parameter, with the desired CL (σ^{CL}). This procedure shields against regions where the background gives many events, as the low energy part of the spectrum, since it is not probable to find the maximum gap there. In this way, the method is naturally applied in region where the background has not a large impact on the detector sensitivity. This is a recursive method where one tries and rejects different values of the σ until the one that satisfy the CL condition is found. Very large values of the cross section can a priori be excluded since it is not probable to observe zero events in gaps which provide a huge number of expected recoils. Going towards low values for the σ it is necessary to define a criterion to decide if a certain value can be accepted or rejected. Assuming a certain hypothesis on σ being the correct value, one could reject it, as too high, if random experiments would almost always observe less events in their maximum gap. Thus, the procedure simply compare different hypothesis on the signal

strength and returns, as upper limit, the one that gives with C_0 probability a lower number of expected events compared with the observed one. Being X the observed maximum gap, if the probability to observe a lower value for x (the random maximum gap) is C_0, then one can reject the hypothesized value of the cross section with a CL of C_0. The probability C_0 is given by [181]:

$$C_0 = \sum_{k=0}^{m} \frac{(kx-\mu)^k e^{-kx}}{k!}\left(1+\frac{k}{\mu-kx}\right), \tag{7.40}$$

where μ is the total number of the expected signal events, i.e. the integral of the dark matter recoil energy spectrum over the whole energy range, x is the maximum gap and m is the largest integer $\leq \mu/x$. The value of the cross section at a certain CL is obtained by applying a recursive procedure to equation (7.40) until $C_0 = \text{CL}$. As introduced at the beginning of the section, this is an unbinned method since we are dealing with integrals over energy ranges thus, no matter how the events have been binned. It is also clear that regions where the background gives particularly many events are automatically excluded since it is not probable to find the maximum gap there. Thus, this method effectively excludes regions where unknown backgrounds is especially dangerous.

7.3 Sensitivity with LY = 4.6 pe/keV$_{ee}$

Having the background (ER+NR) and WIMP spectra as function of the S1 (Section 6.7 and 7.1), it is now possible to evaluate the sensitivity of XENON1T. To do that, MC simulations have been used. The procedure is first presented for a fixed WIMP mass, for example 100 GeV/c^2, then the generalization will be straightforward. For each value of the dark matter mass, 10^5 random experiments have been run. For each one, the number of observed events is randomly extracted from a Poissonian distribution with mean equal to the number of expected background events:

$$n^{\text{obs}} = \text{Poiss(exp. bkg events)} \tag{7.41}$$

To each observed event, a value for the S1 is randomly extracted from the total (ER+NR) background-only spectrum:

$$S1_i = \text{random(ER + NR)};\ i = 1, 2, ..., n^{\text{obs}}. \tag{7.42}$$

Then, the gaps are evaluated:

$$x_i(\sigma) = \int_{S1_i}^{S1_{i+1}} \frac{dN_{\text{WIMP}}(\sigma)}{dS1} dS1, \tag{7.43}$$

and the different values of σ are tested until equation (7.40) is solved for $C_0 = 0.9$. This will give a value for the cross section upper limit at a CL = 90%, σ^{90}. Having solved equation (7.40) 10^5 times, we end up with a distribution for the σ^{90}. The final upper limit on the cross section, for the given WIMP mass, is the median of the σ^{90} distribution. The 50% quantile represents a more suitable choice with respect to the mean since the latter is more affected from fluctuations towards higher or lower values of the σ^{90}. In figure 7.7 is shown an example of the σ^{90} distribution for a WIMP mass of 20 and 100 GeV/c^2; assuming an electric field of 530 V/cm (as in XENON100) and a LY (section 6.7) equal to 4.6 pe/keV$_{ee}$.

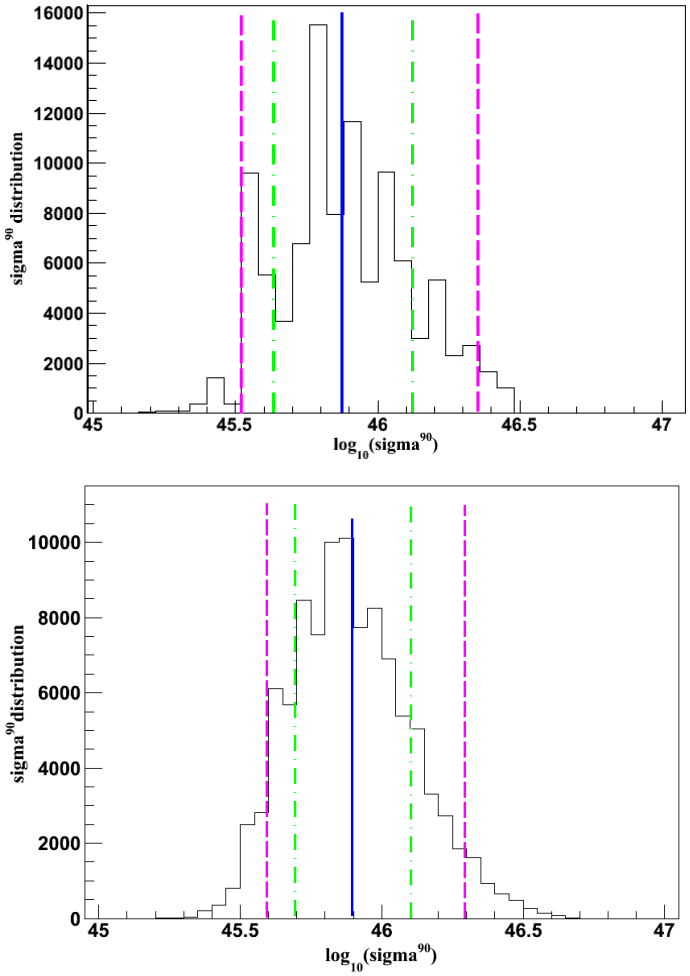

Figure 7.7: Distribution of the σ^{90} for a WIMP mass of 20 GeV/c^2 (top) and 100 GeV/c^2 (bottom). The blue line is the median of the distribution while the magenta and green lines represent the 5-95% and 16-84% quantiles, respectively.

The respective WIMP S1 search region is [3, 70] pe, where the low edge of the interval

has been chosen to be close, as much as possible, to the detector energy threshold while 70 pe is the conversion of the upper bound of the WIMP search region, i.e. 12 keV$_{ee}$ or 50 keV$_r$ (Section 6.1). Moreover, to reach the goal of having less than 1 background event in the fiducial volume in 1 year of exposure, a discrimination of 99.75% is applied to the ER, which gives an acceptance for the NR ones of about 40%. With these conditions, the total mean number of background expected events in 1 tonne of LXe fiducial volume and considering 2 years of exposure is 1.17. The respective sensitivity plot is shown in figure 7.8. The minimum for the cross section has been found to be $1.87 \cdot 10^{-47}$ cm^2 for a WIMP of mass 45 GeV/c^2. The limits in figure 7.8 have been obtained considering the $\mathcal{L}_{eff}$ equal to zero below 3 keV$_r$, which is the lowest measured point (figure 3.19).

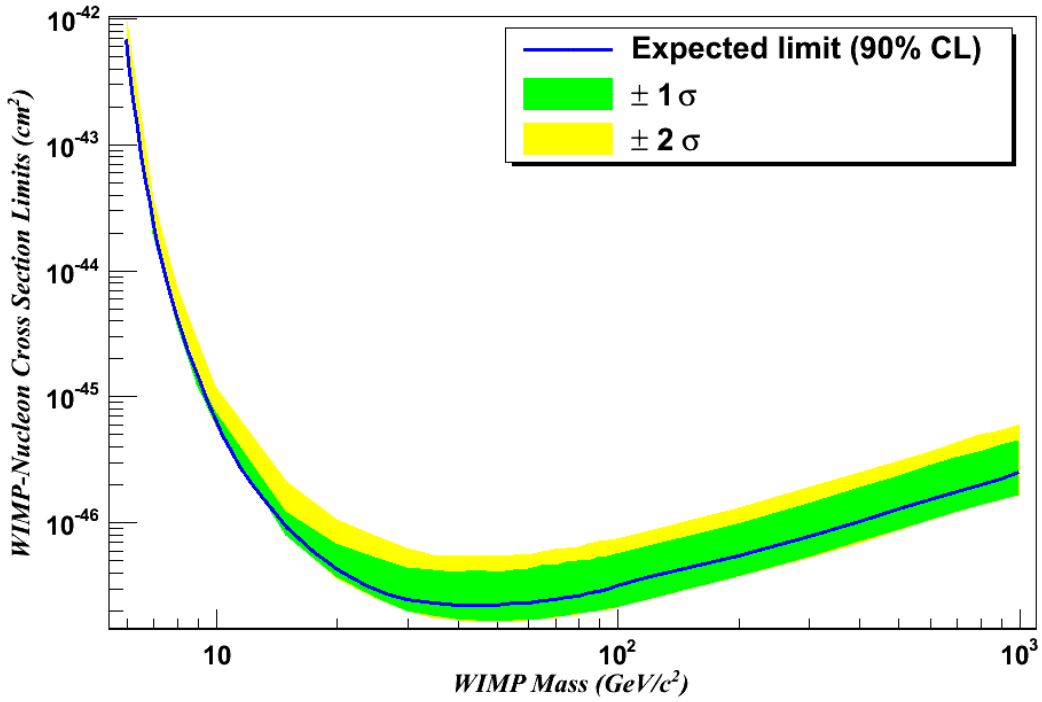

Figure 7.8: XENON1T sensitivity, with LY = 4.6 pe/keV$_{ee}$, setting the $\mathcal{L}_{eff}$ to 0 (Section 3.6) for recoil energies below 3 keV$_r$. The blue curve represents the sensitivity at the 90% CL as function of the WIMP mass. The yellow and the green bands are the contours at $\pm$ 2 σ and $\pm$ 1 σ, respectively.

As we can see, the green band and the blue line are pushed towards the bottom part of the yellow band. This behavior is due to the very low background. In fact, the number of observed events is given by a Poissonian extraction with the mean equal to the expected background events, 1.17 in this case. With such a low number, the probability to observe 0 events is greater than 30%. This means that in more than 30% of the cases the limit is evaluated with 0 events giving always the same value for the

σ^{90}. This squeezes the σ^{90} distribution towards its lower bound. Since the bottom part of the yellow and green band represent the 5% and 16% quantiles of the distribution, they are basically overlapped. The median is not superimposed but still very close to them. Increasing the background, the bands and the blue line will be more centered between each other, as expected. Besides previous case, it is also possible to extrapolate the behavior of the $\mathcal{L}_{eff}$ down to 1 keV$_r$, red solid curve in figure 3.19. Below such an energy the $\mathcal{L}_{eff}$ is 0. In this case the sensitivity becomes as shown in figure 7.9 but the minimum for the cross section is found to be almost at the same value for the case showed in figure 7.8.

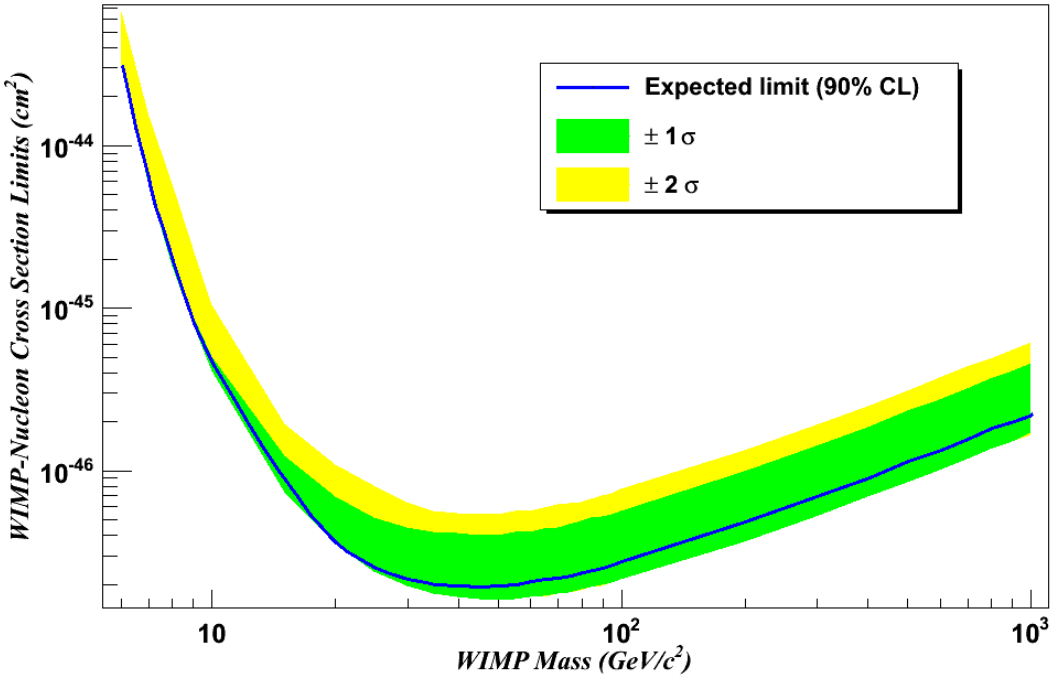

Figure 7.9: XENON1T sensitivity, with LY = 4.6 pe/keV$_{ee}$, using the $\mathcal{L}_{eff}$ extrapolation down to 1 keV$_r$. The blue curve represents the sensitivity at the 90% CL as function of the WIMP mass. The yellow and the green bands are the contours at $\pm$ 2 σ and $\pm$ 1 σ, respectively.

Comparing the limits with and without the $\mathcal{L}_{eff}$ extrapolation, figure 7.10, we see that even if they share the same minimum, they are different at very low WIMP masses. The difference between the limits is not negligible for very low WIMP masses, $\lesssim$ 20 GeV/c^2, because their spectra fall much faster than the higher mass ones, figure 7.11. From figures 7.10 and 7.11 it is clear that the $\mathcal{L}_{eff}$ cut has a larger impact on the low WIMP mass spectra while for higher masses ($m_\chi \gtrsim 20$ GeV/c^2) it is negligible. Indeed, for $m_\chi < 20$ GeV/c^2, the spectra used for the gaps evaluation have very few events

when $\mathcal{L}_{eff} = 0$ below 3 keV$_r$ compared with the case where the $\mathcal{L}_{eff}$ extrapolation is used. Having less events in the gaps, the value required for σ^{90} to observe 0 events in the maximum gap in the 90% of the times is lower, thus resulting in stronger limits.

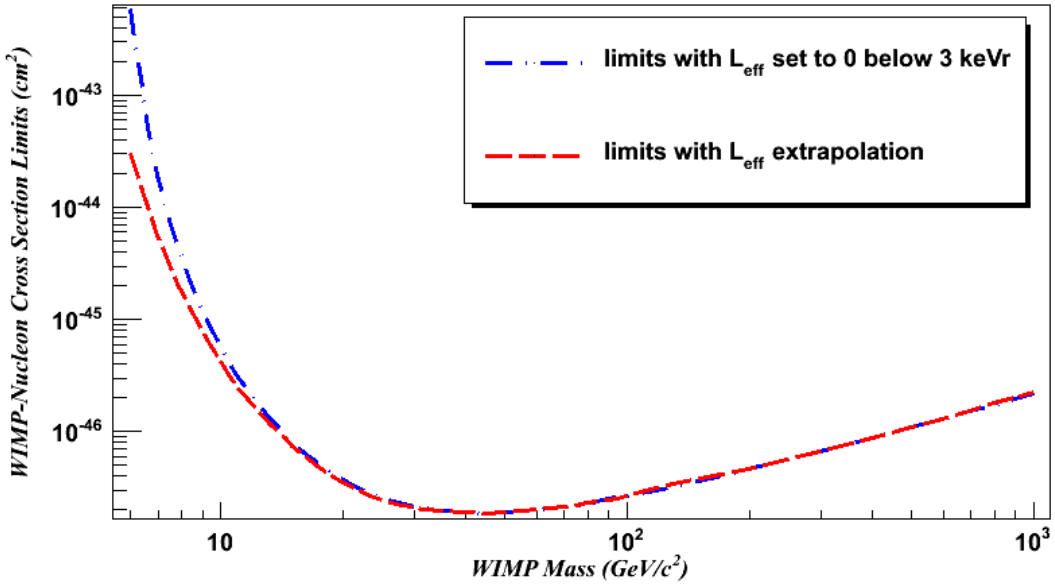

Figure 7.10: Comparison between sensitivities, with LY = 4.6 pe/keV$_{ee}$, considering the $\mathcal{L}_{eff}$ extrapolation (red dashed curve) and setting it to 0 for recoil energies below 3 keV$_r$ (blue dash-dotted curve).

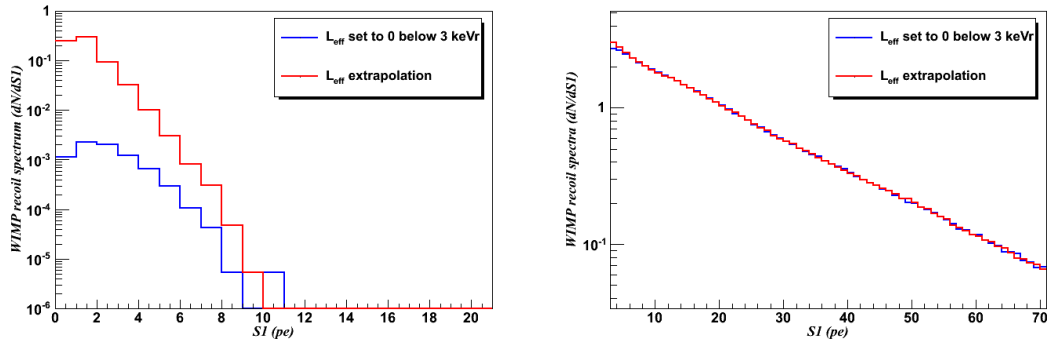

Figure 7.11: Left, WIMP recoil spectrum ($\sigma = 1 \cdot 10^{-40}$ cm^2) for a $m_\chi = 6$ GeV/c^2. Blue (red) line is the spectrum considering a $\mathcal{L}_{eff}$ set to 0 below 3 keV$_r$ (with $\mathcal{L}_{eff}$ extrapolation). Right, same as left but for $m_\chi = 100$ GeV/c^2.

7.4 Sensitivity with LY = 5.6 pe/keV$_{ee}$

Improving the transparency of the meshes (Section 5.6), for example using for all of them a wire pattern geometry with the only exception of the anode, the mean S1-yield (Section 6.7) increases from 4.6 pe/keV$_{ee}$ up to 5.6 pe/keV$_{ee}$ (with an electric field of 530 V/cm, as in XENON100). Having considered this hypothesis about the meshes during the detector design, we evaluate the sensitivity also in such a condition. With the LY equal to 5.6 pe/keV$_{ee}$, the S1 search region becomes [3, 85] pe where, as before, the upper bound is the conversion of the 12 keV$_{ee}$ energy line. The total mean number of expected background events in 1 tonne of LXe fiducial volume and considering 2 years of exposure is 1.21. The respective sensitivity plot is shown in figure 7.12.

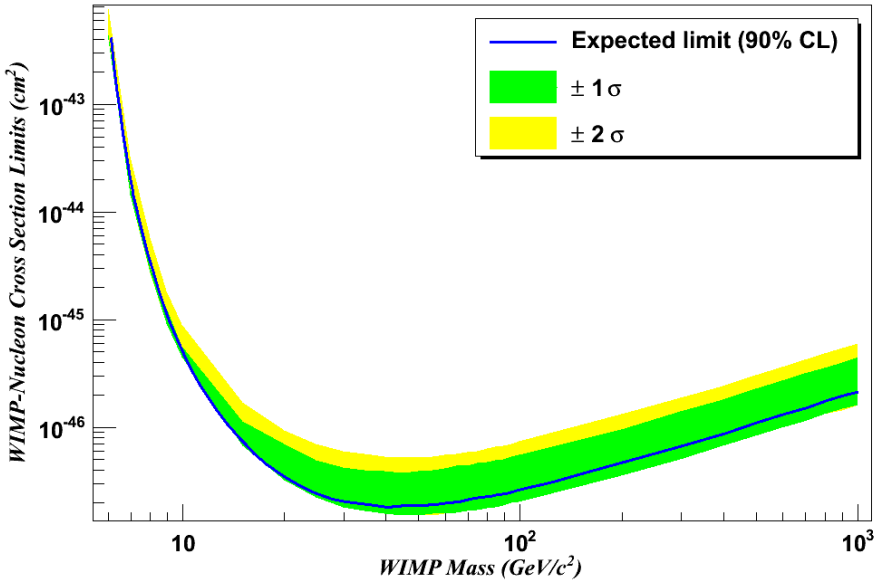

Figure 7.12: XENON1T sensitivity, with LY = 5.6 pe/keV$_{ee}$, setting the $\mathcal{L}_{eff}$ to 0 for recoil energies below 3 keV$_r$. The blue curve represents the sensitivity at the 90% CL as function of the WIMP mass. The yellow and the green bands are the contours at ± 2 σ and ± 1 σ, respectively.

The minimum for the cross section has been found to be $1.79 \cdot 10^{-47}$ cm^2 for a WIMP of mass 40 GeV/c^2. Figure 7.12 has been obtained considering the $\mathcal{L}_{eff}$ set to 0 for recoil energy below 3 keV$_r$. Using the $\mathcal{L}_{eff}$ extrapolation, the minimum for the cross section is at $1.80 \cdot 10^{-47}$ cm^2 for a WIMP of mass 40 GeV/c^2, figure 7.13. As already obtained for the LY= 4.6 pe/keV$_{ee}$, also in this case the sensitivity is stronger, for very low masses, when the $\mathcal{L}_{eff}$ extrapolation is used, figure 7.14. The current choice for the electrodes of the TPC is with the meshes, as described in section 5.6, because of its simplicity in the

construction. For this reason, from now on, we will focus on the sensitivity estimation using a LY of 4.6 pe/keV$_{ee}$.

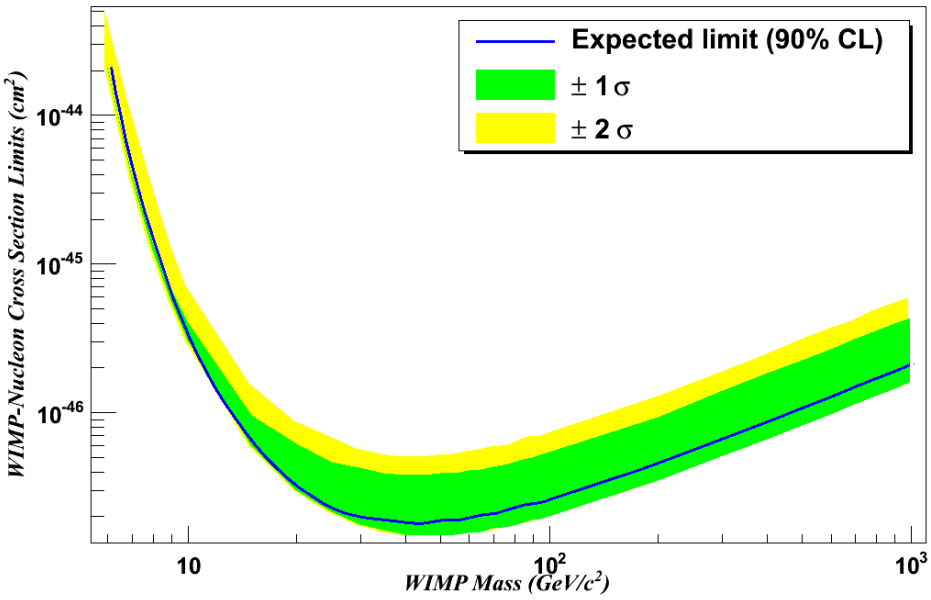

Figure 7.13: XENON1T sensitivity, with LY = 5.6 pe/keV$_{ee}$, using the $\mathcal{L}_{eff}$ extrapolation down to 1 keV$_r$. The blue curve represents the sensitivity at the 90% CL as function of the WIMP mass. The yellow and the green bands are the contours at ± 2 σ and ± 1 σ, respectively.

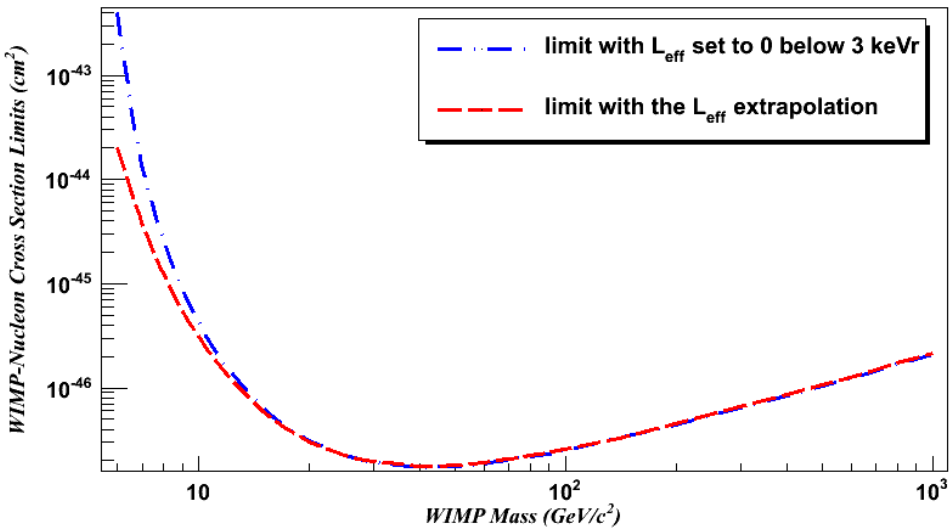

Figure 7.14: Comparison between sensitivities, with LY = 5.6 pe/keV$_{ee}$, with the $\mathcal{L}_{eff}$ extrapolation (red curve) and setting it to 0 for recoil energies below 3 keV$_r$ (blue curve).

7.5 Sensitivity for different ^{222}Rn contaminations

The limits obtained until now, have been evaluated considering a ^{222}Rn contamination of 1 μBq/kg (Subsection 6.4.2). This value is the goal chosen by the XENON collaboration. An increase of this quantity will clearly affect the experimental sensitivity. As example, considering a factor 3 (or 10) more ^{222}Rn contamination, i.e. 3 (or 10) μBq/kg, the minimum for the cross section moves from $1.87 \cdot 10^{-47}$ cm^2 for a WIMP of mass 45 GeV/c^2 (Section 7.3) to $2.15 \cdot 10^{-47}$ (or to $2.94 \cdot 10^{-47}$) cm^2 for a WIMP of mass 40 GeV/c^2, figures 7.15 - 7.17.

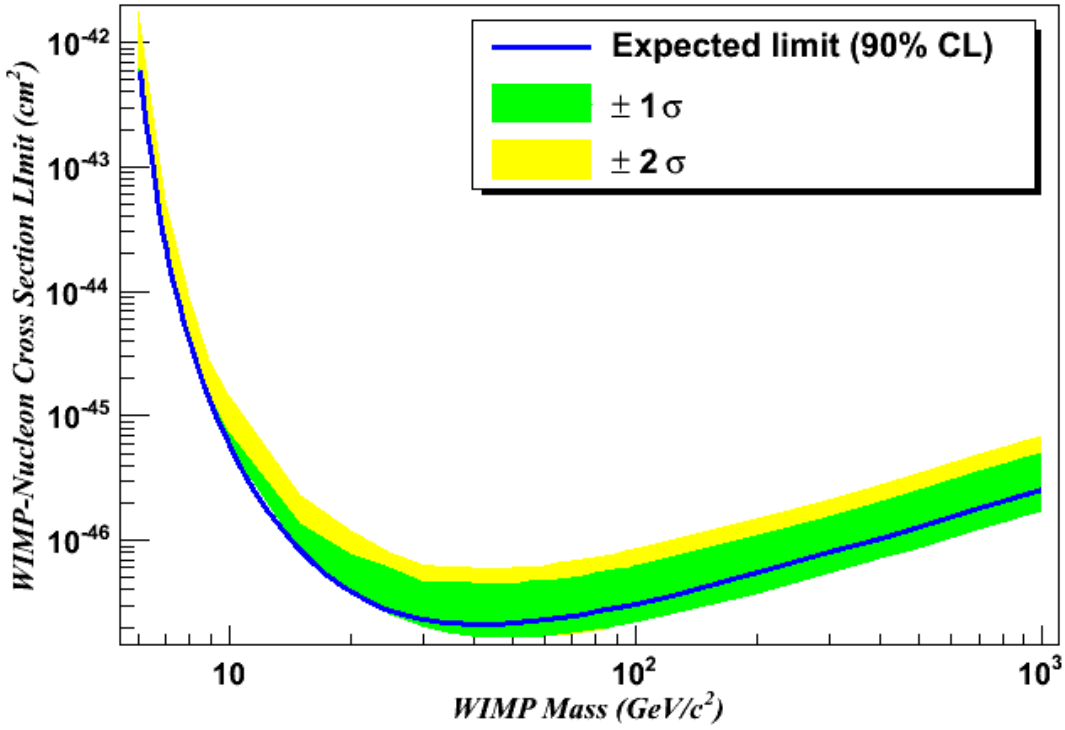

Figure 7.15: XENON1T sensitivity, blue curve, for: 3 μBq/kg of ^{222}Rn; LY = 4.6 pe/keV$_{ee}$ and $\mathcal{L}_{eff} = 0$ for $E_r \leq 3$ keV$_r$. Also shown is the contour at $\pm$ 2(1) σ yellow (green) band.

The curves with higher ^{222}Rn contamination have weaker limits, i.e. higher σ^{90}, because of the higher number of background events: 1.5 and 2.7 for contaminations of 3 and 10 μBq/kg, respectively. The difference is negligible for very low masses, $\lesssim 15$ GeV/c^2, because in such cases the gaps are already very small compared to the ones from higher mass WIMPs, figure 7.18. Thus, an increase in the number of background events, i.e. a reduction in the gaps dimensions, will not affect the sensitivity.

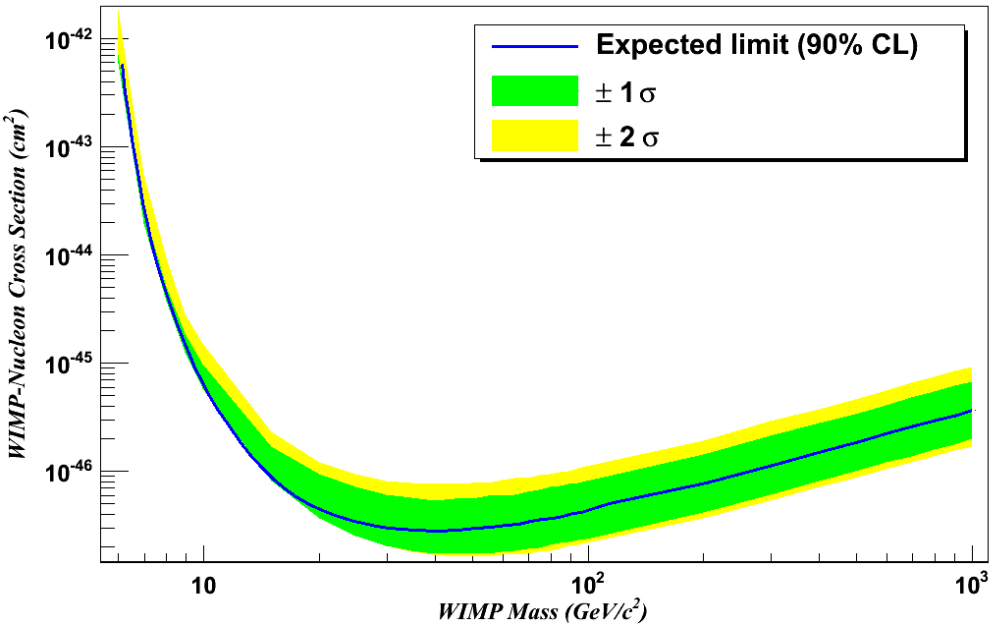

Figure 7.16: Same as figure 7.15 but assuming a contamination of 10 μBq/kg of ^{222}Rn.

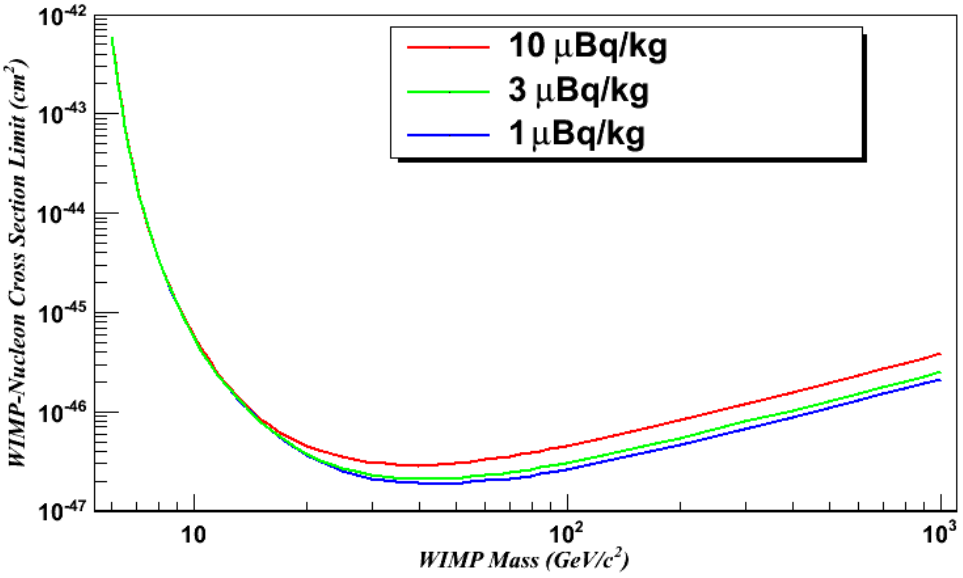

Figure 7.17: Comparison between limits obtained with different values of the ^{222}Rn contaminations: 1 μBq/kg (blue curve), 3 μBq/kg (green curve) and 10 μBq/kg (red curve). All the sensitivities have been evaluated using LY = 4.6 pe/keV$_{ee}$ and setting the $\mathcal{L}_{eff}$ to 0 for recoil energies below 3 keV$_r$.

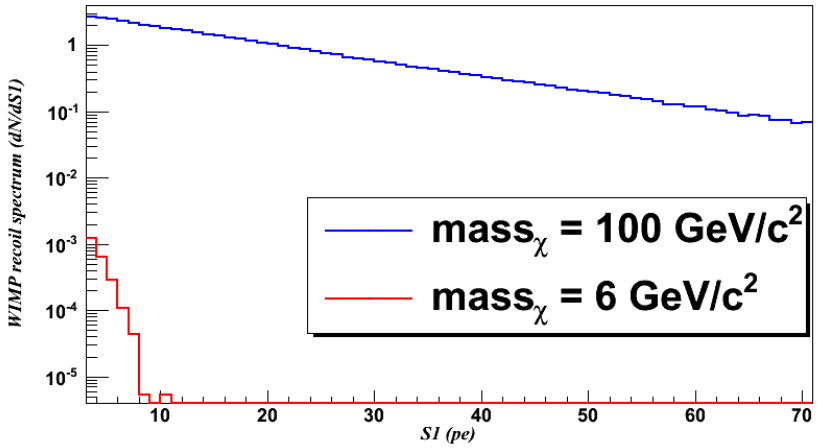

Figure 7.18: Comparison between WIMP spectra for $m_\chi = 6$ GeV/c^2 (red line) and $m_\chi = 100$ GeV/c^2 (blue line), with $\sigma = 1. \cdot 10^{-40}$. Assuming $\mathcal{L}_{eff} = 0$ below 3 keV$_r$.

7.6 Sensitivity as function of the exposure time

The sensitivity has also been studied as function of the exposure time, i.e. the time of data acquisition. Indeed, having the spectra expressed in ev/day/kg/pe and fixing the S1 search region and the fiducial volume, the number of expected events is directly proportional to the exposure time. In such a study we assumed: LY = 4.6 keV$_{ee}$, ^{222}Rn concentration of 1 μBq/kg and the [3, 70] pe WIMP search region. For the different values of the exposure time, the number of background events are: 0.58 in 1 t-y; 1.17 in 2 t-y (the value already used in the previous sections); 1.75 in 3 t-y; 2.33 in 4 t-y and 2.92 in 5 t-y. Different acquisition times give different sensitivities, figures 7.19-7.22. The sensitivity for 2 years of exposure is shown in figure 7.8 and, hence, it is not represented here. Clearly, an increase in the exposure time increases also the signal events as well as the background events. With a higher background, the median and the $\pm 1\sigma$ band are more centered with respect the $\pm 2\sigma$ band, figure 7.22. Figures 7.19 - 7.22 have been obtained considering 1 tonne of fiducial volume and varying only the exposure time. We also have assumed LY = 4.6 pe/keV$_{ee}$ and set the $\mathcal{L}_{eff}$ to 0 for recoil energies below 3 keV$_r$. The minima for the different cases are:

- 1 t-y; $3.25 \cdot 10^{-47}$ cm^2;
- 2 t-y; $1.87 \cdot 10^{-47}$ cm^2;
- 3 t-y; $1.61 \cdot 10^{-47}$ cm^2;
- 4 t-y; $1.45 \cdot 10^{-47}$ cm^2;

- 5 t-y; $1.40 \cdot 10^{-47}$ cm^2;

all obtained for a WIMP mass of 45 GeV/c^2. As expected, the sensitivity improves increasing the exposure time, figure 7.23.

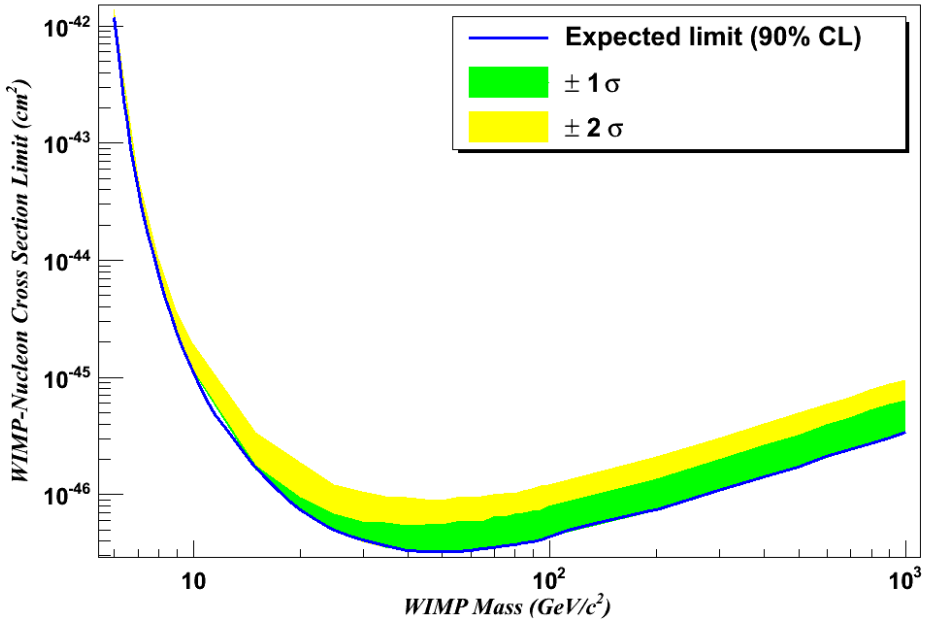

Figure 7.19: XENON1T sensitivity for 1 t-y exposure time. The blue curve represents the sensitivity at the 90% CL, as function of the WIMPs mass. The yellow and the green bands are the contours at $\pm$ 2 σ and $\pm$ 1 σ, respectively.

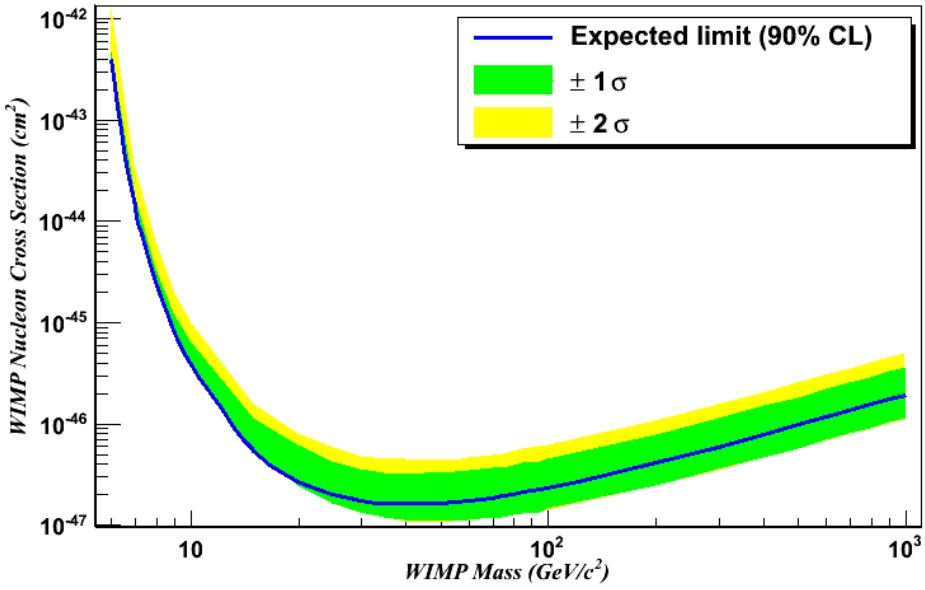

Figure 7.20: Same as figure 7.19 but considering 3 t-y exposure time.

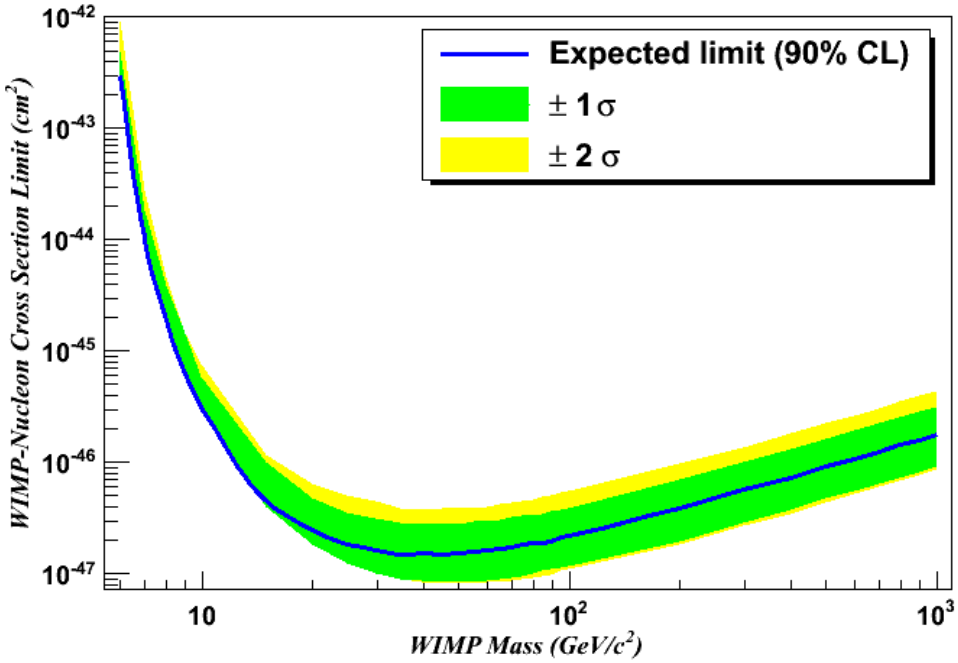

Figure 7.21: XENON1T sensitivity for 4 t-y exposure time. The blue curve represents the sensitivity at the 90% CL, as function of the WIMPs mass. The yellow and the green bands are the contours at $\pm$ 2 σ and $\pm$ 1 σ, respectively.

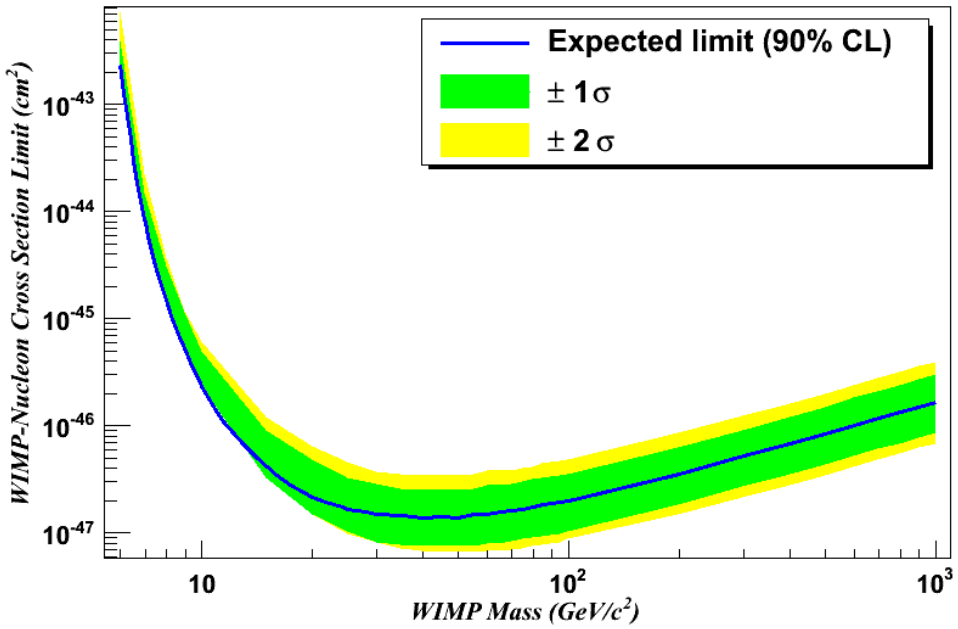

Figure 7.22: Same as figure 7.21 but considering 5 t-y exposure time.

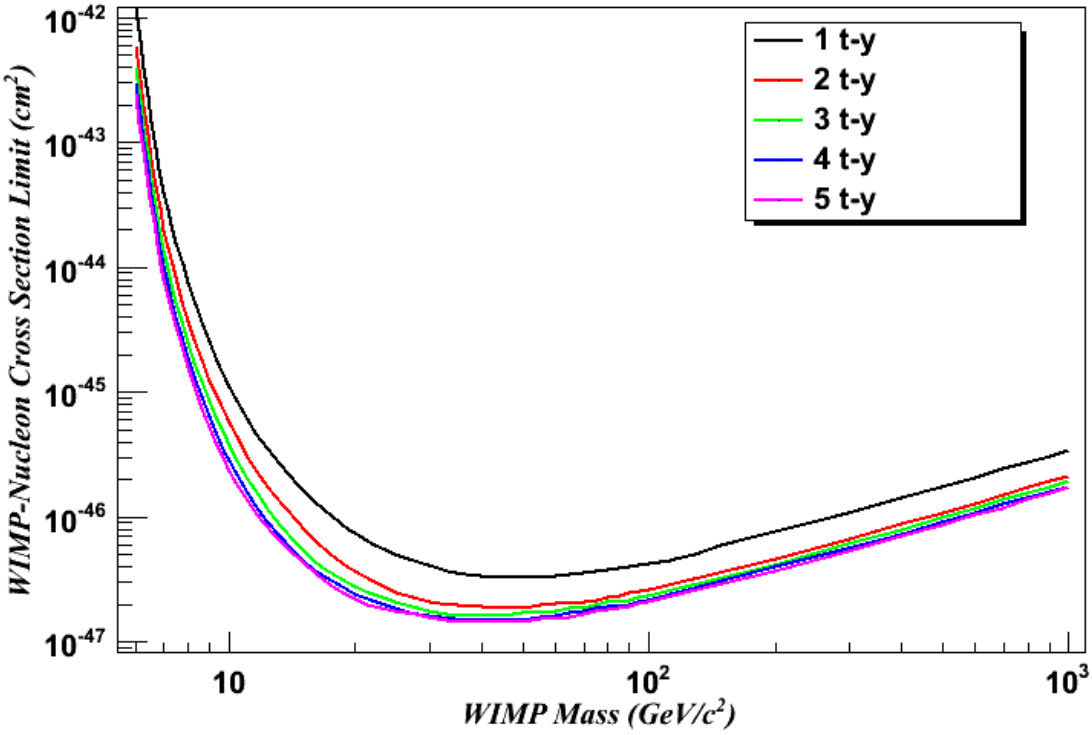

Figure 7.23: Comparison between sensitivities computed for different exposure times. The curves have been obtained with LY = 4.6 pe/keV$_{ee}$ and setting the $\mathcal{L}_{eff}$ to 0 for recoil energies below 3 keV$_r$.

Finally, a comparison between the minima for the cross section, as function of the exposure time, is shown in figure 7.24.

7.7 An alternative statistical test: the Likelihood Ratio method

To cross check the results obtained with the *Maximum Gap* method, we evaluate the XENON1T sensitivity also with a different statistical test: the *Likelihood Ratio* method.

A statistical test is used to make a statement on how well the observed data are in agreement with some predicted probability, i.e. a hypothesis. The hypothesis under test is usually called the *null hypothesis*, $\mathbf{H_0}$, and it is tipically tested against others called *alternative hypotheses*, $\mathbf{H_1}$, $\mathbf{H_2}$, etc. To investigate between the different H_i, it is required a *test statistic* (t): a one-dimensional or multi-dimensional function of the data sample, $\mathbf{x}$. The test statistic is characterized by different p.d.f. relative to the different hypotheses: $g(t(\mathbf{x})|H_0)$, $g(t(\mathbf{x})|H_1)$, etc. A criterion that can be used to decide if to

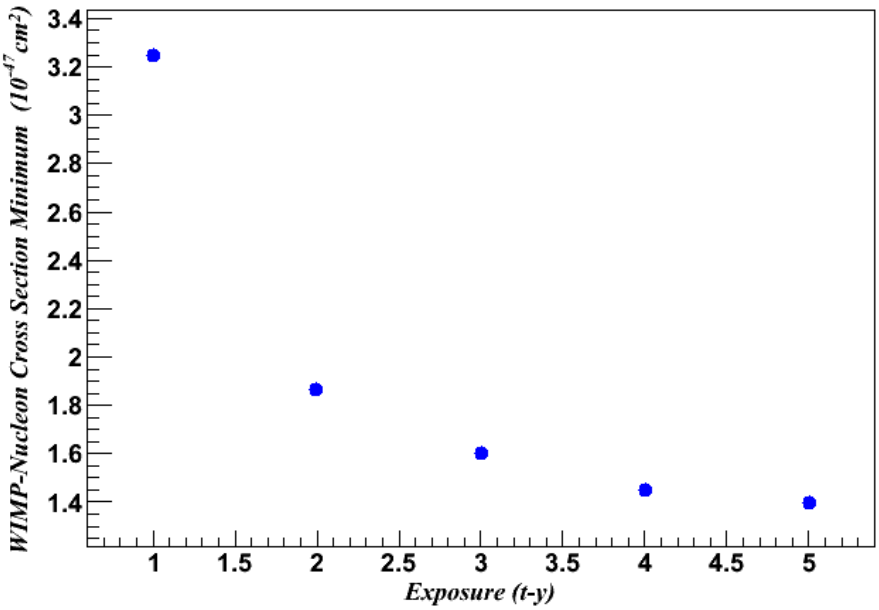

Figure 7.24: Minima for WIMP-nucleon cross section as function of the exposure time.

reject or to accept a given H_i, is based on the definition of the so called *critical region*: if the value of the test statistic falls inside this region, then H_0 is rejected otherwise it is accepted. The *significance level of the test*, α, i.e. the probability for $t(\mathbf{x})$ to be found inside its critical region, is defined as:

$$\alpha = \int_{t^{\text{low}}(\mathbf{x})}^{\infty} g(t(\mathbf{x})|H_0)dt, \tag{7.44}$$

where the $t^{\text{low}}(\mathbf{x})$ is the low edge of the critical region. When looking for upper limits on parameters of some new phenomenon, it is usually assumed that the model containing signal plus background represents the null hypothesis, H_0, that is tested against the background-only hypothesis, H_1. The level of agreement between data and a certain hypothesis H_i is quantified by using the p-value that represents the probability of observing data with less or equal compatibility with the H_i. Thus, the hypothesis is rejected if p is observed below a certain threshold. In a frequentist approach, starting from the Neyman-Pearson lemma, the best test statistic in the sense of maximum power (and hence maximum signal purity) for a given significance level (or selection efficiency) is given by the *Likelihood Ratio* [228, 229]:

$$\lambda(\mu) = \frac{\max\limits_{\mu \text{ fixed}} \mathcal{L}(\mu, \hat{\hat{\theta}})}{\mathcal{L}(\hat{\mu}, \hat{\theta})};\ \theta \in \mathbb{R}^n, \tag{7.45}$$

where μ represents the *parameter of interest* (i.e. the one under estimation) and θ are

other parameters in the model, called *nuisance parameters*. These nuisance parameters are obtained from the fit to the data and they introduce a broadening in the likelihood, as functions of μ, with respect to the case where they are a-priori fixed. In equation (7.45), the numerator represents the likelihood function maximized for a fixed value of μ: indeed, the $\hat{\hat{\theta}}$ are the conditional Maximum Likelihood Estimators (MLEs) of the nuisance parameters when μ is fixed. At the denominator there is, instead, the maximized (unconditional) likelihood function, where $\hat{\mu}$ and $\hat{\theta}$ are the maximum estimators of μ and θ. Clearly $\lambda \in [0;1]$, where values close to 0 represent great incompatibility between data and hypothesis. A more suitable expression for the test statistic is given by:

$$q_\mu = -2\ \ln\lambda(\mu), \tag{7.46}$$

where $q_\mu \in [0, \infty]$, with value of the test close to zero indicating a good agreement between data and hypothesis. From an observed data sample, $\mathbf{x}$ ($\mathbf{x} \in \mathbb{R}^{\mathbf{n}}$), one can directly quantify the discrepancy between data and the value of the parameter μ, given a certain H, as:

$$p_\mu = \int_{q_\mu^{obs}}^{\infty} f(q_\mu|H)dq, \tag{7.47}$$

where q_μ^{obs} is the value of test statistic from the observed data sample and $f(q_\mu|H)$ is its p.d.f. under the tested hypothesis H. From equation (7.47) it is clear that, in order to evaluate the p-value, the p.d.f. of the q_μ under the different hypotheses are needed. Such distributions can be obtained by means of MC simulations.

7.7.1 XENON1T sensitivity based on the Likelihood Ratio

For simplicity, instead of the cross section, the analysis has been carried out considering the expected number of signal events, μ_s, that has a one to one correspondence with the assumed value of σ.

The test statistic has been defined as:

$$q_{\mu_s} = \begin{cases} -2\ \ln\frac{L(\mu_s,\hat{\hat{\theta}}(\mu_s))}{L(\hat{\mu}_s,\hat{\theta})} & \hat{\mu}_s < \mu_s \\ \\ 0 & \hat{\mu}_s > \mu_s \end{cases} \tag{7.48}$$

The last case has been set since we are interested only in upper limits. The choice of the correct form for q_{μ_s} is based on μ_s, the expected mean number of events, and $\hat{\mu}_s$, the maximum likelihood estimator for μ_s.

Given a certain WIMP mass, to test different hypotheses about μ_s, the knowledge of the p.d.f. of the test statistic q_{μ_s} is required. To build $f(q_{\mu_s}|H_{\mu_s})$, the p.d.f. of q_{μ_s} for

the hypothesis H_{μ_s} of a signal strength μ_s in addition to the background, we generated $\mathcal{O}(10^4)$ MC toy experiments for each value of μ_s up to $\mu_s = 20$. For the $f(q_{\mu_s}|H_0)$, the p.d.f. of the background-only hypothesis H_0, we generate $\mathcal{O}(10^4)$ MC toy experiments with $\mu_s = 0$.

In the toy experiments the generation of the signal, n_s^{obs}, and background, n_b^{obs}, events has been performed in a way similar to what has been done for the Maximum Gap analysis: Poissonian extractions with mean equal to the mean number of expected signal (μ_s) and background (μ_b) events and S1 randomly extracted from their spectra. In addition to the S1 observable we used also a discrimination parameter Y, with a distribution modeled as the usual $log_{10}(S2/S1)$ (figure 4.16), approximated as a Gaussian. In particular, ER background events are distributed as Gauss(0, 1) and NR events (both background and signal) as Gauss(-2.58, 0.92). Thus, we have a 99.5% discrimination below the median of the NR distribution (i.e. 50% NR acceptance) and a 99.75% ER discrimination with 40% acceptance, as it was measured in the XENON100 experiment. In this way we use in the analysis the whole sample of events without performing any a-priori selection on the discrimination parameter: i.e. we keep also all the electron recoil background events. In figure 7.25 we show the distribution in S1 and Y of a single toy experiment, where we superimposed the background with 50 signal events ($m_\chi = 40$ GeV/c^2). The number of signal events is chosen so large just for illustration purpose.

The likelihood function is the so-called *extended maximum likelihood*, since also the number of expected events is treated as variable of the experiment, and it is defined as:

$$L(\mu_s) = \frac{e^{-(\mu_s+\mu_b)}(\mu_s+\mu_b)^{n^{obs}}}{n^{obs}!} \prod_{i=1}^{n^{obs}} \left[\frac{\mu_s \; f_s(S1_i) \; g_s(Y_i) + \mu_b \; f_b(S1_i) \; g_b(Y_i)}{\mu_s + \mu_b} \right], \quad (7.49)$$

where $n^{obs} = n_s^{obs} + n_b^{obs}$ is the total number of the observed events, while $\mu_{s,b}$ are the expected mean number of signal and background events, respectively; $f_{s,b}$ are the p.d.f. in S1, and $g_{s,b}$ are the p.d.f. in the discrimination parameter Y. Using this form for the likelihood function, the analysis is said *unbinned*.

To estimate the XENON1T sensitivity many background-only experiments have been generated and the test statistic, $q_{\mu_s}^{obs}$, is evaluated to calculate the p-value. Here, the knowledge of the $f(q_{\mu_s}|H_{\mu_s})$ and $f(q_{\mu_s}|H_0)$ p.d.f. previously calculated is used. The former p.d.f. is used to evaluate the level of disagreement between current data and the signal hypothesis, assuming the signal hypothesis true, and it is given by:

$$p_s = \int_{q_{\mu_s}^{obs}}^{\infty} f(q_{\mu_s}|H_{\mu_s}) dq_{\mu_s}, \quad (7.50)$$

where $q_{\mu_s}^{obs}$ is the value for the statistic given by the data. To find the value of the cross section at the 90% CL, one has to look for a value of μ_s for which the integral in equation

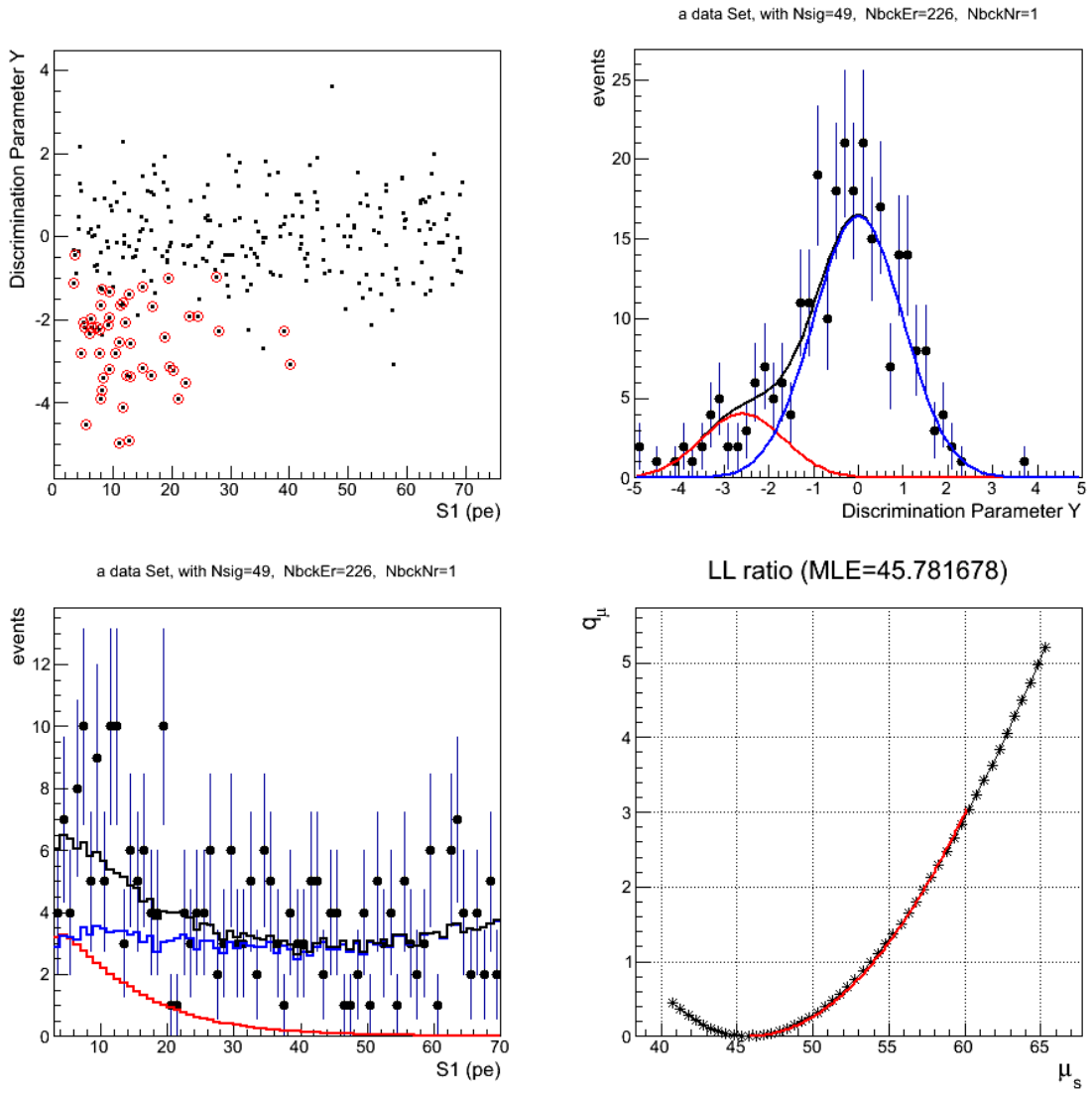

Figure 7.25: Illustration of a single MC toy experiment. Top-left: distribution in S1,Y of the events (black dots); the signal events are emphatized with the red circle. Top-right: projection in the discrimination parameter Y; in red the signal events, in blue the background and in black their sum. Bottom-left: projection in S1; in red the signal events, in blue the background and in black their sum. Bottom-right: values of the statistic test q_μ as a function of different tested values for μ_s.

(7.50) is equal to 0.1. In the case of downward fluctuations of the background it can happen that small cross sections, to which the experiment may not be sensitive, are excluded. In order to avoid this, a standard approach called "CLs" [230, 231] is used,

where p_s is modified as:

$$p_s \rightarrow p'_s = \frac{p_s}{1 - p_b}, \tag{7.51}$$

where

$$1 - p_b = \int_{q_\mu^{obs}}^{\infty} f(q_{\mu_s}|H_0) dq_{\mu_s}. \tag{7.52}$$

Equation (7.52) expresses the probability of the test statistic q_{μ_s} to be larger than the observed one under the background-only hypothesis H_0. In this case, the upper limit on the cross section (90% CL), as function of the WIMP mass, is found solving the equation:

$$p'_s(\mu_s^{90\%CL}) = 0.1 \tag{7.53}$$

for each WIMP mass. Equation (7.53) can be solved numerically testing various values of μ_s until the one which satisfies the equation is found, called $\mu_s^{90\%CL}$. To do this it is necessary to evaluate the integrals in equations (7.50) and (7.52) for each value of the cross section that one wants to test, so it is mandatory to know the p.d.f. of q_{μ_s} under both the hypothesis H_{μ_s} and H_0. It has to be mentioned that sometimes it is not necessary to evaluate the p.d.f. $f(q_{\mu_s}|H_{\mu_s})$. Indeed, for a large number of events, it is possible to apply the Wilks theorem [232], which ensures that the p.d.f. of $f(q_{\mu_s}|H_{\mu_s})$ follows a chi-square function, and so calculate it analytically.
We show here the results of the XENON1T sensitivity, using the same assumptions made in section 7.3: LY= 4.6 pe/keV$_{ee}$, 1 μBq/kg of ^{222}Rn contamination and $\mathcal{L}_{eff} = 0$ for recoil energies below 1 keV$_r$. The resulting limits are shown in figure 7.26: the minimum is found at $\sigma = 1.21 \cdot 10^{-47}$ cm^2 for $m_\chi = 40$ GeV/c^2 (90% CL). In the same figure we report also the result obtained with the Maximum Gap method (with the same assumptions), see figure 7.9, where the minimum was at $\sigma = 1.87 \cdot 10^{-47}$ cm^2 for $m_\chi = 45$ GeV/c^2 (90% CL). The two results differ by less than a factor 2; we consider this an acceptable agreement given the intrinsic differences in the two statistical methods.

So far, we did not take into account the uncertainty in the NR energy scale. We plan to continue the study of the sensitivity including the $\mathcal{L}_{eff}$ uncertainty as a nuisance parameter, using the full power of the *Profile Likelihood* method which is a natural extension of the Likelihood Ratio method.

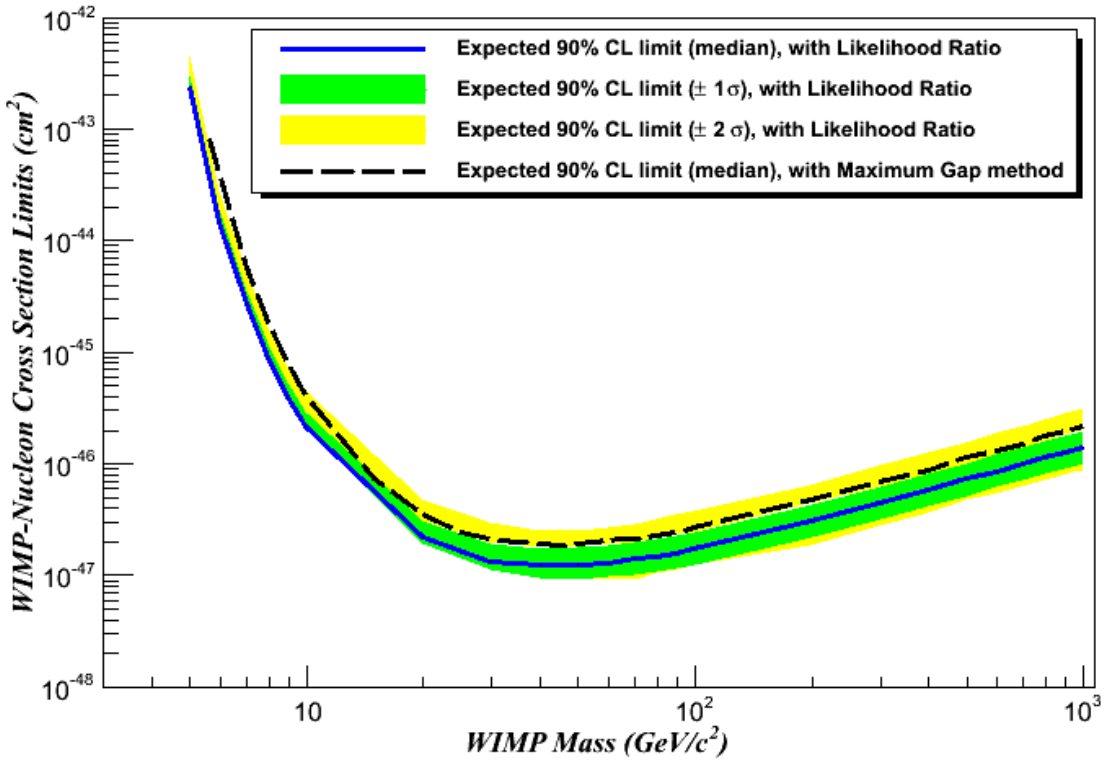

Figure 7.26: XENON1T sensitivity (blue curve), evaluated with the Likelihood Ratio method, assuming: LY = 4.6 pe/keV$_{ee}$, setting the $\mathcal{L}_{eff} = 0$ for $E_r \leq 3$ keV$_r$. The blue curve represents the sensitivity at the 90% CL as function of the WIMP mass. The yellow and the green bands are the contours at $\pm$ 2 σ and $\pm$ 1 σ, respectively. As comparison, the limits evaluated with the Maximum Gap method are also shown.

Summary and Conclusions

Despite the scientific achievement of the last decades in the astrophysical and cosmological fields, the majority of the Universe energy content is still unknown. Perhaps, the dark matter discovery will address the *missing mass problem* but experimental results, based on both direct and indirect detection techniques, have not yet confirmed any positive signal from such a kind of matter. Due to the very small cross section for WIMP interactions, the number of expected events is very limited ($\sim$ 1 ev/tonne/year), thus requiring detectors with large target mass and low background level. The use of double phase, LXe/GXe, TPC represents one of the most promising techniques for this kind of search. Indeed, two experiments based on this technology, XENON100 [8] and LUX [10], published the most stringent limits on WIMP-nucleon scattering cross section, σ^{DM}, in 2012 and 2013, respectively. Driven by the excellent results achieved, the XENON collaboration is now focusing on the realization of the first tonne scale LXe-based detector, named XENON1T. The goal of the new experiment is to lower by about two order of magnitudes the current sensitivity to WIMP-nucleon interactions, reaching a minimum for σ^{DM} of the order of 10^{-47} cm^2. To achieve this goal, a background reduction of a factor hundred with respect to XENON100 is mandatory.

In this PhD thesis I report the work concerning the characterization and evaluation, through MC simulations, of the background of the XENON1T detector and the determination of the sensitivity of the experiment. To this aim we implemented, with very high accuracy, the geometry of the main components of the experiment: the two cryostats, the field cage, the electrodes, the PMTs together with their support structures, the diving bell, the bottom filler and the meshes for the electric field generation (Sections 5.1 - 5.6). Using the detector material contaminations, evaluated through a detailed screening (Section 6.2), the electromagnetic and nuclear recoil (ER and NR) backgrounds have been characterized and quantified.

The ER has been divided into two contributions, namely the **internal** (Section 6.3), from the materials, and the **intrinsic** (Section 6.4), from sources intrinsic to the detection medium itself (^{85}Kr and ^{222}Rn) and physical backgrounds (solar neutrinos and

^{136}Xe double-beta decays). Concerning the NR, the proper neutron yield (table 6.6) from each source has been considered.

For some material contaminations, only upper limits have been found during the screening campaign, table 6.2. For this reason, the background has been first evaluated using such upper limits and then it has been evaluated setting them to 0. In this way we obtained the upper and the lower limit for the background.

In the analysis of the simulation outputs, several cuts have been applied to the data: the fiducial volume cut, which allows to select only the events in the inner region of the LXe; the single scatter cut, since WIMPs are expected to give at most one recoil inside the target volume; the energy cut to select only the events inside the dark matter search region [5, 50] keV$_r$ that corresponds to the [2, 12] keV$_{ee}$ energy window in ER equivalent energy (Sections 3.6 and 6.1).

The fiducialization of the volume is used to reduce the backgrounds from the detector materials: thanks to the LXe self-shielding ability particles such as γ and e$^-$ have very low probability to reach the inner part of the target volume. In this work, as reference, it is used a fiducial volume of 1 tonne.

From the background spectra, the total number of the expected ER background events has been estimated. For the detector materials, figures 6.4 and 6.5, it results:

$$[\mathbf{6.7^{\pm 0.3}},\ \mathbf{7.3^{\pm 0.3}}]\ \cdot\ \mathbf{10^{-6}\ events/kg/day/keV}_{ee},$$

corresponding to

$$[\mathbf{25^{\pm 1}},\ \mathbf{27^{\pm 1}}]\ \mathbf{events/y}\ \text{(in 1 tonne FV)},$$

where the highest contribution comes from the cryostat shell contaminations, about half of the total ER background from materials (table 6.3 and figure 6.9), mainly from ^{60}Co; the photomultipliers accounts for about 20% and the other stainless steel components for about 15%. The contribution from PTFE and Copper is about 1%. For what concerns the intrinsic sources, figures 6.13 and 6.14, the background is:

$$(\mathbf{2.8 \pm 0.3}) \cdot \mathbf{10^{-5}\ events/kg/day/keV}_{ee},$$

corresponding to

$$\mathbf{102 \pm 11\ events/y}\ \text{(in 1 tonne FV)}.$$

From this study it results that the main contribution to the ER background, considering the WIMP search energy region, comes from the intrinsic sources, figure 6.12 and table 6.5. Using also the information from the ER background behavior, as function of the fiducial mass, the main results of the present work can be summarized as follows (Section 6.5):

- in [2, 12] keV$_{ee}$ and in 1 tonne fiducial volume the main contributions to the ER background come from ^{222}Rn, solar neutrinos and ^{85}Kr (figures 6.12 - 6.16);
- for energies above 300 keV$_{ee}$, in 1 tonne fiducial volume, the detector materials give the highest contribution (figure 6.13).
- in [2, 12] keV$_{ee}$ and for fiducial volumes larger than 1400 kg, the background from detector materials becomes dominant (figure 6.17);
- in the energy range [20, 300] keV$_{ee}$, in 1 tonne fiducial volume, the $2\nu2\beta$ decay of the ^{136}Xe becomes dominant (figures 6.13 and 6.14).

For what concerns the NR background (Section 6.6), its contribution to the total background has been evaluated in:

$$\mathbf{0.5 \pm 0.1\ events/y}\ \text{(in 1 tonne FV)}.$$

The largest fraction of background events comes from the Cryostat SS (28%), PMTs (23%, mostly from the ceramic stem), PTFE (18%), PMT bases (12%), SS of the TPC (10%) and of the Bottom Filler (8%), figure 6.21.
The contribution from cosmogenic neutrons is negligible (Section 6.6.2). Thanks to the Muon Veto system of XENON1T [204] (Section 4.4.1), the background from muon induced neutrons is below 0.01 ev/y in 1 tonne fiducial volume inside the WIMP search energy region.
Due to the different light yield of ER and NR (Sections 3.4 - 3.6), it has been performed a conversion of the total ER and NR background recoil spectra from energy to S1 signal (pe). This permitted to sum them on a common scale (Section 6.7), thus allowing the evaluation of the total background of the XENON1T experiment. For the conversion of the ER, it was used the NEST model, figure 6.24, while for NR we used the light and charge yields evaluated in the XENON100 experiment [221], figures 6.25 and 6.26.
For the sensitivity evaluation, the expected WIMP recoil spectra for different dark matter masses, from 5 GeV/c^2 up to 1000 GeV/c^2, have been used (Section 7.1). The study of the sensitivity of the XENON1T experiment has been carried out by using the *Maximum Gap method* [181] (Section 7.2). It is a recursive method used to test the different values of the WIMP-nucleon interaction cross section until the desired CL is reached. To achieve a sensitivity to WIMP-nucleon cross section of the order 10^{-47} cm^2, that is the XENON1T goal, about 1 background event in the fiducial volume is required. Assuming the same particle discrimination obtained in XENON100, figure 4.16, it was considered in the computation a 99.75% rejection level for ER, that corresponds to a 40% acceptance for NR. With a light yield of 4.6 pe/keV$_{ee}$ (Section 7.3) the WIMP search region is

[3, 70] pe and the total background events, in 2 tonne-years of FV, resulted in 1.17. For such a case, the sensitivity, considering a 90% CL, is shown in figure 7.8. This analysis permitted to find the minimum of the cross section at:

$$\sigma = \mathbf{1.87 \cdot 10^{-47}\ cm^2} \text{ at } \mathbf{m_\chi = 45\ GeV/c^2}.$$

The study was also extended to evaluate the sensitivity for a higher light yield: LY = 5.6 pe/keV$_{ee}$ (Section 7.4, figure 7.12). In such a case, the WIMP search region becomes [3, 85] pe and number of background events is 1.21. The analysis showed the minimum for the cross section at:

$$\sigma = \mathbf{1.79 \cdot 10^{-47}\ cm^2} \text{ at } \mathbf{m_\chi = 40\ GeV/c^2}.$$

The presented results have been obtained setting the relative scintillation efficiency, $\mathcal{L}_{eff}$, to 0 (figure 3.19), for recoil energies below 3 keV$_r$. The analysis of the XENON1T sensitivity has also been performed by using an extrapolation of the $\mathcal{L}_{eff}$ down to 1 keV$_r$, figures 7.9 and 7.13; the results have been compared with the previous sensitivity studies (figures 7.10 and 7.14), showing an improvement for WIMP masses < 20 GeV/c^2. In order to evaluate the impact of the intrinsic background, where it was first assumed a contamination of 1 μBq/kg for the ^{222}Rn that represents the actual XENON1T goal, the sensitivity study was extended to contaminations of ^{222}Rn as high as 3 and 10 μBq/kg (Section 7.5), figures 7.15 - 7.17. The minima for the cross section have been found at $\mathbf{2.15 \cdot 10^{-47}\ cm^2}$ and $\mathbf{2.94 \cdot 10^{-47}\ cm^2}$ both at a WIMP of mass $\mathbf{40\ GeV/c^2}$ for 3 and 10 μBq/kg contaminations, respectively. The last study on the sensitivity has been conducted assuming different values for the exposure time: in 5 t-y the sensitivity reaches a minimum at $\mathbf{1.40 \cdot 10^{-47}\ cm^2}$ for $\mathbf{m_\chi = 45\ GeV/c^2}$, figures 7.19 - 7.24.
To have an independent check of the results obtained with the Maximum Gap analysis, the sensitivity of XENON1T has also been evaluated using the *Likelihood Ratio* (Section 7.7). The method is used to test signal hypotheses, H_{μ_s}, assuming different values on the cross section for WIMP-nucleon interactions, against the background-only hypothesis, H_0. To do that, the required test statistic is given by the ratio of the likelihood under H_{μ_s} and H_0.

For the analysis we considered: LY= 4.6 pe/keV$_{ee}$, 1 μBq/kg of ^{222}Rn contamination and the $\mathcal{L}_{eff} = 0$ for recoil energies below 1 keV$_r$. We did not apply any discrimination cut to select NR; we used the whole sample of events considering for each event its probability to be signal or background (figure 7.25). At the end of the analysis the minimum for the sensitivity has been found at $\sigma = \mathbf{1.21 \cdot 10^{-47}\ cm^2}$, for $\mathbf{m_\chi = 40\ GeV/c^2}$. The result differs by less than a factor 2 with respect to what obtained with the Maximum Gap method; we consider it an acceptable agreement given the intrinsic

differences in the two statistical methods. So far, we did not take into account the uncertainty in the NR energy scale. We plan to continue the study of the sensitivity including the $\mathcal{L}_{eff}$ uncertainty as a nuisance parameter, using the full power of the *Profile Likelihood* method which is a natural extension of the Likelihood Ratio method.

From the study developed in my PhD thesis we can conclude that:

- thanks to a severe screening and purification campaign, to the LXe self-shielding and particle discrimination abilities, the goal of having about 1 background event in the reference 1 tonne fiducial volume and in 2 years of exposure can be reached;
- having such a low background, the XENON1T experiment will be sensitive to WIMP-nucleon scattering cross section of $\mathbf{1.87 \cdot 10^{-47}\ cm^2}$ at $\mathbf{m_\chi = 45\ GeV/c^2}$, with 90% CL, about two orders of magnitude better than the current experiments;
- the results from the Maximum Gap method have been confirmed by the Likelihood Ratio method, thus giving more robustness to such results.

A final comparison, between the limits from various experiments is shown in figure 7.27. The orange dashed line represents the neutrino coherent bound, below which the NR from neutrinos will be the dominant background process. It represents an irreducible source of events since it mimics a WIMP-nucleon interaction and new detection techniques will be required to probe lower values of the cross section.

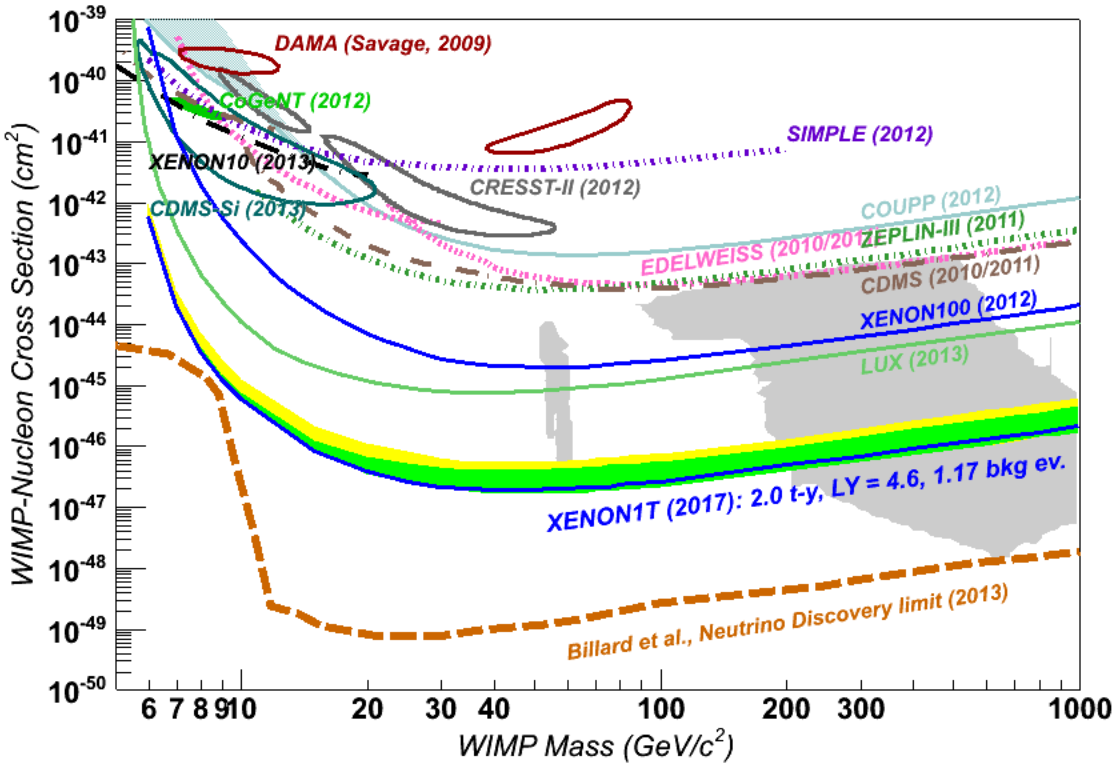

Figure 7.27: Comparison between sensitivities, at 90% CL from different experiment: DAMA exclusion region (dark red), XENON100 (blue), LUX (green), XENON1T (red dashed), XENONnT (black dashed) and the neutrino bound (orange dashed). Also superimposed is the XENON1T sensitivity (yellow and green bands with the solid blue curve inside) evaluated with the Maximum Gap method assuming: LY = 4.6 pe/keV$_{ee}$, 1.17 background events (corresponding to 1 μBq/kg of ^{222}Rn contamination) and a $\mathcal{L}_{eff}$ set to 0 for recoil energies below 3 keV$_r$ and a 2 tonne-years exposure time.

Bibliography

[1] N. Jarosik et al., Seven-Year Wilkinson Microwave Anisotropy Probe (WMAP) Observations: Sky Maps, Systematic Errors, and Basic Results, ApJS **192**, 14 (2011).

[2] G. R. Blumenthal et al., Formation of galaxies and large-scale structure with cold dark matter, Nature **311**, 517-525 (1984).

[3] M. Davis et al., The evolution of large-scale structure in a universe dominated by cold dark matter, ApJ **292**, 371-394 (1985).

[4] D. Clowe et al., A direct empirical proof of the existence of dark matter, ApJ **648**, 109 (2006).

[5] C. L. Bennett et al., Nine-year Wilkinson Microwave Anisotropy Probe (WMAP) Observations: Final Maps and Results, ApJS **208**, 20 (2013).

[6] P. Ade et al., Planck 2013 results. XVI. Cosmological parameters, A&A **571**, A16 (2014).

[7] G. Jungman, M. Kamionkowski and K. Griest, Supersymmetric Dark Matter, Phys. Rept. **267**, 195-373 (1996).

[8] E. Aprile et al., Dark Matter Results from 225 Live Days of XENON100 Data, Phys. Rev. Lett. **109**, 181301 (2012).

[9] E. Aprile et al., Limits on spin-dependent WIMP-nucleon cross sections from 225 live days of XENON100 data, Phys. Rev. Lett. **111**, 021301 (2013).

[10] D. S. Akerib et al., First results from the LUX dark matter experiment at the Sanford Underground Research Facility, Phys. Rev. Lett. **112**, 091303 (2014).

[11] E. Aprile et al., The XENON1T Dark Matter Search Experiment, arXiv:1206.6288 [astro-ph.IM].

[12] E. Aprile et al., Study of the electromagnetic background in the XENON100 experiment, Erratum: Phys. Rev. Lett. **D 85**, 029904 (2012).

[13] E. Armengaud et al., Background studies for the EDELWEISS Drak Matter Experiment, Astropart. Phys. **47**, 1-9 (2013).

[14] D. S. Akerib et al., Radiogenic and Muon-Induced Backgrounds in the LUX Dark Matter Detector, Astropart. Phys. **62**, 33-46 (2015).

[15] E. Aprile et al., The neutron background of the XENON100 dark matter search experiment, J. Phys. G: Nucl. Part. Phys. **40**, 115201 (2013).

[16] Virginia Trimble, in D. Cline, ed.: *Sources of Dark Matter in the Universe*, (World Scientific, 1994).

[17] G. Dalba: *Il teorema del viriale*, www.science.unitn.it/ fisica1/fisica1/appunti/sparsi/viriale/viriale.pdf

[18] K. G. Begeman, A. H. Broeils and R. H. Sanders, Extended rotation curves of spiral galaxies - Dark haloes and modified dynamics, MNRAS (ISSN 0035-8711) **249**, 523-537 (1991).

[19] Massimo Meneghetti, teaching notes. http://pico.bo.astro.it/ massimo/pico/Teaching.html

[20] C. Alcock et al., The MACHO Project: Microlensing Results from 5.7 Years of LMC Observations, ApJ **542**, 281-307 (2000).

[21] A. A. Penzias and R. W. Wilson., A Measurement of excess antenna temperature at 4080-Mc/s, ApJ **142**, 419-421 (1965).

[22] C. L. Bennett et al., Nine-Year Wilkinson Microwave Anisotropy Probe (WMAP) Observations: Final Maps and Results, ApJS **208**, 20 (2013).

[23] R. Sachs and A. Wolfe, Perturbations of a Cosmological Model and Angular Variations of the Microwave Background, ApJ **147**, 73 (1967).

[24] P. A. R. Ade et al., Planck 2013 results. XV. CMB power spectra and likelihood, A&A **571**, A15 (2013).

[25] Lahav, Ofer et al., The Cosmological Parameters 2014, arXiv:1401.1389 [astro-ph.CO].

[26] R. A. Alpher, H. Bethe, and G. Gamow, The origin of chemical elements, Phys. Rev. **73**, 803-804 (1948).

[27] C. Amsler et al., The review of particle physics, Phys. Lett. **B 667**, 1 (2008).

[28] Y. I. Izotov et al., Helium abundance in the most metal-deficient blue compact galaxies: I Zw 18 and SBS 0335-052, ApJ **527**, 757-777 (1999).

[29] C. Charbonnel and F. Primas, The Lithium Content of the Galactic Halo Stars, A&A **442**, 961-992 (2005) astro-ph/0505247.

[30] J. P. Ostriker and P. J. E. Peebles, A Numerical Study of the Stability of Flattened Galaxies: or, can Cold Galaxies Survive?, ApJ **186**, 467-48O (1973).

[31] H.-C. Cheng, J. L. Feng and K. T. Matchev, Kaluza-Klein Dark Matter, Phys. Rev. Lett. **89**, 211301 (2002).

[32] S. Riemer-Sorensen, D. Parkinson and T. M. Davis, Combining Planck with Large Scale Structure gives strong neutrino mass constraint, Phys. Rev. **D 89**, 103505 (2014).

[33] J. R. Bond and A. S. Szalay, The collisionless damping of density fluctuations in an expanding universe, ApJ **274**, 443-468 (1983).

[34] M. S. Turner, Cosmic and local mass density of "invisible" axions, Phys. Rev. **D 33**, 889 (1986).

[35] K. Zioutas et al., First results from the cern axion solar telescope (cast), Phys. Rev. Lett. **94**, 121301 (2005).

[36] E. Zavattini et al., New PVLAS results and limits on magnetically induced optical rotation and ellipticity in vacuum., Phys. Rev. **D 77**, 032006 (2008).

[37] E. Aprile et al., First Axion Results from the XENON100 Experiment, Phys. Rev. **D 90**, 062009 (2014).

[38] M. Dine, W. Fischler, and M. Srednicki, A simple solution to the strong CP problem with a harmless axion, Phys. Lett **B 104**, 199-202 (1981).

[39] M. A. Shifman, A. I. Vainshtein, and V. I. Zakharov., Can confinement ensure natural CP invariance of strong interactions?, Nucl. Phys. B **166**, 493-506 (1980).

[40] T. Moroi, H. Murayama and M. Yamaguchi, Cosmological constraints on the light stable gravitino, Phys. Lett. **B 303**, 289-294 (1993).

[41] M. Bolz, A. Brandenburg and W. Buchmüller, Thermal production of Gravitinos, Nucl. Phys. **B 606**, 518-544 (2001).

[42] V. Berezinsky, M. Kachelriess and A. Vilenkin, Ultrahigh Energy Cosmic Rays without Greisen-Zatsepin-Kuzmin Cutoff, Phys. Rev. Lett. **79**, 4302 (1997).

[43] P. Gondolo, Phenomenological Introduction to Direct Dark Matter Detection, arXiv:hep-ph/9605290 [hep-ph].

[44] M. W. Goodman and E. Witten, Detectability of certain dark-matter candidates, Phys. Rev.**D 31**, 3059 (1985).

[45] T. Falk, K. A. Olive and M. Srednicki, Heavy Sneutrinos as Dark Matter, Phys. Lett. **B 339**, 248-251 (1994).

[46] R. Bernabei et al., The DAMA/LIBRA apparatus, Nucl. Instrum. Meth. **A 592**, 297-315 (2008).

[47] R. Bernabei et al., The Annual Modulation Signature for Dark Matter: DAMA/LIBRA-Phase1 Results and Perspectives, Advances in High Energy Physics **2014**, 605659 (2014).

[48] K. Blum, DAMA vs. the annually modulated muon background, arXiv:1110.0857 [astro-ph.HE].

[49] R. Bernabei et al., No role for muons in the DAMA annual modulation results, Eur. Phys. J. **C 72**, 2064 (2012).

[50] R. Bernabei et al., Final model independent result of DAMA/LIBRA-phase1, Eur. Phys. J. **C 73**, 2648 (2013).

[51] C. E. Aalseth et al., CoGeNT: A Search for Low-Mass Dark Matter using p-type Point Contact Germanium Detectors, Phys. Rev. **D 88**, 012002 (2013).

[52] S. Chang et al., CoGeNT Interpretation, JCAP **08**, 018 (2010).

[53] C. E. Aalseth et al., Search for An Annual Modulation in Three Years of CoGeNT Dark Matter Detector Data, arXiv:1401.3295v1 [astro-ph.CO].

[54] E. Armengaud et al., A search for low-mass WIMPs with EDELWEISS-II heat-and-ionization detectors, Phys. Rev. **D 86**, 051701(R) (2012).

[55] A. Broniatowski et al., A new high-background-rejection dark matter Ge cryogenic detector, Phys. Lett. **B 681**, 305-309 (2009).

[56] E. Armengaud et al., Final results of the EDELWEISS-II WIMP search using a 4-kg array of cryogenic germanium detectors with interleaved electrodes, Phys. Lett. **B 702**, 329-335 (2011).

[57] R. Bernabei et al., First results from DAMA/LIBRA and the combined results with DAMA/NaI, Eur. Phys. J. **C 56**, 333-335 (2008).

[58] G. Angloher et al., Results from 730 kg days of the CRESST-II Dark Matter Search, Eur. Phys. J. **C 72**, 1971 (2012).

[59] R. W. Schnee et al., The SuperCDMS Experiment, arXiv:astro-ph/0502435v1 [astro-ph].

[60] W. Rau et al., CDMS and SuperCDMS, J. Phys.: Conf. Ser. **375**, 012005 (2012).

[61] R. Agnese et al., Search for Low-Mass Weakly Interacting Massive Particles with SuperCDMS, Phys. Rev. Lett. **112**, 241302 (2014).

[62] R. Agnese et al., Silicon Detector Dark Matter Results from the Final Exposure of CDMS II, Phys. Rev. Lett. **111**, 251301 (2013).

[63] C. Savage et al., Compatibility of DAMA/LIBRA dark matter detection with other searches, JCAP **04**, 010 (2009).

[64] Z. Ahmed, et al., Results from the Final Exposure of the CDMS II Experiment, Science **327**, 1619 (2010).

[65] Z. Ahmed et al., Results from a Low-Energy Analysis of the CDMS II Germanium Data, Phys. Rev. Lett. **106**, 131302 (2011).

[66] R. Agnese et al., CDMSlite: A Search for Low-Mass WIMPs using Voltage-Assisted Calorimetric Ionization Detection in the SuperCDMS Experiment, Phys. Rev. Lett. **112**, 041302 (2014).

[67] J. Angle, et al., A search for light dark matter in XENON10 data, Phys. Rev. Lett. **107**, 051301 (2011).

[68] D. S. Akerib, X. Bai, S. Bedikian, The Large Underground Xenon (LUX) Experiment, Nucl. Inst. and Meth. in Phys. Res. **A 704**, 111-126 (2013).

[69] D. Akimov et al., WIMP-nucleon cross-section results from the second science run of ZEPLIN-III, Phys. Lett. **B 709**, 14-20 (2012).

[70] M. Felizardo et al., Final Analysis and Results of the Phase II SIMPLE Dark Matter Search, Phys. Rev. Lett. **108**, 201302 (2012).

[71] C. E. Aalseth et al., CoGeNT: A search for low-mass dark matter using p-type point contact germanium detectors, Phys. Rev. **D 88**, 012002 (2013).

[72] DM Tools - http://dmtools.brown.edu:8080/

[73] G. Angloher et al., Commissioning Run of the CRESST-II Dark Matter Search, Astrop. Phys. **31**, 270-276 (2009).

[74] G. Angloher et al., Results on low mass WIMPs using an upgraded CRESST-II detector, Eur. Phys. J. **C 74**, 3184 (2014).

[75] A. Brown et al., Extending the CRESST-II commissioning run limits to lower masses, Phys. Rev. Lett. **D 85**, 021301(R) (2012).

[76] A. Gütlein, *Feasibility Study for a First Observation of Coherent Neutrino Nucleus Scattering Using Low-Temperature Detectors*, Ph.D. thesis, Technische Universität München, 2013.

[77] G. Steigman et al., Weakly interacting massive particles and solar oscillations, Astron. **J83**, 1050-1061 (1978).

[78] D. N. Spergel and W. H. Press, Effect of hypothetical, weakly interacting, massive particles on energy transport in the solar interior, ApJ **294**, 663-673 (1985).

[79] R. Kappl, M. W. Winkler, New Limits on Dark Matter from Super-Kamiokande, Nucl. Phys. **B 850**, 505-521 (2011).

[80] G. Busoni, A. De Simone and W. C. Huang, On the Minimum Dark Matter Mass Testable by Neutrinos from the Sun, JCAP **1307**, 010 (2013).

[81] K. Griest and D. Seckel, Cosmic Asymmetry, Neutrinos and the Sun, Nucl. Phys. **B 283**, 681 (1987), 681.

[82] P. Cushman et al., Snowmass CF1 Summary: WIMP Dark Matter Direct Detection, arXiv:1310.8327 [hep-ex].

[83] C. Chian-Shu et al., Probing Dark Matter Self-Interaction in the Sun with IceCube-PINGU, JCAP **1410**, 10, 049 (2014).

[84] Shmuel Nussinov, Lian-Tao Wang and Itay Yavin , Capture of Inelastic Dark Matter in the Sun, JCAP **0908**, 037 (2009).

[85] F. W. Stecker, S. Rudaz and T. F. Walsh, Galactic anti-protons from photinos, Phys. Rev. Lett. **55**, 2622-2625 (1985).

[86] S. Rudaz and F. W. Stecker, Cosmic ray anti-protons, positrons and gamma-rays from halo dark matter annihilation, ApJ **325**, 16-25 (1988).

[87] L. Bergstrom, J. Edsjo and P. Ullio, Cosmic antiprotons as a probe for supersymmetric dark matter?, ApJ **526**, 215-235 (1999).

[88] M. Di Mauro et al., Interpretation of AMS-02 electrons and positrons data, JCAP **1404**, 006 (2014).

[89] S. A. I. Mognet et al., The Prototype GAPS (pGAPS) Experiment, Nucl. Instrum. Meth. **A735**, 24-38 (2014).

[90] H. Fuke et al., Search for Cosmic-Ray Antideuterons, Phys. Rev. Lett. **95**, 081101 (2005).

[91] H. Baer et al., Low energy antideuterons: shedding light on dark matter, JCAP **0512**, 008 (2005).

[92] A. Ibarra et al., Indirect Searches for Decaying Dark Matter, Int. J. Mod. Phys. **A 28**, 1330040 (2013).

[93] A. Ibarra and S. Wild, Determination of the cosmic antideuteron flux in a Monte Carlo approach, Phys. Rev. **D 88**, 023014 (2013).

[94] E. Aliu et al., VERITAS Deep Observations of the Dwarf Spheroidal Galaxy Segue 1, Phys. Rev. **D 85**, 062001 (2012).

[95] A. Ibarra, D. Tran and C. Weniger, Decaying dark matter in light of the PAMELA and Fermi LAT data, JCAP **01**, 009 (2010).

[96] S. Fukuda et al., The Super-Kamiokande detector, Nucl. Instrum. and Meth. **A 501**, 418-462 (2003).

[97] T. Tanaka et al., An Indirect Search for Weakly Interacting Massive Particles in the Sun Using 3109.6 Days of Upward-going Muons in Super-Kamiokande, ApJ **742**, 78 (2011).

[98] G. Wikström and J. Edsjö, Limits on the WIMP-nucleon scattering cross-section from neutrino telescopes, JCAP **0904**, 009 (2009).

[99] H. S. Lee et al., Limits on Interactions between Weakly Interacting Massive Particles and Nucleons Obtained with CsI(Tl) Crystal Detectors, Phys. Rev. Lett. **99**, 091301 (2007).

[100] S. Archambault et al., Dark Matter Spin-Dependent Limits for WIMP Interactions on ^{19}F by PICASSO, Phys. Lett. **B 682**, 185-192 (2009).

[101] J. Braun et al., Searches for WIMP Dark Matter from the Sun with AMANDA, arXiv:0906.1615 [astro-ph.HE].

[102] R. Kappl, M. Ratz and M. W. Winkler, Light dark matter in the singlet-extended MSSM, Phys. Lett. **B 695**, 169-173 (2001).

[103] W. B. Atwood et al., The Large Area Telescope on the Fermi Gamma-ray Space Telescope Mission, ApJ **697**, 1071-1102 (2009).

[104] G. Zaharijas, A. Morselli and E. Nuss, Fermi Large Area Telescope as a dark matter search tool, in Cosmology and Particle Physics beyond Standard Models: Ten Years of the SEENET-MTP Network, CERN-Proceedings-2014-001, pp.171-176 (2014).

[105] O. Adriani et al., PAMELA Results on the Cosmic-Ray Antiproton Flux from 60 MeV to 180 GeV in Kinetic Energy, Phys. Rev. Lett. **105**, 121101 (2010).

[106] A. A. Abdo et al., Measurement of the Cosmic Ray $e^+ + e^-$ Spectrum from 20 GeV to 1 TeV with the Fermi Large Area Telescope, Phys. Rev. Lett. **102**, 181101 (2009).

[107] M. Ackermann et al., Search for Gamma-ray Spectral Lines with the Fermi Large Area Telescope and Dark Matter Implications, Phys. Rev. **D 88**, 082002 (2013).

[108] R. Abbasi et al., Limits on a muon flux from neutralino annihilations in the Sun with the IceCube 22-string detector, Phys. Rev. Lett. **102**, 201302 (2009).

[109] G. Ingelman and M. Thunman, High energy neutrino production by cosmic ray interactions in the Sun, Phys. Rev. **D 54**, 4385-4392 (1996).

[110] R. Carsten et al., Superheavy dark matter and IceCube neutrino signals: bounds on decaying dark matter, arXiv:1408.4575.

[111] R. Abbasi et al., Search for dark matter from the Galactic halo with the IceCube Neutrino Telescope, Phys. Rev. **D 84**, 022004 (2011).

[112] M. Agullar et al., Electron and Positron Fluxes in Primary Cosmic Rays Measured with the Alpha Magnetic Spectrometer on the International Space Station, Phys. Rev. Lett. **113**, 121102 (2014).

[113] C. Qing-Hong et al., Leptophilic Dark Matter and AMS-02 Cosmic-ray Positron Flux, arXiv:1409.7317 [hep-ph].

[114] New results from the Alpha Magnetic Spectrometer on the International Space Station, PRESS RELEASE, AMS Collaboration, CERN, Geneva, 18 September 2014, http://www.ams02.org/2014/09/new-results-from-the-alpha-magnetic-spectrometer-on-the-international-space-station/

[115] A. Ibarra et al., Dark matter annihilations and decays after the AMS-02 positron measurements, Phys. Rev. **D 89**, 063539 (2014).

[116] M. Agullar et. al., First Result from the Alpha Magnetic Spectrometer on the International Space Station: Precision Measurement of the Positron Fraction in Primary Cosmic Rays of 0.5-350 GeV, Phys. Rev. Lett. **110**, 141102 (2013).

[117] M. A. DuVernois et. al., Cosmic ray electrons and positrons from 1-GeV to 100-GeV: Measurements with HEAT and their interpretation, ApJ **559**, 296-303 (2001).

[118] O. Adriani et. al., Cosmic-Ray Positron Energy Spectrum Measured by PAMELA, Phys. Rev. Lett. **111**, 081102 (2013).

[119] M. Ackermann et. al., Fermi LAT Search for Dark Matter in Gamma-ray Lines and the Inclusive Photon Spectrum, Phys. Rev. **D 86**, 022002 (2012).

[120] R. Bernabei et al., New results from DAMA/LIBRA, Eur. Phys. J. **C 67**, 39-49 (2010).

[121] C. E. Aalseth et al., Results from a Search for Light-Mass Dark Matter with a p-type Point Contact Germanium Detector, Phys. Rev. Lett. **106**, 131301 (2011).

[122] R. Agnese et al., Silicon Detector Dark Matter Results from the Final Exposure of CDMS II, Phys. Rev. Lett. **111**, 251301 (2013).

[123] Y. Bai and J. P. Fox, Resonant Dark Matter, JHEP **0911**, 052 (2009).

[124] T. Aaltonen et al., Search for Long-Lived Massive Charged Particles in 1.96 TeV $\overline{p}p$ Collisions, Phys. Rev. Lett. **103**, 021802 (2009).

[125] D. Smith and N. Weiner, Inelastic dark matter, Phys. Rev. **D 64**, 043502 (2001).

[126] S. Chang, N. Weiner and Itay Yavin, Magnetic Inelastic Dark Matter, Phys. Rev. **D 82**, 125011 (2010).

[127] M. T. Ressell and D. J. Dean, Spin-dependent neutralino-nucleus scattering for **A** $\sim$ **127** nuclei, Phys. Rev. **C 56**, 535 (1997).

[128] K. Sigurdson et al., Dark-matter electric and magnetic dipole moments, Phys. Rev. **D 70**, 083501 (2004).

[129] B. Batell, M. Pospelov, and A. Ritz, Direct Detection of Multi-component Secluded WIMPs, Phys.Rev. **D 79**, 115019 (2009).

[130] P. W. Graham, Exothermic Dark Matter, Phys. Rev. **D 82**, 063512 (2010).

[131] M. Pospelov, N. Weiner and I. Yavin, Dark Matter detection in two easy step, Phys. Rev. **D 89**, 055008 (2014).

[132] D. Smith and N. Weiner, Inelastic dark matter, Phys. Rev. **D 64**, 043502 (2001).

[133] J. L. Feng et al., Isospin-Violating Dark Matter, Phys. Lett. **B 703**, 124-127 (2011).

[134] S. Chatrchyan et al., Search for dark matter and large extra dimensions in monojet events in pp collisions at $\sqrt{s} = 7$ TeV, JHEP **1209**, 094 (2012).

[135] J. L. Feng et al., Xenophobic Dark Matter, Phys. Rev. **D 88**, 1, 015021 (2013).

[136] J. I. Collar and N. E. Fields, A Maximum Likelihood Analysis of Low-Energy CDMS Data, arXiv:1204.3559 [astro-ph.CO].

[137] D. S. Akerib et al., Technical Results from the Surface Run of the LUX Dark Matter Experiment, Astropart. Phys. **45**, 34-43 (2013).

[138] Mordehai Milgrom, MOND theory, arXiv:1404.7661 [astro-ph.CO].

[139] S. Trippe, The "Missing Mass Problem" in Astronomy and the Need for a Modified Law of Gravity, arXiv:1401.5904 [astro-ph.CO].

[140] G. Lake, Testing modifications of gravity, ApJ Lett. **345**, L17-L19 (1989).

[141] T. Randriamampandry and C. Carignan, Galaxy Mass Models: MOND versus Dark Matter Halos, Mon. Not. Roy. Astron. Soc. **439**, 2132 (2014).

[142] Se-H. Oh et al., High-resolution dark matter density profiles of THINGS dwarf galaxies: correcting for noncircular motions, The Astronomical Journal **136**, 2761 (2008).

[143] R. A. Swaters, R. H. Sanders, S. S. McGaugh, Testing Modified Newtonian Dynamics with Rotation Curves of Dwarf and Low Surface Brightness Galaxies, ApJ **718**, 380-391 (2010).

[144] A. Miceli1 et al., Liquid Xenon Detectors for Positron Emission Tomography, J. Phys.: Conf. Ser. **312**, 062006 (2011).

[145] http://www.webelements.com

[146] A. G. Manalaysay: *Studies of the Scintillation and Ionization Properties of the Liquid Xenon for Dark Matter Detection.*
Qualifying examination, Dept. of Physics, Univ. of Florida, Feb. 2006.
www.phys.ufl.edu/∼aaronm/qual/qual-eps.pdf

[147] J. Engel, Nuclear Form Factors for the Scattering of Weakly Interacting Massive Particles, Phys. Lett. **B 264**, 114-119 (1991).

[148] M. J. Berger, J. S. Coursey, M. A. Zucker, and J. Chang. *XCOM: Photon Cross Sections Database.*

[149] J. F. Ziegler, *Stopping and ranges of ions in matter. A collection of tools for calculating the transport of ions in matter.*

[150] A. Hitachi, Properties of liquid xenon scintillation for dark matter searches, Astropart. Phys. **24**, 247-256 (2005).

[151] S. Kubota et al., Recombination luminescence in liquid argon and in liquid xenon, Phys. Rev. **B 17**, 2762 (1978).

[152] U. Fano, Ionization Yield of Radiations. II. The Fluctuations of the Number of Ions, Phys. Rev. **72**, 26 (1947).

[153] K. Masuda, T. Doke and T. Takahashi, A liquid xenon position sensitive gamma-ray detector for positron annihilation experiments, Nucl. Instr. Methods **188**, 629-638 (1981).

[154] T. Doke et al., Absolute Scintillation Yields in Liquid Argon and Xenon for Various Particles, Jpn. J. Appl. Phys. **41**, 1538 (2002).

[155] G. Bakale, U. Sowada and W. F. Schmidt, Effect of an electric field on electron attachment to sulfur hexafluoride, nitrous oxide, and molecular oxygen in liquid argon and xenon, J. Phys. Chem. **80**, 2556-2559 (1976).

[156] J. B. Birks, *The Theory and Practice of Scintillation Counting*, (Pergamon, Oxford,1964).

[157] A. Hitachi, T. Doke and A. Mozumder, Luminescence quenching in liquid argon under charged-particle impact: Relative scintillation yield at different linear energy transfers, Phys. Rev. **B 46**, 11463 (1992).

[158] A. Hitachi et al., Effect of ionization density on the time dependence of luminescence from liquid argon and xenon, Phys. Rev. **B 27**, 5279 (1983).

[159] R. Platzman, Total ionization in gases by high-energy particles - an appraisal of our understanding, Int. J. of App. Rad. and Isot. **10**, 116-127 (1961).

[160] J. Thomas and D. A. Imel, Recombination of electron-ion pairs in liquid argon and liquid xenon, Phys. Rev. **A 36**, 614 (1987).

[161] S. Kubota et al., Dynamical behavior of free electrons in the recombination process in liquid argon, krypton, and xenon, Phys. Rev. **B 20**, 3486-3496 (1979).

[162] E. Aprile et al., Observation of Anti-correlation Between Scintillation and Ionization for MeV Gamma Rays in Liquid Xenon, Phys. Rev. **B 76**, 014115 (2007).

[163] S. Belogurov et al.,*High Pressure Gas Scintillation Drift Chamber With Photomultipliers Inside of Working Medium*,
Nuclear Science Symposium and Medical Imaging Conference Record, vol. 1, pp. 519-523 (1995).

[164] B. Edwards et al., Measurement of Single Electron Emission in Two-Phase Xenon, Astropart. Phys. **30**, 54-57 (2008).

[165] L. D. Landau and E. M. Lifshitz, *Electrodynamics of Continuous Media*, Butterworth-Heinemann, Oxford, second edition, 1984.

[166] E. Aprile and T. Doke, Liquid xenon detectors for particle physics and astrophysics, Rev. Mod. Phys. **82**, 2053-2097 (2010).

[167] L. M. Barkov et al., Measurement of the refractive index of liquid xenon for intrinsic scintillation light, Nucl. Instrum. Meth. **A 379**, 482-483 (1996).

[168] E. Aprile et al., Observation of anticorrelation between scintillation and ionization for MeV gamma rays in liquid xenon, Phys. Rev. **B 76**, 014115 (2007).

[169] J. Lindhard et al., Integral Equations Governing Radiation Effects, Mat. Fys. Medd **33**, 10 (1963).

[170] G. Plante et al., New measurement of the scintillation efficiency of low-energy nuclear recoils in liquid xenon, Phys. Rev. **C 84**, 045805 (2011).

[171] F. Arneodo et al., Scintillation Efficiency of nuclear recoil in Liquid Xenon, Nucl. Instrum. Meth. **A 449**, 147 (2000).

[172] E. Aprile et al., Design and Performance of the XENON10 Dark Matter Experiment, Astropart. Phys. **34**, 679-698 (2011).

[173] E. Aprile et al., The XENON100 Dark Matter Experiment, Astropart. Phys. **35**, 573-590 (2012).

[174] http://www.hamamatsu.com/

[175] J. Angle et al., First Results from the XENON10 Dark Matter Experimentat the Gran Sasso National Laboratory, Phys. Rev. Lett. **100**, 021303 (2008).

[176] J. Angle et al., Limits on Spin-Dependent WIMP-Nucleon Cross Sections from the XENON10 Experiment, Phys. Rev. Lett. **101**, 091301 (2008).

[177] D. S. Akerib et al., Limits on Spin-Independent Interactions of Weakly Interacting Massive Particles with Nucleons from the Two-Tower Run of the Cryogenic Dark Matter Search, Phys. Rev. Lett **96**, 011302 (2006).

[178] A. Manzur et al., Scintillation efficiency and ionization yield of liquid xenon for monoenergetic nuclear recoils down to 4 keV, Phys. Rev. **C 81**, 025808 (2010).

[179] P. Sorensen et al., *Lowering the low-energy threshold of xenon detectors*, Proceedings of Science, PoS (IDM2010) 017.

[180] E. Aprile et al., Simultaneous Measurement of Ionization and Scintillation from Nuclear Recoils in Liquid Xenon for a Dark Matter Experiment, Phys. Rev. Lett. **97**, 081302 (2006).

[181] S. Yellin, Finding an Upper Limit in the Presence of Unknown Background, Phys. Rev. **D 66**, 032005 (2002).

[182] D. S. Akerib et al., Low-threshold analysis of CDMS shallow-site data, Phys. Rev. **D 82**, 122004 (2010).

[183] E. Aprile et al., First Dark Matter Results from the XENON100 Experiment, Phys. Rev. Lett. **105**, 131302 (2010).

[184] C. Savage et al., XENON10/100 dark matter constraints in comparison with CoGeNT and DAMA: Examining the Leff dependence, Phys. Rev. **D 83**, 055002 (2011).

[185] V. N. Solotov et al., Measurement of the refractive index and attenuation length of liquid xenon for its scintillation light, Nucl. Instr. Meth. Phys. Res. Sect. **A 516**, 462-474 (2004).

[186] E. Aprile et al., Likelihood approach to the first dark matter results from XENON100, Phys. Rev. **D 84**, 052003 (2011).

[187] A. Fowlie et al., Constrained MSSM favoring new territories: The impact of new LHC limits and a 125 GeV Higgs boson, Phys. Rev. **D 86**, 075010 (2012).

[188] J. Menendez, D. Gazit and A. Schwenk, Spin-dependent WIMP scattering off nuclei, Phys. Rev. **D 86**, 103511 (2012).

[189] Z. Ahmed et al., Search for Weakly Interacting Massive Particles with the First Five-Tower Data from the Cryogenic Dark Matter Search at the Soudan Underground Laboratory, Phys. Rev. Lett. **102**, 011301 (2009).

[190] P. Toivanen et al., Large-scale shell-model calculations of elastic and inelastic scattering rates of lightest supersymmetric particles (LSP) on ^{127}I, ^{129}Xe, ^{131}Xe, ^{133}Cs nuclei, Phys. Rev. **C 79**, 044302 (2009).

[191] S. Archambault et al., Constraints on Low-Mass WIMP Interactions on 19F from PICASSO, Phys. Lett. **B 711**, 153-161 (2012).

[192] E. Behnke et al., First dark matter search results from a 4-kg CF_3I bubble chamber operated in a deep underground site, Phys. Rev. **D 86**, 052001 (2012).

[193] M. Felizardo et al., Final Analysis and Results of the Phase II SIMPLE Dark Matter Search, Phys. Rev. Lett. **108**, 201302 (2012).

[194] S. C. Kim et al., New Limits on Interactions between Weakly Interacting Massive Particles and Nucleons Obtained with CsI(Tl) Crystal Detectors, Phys. Rev. Lett. **108**, 181301 (2012).

[195] M. G. Aartsen et al., Search for Dark Matter Annihilations in the Sun with the 79-String IceCube Detector, Phys. Rev. Lett. **110**, 131302 (2013).

[196] S. Dimopoulos, G. D. Starkman and B. W. Lynn., Atomic enhancements in the detection of weakly interacting particles, Phys. Lett. **B 168**, 145-150 (1986).

[197] E. Armengaud et al., Axion searches with the EDELWEISS-II experiment, JCAP **1311**, 067 (2013).

[198] K. Abe et al., Search for solar axions in XMASS, a large liquid-xenon detector, Phys. Lett. B **724**, 46-50 (2013).

[199] A. Derbin et al., Constraints on the axion-electron coupling constant for solar axions appearing owing to bremsstrahlung and the compton process, JETP Lett. **95**, 339-344 (2012).

[200] P. Gondolo and G. G. Raffelt, Solar neutrino limit on axions and keV-mass bosons, Phys. Rev. **D 79**, 107301 (2009).

[201] N. Viaux, Neutrino and Axion Bounds from the Globular Cluster M5 (NGC 5904), Phys. Rev. Lett. **111**, 231301 (2013).

[202] M. Aglietta et al., Muon depth-intensity relation measured by LVD underground experiment andcosmic-ray muon spectrum at sea level, Phys. Rev. **D 58**, 092005 (1998).

[203] M. Ambrosio et al., Measurement of the residual energy of muons in the Gran Sasso underground Laboratories, Astropart. Phys. **19**, 313-328 (2003).

[204] E. Aprile et al., Conceptual design and simulation of a water Cherenkov muon veto for the XENON1T experiment, JINST **9**, P11006 (2014).

[205] G. Heusser et al., ^{222}Rn detection at the μBq/m3 range in nitrogen gas and a new Rn purification technique for liquid nitrogen, App. Rad. Isot. **52**, 691-695 (2000).

[206] L. Baudis et al., Gator: a low-background counting facility at the Gran Sasso Underground Laboratory, JINST **6**, P08010 (2011).

[207] X. Du et al., An atom trap system for practical ^{81}Kr dating, Rev. Sci. Instrum. **75**, 3224 (2004)

[208] J. N. Bachall and C. Pena-Garay, Solar models and solar neutrino oscillations, New J. Phys. **6**, 63 (2004).

[209] M. Auger et al., Search for Neutrinoless Double-Beta Decay in ^{136}Xe with EXO-200, Phys. Rev. Lett. **109**, 032505 (2012).

[210] K. Zuber, On the physics of massive neutrinos, Phys. Rept. **305**, 295-364 (1998).

[211] O. A. Ponkratenko, V. I. Tretyak and Y. G. Zdesenko, The event generator DECAY4 for simulation of double beta processes and decay of radioactive nuclei, Phys. Atom. Nucl. **63**, 1282-1287 (2000).

[212] M. Agostini et al., Measurement of the half-life of the two-neutrino double beta decay of ^{76}Ge with the GERDA experiment, J. Phys. G: Nucl. Part. Phys. **40**, 035110 (2013).

[213] W.B. Wilson et al. SOURCES-4A, Technical Report LA-441 13539-MS, Los Alamos (1999).

[214] M. J. Carson et al., Neutron background in large-scale xenon detectors for dark matter searches, Astropart. Phys. **21**, 667-687 (2004).

[215] M. Selvi: *Review of Monte Carlo simulations for backgrounds from radioactivity*, Proceedings of the Low Radioactivity Techniques 2013 (LRT 2013) Workshop, April 2013, LNGS, Italy. AIP Conference Proceedings Volume 1549, page 213.

[216] D. Mei, C. Zhang, and A. Hime, Evaluation of (α, n) image induced neutrons as a background for dark matter experiments, Nucl. Instr. Meth. Phys. Res. Sect. **A 606**, 651-660 (2009).

[217] M. Szydagis et al., NEST: a comprehensive model for scintillation yield in liquid xenon, JINST **6**, P10002 (2011).

[218] M. Szydagis et al., Enhancement of NEST Capabilities for Simulating Low Energy Recoils in Liquid Xenon, JINST **8**, C10003 (2013).

[219] http://nest.physics.ucdavis.edu/site/

[220] E. Aprile et al., Simultaneous Measurement of Ionization and Scintillation from Nuclear Recoils in Liquid Xenon as Target for a Dark Matter Experiment, Phys. Rev. Lett. **97**, 081302 (2006).

[221] E. Aprile et al., Response of the XENON100 Dark Matter Detector to Nuclear Recoils, Phys. Rev. **D 88**, 012006 (2013).

[222] E. Aprile et al., Observation and applications of single-electron charge signals in the XENON100 experiment, J. Phys. G: Nucl. Part. Phys. **41**, 035201 (2014)

[223] E. I. Gates, G. Gyuk, and M. S. Turner, The Local Halo Density, ApJ **449**, L123-126 (1995).

[224] J. D. Lewin and P. F. Smith, Review of mathematics, numerical factors, and corrections for dark matter experiments based on elastic nuclear recoil, Astropart. Phys. **6**, 87-112 (1996).

[225] J. Engel, Nuclear Form Factors for the Scattering of Weakly Interacting Massive Particles, Phys. Lett. **B 264**, 114-119 (1991).

[226] J. Engel, S. Pittel and P. Vogel, Nuclear Physics of Dark Matter Detection, Int. J. Mod. Phys. **E 1**, 1-37 (1992).

[227] D. R. Tovey et al., A New Model-Independent Method for Extracting Spin-Dependent Cross Section Limits from Dark Matter Searches, Phys.Lett. **B 488**, 17-26 (2000).

[228] Glen Cowan, *Discovery sensitivity for a counting experiment with background uncertainty*, draft 1.1, 30 May (2012).

[229] G. J. Feldman and D. Cousins, A Unified Approach to the Classical Statistical Analysis of Small Signals, Phys. Rev. **D 57**, 3873-3889 (1998).

[230] T. Junk, Confidence Level Computation for Combining Searches with Small Statistics, Nucl. Instrum. Meth. **A 434**, 435-443 (1999).

[231] A. L. Read, Presentation of search results: The CL(s) technique, J. Phys. **G 28**, 2693-2704 (2002).

[232] S. S. Wilks, The Large-Sample Distribution of the Likelihood Ratio for Testing Composite Hypotheses, Ann. Math. Statist. **9**, 60-62 (1938).